An extended zero-dimensional simulation for HPCR diesel engines

Arya, Shahram Khalil

Award date:
2002

Awarding institution:
University of Bath

AN EXTENDED ZERO-DIMENSIONAL SIMULATION FOR HPCR DIESEL ENGINES

Submitted by Shahram Khalil Arya
for the degree of Ph.D.
of the University of Bath

February 2002

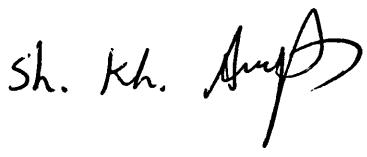

ProQuest LLC
789 East Eisenhower Parkway
P.O. Box 1346
Ann Arbor, MI 48106-1346

I dedicate this work to:

my wife for her patient, encouragement and moral support during the course of this work,

and my son and daughter for accepting me as a part time father during this period.

ABSTRACT

The objective of the present work was to develop the existing ODES code, using an essentially zero-dimensional approach to provide detailed insights into the internal processes of the modern high speed direct injection (HSDI) Diesel engine with high pressure common rail (HPCR) fuel injection. Therefore, this work has concentrated on the development of new submodels for incorporation in an extended form of ODES, as follows:

- The Marzouk-Watson semi-empirical heat release formulation has been replaced by a new fully analytical model for diffusion burning under medium to high load conditions and represents a development of the work of Chmela and Orthaber.
- The Wolfer ignition delay period formulation which does not account explicitly for injection conditions and was developed for engines with relatively low injection pressures has been replaced by a comprehensive semi-analytical model based in part on the work of Siebers and Higgins on the concept of lift-off length.
- A phenomenological fuel spray propagation and entrainment model for non-evaporating, evaporating and ultimately combusting sprays, both in undeflected and deflected form.
- A generalized analytical model for swirl generation in combustion bowl of various geometries, starting with a known swirl ratio at inlet valve closing (IVC). The swirl model, in turn, interacts and is part of, a combined spray-swirl model.
- Finally, all new submodels have been fully integrated into a new comprehensive simulation package designated ODES 4-4.

The code has been extensively validated with respect to performance and heat release against experimental limiting torque curve (LTC) results obtained on a 1.8 litre HSDI Diesel engine with HPCR fuel injection.

In the absence of optical access to the combustion space the predictions concerning swirl and spray/swirl interactions cannot be correlated with experimental results but could be checked independently against predictions from appropriate CFD codes.

ACKNOWLEDGMENTS

I would like to express my sincere gratitude to my supervisor Prof. F.J.Wallace, for his kind guidance, valuable comments and suggestions, constructive criticism and continued support throughout this research and his patience during the writing-up period.

I am grateful to my other supervisor Dr. J. Gary Hawley for his continuous guidance and support throughout my research and his thorough review of the manuscript.

My special thanks to Mr. Allan Cox for the provision of experimental data and his generous co-operation throughout the AVL software work, and also to Mr. David Barker and Mr. Duncan Green for their support on computer matters.

I owe many thanks to my officemates, Dr. Niall Campbell, Dr. Kevin Robinson, Mr. Matthew Leathard, Mr. Alexious Vagenas and Mr. Won Tae Kim for providing a friendly and comfortable space during this work.

Finally, I take the opportunity to gratefully acknowledge the generous financial support provided by the Ministry of Science, Research and Technology of Islamic Republic of Iran.

CONTENTS

PART 2: DEVELOPMENT OF NEW SUBMODELS

Section 1: Spray and swirl modelling under motoring conditions

APPENDIXES

NOMENCLATURE

Upper case

A_N	Nozzle hole area
B	Bore
C_a	Area contraction coefficient
C_d	Discharge coefficient
C_f	Drag coefficient
C_n	Effective needle discharge [equ. (5.2)]
C_v	Velocity coefficient
D	Diameter
D_N	Nozzle diameter
D_{ig}	Duration of ignition delay
D_{inj}	Duration of injection
E	Entrainment
E_a	Activation energy
KE	Kinetic energy
L_0	Lift-off length
M	Momentum
N	Number of zone
N_e	Engine speed
NO, NO_2, NO_x	Oxides of nitrogen
R	Radius,
	Gas constant
S	Stroke
T	Temperature
V	Volume

Lower case

f	Friction factor

k_1.....k_4	Scale factors in Marzouk-Watson model,
	Reaction constants [equ. (2.32)]
m	Mass
$\dot{m}$	Mass flow rate
p	Pressure
s	Spray tip penetration distance
t	Time
t^+	Time scale [equ. (3.25)]
u	Specific internal energy
v	Specific volume,
	Velocity
v_1	Spray mean velocity based on NO_x model
v_2	Spray mean velocity based on phenomenological model
w_{p1},w_{p2}	Adjustable coefficient for premixed combustion
w_{D1},w_{D2}	Adjustable coefficient for diffusion combustion
x	Distance
x^+	Length scale [equ.(5.13)]

Greek Characters

α	Angle
α_h	Fuel mass fraction relative to total injected fuel mass
α_k	Fraction of kinetic energy dissipation relative to total kinetic energy
Δ	Difference
δ	Adjustable constant [equ. (6.27)]
ϕ	Equivalence ratio
γ	Specific heat ratio c_p/c_v
μ_l	Viscosity
θ	Spray cone half angle,
	Angle
ρ	Density
σ_l	Surface tension [equ. (3.14)]
τ	Shear stress,

	Dimensionless time
ω	Swirl angular velocity
ζ_{st}	Stoichiometric air [equ. (5.12)]

Subscripts

a	Air
b	BOWL,
	Burned gas,
	Break-up
cyl	Cylinder
com	Combustion
e	Entrainment
f	Fuel,
	Friction
g	Gas
id	Ignition delay
ig	Ignition
inj	Injection
l	Liquid
m	Main cylinder
max	Maximum
min	Minimum
sp	Spray
tot	Total
u	Unburned,
	Undeflected
z	Zone

Abbreviations

ATDC	After top-dead-centre
ASI	After start of injection
BTDC	Before top-dead-centre

bsfc	Brake specific fuel consumption
CA	Crank angle
CFD	Computational fluid dynamic
CR	Common rail
DI	Direct injection
equ.	Equation
EVC	Exhaust valve closure
EMAT	Simple component matching model
HPCR	High-pressure common rail
HR	Heat release
HSDI	High-speed direct injection
IVC	Intake valve closure
LTC	Limited torque curve
ODES	Otto-Diesel engine simulation code
PLN	Pump-line-nozzle
ROHR	Rate of heat release
SoI	Start of injection
SR	Swirl ratio
VCO	Valve covered orifice

LIST OF TABLES

LIST OF FIGURES

Chapter 4

Chapter 5

Chapter 6

Chapter 7

Chapter 8

Chapter 9

CHAPTER 1

Objective of project and outline of thesis contents

1.1 Objective of project

Cycle simulation programs for Diesel engines have been in use for some 40 years, and have become increasingly sophisticated as our knowledge of the internal processes-gas exchange, heat transfer and especially combustion- has grown.

At the University of Bath an essentially conventional "zero-dimensional" filling-and-emptying model designated 'ODES' (Otto-Diesel-Engine-Simulation) using the *Marzouk-Watson* shape functions for heat release [1] and a very flexible structure to accommodate both two stroke and four stroke engines with a wide variety of turbo-charging and compounding configurations, has been used as the standard in-house code to support a wide range of research projects.

Numerous additions have been made to the basic code by previous workers, including a relatively simple multi-zone model, which dispenses with the need for spatial definitions of individual zones, for the prediction of nitric oxide formation [2].

- **Primary objective of present work**

The primary objective of the present work was to develop the existing ODES code, still using an essentially zero-dimensional approach to provide detailed insights into the internal processes of the modern high speed direct injection (HSDI) Diesel engine with high pressure common rail (HPCR) fuel injection. At present such insights can only be provided by much more complex quasi-dimensional, i.e. multi-zone combustion models with spatial definitions of individual zones, *Watson and Meguerdichian* [3], or by fully 3-dimensional CFD models, such as the codes developed by *Gosman and co-workers* [4] at Imperial college or the various KIVA codes developed in the USA [5].

The present project has therefore concentrated on the development of new submodels for incorporation in an extended form of ODES, as follows:

1. A phenomenological fuel spray propagation and entrainment model for non-evaporating, evaporating and ultimately combusting sprays, both in undeflected and deflected form.
2. A generalized analytical model for swirl generation in combustion bowl of various geometries, starting with a known swirl ratio at inlet valve closing (IVC).
3. A phenomenological model for spray-swirl interaction.
4. A new model for ignition delay for engines with HPCR injection systems to replace existing empirical formulations such as *Wolfer* [6] based on earlier low or medium pressure pump-line-nozzle (PLN) systems.
5. A new wholly analytical model for heat release predictions for engines with HPCR injection systems in which diffusion burning is dominant at medium to high loads.

- **Secondary objective of present work**

The secondary objective of the present work was the validation of the new program against experimental performance and heat release results on the limiting torque curve (LTC) obtained on a 1.8 litre HSDI Diesel engine with HPCR fuel injection.

1.2 Structure of thesis

The thesis is presented in three parts.

Part 1: Introduction

Chapter 1: Objective of present work and outline of thesis contents

Chapter 2: A survey of Diesel cycle simulation

Part 2: Development of new submodels

Section 1: Spray and swirl modelling under non-combusting conditions

Chapter 3: Spray modelling

A survey of existing experimental and analytical techniques followed by a comprehensive new phenomenological model for propagation and entrainment of non-combusting sprays, in undeflected or deflected form.

Chapter 4: Swirl generation in combustion bowl under motoring conditions

A comprehensive analytical model based on the principle of conservation of angular momentum, tracing the simultaneous development of in-cylinder and in-bowl swirl. Two basic bowl geometries are investigated.

Section 2: Combustion modelling

Chapter 5: Injection conditions and ignition delay

A previously existing formulation incorporated in ODES, calculates ignition delay based on the *Wolfer* [6] correlation, which refer to pump-line-nozzle systems with lower injection pressures.

A new ignition delay formulation has been developed based on lift-off-length due to *Siebers* and *Higgins* [7], appropriate to HPCR fuel injection systems.

Chapter 6: A new analytical heat release model for engines

Based on the work of *Chmela and Orthaber* [8], a wholly analytical solution of the heat release process assuming diffusion burning to be dominant has been developed.

Chapter 7: Calibration of new heat release model

Calibration against limiting torque curve (LTC) results for performance and heat release from the 1.8 litre HSDI test engine.

Chapter 8: Spray development under combusting conditions

The previous phenomenological model in chapter 3 is supplemented by a step-by-step analysis of the developing spray based on successive zones derived from the NO_x submodel [2].

This is followed by an analysis of spray-swirl interaction under firing conditions

Part 3: Application of the new integrated code and conclusions

Chapter 9: Overall results using integrated program

Validation of program output against experimental results from the 1.8 litre HSDI test engine applicable to the limiting torque curve (LTC).

Chapter 10: Conclusions and suggestions for further work

Appendix A: NO_x emission submodel

Appendix B: Spray formation and spray-swirl interaction coding

Appendix C: Overall programming structure of ODES 4-4.

1.3 References

1. **Watson, N., Pilley, A.D., and Marzouk, M.**, "A Combustion Correlation for Diesel Engine Simulation", SAE 860029 (1980).

2. **Wallace, F.J.**, "Presentation of Simulation Package ODES at University Internal Combustion Group (UNICEG) meeting", University College London, December 1993.

3. **Meguerdichian, M., and Watson, N.**, "Prediction of Mixture Formation and Heat Release in Diesel Engines", SAE 780225 (1978).

4. **Gosman, A.D., and Harvey, P.S.**, " Computer Analysis of Fuel-Air Mixing and Combustion in an Axi-symmetric DI Diesel", SAE 820036 (1982).

5. **Amsden, A.A, Butler, T.D. et al**, "KIVA- A Comprehensive Model for 2-d and 3-d Engine Simulation", SAE 850554 (1985).

6. **Wolfer, H. H.**, "Der Zundverzug im Dieselmotor" VDI. Forsh.-ht, 392, 15, (1938).

7. **Siebers, D.L., and Higgins, B.S.**, "Effects of injector conditions on the flame lift-off length of direct injection diesel sprays", Proc. THIESEL 2000, pp.303-321, Valencia, September 13-15, (2000).

8. **Chmela, F.G., and Orthaber, G.C.**, "Rate of Heat Release Prediction for Direct Injection Diesel Engines Based on Purely Mixing Controlled Combustion", SAE Paper No. 1999-01-0186 (1999)

CHAPTER 2

A survey of Diesel cycle simulation

2.1 Introduction

The operating cycle of a diesel engine can be broken down into a sequence of separate processes: intake, compression, combustion, expansion and exhaust.

With mathematical models for each of the process simulation of a complete engine cycle can be built up which can be analysed to provide information on engine performance. Models of individual engine processes at various levels of approximation have been developed.

The selection and use of a mathematical model of engine combustion depend to a considerable extent on the phenomena that researchers wish to resolve and on available computational resources.

Preliminary estimates of thermal engine efficiency and power output can be obtained from air standard cycles, which neglect gas exchange processes, heat transfer to cylinder walls, and variation of specific heats with temperature. Better estimates can be obtained from equilibrium charts, which provide the temperature and composition of the combustion products for adiabatic processes at constant volume and constant pressure. However, both air standard cycles and equilibrium charts overestimate the maximum cylinder pressure and temperature and the engine power output, because they neglect heat transfer losses and simulate combustion as a heat addition process that occurs at constant volume and constant pressure.

More detailed mathematical models of diesel engines account for the temporal or temporal and spatial variations of the charge pressure, temperature and composition, the heat transfer losses, the gas exchange processes, the flows in the manifolds and around the intake and exhaust valves, and so on.

Mathematical models can be classified into three groups; in order of increasing complexity, they are:

(i) Zero-dimensional models (or phenomenological models). These use an empirical heat release model, in which time is the only independent variable.

(ii) Quasi-dimensional models. These use a separate submodel for turbulent combustion to derive a heat release model.

(iii) Multi-dimensional models. These models solve numerically the equations for mass, momentum, energy and species conservation in three dimensions, in order to predict the temporal and spatial variations of the flow field, temperature, composition, pressure, and turbulence within the combustion chamber.

2.2 Alternative modelling strategies

2.2.1 Air standard cycle

Air standard cycles are a useful introduction to the most detailed thermodynamic models presented in the next sections. They assume that the mixture charge is pure air with constant specific heats at constant volume and constant pressure, neglect the intake and exhaust processes (i.e., a fixed mass of air is the working fluid throughout the engine cycle). Also in air standard cycle the combustion process is replaced by a heat transfer process from an external source, and completes the cycle by heat transfer to the surroundings until the air pressure and temperature correspond to the initial condition, see any internal combustion engine text book, such as *Heywood* [1].

The limited-pressure combustion cycle, shown in figure 2.1, consists of isentropic compression (1-2), heat addition at constant volume (2-3), heat addition at constant pressure (3-4), isentropic expansion (4-5), and heat transfer at constant volume (5-1).

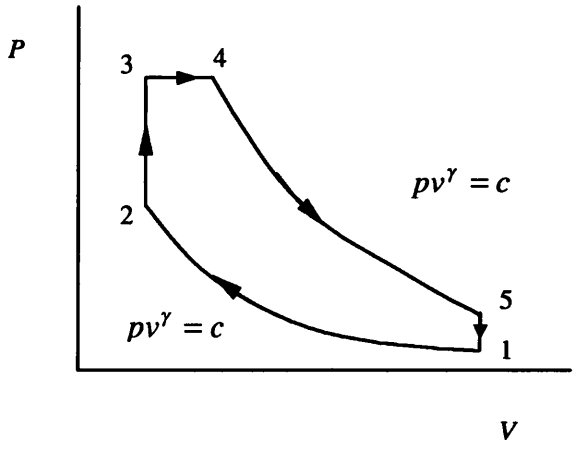

Figure 2.1: Air standard cycle

Although air standard cycles do not portray correctly what occurs in the actual process in a real engine, they indicate the effect upon the thermal efficiency and specific output of altering variables of the cycle, such as the compression ratio, initial and maximum pressures, the quantity of heat added per cycle, and are useful for comparing different cycles.

2.2.2 Modified air standard cycle

The obvious extension of the simple air standard cycle is to introduce modification allowing for

i) Change of chemical composition and temperature and effect on gas properties

ii) Throttling losses through valves, by adjustment of induction and exhaust pressure levels and allowance for pumping work

iii) Heat transfer on simple 'aggregate' basis

iv) Departures from idealised constant volume and/or constant pressure combustion by use of 'diagram factor'

This modified air standard cycle technique, shown in figure 2.2, has been used very successfully at the University of Bath, but it necessarily requires some 'fudge factor' data specific to a particular engine.

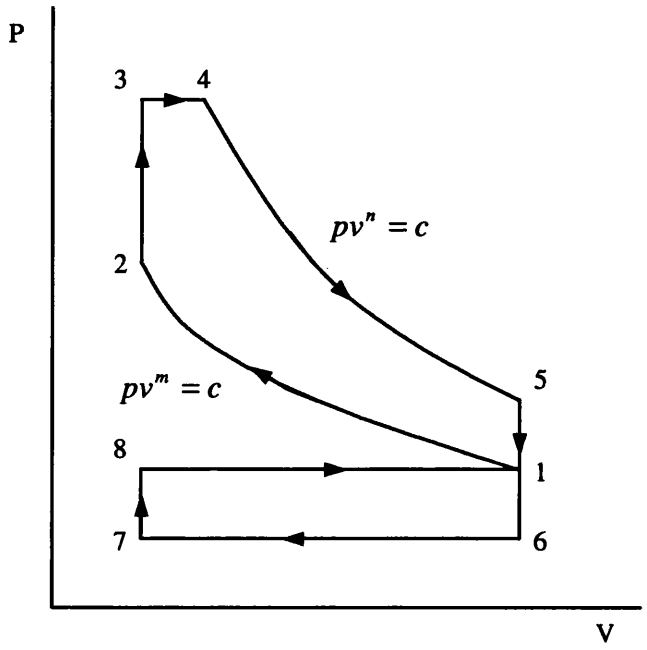

Figure 2.2: Modified air standard cycle

2.2.3 Simple component matching (EMAT)

The simple component matching models has been introduced at Bath University by *Way*, and then developed by *Wallace and Associates* [2], for turbocharger matching and diesel engine performance calculation. The model has a modular structure, with a series of subroutines describing the individual component, i.e., engine, compressor, turbine, cooler, gas properties, and interpolation and iteration.

A major program (EMAT) links all these subroutines together and the matching condition are found by iteration, to establish the equilibrium conditions for the turbocharger (i.e., power and mass flow). The iterative solution is completed after three nested lops are satisfied, i.e.,

i) Compressor-engine mass flow balance,

ii) Engine-turbine mass flow balance,

iii) Turbocharger power balance

This model is based on simplified cycle analysis methods, involving the modelling of the thermodynamic and gas dynamic processes in such a manner that much of the resultant numerical information can be presented in the form of performance maps not only for compressors and turbines, but also for the engine. In computer program terms, these maps are presented as multi-dimensional numerical arrays to which the various compatibility conditions appropriate to engine compressor-turbine combinations are then applied.

The model still divides the cycle into a very large number of very small steps, as is the case with so-called step-by-step programs, and therefore retains some of the computational speed and simplicity associated with such cycle. However it makes use of recent findings based on detailed experimental investigations into heat release and heat transfer, and simplified models of these processes as previously only found in the computationally much more demanding step-by-step programs to produce an altogether more realistic use of the 'fudge factors' associated with earlier simple modified air standard cycle models.

Figure 2.3 shows the simple component matching models, in which basically the sequence of closed period calculations starts from initially assumed trapped condition at position 1 (to be modified by subsequent open period calculations), calculates the compression process 1-2 without heat transfer, uses a modified constant volume heat

release process 2-3, starting 5° BTDC and terminating 5° ATDC. The fraction α of the injected fuel burnt being a function of both injection timing and rate, followed by constant pressure burning 3-4 of a fraction $\beta = (1-\alpha)/2$, and a final constant 'slope' burning 4-5 of an equal fraction β, this latter curve 4-5 then merging smoothly with the expansion curve 5-6 without heat transfer.

Heat transfer is calculated separately and subtracted first from β to β_1, the remainder from α to give α_1 if β is not sufficient. Effective inlet valve closing and exhaust valve opening are taken respectively as 15° before and after the respective 'geometric' timings.

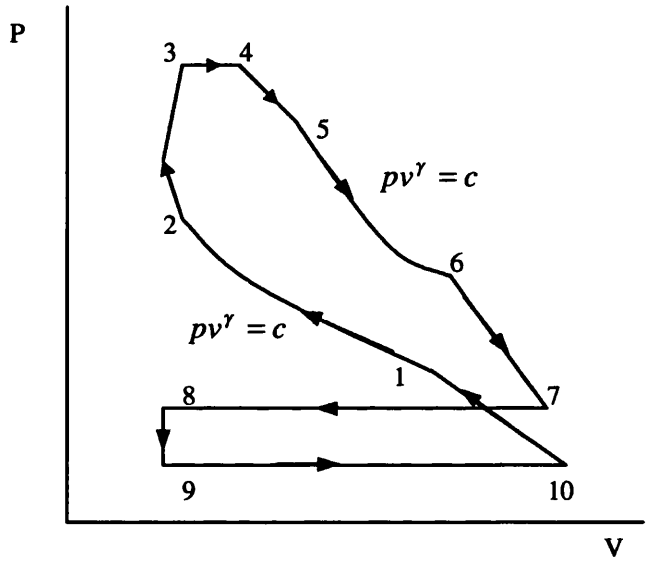

Figure 2.3: Simple component matching cycle

The open period divides itself into,

i) The blow down period 6-7

ii) The exhaust period 7-8

iii) The overlap period 8-9

iv) The suction period 9-10

v) The pre-compression period 10-1

The exhaust and inlet period pressures (in the cylinder) are assumed to be related to the known exhaust and inlet manifold pressures via simple mean valve pressure drop equations.

2.2.4 Heat release modelling

2.2.4.1 Zero-dimensional models

In zero-dimensional modelling, single-zone, the cylinder charge (i.e., the mixture in the cylinder) is assumed to be uniform in both composition and temperature, and the first law of thermodynamics is used to calculate the incremental temperature change of the cylinder gases as a function of piston work, heat transfer to cylinder walls, and fuel heat release. The latter being based on an empirical correlation for particular engine types and drawing a distinction between premixed and diffusion, i.e., mixing controlled burning, *Krieger and Borman* [3], *Watson et al* [4]. In *Watson* model, the effect of ignition delay, which is separately calculated using established empirical correlation, is reflected in the magnitude of the premixed burning "spike" (see figure 2.4), but there is no direct correlation between injection rate and rate of heat release. The instantaneous state of mixture can be described by the mixture pressure, p, temperature, T, and equivalence ratio, φ. Fuel is added to the cylinder throughout the combustion period to increase the energy and fuel-air ratio of the charge; however, the simulated fuel addition has no physical relationship with the actual fuel-injection process except that its total mass is equal to the actual fuel mass.

Single-zone models yield a system of ordinary differential equations for the mixture pressure, temperature, and mass. However, they do not account for the pressure of vaporizing liquid droplets, air entrainment, combustion chamber geometry, and spatial variation of the mixture composition and temperature.

Single-zone models can be used to analyse the heat release rate from experimentally determined pressure diagrams using the first law of thermodynamics; such a model was developed by *Krieger and Borman* [13]. Alternatively, single-zone models can be used as predictive tools if the heat release or the fuel mass-burning rate is specified. Figure 2.4 shows schematically a typical heat release rate diagram for a diesel engine. The heat release rate may account for both premixed and diffusive burning by means of, for example, a Wiebe function. Premixed burning occurs in the first stages of combustion, where the fuel is vaporized and mixed with the fresh mixture. Once the premixed fuel-air mixture is consumed, diffusive burning takes place and governs most of the combustion duration. Many attempts have been made to produce

simplified combustion models, but these are not accurate enough to be used in all cases. An alternative semi-empirical approach is usually adopted. The remainder of this section considers some of the different types of the combustion model that are used in a complete single-zone mathematical model.

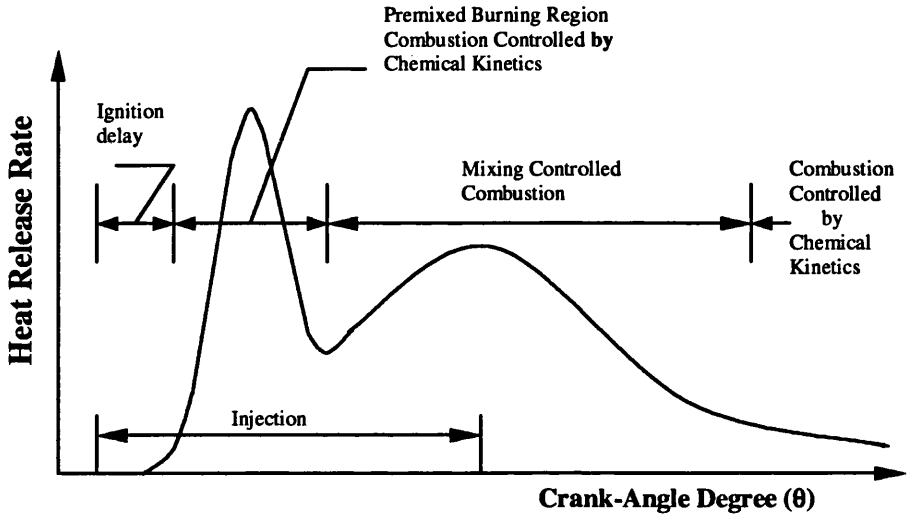

Figure 2.4: Schematic of the heat release rate in DI diesel engine

a) Wiebe model

The convenience of a diesel engine matching program can be greatly enhanced by building-in an algebraic expression for the heat release rate. Since the actual rate will vary with speed, load, injection timing, engine type, etc., a simple empirical correlation is required whose 'constants' may be chosen to suit particular engines and operating conditions. Probably the most widely used correlation is based on the *Wiebe* function [5]. This is a simple algebraic formula, for the fuel burnt, as a fraction of the total fuel injected as follow:

$$FB = 1 - \exp\left(-K_2(t)^{(K_1+1)}\right) \tag{2.1}$$

or in differential form (fuel burnt/total fuel injected)

$$FBR = K_2(K_1+1)t^{K_1}\exp\left(-K_2(t)^{(K_1+1)}\right) \tag{2.2}$$

where FB = fraction of fuel burnt/total injected per cycle per cylinder

FBR = non-dimensional fuel burning rate [$=d(FB)/dt$]

t = time from ignition, non-dimensionalised over the total time allowed for combustion ($=\Delta t/\Delta t_{com}$)

K_1 = shape factor for the curve

K_2 = combustion efficiency coefficient.

The non-dimensional fuel burning rate is related to the heat release rate by the calorific value of the fuel, if all fuel is burnt and dissociation is neglected (dissociation reduces heat release).

Woschni and Anisits [6] developed a Wiebe function correlation from test results relating to a larger industrial-type engine. The basis of their approach was not to define the heat release or fuel-burning pattern directly, but rather to assume that a diagram was known at one condition and to define its change as condition varied. Their value for K_2 was 6.9 (ensuring that combustion is 100 per cent complete at the burning period). The change of shape factor (K_1) with running condition is given by the expression:

$$K_1 = K_{1_{ref}} \left(\frac{ID_{ref}}{ID} \right)^a \left(\frac{p_z}{p_{z_{ref}}} \times \frac{T_{z_{ref}}}{T_z} \right) \left(\frac{N_{e_{ref}}}{N_e} \right)^b \tag{2.3}$$

where p_z and T_z : pressure and temperature at the beginning of compression;

ID : ignition delay

N_e : engine speed

a : empirical constants (0.5 suggested)

b : empirical constants (0.3 suggested).

The subscript *ref* is used to relate to datum conditions at which the heat release rate is known. The variation of ignition delay with running conditions can be calculated by using well-established *Wolfer* [8] correlation, as below:

$$ID = a p_m^b \exp\left(\frac{c}{T_m} \right) \tag{2.4}$$

where a, b, and c are empirical constants and p_m and T_m are the arithmetic mean pressure and mean temperature in the cylinder during ignition delay, respectively.

In addition, the variation of combustion duration with running conditions is required for the denominator of the dimensionless time function (t) in equation (2.2). *Woschni and Anisits* [6] data gives

$$\Delta t_{com} = \Delta t_{com_{ref}} \left(\frac{F}{F_{ref}} \right)^{0.6} \left(\frac{N_e}{N_{e\,ref}} \right)^{0.5} \tag{2.5}$$

where F is the equivalence ratio.

Equation (2.2) to (2.5) may be used to predict the heat release rate at other conditions. In order to describe the premixed and diffusive combustion periods observed in Diesel engines, two Wiebe functions could be used as follows, *Miyamoto et al* [7]:

$$\frac{dQ}{d\theta} = 6.9\frac{Q_p}{\theta_p}(M_p+1)\left(\frac{\theta}{\theta_p}\right)^{M_p}\exp\left[-6.9\left(\frac{\theta}{\theta_p}\right)^{M_p+1}\right] + 6.9\frac{Q_d}{\theta_d}(M_d+1)\left(\frac{\theta}{\theta_d}\right)^{M_d}\exp\left[-6.9\left(\frac{\theta}{\theta_d}\right)^{M_d+1}\right] \quad (2.6)$$

where the subscripts p and d refer to premixed and diffusive combustion, respectively, and M, θ, and Q are shape factors, the duration of the energy release, and characterise the heat release in premixed and diffusive combustion, respectively.

Miyamoto et al [7] performed experiments in DI and IDI diesel engines for a range of speeds, loads, injection timings, fuels, and steady and transient conditions. They analyzed the combustion rate by means of a double Wiebe function (equation 2.6). They found that M_p, M_d, and θ_p remained almost constant in both DI and IDI diesel engines (M_p = 3 for DI and IDI engines; M_d = 0.5, 0.9 for DI and IDI engines respectively; and θ_p = 7°CA (crank-angle degrees) for DI and IDI engines). However, the values of Q_p, Q_d, and θ_d were found to depend on the fuel-injection rate and ignition delay time.

The premixed combustion parameter Q_p correlated linearly with the amount of fuel injected during the ignition delay time, and the duration of the diffusive burning θ_d was a linear function of the diffusive combustion parameter Q_d. The engine smoke, noise, and thermal efficiency were found to correlated with Q_p and θ_p. Both the smoke and the noise can be reduced by decreasing Q_p while maintaining a value of θ_p less than 60 °CA (crank-angle degrees).

b) Marzouk - Watson model

The heat release period that can be seen in figure 2.4 consists of two different modes of burning premixed and diffusive burning. These two modes are assumed to proceed consecutively from the ignition point, the former being of short duration.

Watson et al [4] suggested that the shape of the heat release curve (K_I), would be produced by combining two functions, with a phase proportionality factor as below:

$$FBR(\tau) = \beta . f_1(\tau) + (1-\beta) f_2(\tau) \qquad (2.7)$$

where, $FBR(\tau)$: non-dimensional fuel burning rate

$f_1(\tau)$: 'premixed' burning function

$f_2(\tau)$: 'diffusion' burning function

β : phase proportionality factor between premixed and diffusion burning.

τ : dimensionless time = (θ - θ_{ig}) / (θ_{end} - θ_{ig})

θ_{ig} is the ignition angle; θ_{end} is the crank-shaft angle at the end of combustion;

θ is the crank-shaft angle (θ = rev/min . t).

Note that β denotes the proportion of the total fuel that burns in the first (premixed) phase, and is to be established. Function $f_1(\tau)$ and $f_2(\tau)$ replace the Wiebe type expression and relate to the premixed and diffusion burning phases respectively. Thus the burning rate curve is expressed as phase proportionality factor (equation 2.7).

The quantity of fuel reacted by premixed burning is largely governed by the amount of fuel injected during the ignition delay period. Experimental evidence shows that this may be related to the trapped equivalence ratio as well as the delay period, ms. The shapes of the component burning functions have been found to depend on ignition delay, trapped equivalence ratio and engine speed only, for a particular type engine. A best fit regression of test data, for $f_1(\tau)$ gave:

$$f_1(\tau) = c_1 c_2 \tau^{c_1 - 1} \left(1 - \tau^{c_1}\right)^{c_2 - 1} \qquad (2.8)$$

With a sufficiently large value of c_2 (up to 5000), this expression is capable of producing very steep rates of rise and decay, similar to that in a diesel engine. In addition, integration of expression (2.8) over the combustion duration gives, as required, a value of unity.

The Wiebe function is used for $f_2(\tau)$ since this can realistically represent the diffusion burning phase with its exponential decay. Thus:

$$f_2(\tau) = c_3 c_4 \tau^{c_4 - 1} \exp\left(-c_3 \tau^{c_4}\right) \qquad (2.9)$$

Values of c_1, c_3, and c_4 and their correlation with engine operating conditions are then required. These have been obtained from experimental data as follows:

$$c_1 = 2.0 + 1.25 \times 10^{-8} (ID \cdot N_e)^{2.4} \quad , \quad c_2 = 5000 \qquad (2.10)$$

$$c_3 = 14.2\, F_{ig}^{-0.644} \quad , \quad c_4 = 0.791\, c_3^{0.248} \qquad (2.11)$$

Also:

$$\beta = 1 - 0.926\, F_{ig}^{0.37} (ID)^{-0.26} \qquad (2.12)$$

where N_e is the engine speed (rev/min), F_{ig} is the equivalence ratio at the time of ignition, and ID is the ignition delay period (ms) that may be computed by using *Wolfer* [8] correlation (equation 2.4) or similar formula.

In the simulation code ODES, Otto-Diesel-Engine-Simulation, developed at the University of Bath by *Wallace and co-workers* [9], additional flexibility is obtained by the use of scale factors, which can be applied to each of the coefficient c_1, c_2, c_3 and c_4. These adjustable scale factors k_1, k_2, k_3, and k_4 can be taken as one, which implies the direct use of *Marzouk and Watson* [4] correlation. This expression is valid for direct injection diesel engines from the high-swirl to quiescent chamber type. For further adjustment of this expression to fit test data, a decrease of k_1 and increase of k_2 will speed up the initial stage of pre-mixed burning, a decrease of k_3 and an increase of k_4 will give quicker diffusion burning.

c) Chmela and Orthaber model

Recently, *Chmela and Orthaber* [10] developed a much more fundamental analytical approach for pure diffusion burning, i.e. mixing controlled burning, as found in high pressure common rail (HPCR) systems at high loads, in which the key constituent elements viz. fuel preparation rate for burning as a function of injection rate and the influence of spray turbulence kinetic energy on the rate of burning are represented by two basic differential equations, leading to a fuel preparation function F_1 and a turbulent kinetic energy dissipation function F_2. The general description of the model is fully discussed in chapter 6, section 6.2.

2.2.4.2 Quasi-dimensional models

Although single-zone combustion models can be used successfully to predict engine performance it is obvious that the assumption of homogeneous dispersion of the injected fuels is clearly unrealistic. It is well established that the fuel is dispersed in the form of droplets and that there are fuel-rich and fuel-free zones in the combustion chamber of a diesel engine. This heterogeneity affects the temperature and composition within the combustion chamber and the fuel-burning rate.

Several multi-zone models have been developed to analyse combustion in DI diesel engines. Most of these models use experimental and theoretical correlation for the fuel jet penetration, and divide the chamber into burning and non-burning zones. The effects of swirl on the fuel deflection can be empirically introduced into the models.

The simplest form of multi-zone model is the two-zone model, *Whitehouse and Sareen* [11]. The cylinder charge is divided into a burning and non-burning zone, with air entrainment from the later to the former. However, it makes the unrealistic assumption of a uniform mixture composition in the burning zone. True multi-zone models simulate a much more realistic process.

A general study of the available literature has revealed two different types of zoning method. The first method separates the fuel into individual packets, which have trajectories depending on their radial position relative to the axis of the jet [12, 13, and 14]. As an example, in the following section the model produced by *Meguerdichian & Watson* [12] will be briefly described.

The other method of zoning, as used by *Shahed, Chiu, and Lyn* [15, 16], has a system of expanding zones with iso-equivalence ratio boundaries. The main principle of this model is described in section 2.2.4.2b.

a) Meguerdichian model

Meguerdichian and Watson [12] developed a multi-zone model to predict mixture formation and the rate of heat release in diesel engines.

The mixture formation model is based on consideration of typical sprays formed as a result of fuel injection through a multi-hole nozzle. Initially, the fuel spray is considered as a circular free jet of two-dimensional form, figure 2.5, which is described by three empirically derived mathematical functions. Two of these are *Abramovich* [17] profiles for velocity and concentration that are as follows:

Velocity profile $$\frac{v}{v_m} = \left[1 - \left(\frac{y}{b}\right)^{1.5}\right]^2 \qquad (2.13)$$

Concentration profile $$\frac{C}{C_m} = 1 - \left(\frac{y}{b}\right)^{1.5} \qquad (2.14)$$

The third is a tip penetration equation for a straight jet taken from *Hay and Jones* [18], which is:

$$\frac{x_f}{D_N} = 2.28\left(\frac{v_N \cdot t}{D_N}\right)^{0.5} \tag{2.15}$$

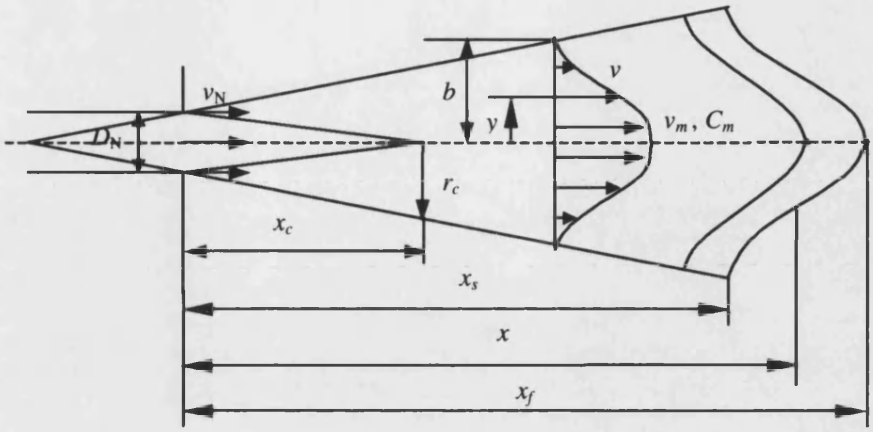

Figure 2.5: The circular free jet [12]

The next step is to divide the injected fuel into zones of equal fuel mass, moving within the jet boundaries (figure 2.6). This is achieved by dividing the spray into unequal layers (thinner near centreline region). Each layer is further subdivided by the contours of the jet front, as established at equal time intervals. In this way a relatively large number of zones is obtained.

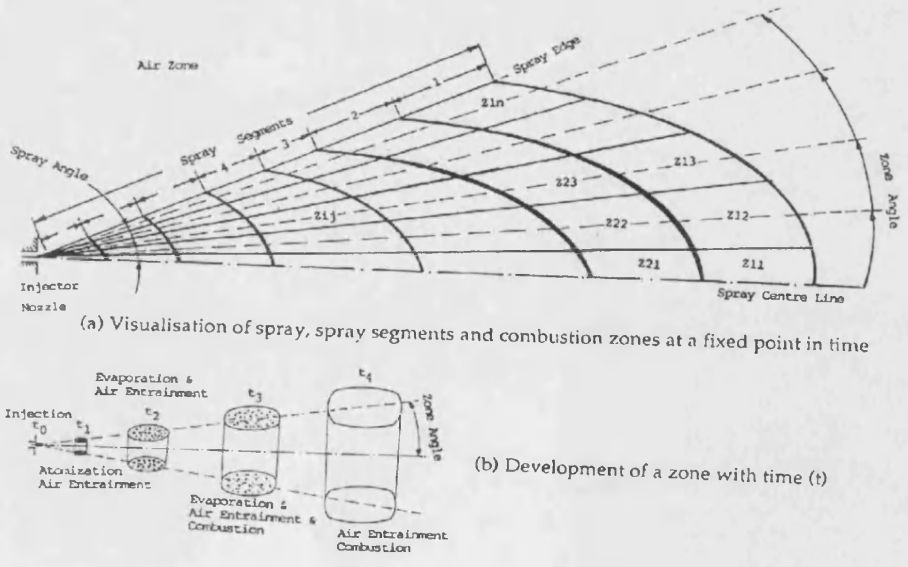

Figure 2.6: Visualisation of multi-zone concept of spray and surrounding air [12]

The shape of the jet front is assumed to resemble the velocity profile. For zones reaching the jet front, a pattern of changing layers is used, compatible with the idea

that these zones do not remain at the front but move sideways to form the developing jet boundaries. The wall jet is considered in a similar manner, except that the inner boundary layer (between the wall and the maximum velocity line) is neglected.

The general approach of the model is to apply the first law of thermodynamics, the equation of state and the burning rate equation to small individual zones, within a fuel spray area. The zone division pattern provides the essential structure for a step-by-step computation of the time-dependent zone variables. Zones in the sprays are termed 'burning zones'. The sum of the volumes of all zones, therefore, is equal to the instantaneous cylinder volume (calculated from engine geometry). The mass of the non-burning-zone at any instance is calculated from a knowledge of the trapped mass in the cylinder and that entrained by the burning zones. The fuel mass burning rate is calculated by the Arrhenious equation, for all zones from the rich to the lean limits of inflammability. The equations are as follows:

a) Energy equation:

$$\frac{d(m_z u_z)}{dt} = -p\frac{dV_z}{dt} + \frac{dq_z}{dt} + h_a\frac{dm_z}{dt} \tag{2.16}$$

where dq_z/dt represents the net rate of heat addition to the zone. For a burning zone, it represents heat release minus heat transfer. m, *u, p, V, and h* are mass, specific internal energy, pressure, volume and specific enthalpy, respectively.

They used Eichelberg's correlation to calculate of the total rate of heat transfer, and assumed it to be shared among individual zones according to their mass and temperature. The actual heat release rate represents the fuel mass-burning rate multiplied by the calorific value of the fuel. The energy equation takes account of the mass change within each zone. The rate of flow of enthalpy into such a zone is ($h_a dm_z/dt$). The same applies to the non-burning zone, except that (dm_z/dt) is negative (mass flow out of the zone).

Temperature dependent polynomial functions are used for mixture properties. For a burning zone, the mass change (dm_z) is solely due to additional air entering the zone.

b) Equation of state:

$$pV_z = m_z R_z T_z \tag{2.17}$$

The equation of state is assumed to apply to each individual zone, including non-burning zone.

c) Burning rate equation:

(for $\Phi_{lean} < \Phi_z < \Phi_{rich}$)

$$\frac{db_z}{dt} = k_s \rho_{az} (1 - b_z)(1 - \Phi_z b_z) \exp\left(\frac{-E}{RT}\right) \qquad (2.18)$$

(outside the inflammability range $db_z/dt = 0$)

where, $b_z = m_{fbz} / m_{fz}$ is the zone fuel mass burnt fraction; concentration are $c_{st} = 0.66$, $c_{rich} = 0.3$, $c_{lean} = 0.025$; the zone equivalence ratio is $\Phi_z = c_z / c_{st}$; $k_s = 5 \times 10^7$ m^3/hg/s; the zone air density is $\rho_{az} = m_{az} / V_z$; and $E = 1.25 \times 10^8$ J/mole.

There are n burning zones and one non-burning zone (n reaches n_{max} at the end of injection and does not change subsequently). Thus the number of equations is 2n+2 for equations (2.16) and (2.17) and n for equation (2.18). There is a further single equation for number of the volume constraint (bringing the total number of equation to 3n+3):

$$\sum_{z=1}^{z=n} V_z = V \qquad (2.19)$$

The total number of unknown variables is b_z(n), T_z(n+1), V_z(n+1), and p.

Meguerdichian and Watson [12] accounted for swirl, which deflects the burning elements, by means of experimental correlation for the spray penetration.

Their model is nevertheless unrealistic and does not truly represent the complex situation that exists behind the jet tip. Furthermore, the concentration values, and the axial velocities of a fully developed jet were used.

b) Shahed model

In the model proposed by *Shahed and co-workers* [15, 16], the spray is treated as a vapour jet in the spray-mixing calculation. The fuel vapour concentration is assumed to be continuous, and the vapour jet is divided into a series of discrete combustion zones. Energy conservation, chemical equilibrium, and nitric oxide finite rate chemistry are applied to each zone.

Experimental conditions covered a wide range of chamber pressure, temperature, swirl level, injection pressure and nozzle hole size. These gave a wealth of data on spray tip and tail velocities, spray width, leading edge shape and spray-swirl interaction. These data were used to fit equations in a form dictated by fundamental fluid dynamics. To obtain the fuel-air distribution within the spray plume, a hyperbolic distribution along

the spray axis and a normal distribution (zero swirl) across the spray was assumed. The distribution functions, the spray growth equations, and the conservation of total fuel mass within the spray plume form the basis of the jet mixing calculations, [16].

At incipient ignition, the combustion chamber is considered divided into (n+2) zones; a zone "A" of the medium (air and residual gas) into which the spray is injected; a zone "C" forming the rich core of the spray; and n zones "B_i" of combustible mixture of varying fuel-air ratios, see figure 2.7. The combustion zone B_i are bounded by the lean and rich flammability limits and intermediate equivalence ratio Φ_i as follows:

$$\Phi_L \leq \Phi_i \leq \Phi_R \tag{2.24}$$

After ignition, which is determined by an ignition delay time correlation, air entrainment continues, and the fresh mixture prepared for combustion is assigned to a new combustion zone B_j. The fuel mass in each combustion zone, except in B_j, is fixed.

The jet-mixing model calculates the initial mass and composition of zones B_i (i=1,n) and C. Before ignition, temperature is assumed to be uniform throughout the chamber and is calculated using the ideal gas law.

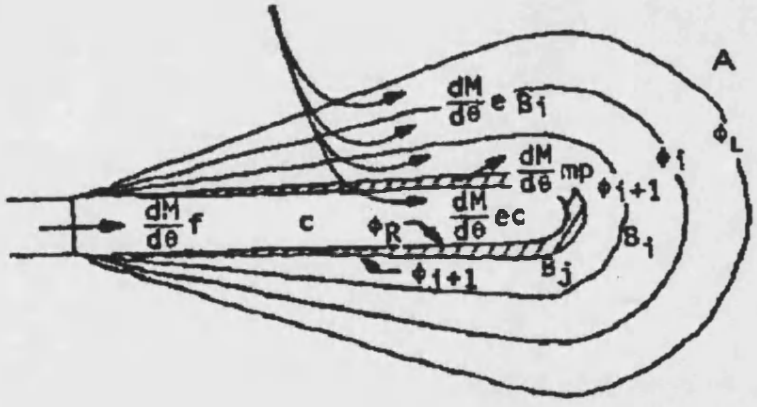

Figure 2.7: Schematic of the progressive evolution of the combustion zones and entrainment rates [15]

The derivation of the conservation equation is as follow:

Conservation of Mass

$$\frac{dm_c}{d\theta} = \frac{dm_f}{d\theta} + \frac{dm_{ec}}{d\theta} - \frac{dm_{mp}}{d\theta} \tag{2.20}$$

Rate of Change of Mass in Zone C = Fuel injection Rate + Medium Entrainment Rate - Mixture Preparation Rate

$$\frac{dm_a}{d\theta} = -\frac{\mathrm{dm_{ec}}}{\mathrm{d}\theta} - \sum_{i=1}^{j} \frac{\mathrm{dm_{ebi}}}{\mathrm{d}\theta} \tag{2.21}$$

Rate of Change of = - Medium Entrainment - Sum of Medium Entrainment

Mass in Zone A Rate into core Rates into Zones B_i

$$\frac{dm_{bi}}{d\theta} = \delta_{ij} \frac{\mathrm{dm_{mp}}}{\mathrm{d}\theta} + \frac{\mathrm{dm_{ebi}}}{\mathrm{d}\theta} \tag{2.22}$$

Rate of Change of = Mixture Preparation - Medium Entrainment

Mass in Zone B_i Rate into the Zone B_i Rates into the Zones B_i

where δ_{ij} is the Kronecker delta (i.e., $\delta_{ij}=0$ if $i \neq j$ and $\delta_{ij}=1$ if $i=j$).

It is noted that because of the definition of δ_{ij} prepared mixture flows only into the zone B_i (i=j) immediately surrounding the core zone C. Further, the mass conservation equation satisfy the constraint for the rate of change of mass in the chamber, i.e.,

$$\frac{dm_c}{d\theta} + \frac{dm_a}{d\theta} + \sum_{i=1}^{j} \frac{\mathrm{dm_{bi}}}{\mathrm{d}\theta} = \frac{\mathrm{dm_f}}{\mathrm{d}\theta} = \frac{dm_{ch}}{d\theta} \tag{2.23}$$

where $dm_f/d\theta$ is the burning rate.

Composition Equation

In order to calculate the fuel-air ratio, an account of the fuel mass in each zone is maintained.

$$\frac{d(m_{bi} f_{bi})}{d\theta} = \delta_{ij} \frac{\mathrm{dm_{mp}}}{\mathrm{d}\theta} f_r + \frac{\mathrm{dm_{ebi}}}{\mathrm{d}\theta} f_a \tag{2.24}$$

where f is fuel mass fraction. Subscripts a, b_i, and c refer to the respective zone, and f_r is fuel mass fraction corresponding to the rich limit of ignition.

Rate of Change of Fuel = Fuel Addition Rate Through + Fuel Addition Rate Through

Mass in Zone B_i Prepared Mixture Medium Entrainment

It is noted that the composition equations do not imply either an unburnt or fully burnt fuel mass fraction. Burnt state is dictated by chemical equilibrium consideration. Fuel fraction in equation (2.24) is used only to calculate fuel-air ratio. Further, "f_a" may have a non-zero value due to recirculated exhaust.

Property calculations for zone C consider unburnt fuel and entrained medium separately. The composition of the entrained medium is given by "f_a". An account of the raw fuel in zone C is maintained in the jet mixing calculations.

Conservation of Energy

$$\frac{d(m_c u_c)}{d\theta} = -p\frac{dV_c}{d\theta} + \frac{\mathrm{dQ_c}}{d\theta} + \frac{\mathrm{dm_f}}{\mathrm{d}\theta} \mathrm{h_f} + \frac{\mathrm{dm_{ec}}}{\mathrm{d}\theta} \mathrm{h_a} - \frac{\mathrm{dm_{mp}}}{\mathrm{d}\theta} \mathrm{h_m} \tag{2.25}$$

$$\frac{d(m_a u_a)}{d\theta} = -p\frac{dV_a}{d\theta} + \frac{dQ_a}{d\theta} - \frac{dm_a}{d\theta}h_a \tag{2.26}$$

$$\frac{d(m_{bi} u_{bi})}{d\theta} = -p\frac{dV_{bi}}{d\theta} + \frac{dQ_{bi}}{d\theta} + \delta_{ij}\frac{dm_{mp}}{d\theta}h_m + \frac{dm_{ebi}}{d\theta}h_a \tag{2.27}$$

Each of the energy conservation equations is simply a reflection of the following:

Rate of Change of Absolute Internal Energy of Zone = − External Work done by the Zone + Heat Transfer to the Zone + Absolute Enthalpy Associated with each Flow into or out of the Zone

Property calculation is based on local temperature, fuel air ratio and chemical equilibrium, *Olikara and Borman* [19].

This model uses *Annand* correlation [20] to calculate convective and radiative heat transfer based on a bulk average temperature defined as:

$$T_{ch} = \frac{\sum_{i=1}^{j} m_{bi}T_{bi} + m_a T_a + m_c T_c}{\sum_{i=1}^{j} m_{bi} + m_a + m_c} \tag{2.28}$$

And the total heat transfer losses are apportioned to the various zones in relation to their mass and temperature as:

$$\frac{dQ_{bi}}{d\theta} = \frac{m_{bi}T_{bi}}{\sum_{i=1}^{j} m_{bi}T_{bi} + m_a T_a + m_c T_c} \times \frac{dQ_{ch}}{d\theta} \tag{2.29}$$

where $dQ_{ch}/d\theta$ represents the total heat transfer losses.

Equation of State

The equation of state,

$$pV = mRT \tag{2.30}$$

is used individually for each zone using local properties.

Volume Constraint

The calculated volumes of all zones should add to the total chamber volume. Thus,

$$V_{ch} = V_c + V_a + \sum_{i=1}^{j} V_{bi} \tag{2.31}$$

Nitric Oxide Kinetics

The NO concentration was calculated by means of the Zeldovich mechanism, (equations i, ii), and all the species except NO were considered to be in local chemical equilibrium.

$$N_2 + O \rightleftharpoons NO + N \qquad \text{(i)}$$

$$O_2 + N \rightleftharpoons NO + O \qquad \text{(ii)}$$

For each zone B_i, the rate of production of nitric oxide due to chemical reaction is given by:

$$\frac{1}{V_{bi}}\frac{d\{[NO]V_{bi}\}}{dt} = k_1[N_2][O] + k_2[O_2][N] - k_3[NO][N] - k_4[NO][O] \qquad (2.32)$$

where k_1, k_2, k_3, and k_4 are the reaction constants.

The chemical rate of production of NO in zones A and C is equal to zero. Using the reaction equations above, the following can be written:

$$\frac{d(m_c N_c)}{d\theta} = \frac{dm_{ec}}{d\theta}N_a - \frac{dm_{mp}}{d\theta}N_c \qquad (2.33)$$

Rate of Change of Mass of NO through in Zone C = Rate of In-Flow of NO through Medium Entrainment − Rate of Out-Flow of NO Through Mixture Preparation

$$\frac{d(m_{bi}N_{bi})}{d\theta} = \frac{d[NO]V_{bi}}{dt}\frac{m_{NO}}{d\theta/dt} + \delta_{ij}\frac{dm_{mp}}{d\theta}N_c + \frac{dm_{ebi}}{d\theta}N_a \qquad (2.34)$$

Rate of Change of Mass of NO in Zone Bi = Rate of Chemical Production of NO in Zone B_i + Rates of In-Flow Associated with Mixture Preparation and Medium Entrainment

where N is mass fraction of nitric oxide; m_{NO} is molecular mass of nitric oxide.

It is noted that N_a may have a non-zero value due to residual or re-circulated exhaust.

c) Dang model

This quasi-dimensional model for diesel engines developed by *D.Dang* and revised by *F.J.Wallace* [9] and incorporated in ODES 2-2, uses input of fuel burn rate, pressure, bulk temperature and bulk equivalence ratio, from the single-zone version of ODES in order to create a relatively simple multi-zone model which does not require spatial definition of the developing spray trajectory or growth by air entrainment etc., but rather relies on the creation of successive notional heat release zones each receiving, over a period defined by the number of separate zones to be created, a mass of fuel derived from the known single-zone burning rate and mass of air controlled by entrainment factor C. The calculations are performed degree-by-degree on the basis of

stoichiometric combustion in a sub-zone followed by transfer of the products to a heat release zone where they mix with entrained air from the surrounding air zone, with or without residuals, until the equivalence ratio in that zone has reached the value corresponding to the trapped air/fuel ratio from the single-zone model. A new heat release zone is crated when the predetermined mass of fuel burnt in that zone N has been exhausted. At this point a new heat release zone N+1 is crated, while entrainment into zone N continues. Thus the total number of zones increases progressively throughout the combustion process.

The extended Zeldovich reaction kinetic scheme is applied to predict, via three separate equations, the rates of formation of N_2 and O, NO and O and NO and H respectively derived from the equilibrium constants of the three basic reactions and the instantaneous concentrations of the reactants relative to their equilibrium values. Many of the basic concepts in this model are derived from *Shahed* [15,16].

The *Dang* [9] model has been used in the present thesis to provide a basic for a simplified method of analysis for spray formation and propagation, which is described in chapter8. The *Dang* analysis itself is given as appendix A.

2.2.4.3 Multi-dimensional models

From a consideration of basic fluid mechanics and thermodynamics, it is possible to derive a set of equations, which given appropriate boundary and initial conditions, will completely determine the movement and state of a fluid in a given geometry. These are the well-known *Navier-Stokes* equations. The solution of these equations has proved extremely complex and it is only in recent years that techniques for using these equations to determine fluid flows in realistic geometries have become available.

Multi-dimensional models of engine combustion incorporate fluid dynamics. They predict temporal and spatial variations of the flow field, temperature, composition, pressure, and turbulence within the combustion chamber. This is achieved by dividing the combustion chamber into many cells that form a three-dimensional mesh, which serves as a framework for constructing finite volume approximations to the governing conservation equations. In multi-dimensional models, the time-dependent, three-dimensional conservation equations of mass, linear momentum, energy and species are time-averaged and the turbulent correlation are considered to be proportional to

the gradients of the mean flow. These equations can then be solved for discrete time steps. These models require considerable computational resources. The advent of super-computers has greatly increased the potential of such models.

In general, two major kinds of activities are involved in multi-dimensional combustion modelling:

- Development of fundamental submodels regarding turbulence, chemical kinetics, turbulence-reaction interaction, spray dynamics, spark ignition and auto-ignition, and transient wall heat transfer,
- Development of multi-dimensional CFD computer codes, emphasising the complex geometry and operating conditions of real engines.

The pace of submodel development strongly depends on our fundamental understanding of these physical/chemical processes, which relies on not only theoretical studies but also experimental observation and diagnostics technology. On the other hand, the development of multi-dimensional CFD codes for IC engine combustion modelling has been progressing rapidly since the late 1970's.

For some years comprehensive numerical models have been developed to simulate the in-cylinder dynamics of advanced combustion engines. The first of these was the two-dimensional RICE code, *Butler et al* [21], which treated the premixed combustion of gaseous fuels in an enclosed bomb. This code was superseded by CONCAS, *Butler et al* [22], which again treated gaseous combustion in two-dimensional (2-D) but with an arbitrary-Lagrangian-Eulerian (ALE) mesh that permitted the piston shape and motion to be included naturally in the calculations. This code was followed by CONCHAS-SPRAY, *Cloutman et al* [23], which treated fuel sprays in the engine cylinder using the spray model developed by *Dukowicz* [24], and later extended by *O'Rourke and Bracco* [25] and *O'Rourke* [26]. KIVA, *Amsden et al* [27], computer code is an outgrowth of the CONCHAS-SPRAY computer program.

The computer code KIVA-II, *Amsden et al* [28], has been widely used for internal combustion engine modelling and other applications. It has integrated all the necessary submodels in order to simulate the complex flow and combustion processes in an engine. Further development of submodels based on KIVA-II has been under development in order to achieve a better prediction of the engine combustion process.

Another series of computer codes for the prediction of the in-cylinder flow, heat transfer and combustion processes occurring in direct-injection diesel engines is the

one which includes codes based on the RPM (Reciprocating Piston Motion) numerical procedure for solving the differential equations governing aforementioned processes and carry the same name as this procedure. The first RPM code supplied was intended for calculation of air motion and heat transfer only and was assembled by *Gosman and Johns* [29]. A second version incorporating additional submodels of the liquid and vapour fuel dispersal processes accompanying fuel injection was subsequently developed, also by the aforementioned. More recently, *Gosman and Harvey* [30] have further extended the methodology to include representation of the combustion processes, including ignition.

Another CFD code is the SPEED diesel combustion code of Imperial College, capable of simulating the injection, mixture formation, ignition, combustion, and pollutant formation processes in diesel and spark ignition engines for single component fuels. The SPEED code applies the finite volume approximation and makes use of unstructured non-orthogonal boundary fitted meshes. The mesh can be moved according to piston and valve motion. A mixed Eulerian-Lagrangian formulation of the finite-volume equations of momentum, mass, species and energy transport is used. The subgrid motion of the flow is modelled by k-ε turbulence model, *Jones et al* [31], modified for the use in engines. The set of differential transport equations is fully implicit in space and is solved using a predictor-corrector procedure, *Issa et al* [32, 33]. For the simulation of the spray break-up the *Ritz-Diwakar* [34] approach is used. The evaporation of single droplets is modelled according to *Borman and Johnson* [35], and the modelling of droplet collision according to *O'Rourke* [26]. The droplet wall interaction modelling has been presented by *Chaves et al* [36]. Combustion is modelled according to *Magnussen,* [37].

The STAR-CD package, developed originally at Imperial College by *Gosman and co-workers*, is a general framework for solving the fundamental equations defining fluid motion in steady state and unsteady flows. This package consists of two modules: *prostar* for model development, setting boundary conditions, and post-processing; and *star* – the main solver.

More recently, *Ikonomou* [38] developed the EPISO engine code, which was originally developed at Imperial College by *Gosman and co-workers*. The purpose of this work was threefold: firstly, adding diesel ignition and combustion models; secondly, to assess the accuracy of the spray prediction method by comparisons with

experimental data; finally, to use the prediction method to attain a better understanding of in-cylinder processes of fuel-air interactions, ignition and combustion in the combustion chamber of direct injection diesel engines.

The PHOENICS code is a general-purpose fluid dynamics program that is intended to be applicable to a wide range of different flows, *Spalding* [39]. The numerical procedure used by PHOENICS is based on the documented SIMPLE algorithm, *Patankar* [40].

PHOENICS is a modular code consisting of three main components: 'Satellite', 'Earth', and 'Photon'.

- 'Satellite' is the pre-processor for setting the input data. It is used to define the numerical mesh and to activate appropriate solution and output options. The Satellite does not communicate with the central equation solver, it merely writes a data file, which is subsequently read by 'Earth'.
- 'Earth' is the main equation solver and is not accessible to the user. However, during the iteration process 'Earth' interacts with a number of subroutines, most notably 'Ground' and 'Grex 2', by means of which the user can influence the equations solved for. The user can also specify his own coding and output sequences in 'Ground' in cases where the options provided in 'Satellite' are not adequate. This need may arise from complex boundary conditions or properly relationships not provided as standard options. Both 'Ground' and 'Grex 2' are organised in a group structure comprising 24 groups, which are visited at specific times during the iteration process.
- 'Photon' is the graphics post-processor. It can present results in three dimensional vector plots and contour plots of the variables solved for. If the results are required in a different format (e.g. velocity profiles, distribution of variables along particular grid lines) it is necessary to introduce new coding in 'Ground' which creates new output files.

The PHOENICS code is written in ANSI Fortran. At the University of Bath, version 1.4 was installed on a departmental VAX 11/750 in the department of mechanical engineering and, since February 1990, runs on SUN Sparc stations connected to a SUN Sparc server 330.

2.3 Conclusions

The approach adopted in the present work is to avoid the use of the complex quasi-dimensional or high-resolution multi-dimensional (CFD) models of sections 2.2.4.2 and 2.2.4.3 respectively, by using the current zero-dimensional model ODES (section 2.2.4.1) together with an existing simplified NO_x prediction submodel (section 2.2.4.2c), as the basis for new simplified submodels for the prediction of:

a) Spray formation and propagation

b) Swirl generation both in the main cylinder and the combustion bowl

c) Spray deflection due to interaction with swirling air in the combustion bowl

d) Heat release including ignition delay

While clearly sacrificing the detailed predictions possible with the more sophisticated models of section 2.2.4.2 and 2.2.4.3, the coarser predictions of the main parameters influencing the combustion process made possible by the proposed method will provide valuable insights while demanding greatly reduced computational effort.

2.4 References

1. **Heywood, J.B.**, "Internal Combustion Engine Fundamental", McGraw-Hill, (1988).

2. **Wallace, F.J., and Associates,** "Engine Matching Computer Program Diesel (EMATD)", University of Bath, Internal Report (User Manual).

3. **Krieger, R.B., and Borman, G.L.**, "The Computation of Apparent Heat Release for Internal Combustion Engines, ASME Paper No. 66-WA/DGP-4 (1966).

4. **Watson, N., Pilley, A.D., and Marzouk, M.**, "A Combustion Correlation for Diesel Engine Simulation", SAE 860029 (1980).

5. **Wiebe, I.**, "Halbempirische Formel dur die Verbrennungsgeschwindigkeit, in krafstoffaufber-eitung und verbrennung bei Dieselmotoren, ed. G. Sitkei, pp. 156-159, Springer-Verlag, Berlin (1964).

6. **Woschni, G.**, "Universally Applicable Equation for the Instantaneous heat Transfer Coefficient in the Internal Combustion Engine", SAE 670931 (1967).

7. **Miyamoto, N., Chikahisa, T., Murayama, T.**, and Sawyer, R., "Description and Analysis of Diesel Engine Rate of Combustion and Performance Using Wiebe's Functions", SAE 850107 (1985).

8. **Wolfer, H.H.**, "Der Zunderzug im Diesel-Motor", CDE-Forschungsheft, Vol. 392, pp. 15-24 (1938).

9. **Wallace, F.J.**, "Presentation of Simulation Package ODES at University Internal Combustion Group (UNICEG) meeting", University College London, December 1993.

10. **Chmela, F.G., and Orthaber, G.C.**, "Rate of Heat Release Prediction for Direct Injection Diesel Engines Based on Purely Mixing Controlled Combustion", SAE 990186 (1999).

11. **Whitehouse, N.D., and Sareen, B.k.**, "Prediction of Heat Release in a quiescent Chamber Diesel Engine Allowing for Fuel/Air Mixing", SAE 740084 (1979).

12. **Meguerdichian, M., and Watson, N.**, "Prediction of Mixture Formation and Heat Release in Diesel Engines", SAE 780225 (1978).

13. **Bazari, Z.**, "A DI Diesel Combustion and Emission Predictive Capability for Use in Cycle Simulation", SAE 920462 (1992).

14. **Hiroyasu, H., Kadota, T., and Arai, M.**, "Development and Use of a Spray Combustion Modelling to Predict Diesel Engine Efficiency and Pollutant Emissions: Part1. Combustion Modelling", Bulleting of the JSME, Vol. 26, No. 214, pp. 569-575 (1983).

15. **Shahed, S. M., Chiu, W. s., and Lyn, W. T.**, "A Mathematical Model of Diesel Combustion", Proceeding of the Institution of mechanical Engineers, C94/75, pp. 119-128 (1975).

16. **Chiu, W. s., Shahed, S. M., and Lyn, W. T.**, "A Transient Spray Mixing Model of Diesel Combustion, SAE 760128 (1976).

17. **Abramovich, R. G. N.**, The Theory of Turbulent Jets, MIT Press, (1963).

18. **Hay, N., and Jones, P.L.**, "Comparison of the various Correlations for Spray Penetration", SAE 720776 (1972).

19. **Olikara, C., and Broman, G.L.**, "A Computer Program for Calculating Properties of Equilibrium Combustion Products with Some Application to ID Engines", SAE 750468 (1975).

20. **Annand, W.J.D.**, "Heat Transfer in the Cylinders of Reciprocating Internal Combustion Engines", Proceeding of the Institution of mechanical Engineers, Vol. 177, No. 36, pp. 973-992 (1963).

21. **Butler, T.D., Farmer, O.A., and Rivard, W.C.**, "RICE: A Computer Program for Multicomponent Chemically Reactive Flows at all Speeds", Los Alamos Scientific Laboratory, Report LA-5812 (1976).

22. **Butler, T.D., Cloutman, L.D., Dukowicz, J.K.**, Ramshaw, J.D., and Krieger, R.B., "Towards a comprehensive Model for Combustion in a Direct-Injection Starified-Charge Engine", in Combustion Modelling in Reciprocating Engines, (eds J.N. Mattavi & C.A. Amann), Plenum Press, NY (1980).

23. **Cloutman, L.D., Dukowicz, J.K., Ramshaw, J.D., and Amsden, A.A.**, "CONCHAS-SPRAY: A Computer Code for Reactive Flows with Fuel Sprays", Los Alamos National Laboratory Report LA-9294-MS (1982).

24. **Dukowicz, J.K.**, "A Particle-Fluid Numerical Model for Liquid Sprays", J. Comp. Physics 35, 229-253 (1980).

25. **O'Roucke, P.J.**, and Bracco, F.V., "Modelling of Drop Interactions in Thick Sprays and Comparison with Experiment", Stratified Charge Automotive Engines Conf. Imech E, Paper No. C404/80 (1980).

26. **O'Roucke, P.J.**, "Collective Drop Effects on Vaporizing Liquid Sprays", PhD Thesis, Univ. Princeton (1981).

27. **Amsden, A.A, Butler, T.D. et al**, "KIVA- A Comprehensive Model for 2-d and 3-d Engine Simulation", SAE 850554 (1985).

28. **Amsden, A.A., O'Roucke, P.J., and Butler, T.D.**, "KIVA-II: A Computer Program for Chemically Reactive Flows with Sprays", Los Alamos National Laboratory, Report LA-11560-MS (1989).

29. **Gosman, A.D., and Johns, R.J.R.**, "Computer Analysis of Fuel-Air Mixing in Direct-Injection Engines", SAE 800091 (1980).

30. **Gosman, A.D., and Harvey, P.S.**, " Computer Analysis of Fuel-Air Mixing and Combustion in an Axisymmetric DI Diesel", SAE 820036 (1982).

31. **Jones, W.P., and Launder, B.E.**, "The Prediction of Laminarization with a two equation Model of Turbulence", Int. J. Heat Mass Transfer, 15, PP.301.

32. **Issa, R.I., Gosman, A.D., and Watkines, A.P.**, "The Computation of Compressible and Incompressible Recirculating Flows by a Non-Iterative Implicit Scheme", J. Comp. Phys., 62, No. 1, pp. 66-82 (1986).

33. **Issa, R.I., Ahmadi-Befrui, B., Beshay, K.R., and Gosman, A.D.**, "Solution of the Implicitly Discretized Reacting Flow equations by Operator-Splitting", Mech. Eng. Dept., Imperial College (1989).

34. **Ritz, R.D., and Diwakar, R.**, "Effect of Drop Breakup on Fuel Sprays", SAE 860469 (1986).

35. **Borman, G.L., and Jhnson, J.H.**, "Unsteady Vaporization Histories and Trajectories of Fuel Drops Injected into Swirling Air", SAE Paper 598C (1962).

36. **Chave, H., Hertschel, W., Obermaier, F., Schindler, K.P., and Weiss, D.**, "Fuel Spray in Diesel Engines. Part II: Spray propagation and Wall Interaction", ATA & DMTI, Proceeding of the 3rd International Conference on 'Innovation and reliability in automotive design and testing', Firenze (1992).

37. **Magnussen, D.F., and Hyertager, B.H.**, "On Mathematical Modelling of Turbulent Combustion with Special Emphasis on Soot Formation and Combustion", 16th Symp. (Int.) on Combustion, The Combustion Institute, pp. 719-729 (1976).

38. **Ikonomou, E.**, "A Computational Study of Diesel Sprays and Combustion", PhD Thesis, Imperial College of Science, Technology and Medicine, London (1995).

39. **Spalding, D.B.**, "The PHOENICS Computer Code", in 'Computer simulation for fluid flow, heat and mass transfer, and combustion in reciprocating engines', ed. N.C. Markatos, Henisphere (1989).

40. **Patankar, S.V.**, "Numerical Heat Transfer and fluid flow", McGraw-Hill (1980).

CHAPTER 3

Spray modelling

3.1 Introduction

The purpose of this chapter is to present the findings of a comprehensive investigation of spray modelling, beginning with a literature survey. In section 3.3, new theoretical treatments of undeflected spray formation based on phenomenological approaches, using the conservation of momentum principle, are developed. This phenomenological model will be used for validation of spray results based on NOx model, which is represented in chapter 8. Section 3.4 is a preliminary assessment of spray deflection under isodense conditions. Again the full treatment for spray deflection under combusting conditions is presented in chapter 8. The chapter closes with the relevant references.

3.2 Survey of existing models

3.2.1 Non-evaporating and evaporating sprays

Several experimental and theoretical works have been performed on non-impinging gaseous and diesel sprays. Most of them conclude with empirical or semi-empirical laws to predict spray characteristics, such as; spray tip penetration, spray cone angle and air entrainment by the spray as global spray features (macroscopic), and axial and transverse velocity distribution as internal dynamics of the spray (microscopic features).

For some situations such as the air atomization sprays and the high-pressure (typically 1400 atm) diesel sprays, the spray momentum is large and the droplet size is very small. These small droplets may vaporize quickly and the spray may be approximated as a gas jet.

Dent [1], based on the experimental information on gas jet mixing developed a spray penetration formula, which was found to agree well with a wide range of experimental data. The basic mixing model is shown in figure 3.1 where v_N is the injection velocity and $v_{cl,x}$ is the centreline velocity at an axial position x. An axial velocity profile and potential core length are assumed to be given by:

$$\frac{v_N}{v_{cl,x}} = \frac{x}{L} \tag{3.1}$$

$$\frac{L}{D_N} = 4\left(\frac{\rho_l}{\rho_g}\right)^{1/2} \tag{3.2}$$

where L is the potential core length, ρ_l and ρ_g are liquid fuel and chamber gas densities respectively, and D_N is the nozzle diameter.

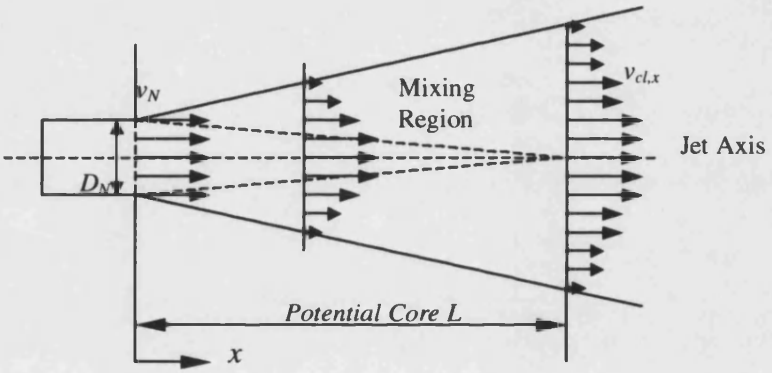

Figure 3.1: Dent mixing model [1]

The centreline velocity, $v_{cl,x}$, is also defined as dx/dt and when used in conjunction with equations (3.1) and (3.2), yields a simple differential equation for the position of the jet tip. Defining a discharge coefficient c_d, as given by equation (3.3), the spray tip penetration by integration of this differential equation is given as:

$$v_N = c_d\left(\frac{2\Delta p}{\rho_l}\right)^{1/2} \tag{3.3}$$

$$x(t) = 3.36c_d^{1/2}\left[\left(\frac{\Delta p}{\rho_g}\right)^{1/2} D_N t\right]^{1/2} \tag{3.4}$$

where Δp is the pressure difference between injection and chamber pressures.

Dent [1] chose to use a representative discharge coefficient of 0.83, and also included temperature effects via a gas density correction term, as shown in equation (3.5).

$$x(t) = 3.07\left(\frac{\Delta p}{\rho_g}\right)^{1/4}(D_N t)^{1/2}\left(\frac{294}{T_g}\right)^{1/4} \tag{3.5}$$

The *Hiroyasu et al* [2, 3] model was derived from liquid jet break-up work based on earlier work by *Levich* [4]. Essentially, the jet is divided into two zones; the initial zone consists of an intact liquid core and the latter zone consists of a mixture of liquid droplets and entrained medium. The liquid jet is assumed to have a much larger density and velocity than the surrounding medium. Any jet disturbance is accelerated by pressure waves induced in the surrounding medium and eventually grows until instability is attained, causing the jet to break up into droplets. Meanwhile, the intact core is assumed to progress at the initial jet velocity but it will eventually break up into many droplets and then advance at a rate proportional to the square root of time.

The break-up length, L_b, is given by:

$$L_b = v_b t_b \cong \alpha\left(\frac{\rho_l}{\rho_g}\right)^{1/2} D_N \tag{3.6}$$

where ρ_l and ρ_g are liquid fuel and chamber gas densities respectively, and D_N is the nozzle diameter. The intact core velocity, v_b, is constant and shown by equation (3.7), and when combined with equation (3.6), the break-up time, t_b, is given by equation (3.8).

$$v_b = c_1\left(\frac{2\Delta p}{\rho_l}\right)^{1/2} \tag{3.7}$$

$$t_b = \frac{\alpha\,\rho_l\,D_N}{\left(2c_1^2\rho_g\Delta p\right)^{1/2}} \tag{3.8}$$

where Δp is the pressure drop across the nozzle.

After break-up, the jet tip penetration is assumed to be of the form:

$$x(t) = \beta\, t^{1/2} \tag{3.9}$$

The parameter β can be found by combining equation (3.6), (3.7), and (3.8) in conjunction with equation (3.9). This yields:

$$\beta = 2^{1/4}(\alpha\, c_1\, D_N)^{1/2}\left(\frac{\Delta p}{\rho_g}\right)^{1/4} \tag{3.10}$$

From a variety of expressions, *Hiroyasu and Arai* [2] determined the constants α and c_1 to be 15.8 and 0.39 respectively. The spray tip penetration is thus divided two zones as given by:

$$0 < t < t_b \qquad x(t) = 0.39\left(\frac{2\Delta p}{\rho_l}\right)^{1/2} t \tag{3.11}$$

$$t > t_b \qquad x(t) = 2.95\left(\frac{\Delta p}{\rho_g}\right)^{1/4} (D_N t)^{1/2} \tag{3.12}$$

Varde et al [5, 6] analysed spray from plain orifices using a single-pulse model; they showed that the spray angle is a function of the orifice dimensions, injection pressure, ambient density, and nozzle length to diameter ratio. The following expression was obtained from their experimental data:

$$\tan\left(\frac{\theta}{2}\right) = A\left(\frac{\rho_g}{\rho_l}\right)^{0.33} \tag{3.13}$$

where ρ_l and ρ_g are the densities of liquid fuel and chamber gas respectively; and A is a constant.

They made measurements of diesel spray penetration at constant injection pressure ranging from 50 to 150 MPa and nozzles diameter of 0.18 mm to 0.53 mm and L_N/D_N ratio (length-to-diameter ratio of the nozzle) between 2 and 10. Based on these results, four non-dimensional parameters were identified to describe spray tip penetration as:

$$A_1 = \Delta p \rho_g D_N^2 / \mu_l^2 \qquad A_2 = \rho_l \sigma_l D_N / \mu_l^2$$
$$A_3 = \rho_l / \rho_g \qquad A_4 = L_N / D_N \tag{3.14}$$

where σ_l and μ_l are the surface tension and the viscosity of the fluid respectively.

After combining these parameters and using the experimental data the following expression was found to correlate with spray penetration:

$$x(t) = 1.1(A_1)^{0.3}(A_2)^{-0.008}(A_3)^{0.5}(A_4)^{0.16} t^{0.55} \tag{3.15}$$

In recent years *Schihl et al* [7] developed a phenomenological zero-dimensional spray penetration model for diesel type conditions for a constant volume chamber. The spray was modelled as an advancing cone, which is well mixed at its tip after passing through initial primary and secondary break-up zones, see figure 3.2. In order to ensure sufficient time for break-up and entrainment, it is assumed that x/d>>1 such that the spray tip density has approximately the same value as the surrounding gas.

A radial polynomial distribution for the velocity, minimal momentum flux induced axially on the cone by entrainment, minimal viscous forces on the cone periphery, negligible body force, and uniform injection velocity profile, which yields the penetration distance as shown below:

$$x(t) = \left(\frac{2c_d}{\tan\theta}\right)^{1/2}\left(\frac{\Delta p}{\rho_g}\right)^{1/4}(D_N t)^{1/2} \tag{3.16}$$

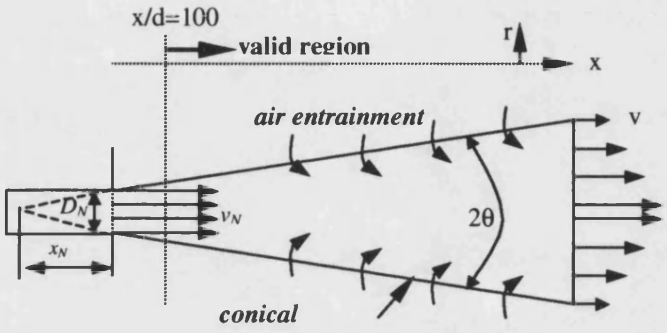

Figure 3.2: Cone model [7]

Mass entrainment may be calculated by integration of the mass flux at distance x and the original nozzle mass flux is deduced as below:

$$\dot{m}_e = \int_0^R \rho_{sp} v \cdot 2\pi r dr - \rho_l \frac{\pi}{4} D_N^2 v_N \tag{3.17}$$

After using a velocity profile such as equation (3.16), the mass entrainment can be found from:

$$\dot{m}_e = \rho_l \pi\, v_N x_N \left(\frac{2\sqrt{2}}{3}\sqrt{\frac{\rho_{sp}}{\rho_l}}x - x_N\right)\tan^2\theta \tag{3.18}$$

where, ρ_{sp} is the spray density and $x_N = D_N/2\tan\theta$ (see fig.3.2)

Reitz and Bracco [8] concluded from their experimental and theoretical results that the spray cone angle for jets in the atomization regimes could be obtained as follows:

$$\tan\frac{\theta}{2} = \frac{1}{A}4\pi\left(\frac{\rho_g}{\rho_l}\right)^{\frac{1}{2}}\frac{\sqrt{3}}{6} \tag{3.19}$$

where ρ_g and ρ_l are gas and liquid densities and A is a constant for a given nozzle geometry. They also suggested an empirical equation for A as below:

$$A = 3.0 + 0.28\left(\frac{L_N}{D_N}\right) \tag{3.20}$$

where L_N/D_N is the length-to-diameter ratio of the nozzle.

Their result indicated that the initial jet divergence angle increases with increasing gas density, and decreases with increasing nozzle length. For the same length, rounded inlet nozzles produce less divergent jets than sharp-edged inlet nozzles.

Payri et al [9] used high speed photography and phase doppler anemometry (PDA) to investigate the characteristic parameters and the evolution of continuous diesel sprays injected against a high density gas. The experimental set-up allows the use of injection systems in actual operating conditions of a supercharged HSDI diesel engine, with maximum gas densities of the order of 30 kg/m^3. The temperature of the gas is room temperature, so that no vaporization is present.

The main results obtained in this study are summarized as follows:

- With a gas density like that of a supercharged HSDI Diesel engine at the end of compression, the spray behaves as a "complete atomized spray", even for very low injection pressures corresponding to that under idle conditions (2 MPa injection pressure).
- The spray angle for complete atomized sprays was found to be independent of injection conditions and only dependent on the gas density. A reduction of the spray angle proportional to $\rho_g^{0.4}$ was observed, which is in agreement with previous works reported in the literature.

Farrel et al [10] investigated the effects of injection pressure, ambient pressure, and multiple injections on the spray characteristics. The injection pressure was varied up to 90 MPa. Double and triple injections along with different dwells under the same injection pressure (90 MPa), ambient density (27 kg/m^3), ambient room temperature, and similar fuel delivery (168 mg/inj) were analyzed to reveal the effect of multiple injections on the spray tip penetration length, the spray cone angle, and droplet size.

They measured the spray cone angle at two regions. One is within 10 mm to 20 mm from the nozzle tip, which is called a near spray angle, and the other is from 20 mm to far downstream which is called a far spray angle (see figure 3.3).

The following summary can be obtained from their experimental data:

- Under high injection pressure (90 MPa), the ambient pressure (ambient density) has less effect on the spray tip penetration than at low injection pressure (45 MPa).
- For multiple injection sprays, the second or third injections penetrate faster than the first spilt spray. The shorter the time spacing between the two split sprays the faster the following split spray can penetrate.
- Higher ambient pressure (ambient density) causes the sprays to have larger spray angles.
- Under high-pressure (90 MPa), the ambient pressure has less effect on the far spray angle than it has at low injection pressure (45 MPa).
- The near spray angles decrease from the start of injection to the end of injection, and after the end of injection the near spray angle increased.
- Multiple injections produced more variation in near spray angle during an entire injection event and generated far larger spray angles than a single injection. Specifically, the near spray angles for multiple injections decreased within every split injection interval and increased during each time spacing between injection intervals and also after end of injection. This may be good for the fuel spray and ambient air mixing; indicating the reason why high injection pressure coupled with selected multiple injection strategies can reduce the emissions and particulate for engine combustion [10].

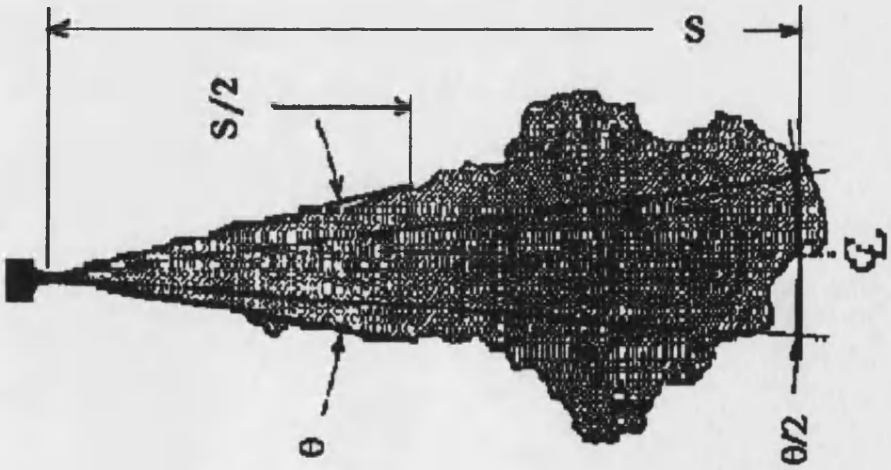

Figure 3.3: Schematics for spray angles and spray tip penetration measurements [10]

Sasaki et al [11] used the laser light sheet imaging and auto-correlation particle image velocimetry (PIV) methods to investigate the air flow velocity distribution around the non-evaporating diesel spray. Their measured results show:

- At the start of injection, the air near the nozzle tip was pushed away by the spray tip. Later on, as the spray grows the airflow direction reversed and flowed toward the fuel spray.
- The air velocity in front of the spray tip is very low compared with the fuel spray tip velocity.
- Measurements at a quasi-steady state injection condition showed that air near the nozzle tip flowed uniformly towards the fuel spray. Downstream from the nozzle tip, the surrounding air generated a turbulent flow along the spray surface.
- In the vicinity of the nozzle tip, the surrounding air velocity increased as the injection velocity increased, and decreased when a micro-hole nozzle was used. The flow direction was unchanged with respect to the injection velocity and nozzle hole diameter.

Levy et al [12, 13] studied a non-reactive diesel spray based on the assumption of a fully atomised jet (AFAJ), in two steps. First, an experimental investigation of the spray is achieved inside a constant volume combustion chamber. The spray characteristics are analyzed by using Phase Doppler Analyser (PDA) instrumentation. Then, numerical computations are conducted with the well-known KIVA-II code.

Tip penetration computed by the KIVA-II code is compared to the empirical relation of *Shahed et al* [14]. The agreement is relatively good. In particular, a square root evolution is predicted by KIVA-II after 0.2 ms. Also their results have shown droplets velocity and diameter can be correctly predicted down stream of the atomization region. A very good agreement was obtained between numerical and experimental probability density function sizes.

Presches et al [15] used an optical measurement technique to investigate the atomization and evaporation of diesel fuel and heavy fuel sprays.

Their results for three-injection pressure (480, 630 and 860 bar) and two chamber temperature (300°C and 400°C), which was varied together with the chamber pressure keeping the air density at a constant level, shows that:

- An increase in the injection pressure from 480 bar to 860 bar yields an increase in the spray length of approximately 27% (larger tip penetration).
- The spray tip penetration at higher chamber temperature decreases since the reduced liquid fuel mass causes a decrease in the spray momentum.
- Temperature seems to have relatively small effects, which can be explained by the boiling point curve of the diesel fuel.
- The spray cone angles scatter around a mean value, which obviously, does not depend on the injection pressure for the pressure condition investigated here.
- No significant influence of the temperature on the spray cone angle.
- An increase in the injection viscosity leads to a significant increase in the spray tip penetration.
- The spray cone angles of the heavy sprays are about 2° to 3° smaller than that of diesel fuel sprays.
- Compared to diesel fuel, heavy fuels are characterised by higher injection viscosity and a significantly lower proportion of low-boiling components.
- For heavy fuel, the sprays become longer and taller, i.e. the spray cones angle decreases.
- Generally, higher injection pressure improves the quality of atomization.

Rajalingam and Farrell [16] investigated experimentally the effect of injection pressure on air entrainment into transient diesel spray.

They used particle image velocimetry (PIV) to make measurements of the air entrainment velocities into the spray as a function of time and space. Also they used a hydraulically actuated, electronically controlled unit injection (HEUI) system to supply the fuel into a pressurised spray chamber. The chamber gas density was maintained at 27 kg/m^3, and the injection pressures were 117.6 MPa and 132.3 MPa.

They reported the following:

- Normal velocity gradually increased towards the tip of the spray to a maximum value and then tailed down as it reached its maximum penetration length.
- Along the edge of the spray the tangential velocities were directed towards the injector orifice (negative direction) and gradually increased in magnitude to a maximum value. As it approached the maximum penetration length the tangential velocity direction changed, towards the spray tip.

- There is minimal variation in the tangential velocities for both pressure cases.
- There is a general increase in the air entrainment mass flux with axial distance along the spray. After the maximum value, there is a sharp decrease in mass flux to the maximum penetration.
- During the final third of the spray the normal velocities and the mass flux were 125% higher for the high injection pressure case.

More recently, *Araneo et al* [17] used different laser based techniques to investigate the effect of gas density on the penetration and the spray angle of a diesel spray and the entrainment of the surrounding air. The experiments were conducted in a constant volume chamber under quiescent conditions. Gas density was varied in a range (from 1.17 to 40 kg/m^3) while keeping temperature constant at ambient conditions.

Their result shows that after an initial transient period, when the measured spray angle varies with time, a quasi-steady period is reached. For gas densities lower than 7 kg/m^3, a steady spray angle was not reached, due to the short observation time (≈0.4 ms). The high-density data are well correlated by the relationship as below:

$$\tan\left(\frac{\theta}{2}\right) = A\left(\rho_g / \rho_f\right)^{1/2} \tag{3.21}$$

where ρ_g and ρ_f are densities of ambient gas and fuel respectively; constant A=0.47 for the LS (low pump speed 500 rev/min) case and A=0.49 for the HS (high pump speed 1200 rev/min) case.

Also their result shows that in the investigated region (up to 60 mm from nozzle tip), the gas density seems to affect only slightly tip penetration, x, for densities up to 7 kg/m^3 and penetration varies almost linearly with time. For densities higher than 12 kg/m^3, the linear part of the penetration is shortened and a power-law close to $t^{0.5}$ applies at later time, accordingly to many previous experimental results. By using a typical power-law, they found the following correlation:

$$x = bt^{0.5}\rho_g^{\gamma} \tag{3.22}$$

where b is a constant and the best fit for $\rho_g \geq 20$ kg/m^3 gives γ= -0.36.

Abraham and Magi [18] developed a virtual liquid source (VLS) model for vaporizing, full-cone diesel sprays which treats the liquid region of the sprays as a source of mass, momentum and energy without directly computing the liquid phase. The penetration length of the liquid phase along the axis of injection and the time it

takes to reach the maximum length are model input parameters and these are obtained form recent measurements reported literature [20].

Their main findings of this study were:

- The comparisons of the computed and measured spray penetration and dispersion angles show adequate agreement for the range of conditions studied, ambient temperatures of about 1000 K and ambient densities of 6.85 kg/m^3 to 58.4 kg/m^3.
- It is also shown that the results are not very sensitive to the two model input parameters of maximum core length and the time to achieve the maximum length. Hence, it is not essential to know these parameters with great accuracy.
- The comparisons of the entrainment characteristics of transient jets computed by employing the VLS model with gas jet model and liquid spray model, for the same jet shows that the VLS model appears to be able to reproduce the entrainment characteristics of sprays.
- Their conditions appear to be satisfied in vaporizing diesel sprays for heavy-duty diesel engine applications. In any application where there may be impingement of the liquid on the piston surface or where the mass of the injected fuel that remains in liquid phase is a significant fraction of the total mass of injected fuel, this model may not be employed.

Arregle et al [19] based on experimental and theoretical works investigated the problem of quantifying and predicting the spray behaviour as a function of the parameters governing the injection process. These parameters were environment gas density (10, 20, and 30 kg/m^3), nozzle hole diameter (0.11, 0.19, and 0.27 mm), and injection pressure (30, 50, 70, 90, and 110 MPa).

Their results for isothermal conditions at room temperature show that very little evaporation occurs:

On the basis of the results obtained when the cone angle reaches a constant value, the following correlation have been obtained:

$$\tan\left(\frac{\theta}{2}\right) \propto D_N^a \; p_{inj}^b \; \rho_g^c \qquad (3.23)$$

with: $0.467 < a < 0.549$

$-0.00963 < b < 0.0284$

$0.308 < c < 0.362$

Which shows an important influence of the nozzle diameter, D_N, or for an injector wall thickness, L_N, constant indirectly the actual variable considered was L_N/D_N, which is a representative parameter of the nozzle injection geometry.

Also the above expression shows no significant influence of the injection pressure, p_{inj}, upon the spray cone angle, θ, that is in agreement with literature.

The experimental results of spray tip penetration have been fitted to the expression:

$$x(t) \propto D_N^a \, p_{inj}^b \, \rho_g^c \tan\left(\frac{\theta}{2}\right)^{-0.5} t^d \qquad (3.24)$$

with: $0.588 < a < 0.629$

$0.274 < b < 0.293$

$-0.255 < c < -0.230$

$0.513 < d < 0.533$

Which shows all of the parameter included in correlation play an important role.

This result confirms that, for a given cone angle, the penetration of diesel sprays is a process similar to that of gaseous jet.

It can be seen from equation (3.24) that higher injection pressure results in a larger tip penetration, which is in agreement with literature.

Siebers D. L. [20] used Mie-scattered light imaging to investigate the maximum axial penetration distance of liquid phase fuel (i.e., the liquid length) in an evaporation diesel spray over a wide range of conditions. The parameters varied in his investigation were the injection pressure (40 to 190 MPa), the orifice diameter (100 to 500 μm) and aspect ratio (2 to 8), the ambient gas temperature (700 to 1300 K) and density (3.3 to 60 kg/m^3), and the fuel volatility and temperature (375 to 440 K).

His main finding were:

- Liquid length decreases linearly with orifice diameter and approaches zero as the orifice diameter approaches zero. This linear dependence is independent of all other parameters.
- Injection pressure has no significant effect on liquid length.
- Liquid length decreases non-linearly with increasing ambient gas density and/or temperature, but with a declining sensitivity to each one as they increase.
- Liquid length decreases linearly with increasing fuel temperature. The decrease measured was about 12% for a 60 K increases in fuel temperature.

- Decreasing fuel volatility increases liquid length.
- The liquid length of multi component fuel is controlled by its lower volatility fraction.
- Orifice aspect ratio has a small and inconsistent effect on liquid length.
- Vaporization in a diesel spray, like diesel combustion after the premixed burn period, is controlled by air entrainment into the spray. For current-technology DI diesel injectors, atomization and local interphase transport processes at droplet surfaces are not a limiting factor for fuel vaporization. Parameters such as injection pressure and orifice diameter appear to affect fuel vaporization through their effect on mixing processes, not through their known affects on droplet size (i.e., atomization).

Recently *Naber and Siebers* [21] proposed an interesting model based on experimental results to investigate the effects of ambient gas density and fuel vaporization on spray characteristics. This is the most comprehensive presentation with details of non-vaporizing and vaporizing sprays with details of penetration, cone angle, etc. Spray penetration and dispersion were explored by comparing injection into non-vaporizing (i.e., ambient temperature) and vaporizing (i.e., 600 K to 1400 K) inert environments over extremely large ranges of ambient gas density. The ambient gas density ranges considered were 3 kg/m^3 to 200 kg/m^3 and 3 kg/m^3 to 61 kg/m^3 for non-vaporizing and vaporizing environment, respectively. Injection pressure and nozzle diameter was varied from 75 to 160 MPa and 0.19 to 0.30 mm, respectively.

Their model is capable of a unique relationship, by introducing a proper scaling of length and time. The tip nozzle distance x and the time were made non-dimensional by using the length scale x^+ and the time scale t^+ defined as:

$$x^+ = \frac{D_f\sqrt{\tilde{\rho}}}{a\tan(\theta/2)} \qquad t^+ = \frac{D_f\sqrt{\tilde{\rho}}}{a\tan(\theta/2)v_N} \tag{3.25}$$

where:

$$\tilde{\rho} = \rho_f/\rho_a \qquad D_f = \sqrt{C_a}D_N \qquad v_N = C_v\sqrt{2\frac{(p_f - p_a)}{\rho_f}} \tag{3.26}$$

The angle θ is the dispersion angle; the constant a is set equal to 0.66; the fuel (ρ_f) and ambient gas (ρ_a) density ratio ($\tilde{\rho}$); the effective diameter, D_f, of the fuel stream existing the orifice with a diameter of D_N; and the fuel velocity at the orifice exit, v_N. The area contraction coefficient, C_a, accounts for fuel flow area loss as a result of

cavitation bubbles reaching the orifice exit or "hydraulic flip". The velocity coefficient, C_v, accounts for head losses through the orifice. The values selected for C_a and C_v were the average values from their experiment: 0.73 and 0.83, respectively. The angles selected were $\theta/2=10^{\circ}$, and $\theta/2=9^{\circ}$ based on selected ambient density, and the pressures p_f and p_a are the fuel pressure in the injector and ambient gas pressure, respectively. Their penetration correlation is as below:

$$\tilde{t} = \frac{\tilde{S}}{2} + \frac{\tilde{S}}{4}\sqrt{1+16\tilde{S}} + \frac{1}{16}\ln\left(4\tilde{S}\sqrt{1+16\tilde{S}}\right) \tag{3.27}$$

The correlation is in the form of dimensionless penetration time ($\tilde{t} = t/t^{+}$) as a function of the dimensionless penetration distance ($\tilde{S} = S/x^{+}$). Two limits of equation (3.27) that can also be referred to in the discussion are the short limit:

$$\begin{array}{ll} Limit & \tilde{S} = \tilde{t} \\ \tilde{t} \to 0 & \end{array} \tag{3.28}$$

and the long time limit:

$$\begin{array}{ll} Limit & \tilde{S} = \tilde{t}^{1/2} \\ \tilde{t} \to \infty & \end{array} \tag{3.29}$$

Figure 3.4 shows the penetration data for all of the non-vaporizing experiments conducted in their investigation, normalized by the length and time scales given by equation (3.25).

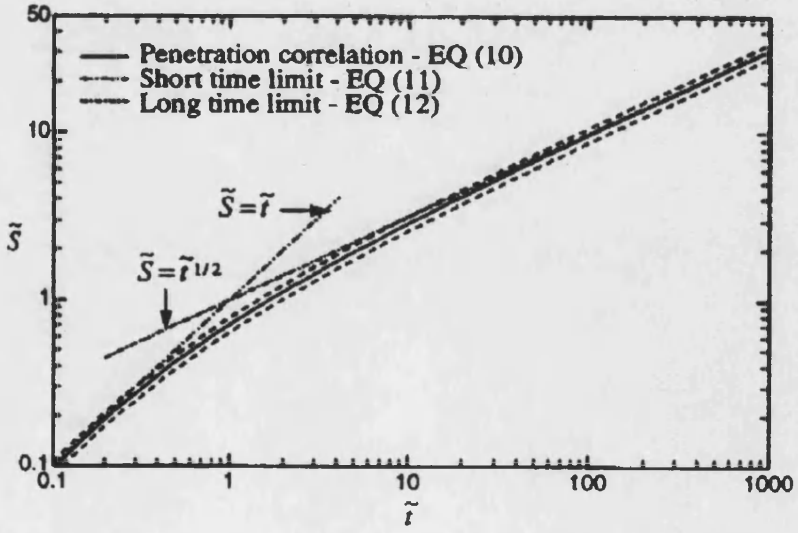

Figure 3.4: The non-vaporizing penetration data versus time in dimensionless coordinates [21].

All of the vaporizing penetration data obtained in their work at an ambient temperature of 1000 K is plotted in Figure 3.5 in the scale coordinates of Figure 3.4.

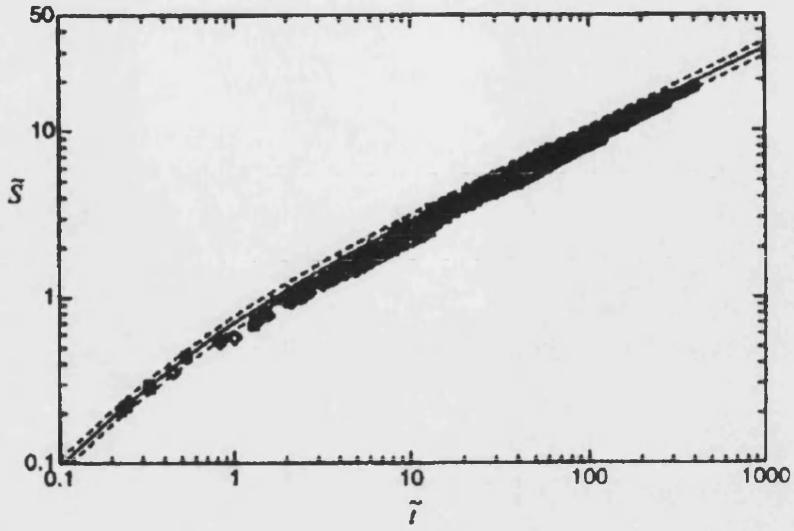

Figure 3.5: The vaporizing penetration data taken at 1000 K versus time in dimensionless coordinates [21].

Figure 3.5 shows that the penetration length and time scales given by equation (3.25) collapse the penetration data from the vaporizing experiments as well as they collapsed the non-vaporizing data in figure 3.4. The scaled penetration data lie in a narrow band near the curve for equation (3.27). Comparing figures 3.4 and 3.5, the only major difference noted between the scaled non-vaporizing data and the vaporizing data is that the vaporizing data lie below the correlation after a $\tilde{t}$ of 0.5.

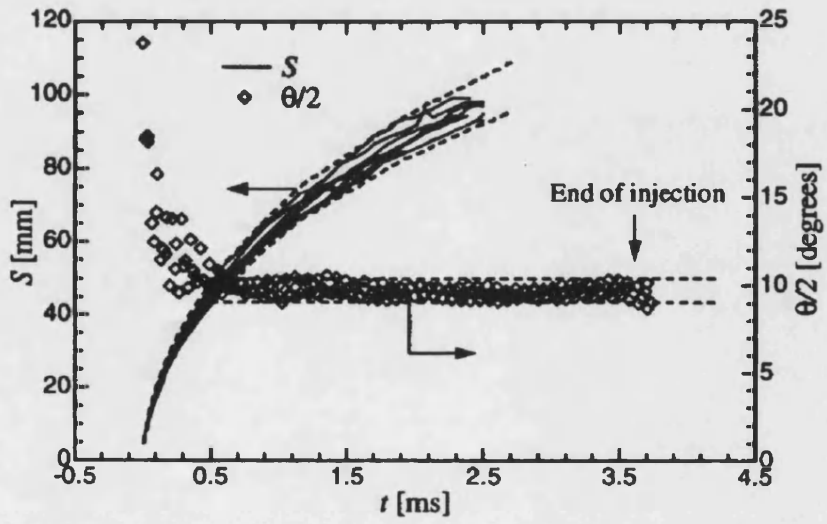

Figure 3.6: Penetration and dispersion angles versus time [21]

Figure 3.6 shows penetration, S, and spray half angles ($\theta/2$) for four film data sets versus time based on a non-vaporizing condition, an injection pressure of 140 ± 1.0 MPa, an Ambient gas density of 30.0 ± 0.05 kg/m^3 and the 0.257 mm orifice diameter tip. The average dispersion angles for the four cases between 0.5 ms and 3.0 ms are 10.0°, 9.5°, 9.5°, and 9.6°.

The analysis of *Naber and Siebers* [21] results shows that ambient gas density has a significantly larger effect on spray penetration and a smaller effect on spray dispersion than has been previously noted. The results also show that vaporization reduces penetration and dispersion by as much as 20% relative to non-vaporizing sprays, but both of these effects decrease with increasing ambient gas density.

3.2.2 Deflected sprays

The matching of swirl and fuel injection has been the subject of much work in the literature. A theoretical approach to the equivalence of fuel sprays and air jets may be seen in the work of *Melton* [22, 23]. *Melton* used simple, yet sound, considerations to show that at distances greater than that required for a typical fuel droplet to collide with its own mass of air the spray characteristics are almost identical to those of an air jet injected under the same conditions. Such considerations led *Lustgarten* [24] to conclude that if a fuel spray in air may be represented by an air jet in air, or a water jet in water, this would enable a drastic "slowing down" of the whole process. This approach was adopted at the University of Bath by *Way* [25]. *Way* constructed a water rig, as shown in figure 3.7, in which flow visualization was achieved by injecting a weak alkali into a weak acid with an indication (phenolphthein), which showed the neutral boundary. By adjusting the relative strengths of the acid and alkali, the boundary at a particular mixture ratio could be shown. Figures 3.8 and 3.9 are two examples taken from *Way* [25], which show the effect at different swirl levels. The numbers indicate spray development with respect to time. Figure 3.8 shows the good mixing pattern of a spray that is well matched to the swirl level, while figure 3.9 shows the effect of overswirl in which the spray fails to reach the wall.

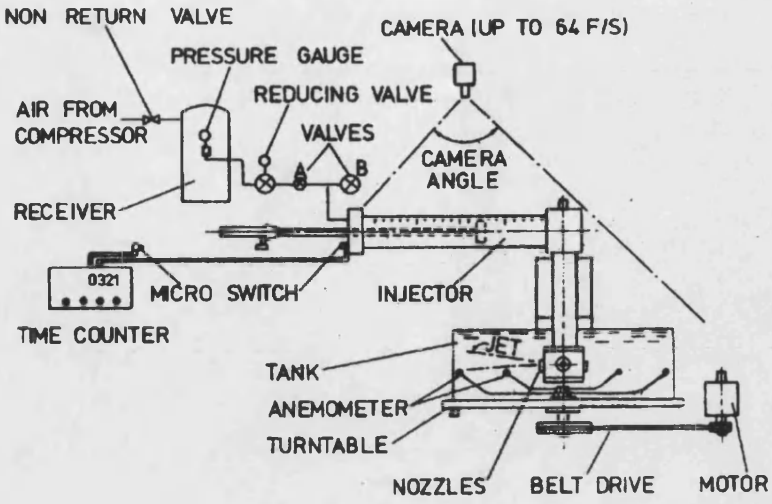

Figure 3.7: Layout of water rig [25]

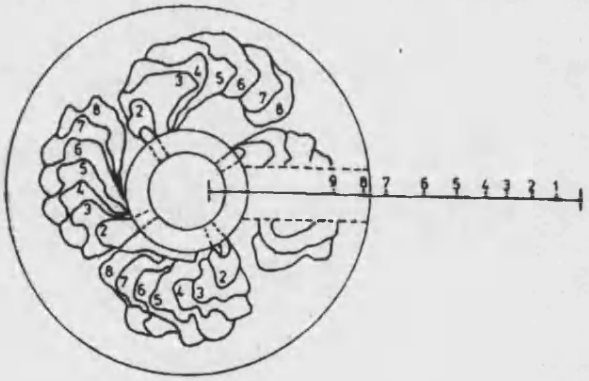

Figure 3.8: Optimum level of swirl [25]

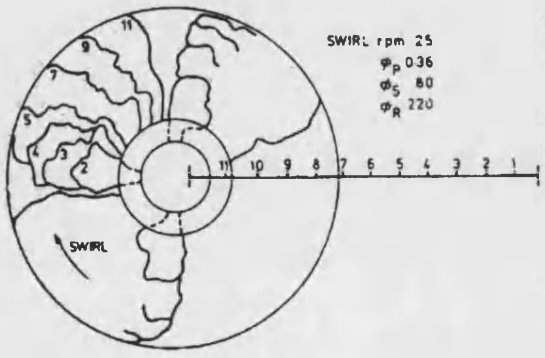

Figure 3.9: Overswirled jet produced by water rig [25]

Tindal et al [26] used an experimental swirl chamber to study the development of the spray, the distribution of fuel and air within it and the effect of air motion on this distribution. A swirl chamber was chosen in preference to an engine so that closer control could be maintained over the operating conditions and the effect of variations between one injection and another could be minimised. The development of the fuel spray was observed by means of single shot high-speed photography through windows in the side walls of the chamber. The procedure was based on a combination of direct shadow and schlieren techniques. Detailed examination of their results indicated that the spray should be considered as made up of several regions with differing characteristics. At the rear of the spray, the core may be considered separately from the region of lower fuel concentration outside it. The core here is almost undeflected by the gas motion and treatment by steady state theory should be adequate. The weaker mixture outside the core drifts downwind with a velocity, which is close to the swirl velocity; its behaviour is likely to be very dependent on the gas motion. The front section of the core is deflected by the swirl and the characteristics of the front penetration through the undisturbed gas ahead of it. Figure 3.10(a) and (b) shows the sketched form of jet at low swirl and high swirl respectively.

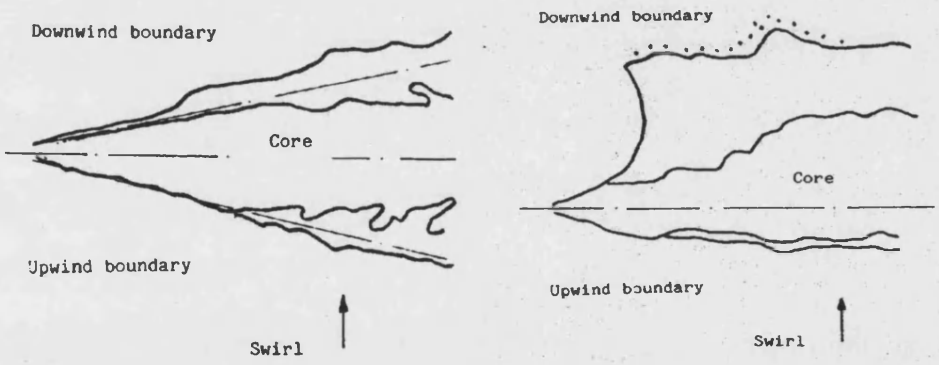

a) Low swirl **b) High swirl**

Figure 3.10: Sketched form of jet at swirl [26]

Binder and Hilburger [27] used a Schlieren method together with high-speed cine photography to study the influence of the relative motion of fuel vapour and air on the mixture formation process in a single cylinder direct injection diesel engine. No information about density gradients within the vapour plume was presented. Some

interesting conclusions are presented, however, particularly with reference to the effect of increasing injection pressure and hence spray velocities.

Their major conclusion was that with the increased fuel velocities, the initial ignition zone was finished from the root of the spray to the spray tip, i.e., in a region of high swirl.

Adler and Lyn [28] described a model for a spray evaporating in swirling air. Their approach adopts the classical turbulent jet theory, *Abramovich* [29], to two-phase sprays, solving integral equations for continuity, momentum, and energy. In addition, the formulation includes an evaporation function based on a mean droplet diameter, which is assumed to be representative of all droplets in the spray. The trajectory is calculated from equilibrium considerations of a spray segment.

Adler and Baron [30] reported an analysis of cross-flow enhanced mixing in single-phase jets. The model was implemented at Bath University by *Packer* [31] with uniform cross-flow replaced by swirl. It comprises two momentum equations in integral form in tangential direction and normal to the centreline.

A re-examination of the fundamental mathematical analysis underlying integral models by *Wilson* [32] led to a spray-mixing model capable of quantitative predictions of the trajectory and inner structure of the spray in a prescribed cross-flow. The model divides the spray into three regions, which are examined separately, (see figure 3.11):

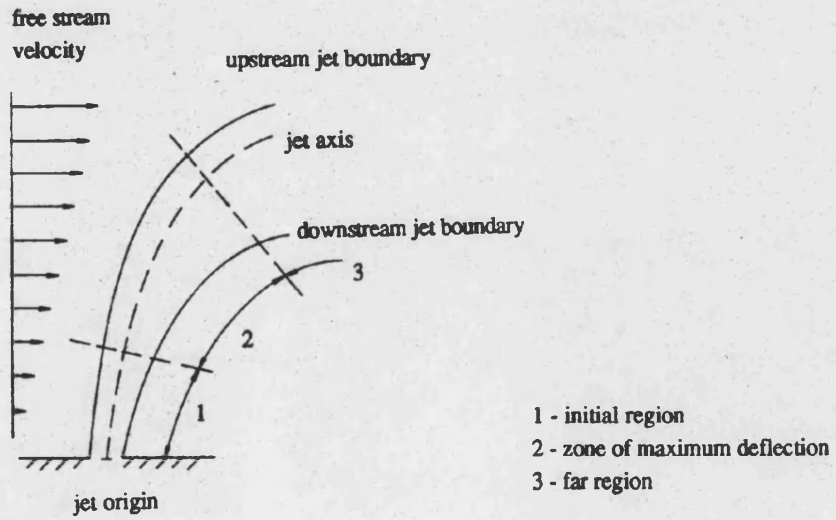

Figure 3.11: Deflected jet in a cross-flow [32]

1. The initial region with enhanced mixing due to lateral shear induced by the cross-flow. The enhanced mixing results in a shorter potential core compared with the axi-symmetric jet.
2. In the region of maximum deflection two entrainment mechanisms are considered:
   (i) Fluid drawn into the low-pressure region at the jet downstream surface.
   (ii) Turbulent entrainment due to the discontinuity in velocities.
3. In the far region the jet approaches asymptotically the main stream, leaving a pair of counter-rotating vortices moving at approximately the speed of the cross-flow. With increasing downstream distance from the point of injection the velocity difference at the jet boundary decreases. Consequently, the angular velocity of the vortices diminishes, so that the entrainment rate and the jet spreading rate decreases.

The model includes the effects of temperature and composition variation. An empirical 'enhanced entrainment coefficient', which takes into account the effect of the cross-flow velocity component normal to the local jet trajectory, is derived to give good agreement with experimental observations reported by *Kamotani and Greber* [33] and others.

3.3 Submodels - Undeflected sprays

3.3.1 New phenomenological approaches (based on conservation of momentum principle)

In order to provide the context for the spray formation approach adopted in this work, this section gives an outline of a basic simple steady incompressible spray model leading to complex transient compressible spray models.

3.3.1.1 Simple undeflected, steady isodense spray with uniform velocity distribution

An incompressible jet is obtained when ambient and injected media have the same density and the Mach number is sufficiently low for compressibility effects to be negligible.

Figure 3.12 illustrates the simple undeflected steady incompressible jet with its potential core [29], and a uniform velocity distribution at any distance x from jet pole O.

This leads to a momentum flux,

$$\begin{aligned} M_x &= \int_0^b \rho_l v^2 2\pi y dy \\ &= \rho_l \pi v^2 b^2 \\ &= \rho_l \pi v^2 x^2 \tan^2\theta \end{aligned} \tag{3.30}$$

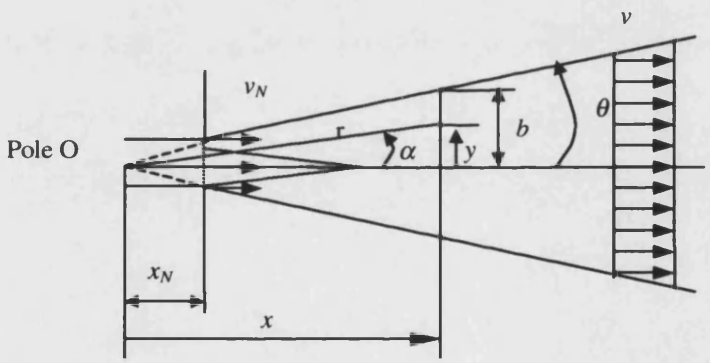

Figure 3.12: Undeflected jet

Introducing semi-included cone angles α and θ such that (see figure 3.12),

$$\begin{aligned} y &= x\tan\alpha \\ b &= x\tan\theta \\ x &= r\cos\alpha \end{aligned} \tag{3.31}$$

where r is the radial propagation.

The incoming momentum flux becomes:

$$M_l = \rho_l \pi x_N^2 v_N^2 \tan^2\theta \tag{3.32}$$

So that by momentum balance, can be obtained:

$$v = \frac{v_N x_N}{x} \tag{3.33}$$

which shows a known hyperbolic distribution for velocity along the jet axis.

$$x = \left(2 v_N x_N t + x_N^2\right)^{\frac{1}{2}} \tag{3.34}$$

Finally, mass entrainment may be calculated by integration of the mass flux at distance x and deducting the original nozzle mass flux, as below:

$$\begin{aligned} \dot{m}_e &= \int_0^b \rho_l v 2\pi y dy - \rho_l \pi v_N x_N^2 \tan^2\theta \\ &= \rho_l \pi v b^2 - \rho_l \pi v_N v_N^2 \tan^2\theta \\ &= \rho_l \pi v_N x_N (x - x_N) \tan^2\theta \end{aligned} \tag{3.35}$$

which shows that the total entrained gas flow rate depends linearly on the orifice diameter, the axial location in the spray, and the injection fuel velocity (where injected fuel velocity is proportional the square root of the pressure drop across the orifice).

3.3.1.2 Simple undeflected impulsive isodense spray with uniform velocity distribution

This case is a simplified version of *Idoum et al* [34]. In this case, again using the uniform velocity profile for velocity distribution leads to the momentum flux to agree with equation (3.30). Also it may be shown that the drag on the head of the spray is given by,

$$DF = \frac{1}{2} \rho_l C_f \pi v^2 x^2 \tan^2\theta \tag{3.36}$$

where C_f is the drag coefficient. In the present treatment $C_f = 0.45$ throughout.
Equating the sum of equations (3.30) and (3.36) to the original nozzle momentum (equation 3.32) can be obtained:

$$v(x,y) = \frac{1}{\left(1 + \frac{C_f}{2}\right)^{1/2}} \frac{v_N x_N}{x} \tag{3.37}$$

From equation (3.37) and (3.31) with $v = \frac{dx}{dt}$

$$x = \left\{ \frac{2 v_N x_N}{\left(1 + \frac{C_f}{2}\right)^{1/2}} t + x_N^2 \right\}^{\frac{1}{2}} \tag{3.38}$$

Mass entrainment may be calculated by:

$$\dot{m}_e = \rho_l \pi v_N x_N \left(\frac{1}{\left(1 + \frac{C_f}{2}\right)^{1/2}} x - x_N \right) \tan^2 \theta \tag{3.39}$$

Which still shows that the total entrained gas flow rate depends linearly on the orifice diameter, the axial location in the spray, and the injection fuel velocity (where injected fuel velocity is proportional the square root of the pressure drop across the orifice), for the simple undeflected, impulsive, isodense spray with uniform velocity distribution.

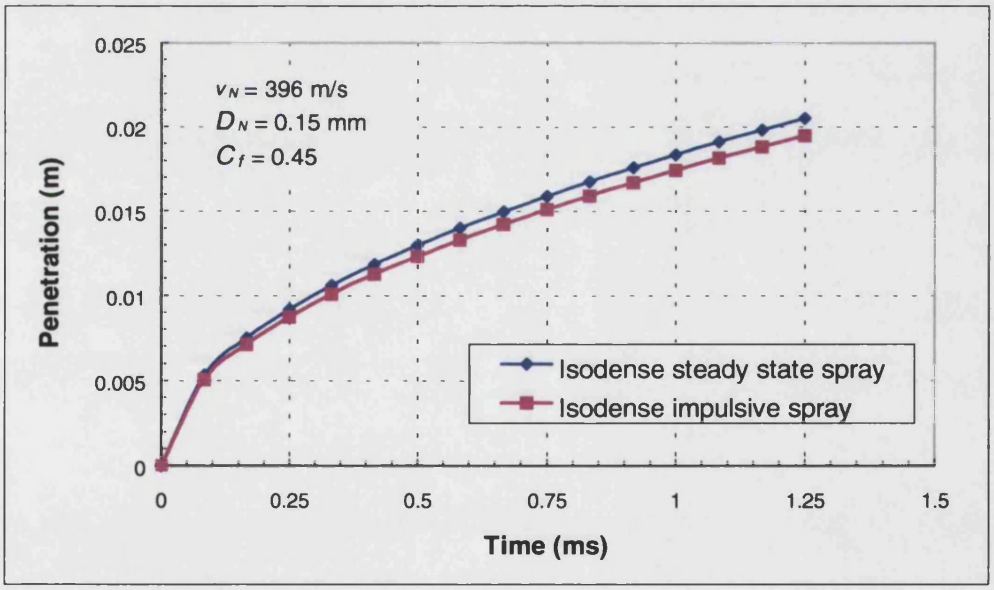

Figure 3.13: Comparison of isodense steady state and impulsive spray propagations

Spray tip penetration distance against time for isodense steady state spray and isodense impulsive spray are shown in figure 3.13. It can be clearly seen that, as expected, the drag force on the head of the spray (impulsive spray), reduces the spray tip penetration distance.

3.3.1.3 Undeflected, impulsive spray with uniform velocity distribution and density effects

The basic theory in previous section has to be modified to incorporate the various densities for injected liquid (ρ_l), surrounding gas zone density (ρ_g) and spray density of the spray in each distance from the pole O (ρ_{sp}).

In this case of study, the incoming liquid momentum flux comes from equation (3.32). The momentum flux at station x becomes:

$$M_x = \rho_{sp}\pi v^2 x^2 \tan^2\theta \tag{3.40}$$

Similarly equation (3.36), the drag on the head of the spray is given by:

$$DF = \frac{1}{2}\rho_g C_f \pi v^2 x^2 \tan^2\theta \tag{3.41}$$

So that by momentum balance can be obtained:

$$v = \sqrt{\frac{\rho_l}{\rho_{sp}}}\frac{v_N x_N}{\left(1+\frac{\rho_g}{\rho_{sp}}\frac{C_f}{2}\right)^{1/2} x} \tag{3.42}$$

Penetration, x, may be derived from equation (3.42) and (3.31) with $v = \frac{dx}{dt}$

$$x = \left\{2\sqrt{\frac{\rho_l}{\rho_{sp}}}\frac{v_N x_N}{\left(1+\frac{\rho_g}{\rho_{sp}}\frac{C_f}{2}\right)^{1/2}} t + x_N^2\right\}^{\frac{1}{2}} \tag{3.43}$$

Finally, mass entrainment may be calculated by integration of the mass flux at distance x and deducting the original nozzle mass flux, as below:

$$\dot{m}_e = \rho_l \pi v_N x_N \left(\sqrt{\frac{\rho_{sp}}{\rho_l}}\frac{1}{\left(1+\frac{\rho_g}{\rho_{sp}}\frac{C_f}{2}\right)^{1/2}} x - x_N\right)\tan^2\theta \tag{3.44}$$

For the air-fuel sprays, which are of primary interest in this thesis, spray mixed density ρ_{sp} during the pre-combustion phase can be determined from a knowledge of,

i) The fuel quantity injected up to time t

ii) The mass of entrained air over the same period t from the entrainment equation (3.44).

The simplest approach would neglect fuel vapour formation during that period giving,

$$V_{sp} = \frac{m_f}{\rho_f} + \frac{m_a}{\rho_a} \tag{3.45}$$

i.e., $$\rho_{sp} = \frac{m_f + m_a}{V_{sp}} \tag{3.46}$$

If evaporation is to be considered, the equation become much more complex, with a modified expression for ρ'_{sp}, as equation (3.47)

$$\rho'_{sp} = \frac{m_a \rho_a + (m_f \rho_f)_v}{m_a + m_f} \tag{3.47}$$

where, $(\rho_f)_v$: density of fuel vapour

$(m_f)_v$: evaporated fuel mass

To illustrate the behaviour of impulsive sprays under isodense and non-isodense conditions, using equations (3.38) and (3.43) respectively, a representative value of ρ_{sp} = 47.0 kg/m^3, together with an air density ρ_a= 37.6 kg/m^3 has been chosen, under the same injection conditions as for the comparison between the steady state and impulsive isodense sprays, equations (3.34) and (3.38), figure 3.13.

These results, for impulsive isodense sprays and non-isodense sprays are shown in figure 3.14.

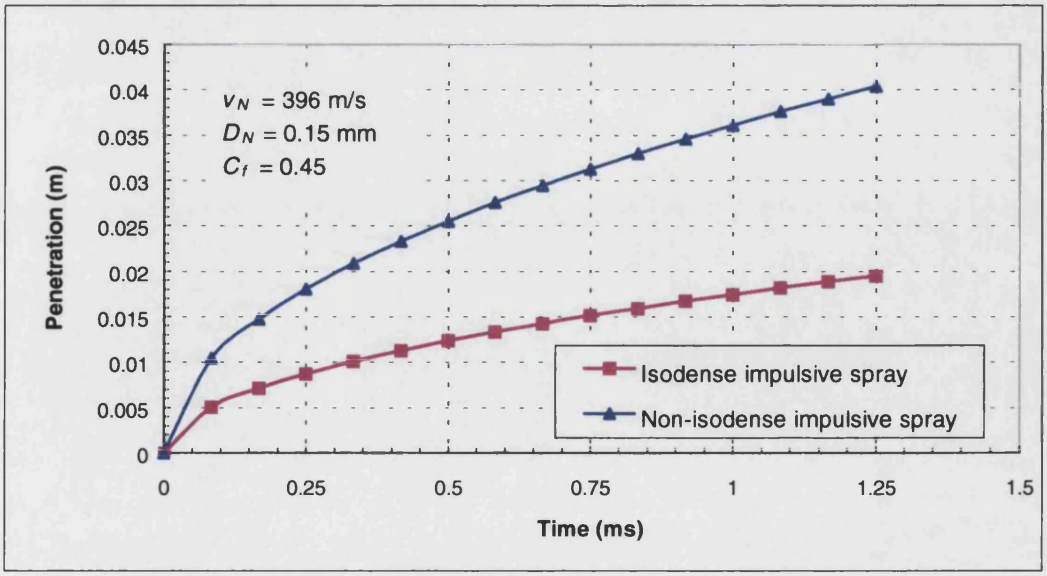

Figure 3.14: Spray tip penetration of non-isodense impulsive spray

The results show very clearly that the penetration for the non-isodense spray, i.e. fuel into air, is much greater than that for the isodense spray, i.e. fuel into fuel. This is to be expected due to the lower momentum of the entrained air, as well as the reduced drag force on the head of the spray.

The equations of section 3.3.1.3 are directly relevant to the solution of the problem of spray formation and deflection in the combustion chamber, which forms one of the main parts of this thesis.

3.4 Submodels – Deflected sprays

3.4.1 Deflected isodense sprays in swirling flow field

This preliminary assessment of spray deflection under isodense conditions follows from the earlier treatment of the undeflected isodense spray in section 3.3.1.2, but with an assumed parabolic form of transverse velocity distribution beyond the potential core (equation 3.48), *Idoum et al* [34].

$$v(x,y)=v_{max}\left(1-\frac{y^2}{b^2}\right) \tag{3.48}$$

It is assumed that the jet is deflected by pressure forces and viscous action, figure 3.15.

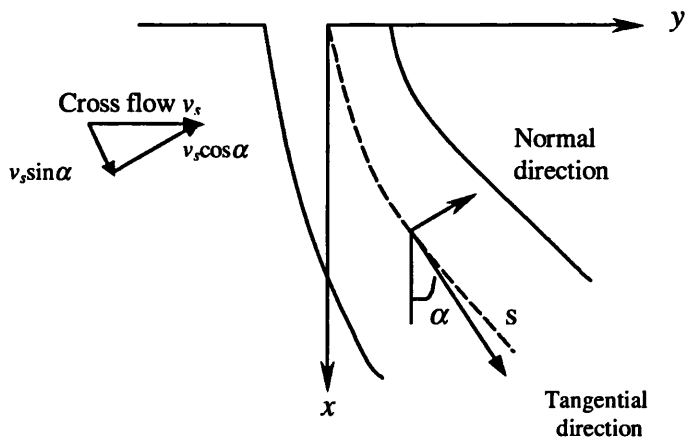

Figure 3.15: Deflected jet in a cross-flow

The entrainment into the jet may be written as:

$$\frac{d\dot{m}_{e_D}}{ds} = \rho_l \, Ev_s \overline{D} \cos\alpha + \frac{d\dot{m}_{e_u}}{ds} \tag{3.49}$$

where E is an entrainment coefficient, v_s is the cross flow velocity, and $\frac{d\dot{m}_{e_u}}{ds}$ is the entrainment rate of the corresponding undeflected free jet, which may be calculated by integration of the mass flux at distance x and deducing the original nozzle mass flux, as equation (3.50),

$$\dot{m}_e = \rho_l \pi v_N x_N \left(\frac{\sqrt{3}}{2\left(1+\frac{C_f}{2}\right)^{1/2}} x - x_N \right) \tan^2\theta \tag{3.50}$$

Considering figure3.15 the drag force on an element of the jet is given by:

$$\frac{dD_f}{ds} = \frac{1}{2} C_f \cdot \rho_l v_s^{\,2} \cos^2\alpha \cdot \overline{D} \tag{3.51}$$

The continuity equation is:

$$\rho_l \frac{d}{ds} \int_A v dA = \frac{d\dot{m}_{e_D}}{ds} \tag{3.52}$$

The tangential rate of change of momentum is:

$$\rho_l \frac{d}{ds} \int_A v^2 dA = \frac{d\dot{m}_{e_D}}{ds} v_s \sin\alpha \tag{3.53}$$

The rate of change of jet momentum normal to the centreline in the cross flow plane is equal to the entrained momentum plus the drag force given by equations (3.49) and (3.51), respectively i.e.

Since radius of curvature $R = \frac{1}{d^2y/dx^2}\left[1+\left(\frac{dy}{dx}\right)^2\right]^{\frac{3}{2}}$ then:

$$\rho_l \int_A v^2 dA \frac{d^2y/dx^2}{\left[1+\left(\frac{dy}{dx}\right)^2\right]^{\frac{3}{2}}} = \left(\frac{d\dot{m}_{e_D}}{ds} + \frac{1}{2} C_f \cdot \rho_l v_s \cos\alpha \cdot \overline{D} \right) v_s \cos\alpha \tag{3.54}$$

To simplify the solution the jet is assumed to have a cross-section area of "equivalent" diameter $\overline{D}$ (i.e. circular).

If the ratio (v/v_s) is not too large then $\alpha \approx 0$ and equations (3.52), (3.53), and (3.54) may be solved in closed form:

if $\alpha \approx 0$ then $dx \approx ds$ and,

$$\rho_l \frac{d}{dx}\left(\bar{v}\frac{\pi}{4}\overline{D}^2\right) = \frac{d\dot{m}_{e_D}}{dx} \tag{3.55}$$

$$\rho_l \frac{d}{dx}\left(\bar{v}^2\frac{\pi}{4}\overline{D}^2\right) = 0 \tag{3.56}$$

and from (3.54)

$$\rho_l \bar{v}^2 \frac{\pi}{4}\overline{D}^2 \frac{d^2y}{dx^2} = \left(\frac{d\dot{m}_{eD}}{dx} + \frac{1}{2}C_f \rho_l v_s \overline{D}\right) v_s \tag{3.57}$$

Equation (3.55) gives an integration and setting

$$\overline{D} = D_N \qquad \text{at} \qquad x = 0$$

$$\overline{D} + \frac{\left(\frac{d\dot{m}_{e_u}}{dx}\right)}{\rho_l E v_s} = \left(D_N + \frac{\left(\frac{d\dot{m}_{e_u}}{dx}\right)}{\rho_l E v_s}\right)\exp(C_1 x) \tag{3.58}$$

where $C_1 = \dfrac{4Ev_s}{\pi D_N v_N}$

Equation (3.57) after integration with $\dfrac{dy}{dx} = 0$ at x = 0 (right angle injection) and substituting for $\overline{D}$ from (3.58) gives:

$$\frac{dy}{dx} = C_2\left[\left(D_N + \frac{\left(\frac{d\dot{m}_{e_u}}{dx}\right)}{\rho_l E v_s}\right)\frac{1}{C_1}\left(e^{C_1 x} - 1\right)\right] + \left[-\frac{C_2\left(\frac{d\dot{m}_{e_u}}{dx}\right)}{\rho_l E v_s} + C_3\right]x \tag{3.59}$$

where $C_2 = \dfrac{4\left(E + \frac{C_f}{2}\right)v_s^2}{\pi D_N^2 v_N^2}$

and $C_3 = \dfrac{4\left(\frac{d\dot{m}_{e_u}}{dx}\right)v_s}{\rho_l \pi D_N^2 v_N^2}$

integration with $y = 0$ at $x = 0$ gives the centreline trajectory

$$y = C_2\left[\left(D_N + \frac{\left(\frac{d\dot{m}_{e_u}}{dx}\right)}{\rho_l E v_s}\right)\right]\frac{1}{C_1}\left[\frac{1}{C_1}\left(e^{C_1 x}-1\right)-x\right]+\left[C_3 - \frac{C_1\left(\frac{d\dot{m}_{e_u}}{dx}\right)}{\rho_l E v_s}\right]\frac{x^2}{2} \qquad (3.60)$$

The trajectories of the upstream and downstream boundaries are obtained from the centreline trajectory and the jet width.

The mean velocity $\bar{v}$ is given by:

$$\bar{v} = v_N \frac{D_N}{\overline{D}} \qquad (3.61)$$

Substituting for $\overline{D}$ from equation (3.58) and replacing $\bar{v}$ with $\frac{dx}{dt}$ gives their expression for time to penetration t:

$$t = \frac{1}{v_N}\left\{\left(1+\frac{\left(\frac{d\dot{m}_{e_u}}{dx}\right)}{E v_s D_N}\right)\left(\frac{1}{C_1}\right)\left(e^{C_1 x}-1\right)-\frac{\left(\frac{d\dot{m}_{e_u}}{dx}\right)}{\rho_l E v_s D_N}x\right\} \qquad (3.62)$$

Figure 3.16 shows the effect of swirl on the jet deflection for the same injection conditions and identical E values.

Also Figures 3.17 shows the effect of the entrainment coefficient, E, on development of swirled jet for identical injection and cross-flow conditions.

In both figures the time shown indicates the time from injection to impingement (in seconds).

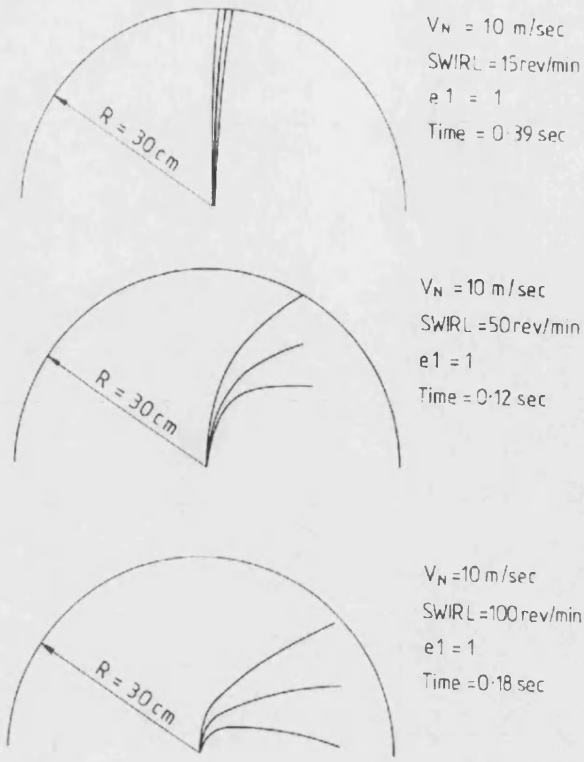

Figure 3.16: Effect of swirl [34]

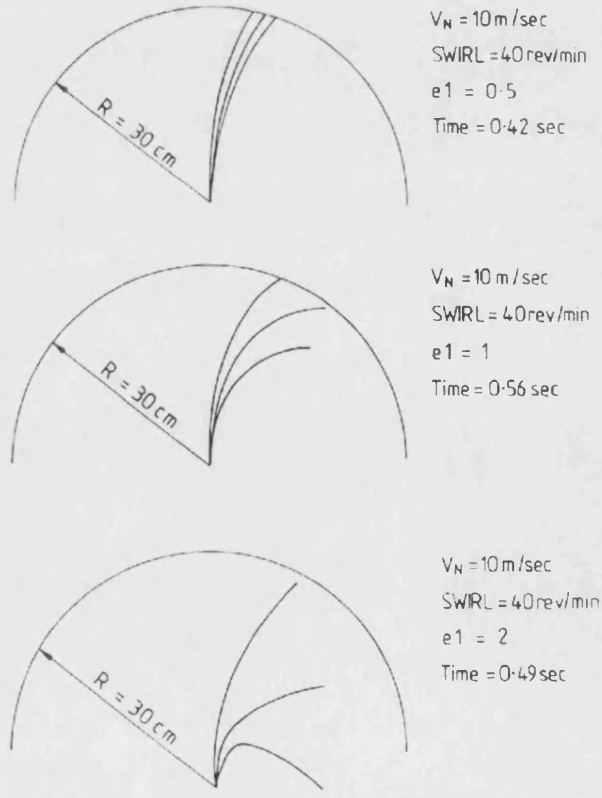

Figure 3.17: Effect of entrainment coefficient [34]

3.5 Discussion

The results of sections 3.3.1.1, 3.3.1.2 and 3.3.1.3, figures 3.13 and 3.14, show very clear differences between the three cases presented, viz.

a) Steady state isodense spray

b) Impulsive isodense spray

c) Impulsive non-isodense spray

With regard to the deflected isodense spray swirling flow, the treatment although involving major mathematical simplifications nevertheless indicates useful treads.

Figure 3.16, showing spray deflection for different rates of swirl and constant entrainment, indicates obvious trends, viz. increasing deflection with increasing swirl rate.

Figure 3.17 for variable rates of entrainment *e* and due to the associated increase in angular momentum transferred from the swirling air to the spray, also increased deflection.

3.6 References

1. **Dent, J. C.**, "A Basis for the Comparison of Various Experimental Methods for Studying Spray Penetration", SAE 710571 (1971).

2. **Hiroyasu, H. and Arai, M.**, "Fuel Spray Penetration and Spray Angle in Diesel Engines", Trans. Of the SAE of Japan, 21 (1980), 5-11.

3. **Arai, M., Tabata, M., Hiroyasu, H., and Shimusu, M.**, "Disintegrating Process and Spray Characterization of Fuel Jet Injected by a Diesel Nozzle", SAE 840275 (1984).

4. **Levich, V. G.**, Physicochemical Hydrodynamics, Prentice-Hall Inc., pp 639-650 (1962).

5. **Varde, K. S., and Popa, D. M.**, "Diesel Fuel Spray Penetration at High Injection Pressures", SAE Paper No. 830448 (1983).

6. **Varde, K. S., Popa, D. M., and Varde, L. K.**, "Spray Angle and Atomization in Diesel Sprays", SAE 841055 (1984).

7. **Schihl, P., Bryzik, W., and Atreya, A.**, "Analysis of Current Spray Penetration Models and Proposal of a Phenomenological Cone Penetration Model", SAE 960773 (1996).

8. **Reitz, R. D., and Bracco, F. V.**, "Mechanism of Atomization of a Liquid Jet", *Physics of Fluids*, vol.25, No.10, pp. 1730-1742, (1982).

9. **Payri, F., Desantes, J. M., and Arregle, J.**, "Characterization of DI Diesel Sprays in High Density Conditions", SAE 960774 (1996).

10. **Farrell, P. V., Chang, C. T., and Su, T. F.**, "high Pressure Multiple Injection Spray Characteristics", SAE 960860 (1996).

11. **Sasaki, S., Akagawa, H., and Tsujimura, K.**, "A Study on Surrounding Air Flow Induced by Diesel Sprays", SAE 980805 (1998).

12. **Levy, N., Amara, S., and Champoussin, J.-C.**, "Simulation of a Diesel Jet Assumed Fully Atomized at the Nozzle Exit", SAE 981067 (1998).

13. **Levy, N., Amara, S., Champoussin, J.-C., and Guerrassi, N.**, "Non-Reactive Diesel Spray Computations Supported by PDA Measurements", SAE 970049 (1997).

14. **Chiu, W. s., Shahed, S. M., and Lyn, W. T.**, "A Transient Spray Mixing Model of Diesel Combustion, SAE 760128 (1976).

15. **Presches, K., Astachow, A., Krüger, G., and Hintze, K.**, "Investigation of the Atomization and Evaporation of Diesel Fuel and Heavy Fuel Sprays Using Optical Measurement Techniques", SAE 1999-01-0520 (1999).

16. **Rajalingam, B.V., and Farrell, P.V.**, "The Effect of Injection Pressure on Air Entrainment into Transient Diesel Sprays, SAE 1999-01-0523 (1999).

17. **Araneo, L., Coghe, A., Brunello, G., and Cossali, G.E.**, "Experimental Investigation of Gas Density Effects on Diesel Spray Penetration and Entrainment", SAE 1999-01-0525 (1999).

18. **Abraham, J., and Magi, V.**, " A Virtual Liquid Source (VLS) Model for Vaporizing Diesel Sprays", SAE 1999-01-0911 (1999).

19. **Arrègle, J., Pastor, J.V.**, and Ruiz, S., "The Influence of Injection Parameters on Diesel Spray Characteristics", SAE 1999-01-0200 (1999).

20. **Siebers, D. L.**, "Liquid-Phase Fuel Penetration in Diesel Sprays", SAE 980809 (1998).

21. **Naber, J. D., and Siebers, D. L.**, "Effect of Gas Density and Vaporization on Penetration and Dispersion of Diesel Sprays", SAE 960034 (1996).

22. **Melton, R.B., and Rogowski, A.R.**, "The Interaction of Air Motion, Fuel Spray and Combustion in the Diesel Combustion Process", ASME Journal of Engineering for Power (1972).

23. **Melton, R.B.**, "Diesel Fuel Injection Viewed as a Jet Phenomenon", SAE 710132 (1971).

24. **Lustgarten, G.**, "Model Investigations of the Mixing and Combustion Process in the Diesel Engine", Sulzer Research No. 1974.

25. **Way, R.J.B.**, "Investigation of Interaction Between Swirl and Jets in Direct Injection Diesel Engines using a Water Model", SAE 770412 (1977).

26. **Tindal, M.J., Williams, T.J., and Harcomb, A.T.**, "Fuel Spray Formation in an Experimental Swirl Chamber", SAE 870451 (1987).

27. **Binder, K., and Hilburger, W.**, "Influence of the Relative Motions of Air and Fuel Vapour on the Mixture Formation Processes of Direct Injection Diesel Engines", SAE 810831 (1981).

28. **Adler, D., and Lyn, W.T.**, "The Steady Evaporation and Mixing of a Spray in a Gaseous Swirl", Int. J. Heat Mass Transfer, Vol. 14, pp 793 (1971).

29. **Abramovich, R. G. N.**, The Theory of Turbulent Jets, MIT Press, (1963).

30. **Adler, D., and Baron, A.**, "Prediction of a Three Dimensional Circular Turbulent Jet in Crossflow", AIAA Journal, Vol. 17, No. 2, pp. 168 (1979).

31. **Packer, J.P.**, "Diesel Type Combustion Studies in High Swirl Chambers", PhD Thesis, University of Bath (1983).

32. **Wilson, M.**, "Integral Modelling of Jets of Variable Composition in Generalised Crossflow", PhD Thesis, University of Bath (1986).

33. **Kamotani, Y., and Greber, I.**, "Experiments on a Turbulent Jet in a Crossflow", Case Western Reserve University, NASA CR-72893 (1971).

34. **Idoum, A., Wallace, F. J., Packer, J. P., and Charlton, S. J.**, "An Experimental and Analytical Study of Jet Impingement and Wall Jets in High Swirl D. I. Diesel Engines using the Hydraulic Analogy", SAE 850263 (1985).

CHAPTER 4

Swirl generation in combustion bowl under motoring conditions

4.1 Introduction

This chapter starts with a brief literature survey of swirl generation in the main cylinder and combustion bowl of direct injection four stroke Diesel engine achieved by the use of directed or helical inlet ports.

A new swirl generation submodel is then developed, based on an assumed known swirl ratio at IVC and the subsequent application of the principles of conservation of mass and angular momentum which govern the reduction of mass and momentum in the main cylinder, and their corresponding increase in the combustion bowl, up to TDC. The reversal of these processes after TDC, under motoring conditions, is also dealt with. The full treatment for swirl generation under firing conditions is presented in chapter 8. The chapter closes with the relevant references.

4.2 Literature survey

4.2.1 General swirl generation mechanism

The discussion of diesel combustion has centred on the spray characteristics. However, the shape of the combustion chamber and the fluid motion in it are also of importance. One of the most important parameters in fluid motion is swirl.

Swirl is usually defined as organised rotation of the charge about the cylinder axis, which is created by bringing the intake flow into the cylinder with an initial angular momentum. Swirl is used especially in HSDI Diesel engines to promote more rapid mixing between the inducted air and the injected fuel.

Swirl producing inlet ports can be categorised under two basic groups depending on whether swirl is produced downstream (post-valve swirl) or upstream of the inlet valve (pre-valve swirl). The directed port and deflector wall port shown in figure 4.1 are two common ways of achieving post- valve swirl and the helical ports shown in figure 4.1 are two examples of pre-valve swirl. Usually, with helical ports, a higher flow discharge coefficient at an equivalent level of swirl is obtained, since the whole periphery of the valve open area can be fully utilised. A higher volumetric efficiency results. Also helical ports are less sensitive to position displacements, such as can occur in casting, since the swirl generated depends mainly on the port geometry above the valve and not the position of the port relative to the cylinder axis.

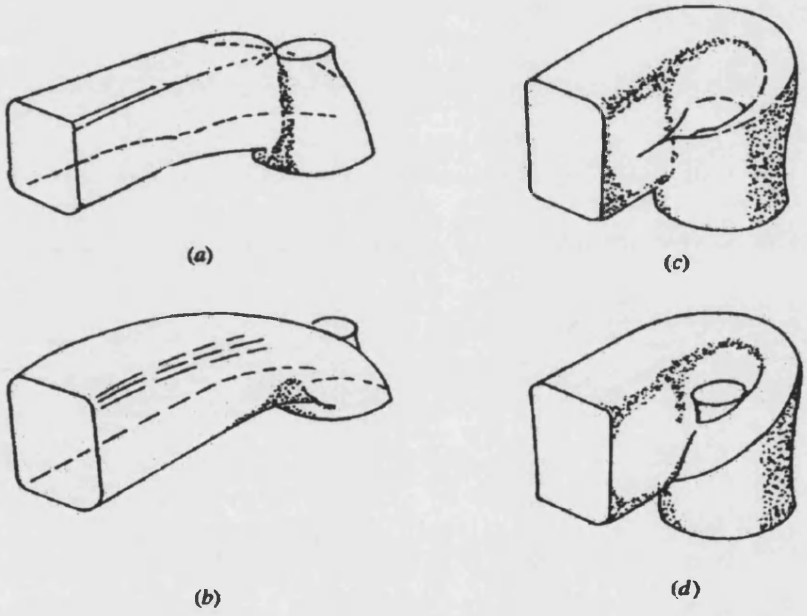

Figure 4.1: Different type of swirl-generation inlet ports: (a) deflector wall; (b) directed; (c) shallow ramp helical; (d) steep ramp helical, [1].

Results from steady flow tests show that helical ports offer advantages over the directed ports in that helical ports produce higher swirl levels at low and medium valve lifts, albeit lower at high valve lifts, do not interfere with the head cooling passages, *Uzkan et al* [2], and are less sensitive to the location in the cylinder head, *Watts and Scott* [3], allowing bigger manufacturing tolerances. In addition, helical ports achieve a more ordered bulk flow, *Wigley and Hawkins* [4], higher discharge coefficients at equivalent swirl ratios and better performance over a wide range of speeds, *Brandl et al* [5]. For these reasons most current HSDI diesel engines use

helical ports, particularly of the shallow ramp type which gives a directional effect, in order to take advantage of the better performance of directional inlet ports at high valve lifts [2].

4.2.2 Swirl and air motion effects in engines

As has already been stated, the key factors in the operation of the small HSDI Diesel engine are:

a) The organised rotation of the air about the cylinder axis, known as swirl
b) The combustion chamber with a bowl-in-piston and small TDC clearance
c) The fuel injection system.

Swirl is induced during intake by specially designed ports and evolves during the induction and most of the compression stroke until about 40° before TDC, when the geometry of the piston forces the air into the bowl, altering the flow field. The mean swirl and turbulence levels combined with injection system characteristics control the mixing process between the air charge and the fuel inside the piston cavity and determine the efficiency of the compression-ignition combustion. Improvements in the overall performance of HSDI Diesel engines in terms of efficiency and emission, require detailed knowledge of the pre-combustion flow field, as determined by the swirl levels and the piston geometry, and in-depth understanding of the fast transient phenomena occurring after the start of fuel injection and during the combustion process.

Empirical research methods employed until about 40 years ago provided qualitative information of the in-cylinder processes which, combined with engineering intuition resulted in rules for the design of improved versions. More recent experimental developments include laser-based techniques such as laser doppler and phase doppler velocimetry, Rayleigh scattering, spontaneous and coherent Raman spectroscopy complemented by more classical techniques such as piezoelectric transducers, high speed photography and spectroscopy to provide detailed mapping of the unsteady three-dimensional velocity, temperature, pressure and concentration fields inside the cylinder.

Hatziapostolou [6] describes an experimental investigation of the in-cylinder flow field in DI Diesel engines under both motored and firing conditions. The experimental

techniques included laser doppler velocimetry, laser beam deflection, high-speed photography and shadowgraphy. The in-cylinder flow during induction and compression was characterised in terms of spatially and temporally resolved ensemble-averaged axial and swirl velocities obtained at engine speed between 1000 to 3000 rev/min for three swirl levels.

In order to get a thorough understanding of in-cylinder gas flow pattern with respect to space as well as time, numerical techniques are used as an alternative to experimental studies. Thus, predictive capabilities can be provided which will give a better understanding of the problems and more confidence in the design. Such a recognised technique is Computational Fluid Dynamics (CFD).

CFD must be used to solve Diesel engine combustion chamber gas flow, with their complex flow fields that do not have known analytical solutions. Moreover they can provide more detailed information than it is possible to obtain with measurements.

The prediction of the gas flow motion and the production of quantitative and qualitative in-cylinder gas flow visualisation data can be performed by the use of general CFD packages.

Berals [7], used the STAR-CD, CFD code as a means directed towards two mains objectives:

1. Computation of the flows during the compression stroke under motored cycle operation, from Bottom Dead Centre (BDC) to the Start of Injection (SOI) to establish the flow pattern at the later point and to enhance the general knowledge of flow patterns in HSDI Diesel engines.
2. Study the effects of the intake flow on the gas flow field calculations achieved at the former stage.

Parametric investigations were performed for different intake conditions to highlight their influence on the flow mean characteristics. Different simplified geometries were implemented in the CFD models to study their sensitivity to their level of detail. Sensitivity is also investigated by varying input parameters such as gas properties, boundary conditions, modelling assumptions, initial conditions, external influences and numerical formulations.

The objective for the CFD models was to get as close as possible to a real engine configuration by taking reference to the new PUMA engines under development at the Ford Motor Company. The PUMA is a HSDI Diesel engine aimed to comply with Euro IV emission regulations.

Figure 4.2 shows two bowl-in-piston geometries used for the CFD code, i.e., the Omega bowl model and the Compact bowl model, the latter having a simple cylindrical shape with the radius and depth of the Omega bowl model.

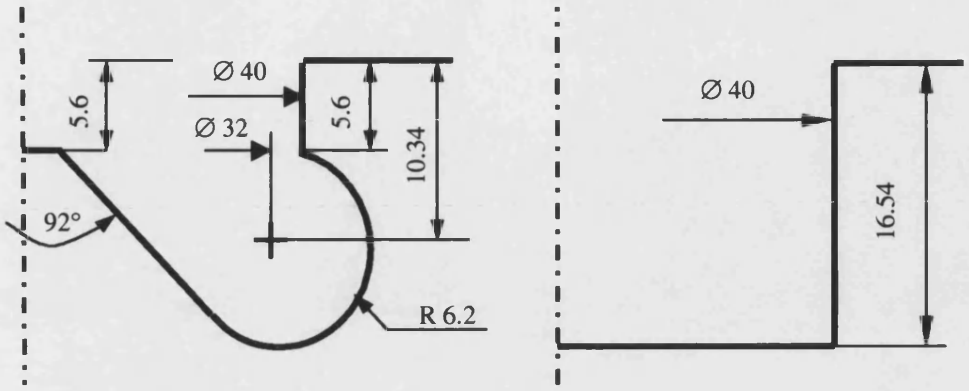

a) The omega model **b) The compact model**

Figure 4.2: Bowl-in-piston geometry [7]

Contours of computed swirl distributions for two models at TDC are shown in figure 4.3. Very similar flow field structures are observed. Peak tangential velocities for the Compact model computations are about 6% higher than those for the Omega model computations.

Also figures 4.4 and 4.5 show axial-radial velocities and contours of computed swirl distribution for the Omega model at different stages of intake and compression stroke of the PUMA type of HSDI Diesel engine, respectively.

It is evident from these illustrations that the method is capable of extremely detailed resolution of the full three-dimensional flow field. Figures 4.3 and 4.5 provide some indication that the swirl pattern within both type of combustion bowl follows broadly solid body rotation pattern.

At an engine speed of 4200 rev/min and an assumed swirl ratio at IVC of 2.5 they indicate maximum linear velocities of the order of 70 m/sec at a radius of 14.5 mm, i.e., a rotational speed of 4820 rad/sec from an initial value of 1100 rad/sec at IVC.

These results will provide a broad guide as to the general validity of the simplified treatment adopted in the present work described in the following section 4.3 the results of which are fully discussed in chapter 9.

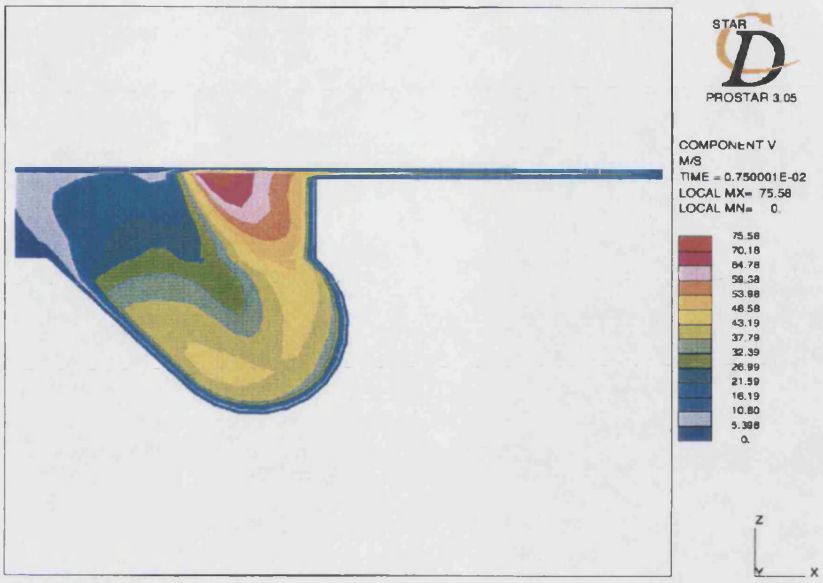

a) Omega bowl

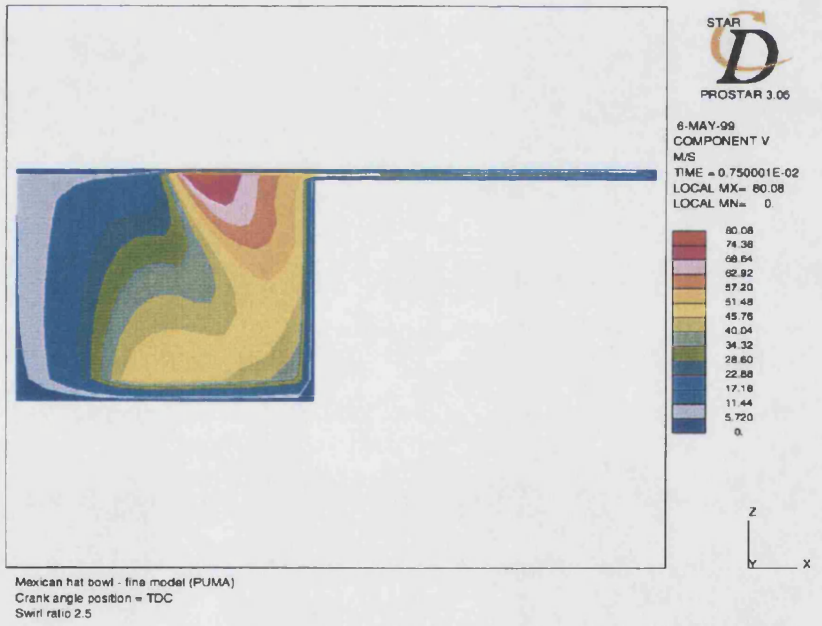

b) Compact bowl

Figure 4.3: Contours of computed swirl distribution at TDC (engine speed at full power condition 4200 rev/min) [7]

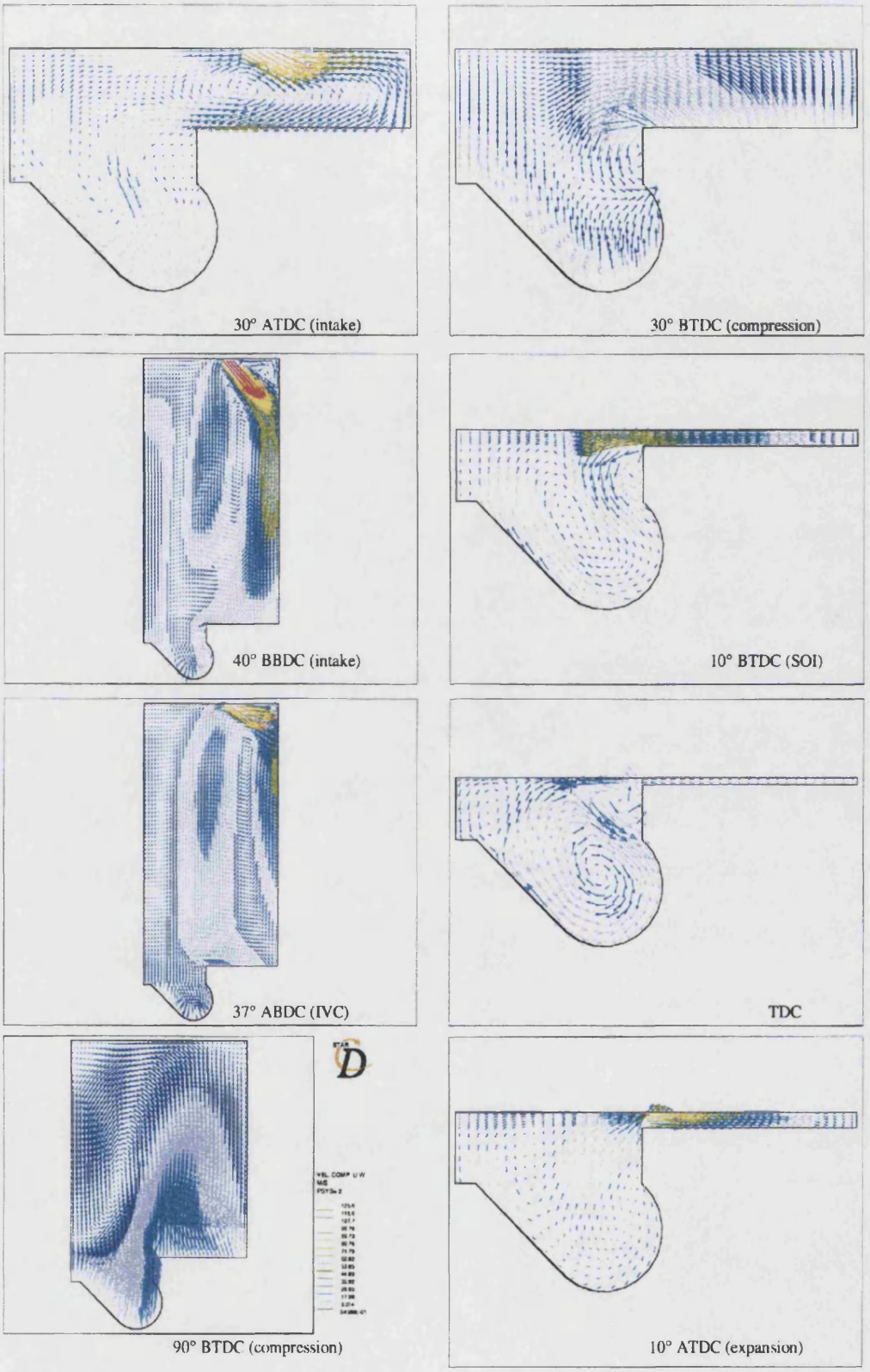

Figure 4.4: Axial-radial velocities (engine speed at full power condition 4200 rev/min) [7]

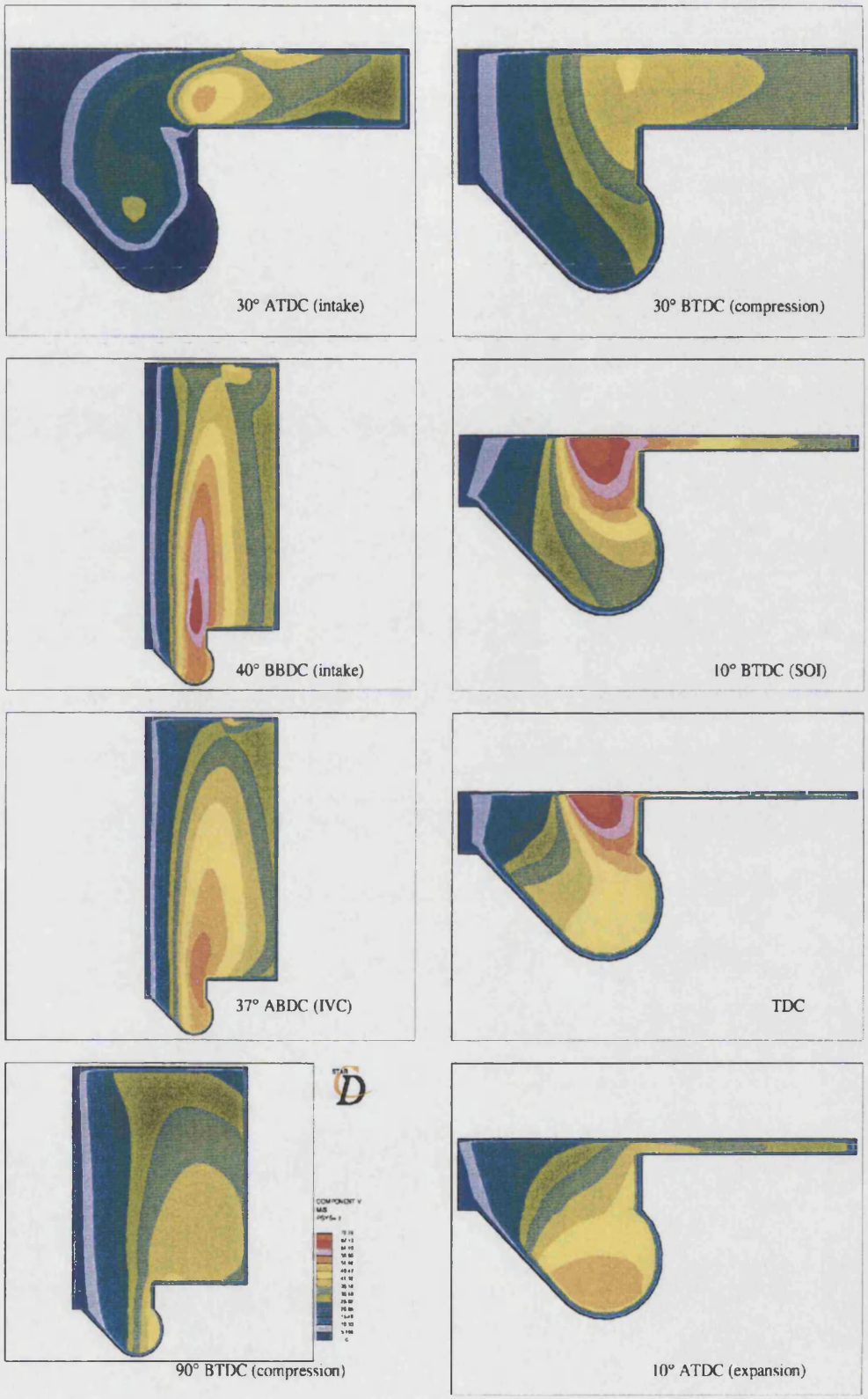

Figure 4.5: Contours of computed swirl distribution (engine speed at full power condition 4200 rev/min) [7]

4.3 Simplified new swirl generation submodel under motoring conditions

As in the case of the simplified spray submodel discussed in section 3.3, the submodel developed for use with the basic program ODES is based on major simplifying assumptions concerning both the nature of the flow and the geometry of the combustion bowl.

The actual bowl shape, figure 4.6(a), is represented by two alternative combustion chamber geometries, viz. compact (bowl radius Rb = 20 mm and depth e = 15.8 mm) figure 4.6(b), and "Mexican Hat" (bowl radius Rb = 30 mm and depth e_1 = 10.0 mm, e_2 = 1.6 mm) figure 4.6(c), while the air-motion both in the main cylinder and in the combustion bowl is assumed to be solid body rotation.

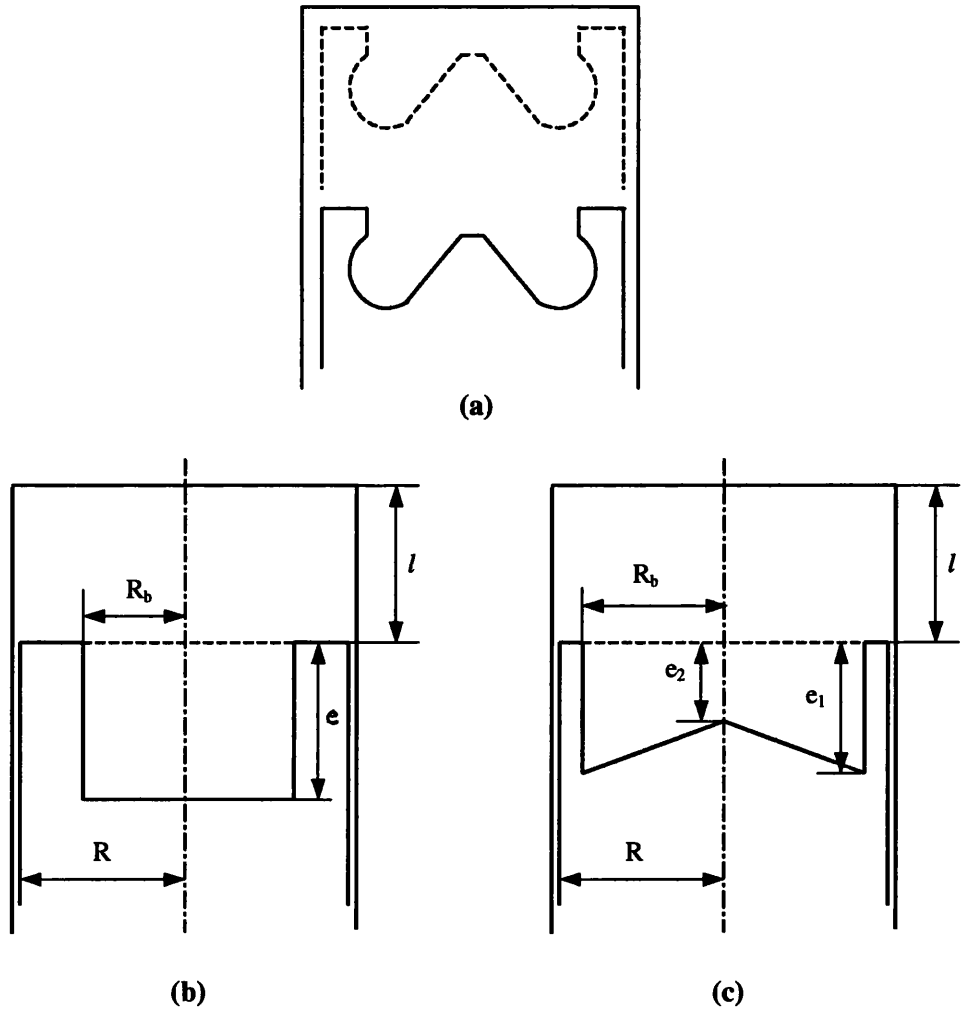

Figure 4.6: Bowl-in-piston

With regard to initial conditions, it is assumed that the angular velocity of solid body rotation in the main cylinder is known at IVC, based on available experimental evidence from swirl-meters.

The calculation than proceed as the basis of conservation of overall angular momentum, including transfer from the main cylinder to the combustion bowl during compression, with due allowance for friction.

4.3.1 Compact small diameter bowl-in-piston chamber (fig. 4.6b)

4.3.1.1 Compression stroke (from IVC to TDC)

The model was developed based on conservation of rate of angular momentum, viz.

rate of change of = rate of inflowing – rate of outflowing – rate of friction

ang. momentum ang. momentum ang. momentum momentum (4.1)

Allowing for bowl volume from fig. 4.6(b),

$$V_b = \pi R_b^2 e \tag{4.2}$$

And V_{cyl} from the cylinder geometry may be obtained from:

$$V_{cyl} = \pi R^2 l + V_b \tag{4.3}$$

or,
$$l = \frac{V_{cyl} - V_b}{\pi R^2} \tag{4.4}$$

and volume of main cylinder can be obtain from:

$$V_m = \pi R^2 l \tag{4.5}$$

Assuming equal densities in bowl & main cylinder, mass in main cylinder is equal:

$$m_m = \pi R^2 l \rho$$

$$m_m = m_{cyl} \frac{\pi R^2 l}{V_{cyl}} \tag{4.6}$$

or,
$$\frac{m_m}{m_{cyl}} = \frac{\pi R^2 l}{V_{cyl}} \tag{4.6A}$$

$\therefore$
$$\frac{d\left(\frac{m_m}{m_{cyl}}\right)}{d\theta} = \pi R^2 \frac{d\left(\frac{l}{V_{cyl}}\right)}{d\theta}$$

$$\frac{d\left(\frac{m_m}{m_{cyl}}\right)}{d\theta} = \pi R^2 \frac{V_{cyl}\frac{dl}{d\theta} - l\frac{dV_{cyl}}{d\theta}}{V_{cyl}^2}$$

From equation (4.4) can be written,

$$\frac{dl}{d\theta} = \frac{1}{\pi R^2}\frac{dV_{cyl}}{d\theta}$$

$\therefore$ from equation (4.3)

$$\frac{d\left(\frac{m_m}{m_{cyl}}\right)}{d\theta} = \frac{V_b}{V_{cyl}^2}\frac{dV_{cyl}}{d\theta} \tag{4.7}$$

and on the other hand left hand side of equation (4.7) can be obtained from:

$$\frac{d\left(\frac{m_m}{m_{cyl}}\right)}{d\theta} = \frac{1}{m_{cyl}}\frac{dm_m}{d\theta} - \frac{m_m}{m_{cyl}^2}\frac{dm_{cyl}}{d\theta}$$

and since, $m_{cyl} = \rho_{cyl} V_{cyl} = \text{constant}$

then: $\frac{dm_{cyl}}{d\theta} = 0$

$\therefore$ $$\frac{d\left(\frac{m_m}{m_{cyl}}\right)}{d\theta} = \frac{1}{m_{cyl}}\frac{dm_m}{d\theta} \tag{4.8}$$

Rate of mass of transfer to bowl equation (4.7) and (4.8) is giving by:

$$\frac{dm_m}{d\theta} = m_{cyl}\frac{V_b}{V_{cyl}^2}\frac{dV_{cyl}}{d\theta}$$

or, $$\frac{dm_m}{d\theta} = \rho_{cyl}\frac{V_b}{V_{cyl}}\frac{dV_{cyl}}{d\theta} \tag{4.9}$$

Also, rate of outflow from main volume (V_m)= – rate of change of mass in cylinder, i.e.,

$\therefore$ $$\frac{dm_{out}}{d\theta} = -\frac{dm_m}{d\theta} = -\rho_{cyl}\frac{V_b}{V_{cyl}}\frac{dV_{cyl}}{d\theta} \tag{4.10}$$

Instantaneous rate of outflowing angular momentum from main cylinder becomes:

$$Mom_{out} = \frac{R^2}{2}\omega\frac{dm_{out}}{dt}$$

or, $$Mom_{out} = -\frac{R^2}{2}\omega\rho_{cyl}\frac{V_b}{V_{cyl}}\frac{dV_{cyl}}{d\theta}\frac{d\theta}{dt} \quad (4.11)$$

also, the rate of change of angular momentum for the main cylinder is given by:

$$\frac{d(I_m\omega)}{dt} = I_m\frac{d\omega}{dt} + \omega\frac{dI_m}{dt}$$

where, $I_m = m_m\frac{R^2}{2}$

and $m_m = \rho_{cyl}(V_{cyl} - V_b)$

$\therefore$ $$\frac{d(I_m\omega)}{dt} = \rho_{cyl}\frac{R^2}{2}(V_{cyl} - V_b)\frac{d\omega}{dt} + \frac{R^2}{2}\omega\frac{dm_m}{dt}$$

or, $$\frac{d(I_m\omega)}{dt} = \rho_{cyl}\frac{R^2}{2}(V_{cyl} - V_b)\frac{d\omega}{dt} + \frac{R^2}{2}\omega\rho_{cyl}\frac{V_b}{V_{cyl}}\frac{dV_{cyl}}{dt} \quad (4.12)$$

A friction term is also included. The wall friction (shear stress) may be expressed in the form,

$$\tau = \frac{1}{2}f\rho_{cyl}(R\omega)^2$$

The liner area is $2(V_{cyl} - V_b)/R$, and the disc area (piston crown area) is πR^2. The approximate integration of moment of friction for the both the piston crown and head areas is added to the moment on the linear walls, giving a total moment of

$$Mom_{fr} = \tau AR$$

where, $A = 2\frac{(V_{cyl} - V_b)}{R} + \pi R^2$

Then, $Mom_{fr} = \frac{1}{2}f\rho_{cyl}(R\omega)^2\left(2\frac{V_{cyl} - V_b}{R} + \pi R^2\right)R$

or, $$Mom_{fr} = \frac{1}{2}f\rho_{cyl}(R\omega)^2\left[2(V_{cyl} - V_b) + \pi R^3\right] \quad (4.13)$$

The friction factor, f, under turbulent conditions may be approximated by,

$$f = \frac{0.046}{(\mathrm{Re})^{0.2}}$$

Finally equation (4.11), (4.12), and (4.13) can then be substituted into equation (4.1) to give,

$$\frac{d(I_m\omega)}{dt} = Mom_{in} - Mom_{out} - Mom_{fr}$$

and for calculation after inlet valve closing (IVC) we know that, $Mom_{in}=0$

$$\therefore \quad \frac{d\omega}{dt} = -f\omega^2\left(2+\frac{\pi R^3}{V_{cyl}-V_b}\right) \tag{4.14}$$

Carrying the time increment, dt, and an initial value of, ω, onto the right hand side yields a differential equation solvable for ω

Finally, an equation has to be formulated for the transfer of momentum to the bowl represented now by the positive term $-\rho_{cyl}\frac{R^2}{2}\omega\frac{V_b}{V_{cyl}}\frac{dV_{cyl}}{d\theta}\frac{d\theta}{dt}$ in equation (4.11).

This momentum is absorbed $\begin{cases} a) \text{ by acceleration} \\ b) \text{ by friction} \end{cases}$

Denoting angular velocity in bowl by ω_b and moment of inertia of bowl by,

$$I_b = m_b\frac{R_b^2}{2},$$

where, $m_b = \rho_{cyl}\pi R_b^2 e$

The acceleration term becomes:

$$\frac{d(I_b\omega_b)}{dt} = I_b\frac{d\omega_b}{dt}+\frac{R_b^2}{2}\omega_b\frac{dm_b}{dt} \tag{4.15}$$

By simple analogy with the model in the main cylinder for calculation of friction term for the bowl, but in here the linear area is equal, $A = 2\pi R_b e + \pi R_b^2$

$$\therefore \quad \left(Mom_{fr}\right)_b = \frac{1}{2}f\rho_{cyl}R_b^2\omega_b^2[\pi R_b(2e+R_b)]R_b \tag{4.16}$$

Also rate of inflowing angular momentum is,

$$\left(Mom_{in}\right)_b = -\rho_{cyl}\frac{R^2}{2}\omega\frac{V_b}{V_{cyl}}\frac{dV_{cyl}}{d\theta}\frac{d\theta}{dt} \tag{4.17}$$

Equation (4.15), (4.16), and (4.17) can then be substituted into equation (4.1) to give,

$$\frac{d\omega_b}{dt} = \frac{\omega_b-\omega\left(\frac{R}{R_b}\right)^2}{V_{cyl}}\frac{dV_{cyl}}{dt} - f\omega_b^2\left(2+\frac{R_b}{e}\right) \tag{4.18}$$

Carrying the time increment, dt, and the angular velocity, ω, for main cylinder from equation (4.14) onto the right hand side and choosing an initial value for ω_b yields an differential equation solvable for ω_b. Clearly equations 4.14 for ω and 4.18 for ω_b are the key equations during the compression stroke.

4.3.1.2 Expansion stroke (from TDC to EVO)

Calculation of the angular velocities for main cylinder and bowl from equation (4.14) and (4.18) is suitable from IVC until TDC, after top dead centre due to mass transfer to main cylinder from bowl, the following relation can be written.

Conservation of angular momentum for bowl,

$$\frac{d(I_b\omega_b)}{dt} = (Mom_{in})_b - (Mom_{out})_b - (Mom_{fr})_b \tag{4.19}$$

where, $(Mom_{in})_b = 0$ and moment of rate of outflowing momentum can be obtain from:

$$(Mom_{out})_b = \int_0^{R_b} \rho_{cyl}(2\pi r v_d)(r\omega_b)rdr$$

or, $$(Mom_{out})_b = \frac{\pi R_b^4}{2}\omega_b v_d \rho_{cyl}$$

where, $$\frac{dm_{out}}{dt} = \pi R_b^2 v_d \rho_{cyl}$$

and v_d is upward transfer velocity.

$\therefore$ $$(Mom_{out})_b = \frac{R_b^2}{2}\omega_b \frac{dm_{out}}{dt}$$

or, $$(Mom_{out})_b = -\frac{R_b^2}{2}\omega_b \rho_{cyl}\frac{V_b}{V_{cyl}}\frac{dV_{cyl}}{dt} \tag{4.20}$$

The friction term for bowl can be obtained by equation (4.16). Equations (4.15), (4.16), (4.20) can then be substituted into equation (4.19) to give,

$$\frac{d\omega_b}{dt} = -f\omega_b^2\left(2+\frac{R_b}{e}\right) \tag{4.21}$$

Carrying the time increment, dt, onto the right hand side of equation (4.21) yields a differential equation solvable for angular velocity in bowl, ω_b, from TDC to EVO.

For main cylinder conservation of angular momentum given by,

$$\frac{d(I_m\omega)}{dt} = Mom_{in} - Mom_{out} - Mom_{fr} \tag{4.22}$$

where, $Mom_{out} = 0$ and moment of rate of inflowing momentum can be obtain from:

$$Mom_{in} = -\frac{R_b^2}{2}\omega_b \rho_{cyl}\frac{V_b}{V_{cyl}}\frac{dV_{cyl}}{dt} \tag{4.23}$$

Also, an equation has to be formulated for the transfer of momentum to the main cylinder represented now by the positive term $\rho_{cyl}\frac{R_b^2}{2}\omega_b\frac{V_b}{V_{cyl}}\frac{dV_{cyl}}{dt}$ in equation (4.20).

This momentum is absorbed $\begin{cases} a) \text{ by acceleration} \\ b) \text{ by friction} \end{cases}$

The acceleration term becomes:

$$\frac{d(I_m\omega)}{dt} = I_m\frac{d\omega}{dt} + \omega\frac{dI_m}{dt}$$

where, $I_m = m_m\frac{R^2}{2}$ and, $m_m = \rho_{cyl}(V_{cyl} - V_b)$

$$\therefore \quad \frac{d(I_m\omega)}{dt} = \rho_{cyl}(V_{cyl} - V_b)\frac{R^2}{2}\frac{d\omega}{dt} + \frac{R^2}{2}\omega\frac{dm_m}{dt}$$

where, $\frac{dm_m}{dt} = \rho_{cyl}\frac{V_b}{V_{cyl}}\frac{dV_{cyl}}{dt}$

$$\therefore \quad \frac{d(I_m\omega)}{dt} = \rho_{cyl}(V_{cyl} - V_b)\frac{R^2}{2}\frac{d\omega}{dt} + \frac{R^2}{2}\rho_{cyl}\frac{V_b}{V_{cyl}}\omega\frac{dV_{cyl}}{dt} \qquad (4.24)$$

The friction term for main cylinder can be obtained by equation (4.13). Equation (4.13), (4.23), and (1.127) can then be substituted into equation (4.22) to give,

$$\frac{d\omega}{dt} = \left[\left(\frac{R_b}{R}\right)^2\omega_b - \omega\right]\frac{V_b}{V_{cyl}(V_{cyl} - V_b)}\frac{dV_{cyl}}{dt} - f\omega^2\left(2 + \frac{\pi R^3}{V_{cyl} - V_b}\right) \qquad (4.25)$$

Carrying the time increment, dt, and the angular velocity, ω_b, for bowl from equation (4.21) onto the right hand side yields a differential equation solvable for ω, from TDC to EVO.

Clearly equations 4.21 for ω_b and 4.25 for ω are the key equations during the expansion stroke.

A listing of the relevant computer program and an example of step by step output (each degree of crank-angle) for evaluation of angular velocity in main cylinder, ω, and bowl, ω_b, from IVC to TDC and then from TDC to EVO is given in the appendix, and figure 4.7, respectively.

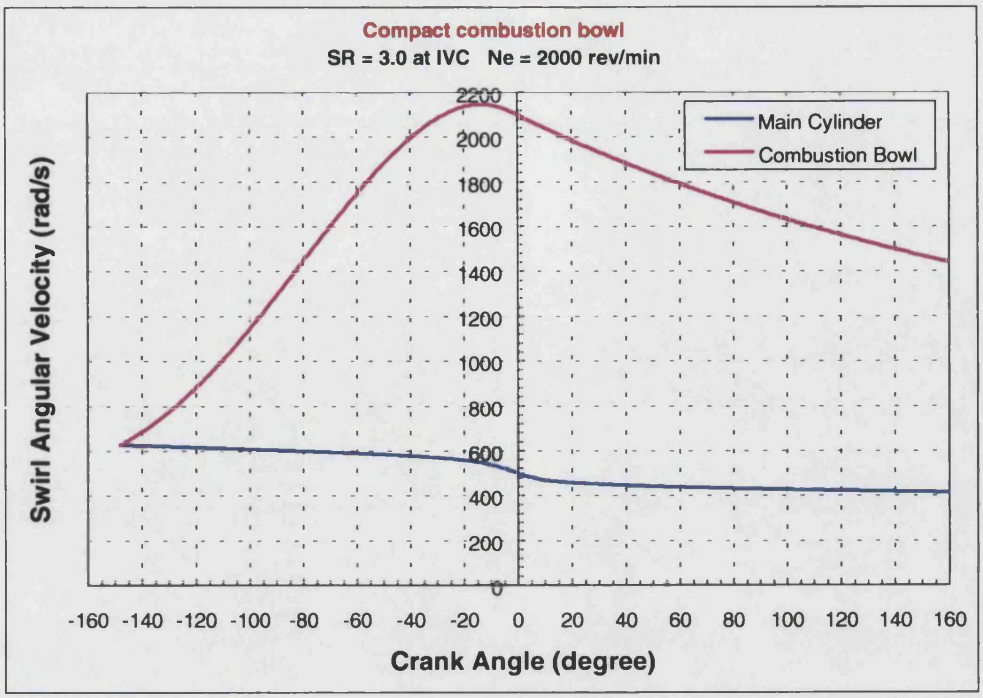

Figure 4.7: Typical swirl velocity in the main cylinder and the combustion bowl

4.3.2 Large diameter Mexican Hat bowl-in-piston chamber (fig. 4.6c)

4.3.2.1 Compression stroke (from IVC to TDC)

Calculation of angular velocity in the main cylinder, ω, during the compression stroke (from IVC to TDC) follows exactly the same pattern as that described in section 4.3.1.1 (equation 4.14), as equation (4.26).

$$\frac{d\omega}{dt} = -f\omega^2\left(2 + \frac{\pi R^3}{V_{cyl} - V_b}\right) \tag{4.26}$$

However, the expression for combustion bowl volume has to be changed to reflect the new geometry as equation (4.27).

$$V_b = \frac{\pi}{3} R_b^2 (2e_1 + e_2) \tag{4.27}$$

Denoting angular velocity in bowl by ω_b and moment of inertia of bowl by,

$$I_b = m_b \frac{R_b^2}{2}\left(\frac{3}{5} \cdot \frac{4e_1 + e_2}{2e_1 + e_2}\right) \tag{4.28}$$

where, $m_b = \rho_{cyl}\pi R_b^2\left(\frac{2e_1+e_2}{3}\right)$

The acceleration term becomes:

$$\frac{d(I_b\omega_b)}{dt} = I_b\frac{d\omega_b}{dt} + \frac{R_b^2}{2}\omega_b\left(\frac{3}{5}\cdot\frac{4e_1+e_2}{2e_1+e_2}\right)\frac{dm_b}{dt} \tag{4.29}$$

By simple analogy with the model in the main cylinder for calculation of friction term for the bowl, but in here the linear area is equal,

$$A = 2\pi R_b e_1 + \pi R_b^2\frac{\sqrt{R_b^2+(e_1-e_2)^2}}{R_b} \tag{4.30}$$

$$\therefore \quad \left(Mom_{fr}\right)_b = \frac{1}{2}f\rho_{cyl}R_b^2\omega_b^2\left[\pi R_b\left(2e_1+\sqrt{R_b^2+(e_1-e_2)^2}\right)\right]R_b \tag{4.31}$$

Also rate of inflowing angular momentum is,

$$\left(Mom_{in}\right)_b = -\rho_{cyl}\frac{R^2}{2}\omega\frac{V_b}{V_{cyl}}\frac{dV_{cyl}}{d\theta}\frac{d\theta}{dt} \tag{4.32}$$

Equation (4.29), (4.31), and (4.32) can then be substituted into equation (4.1) to give,

$$\frac{d\omega_b}{dt} = \frac{1}{V_{cyl}}\cdot\left[\omega_b - \omega\cdot\frac{\left(\frac{R}{R_b}\right)^2}{\frac{3}{5}\cdot\frac{4e_1+e_2}{2e_1+e_2}}\right]\cdot\frac{dV_{cyl}}{dt} - f\omega_b^2\cdot\frac{2e_1+\sqrt{R_b^2+(e_1-e_2)^2}}{\frac{4e_1+e_2}{5}} \tag{4.33}$$

Carrying the time increment, dt, and the angular velocity ω, for main cylinder from equation (4.26) onto the right hand side and choosing an initial value for ω_b yields a differential equation solvable for ω_b. Equation (4.33) reduces to the corresponding form for the compact chamber (equation 4.18) when putting $e_1 = e_2 = e$. Clearly equations 4.26 for ω and 4.33 for ω_b are the key equations for the compression stroke.

4.3.2.2 Expansion stroke (from TDC to EVO)

As has already been stated after top dead centre due to mass transfer to main cylinder from bowl, the following relation can be written.

Again conservation of angular momentum for bowl,

$$\frac{d(I_b\omega_b)}{dt} = \left(Mom_{in}\right)_b - \left(Mom_{out}\right)_b - \left(Mom_{fr}\right)_b \tag{4.34}$$

where, $(Mom_{in})_b = 0$ and moment of rate of outflowing momentum can be obtain from:

$$(Mom_{out})_b = -\frac{R_b^2}{2}\omega_b \cdot \left(\frac{3}{5}\cdot\frac{4e_1+e_2}{2e_1+e_2}\right)\rho_{cyl}\frac{V_b}{V_{cyl}}\frac{dV_{cyl}}{dt} \tag{4.35}$$

The friction term for bowl can be obtained by equation (4.31). Equations (4.29), (4.31), (4.34) can then be substituted into equation (4.35) to give,

$$\frac{d\omega_b}{dt} = -f\omega_b^2 \cdot \frac{2e_1+\sqrt{R_b^2+(e_1-e_2)^2}}{\frac{4e_1+e_2}{5}} \tag{4.36}$$

Carrying the time increment, dt, onto the right hand side of equation (4.36) yields a differential equation solvable for angular velocity in bowl, ω_b, from TDC to EVO.

For main cylinder conservation of angular momentum given by,

$$\frac{d(I_m\omega)}{dt} = Mom_{in} - Mom_{out} - Mom_{fr} \tag{4.37}$$

where, $Mom_{out} = 0$ and moment of rate of inflowing momentum can be obtain from:

$$Mom_{in} = -(Mom_{out})_b = \frac{R_b^2}{2}\omega_b \cdot \left(\frac{3}{5}\cdot\frac{4e_1+e_2}{2e_1+e_2}\right)\rho_{cyl}\frac{V_b}{V_{cyl}}\frac{dV_{cyl}}{dt} \tag{4.38}$$

Also, an equation has to be formulated for the transfer of momentum to the main cylinder represented now by the positive term $\frac{R_b^2}{2}\omega_b \cdot \left(\frac{3}{5}\cdot\frac{4e_1+e_2}{2e_1+e_2}\right)\rho_{cyl}\frac{V_b}{V_{cyl}}\frac{dV_{cyl}}{dt}$ in equation (4.35).

This momentum is absorbed $\begin{cases} a) \text{ by acceleration} \\ b) \text{ by friction} \end{cases}$

The acceleration term becomes:

$$\frac{d(I_m\omega)}{dt} = I_m\frac{d\omega}{dt} + \omega\frac{dI_m}{dt}$$

where, $I_m = m_m\frac{R^2}{2}$ and, $m_m = \rho_{cyl}(V_{cyl} - V_b)$

$$\therefore \quad \frac{d(I_m\omega)}{dt} = \rho_{cyl}(V_{cyl}-V_b)\frac{R^2}{2}\frac{d\omega}{dt} + \frac{R^2}{2}\omega\frac{dm_m}{dt}$$

where, $\frac{dm_m}{dt} = \rho_{cyl}\frac{V_b}{V_{cyl}}\frac{dV_{cyl}}{dt}$

$$\therefore \quad \frac{d(I_m\omega)}{dt} = \rho_{cyl}(V_{cyl} - V_b)\frac{R^2}{2}\frac{d\omega}{dt} + \frac{R^2}{2}\rho_{cyl}\frac{V_b}{V_{cyl}}\omega\frac{dV_{cyl}}{dt} \qquad (4.39)$$

The friction term for main cylinder can be obtained by equation (4.13). Equations (4.13), (4.38), and (4.39) can then be substituted into equation (4.37) to give,

$$\frac{d\omega}{dt} = \left(\frac{3}{5}\cdot\frac{4e_1+e_2}{2e_1+e_2}\right)\left[\left(\frac{R_b}{R}\right)^2\omega_b - \omega\right]\frac{V_b}{V_{cyl}(V_{cyl}-V_b)}\frac{dV_{cyl}}{dt} - f\omega^2\left(2+\frac{\pi R^3}{V_{cyl}-V_b}\right) \qquad (4.40)$$

Carrying the time increment, dt, and the angular velocity, ω_b, for bowl from equation (4.21) onto the right hand side yields a differential equation solvable for ω, from TDC to EVO.

Clearly equations 4.36 for ω_b and 4.40 for ω are the key equations during the expansion stroke.

A listing of the relevant computer program and an example of step by step output (each degree of crank-angle) for evaluation of angular velocity in main cylinder, ω, and bowl, ω_b, from IVC to TDC and then from TDC to EVO is given in the appendix, and figure 4.8, respectively.

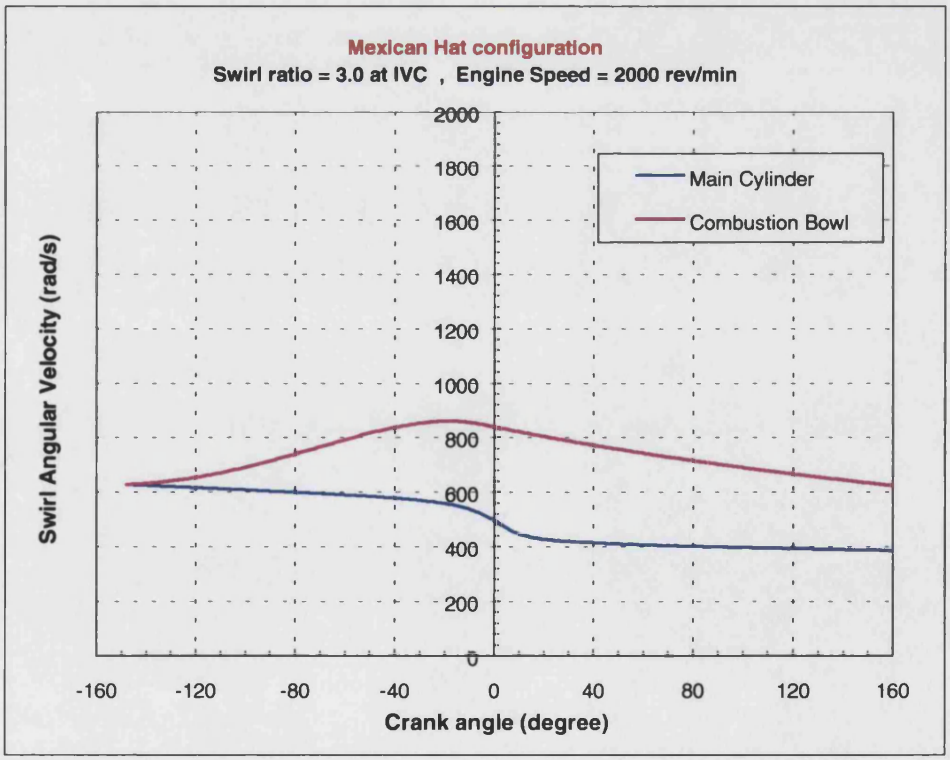

Figure 4.8: Typical swirl velocity in the main cylinder and combustion bowl

4.4 Discussion

The swirl calculations for the two alternatives combustion chambers configurations, the first a simplified form of the geometry associated with moderate injection pressures and the latter with high injection pressures as found in common rail or unit injectors, show marked differences.

The compact chamber leads to much higher absolute swirl angular velocities, and much more rapid attenuation in the bowl.

It is interesting to compare figure 4.7 for motoring swirl in the compact combustion bowl with figures 4.3 and 4.5, again for motoring swirl, but based on CFD results.

Although both operating conditions and bowl shape are somewhat different, with an initial swirl rate at IVC of 628 rad/sec in the present case as against 1100 rad/sec in the former (Puma engine), the maximum bowl swirl rate of 2148 rad/sec, indicating a ratio $\frac{\text{max. bowl swirl}}{\text{main cylinder swirl at IVC}}$ of 3.4 is of the same order as that for the CFD case of $\frac{4820}{1100} = 4.38$. For an even better comparison could use figure 9.16 showing:

CFD model	**The present model**
Puma engine:	1.8 l Ford engine:
Cylinder bore: 86 mm	Cylinder bore: 82.5 mm
Cylinder stroke: 86 mm	Cylinder stroke: 82 mm
Compression ratio: 21.7/1	Compression ratio: 18.2/1
Comb. bowl diameter : 40 mm	Comb. bowl diameter: 40 mm
Comb. bowl depth: 16.54 mm	Comb. bowl depth: 15.8 mm
$\frac{V_{bowl}}{V_{swept}} = 0.0415$	$\frac{V_{bowl}}{V_{swept}} = 0.0453$
Engine Speed: 4200 rev/min	Engine Speed: 4000 rev/min
ω_{IVC} = 1100 rad/sec	ω_{IVC} = 1257 rad/sec
Swirl ratio at IVC = 2.5	Swirl ratio at IVC = 3.0
$\frac{\omega_{max}}{\omega_{IVC}} = 4.38$	$\frac{\omega_{max}}{\omega_{IVC}} = 3.42$

A full discussion of the interaction between combustion bowl swirl and the high velocity fuel spray under firing conditions is given in chapter 8.

4.5 References

1. **Tindal, M.J., Williams, T.S., and Aldoory, M.**, " The Effect of Inlet Port Design on Cylinder Gas Motion in Direct Injection Diesel Engines", In flows in Internal Combustion Engines, pp. 101-111, ASME, New York (1982).

2. **Uzkan, T., Borgnakke, C., and Morel, T.**, "Characterization of Flow Produced by a High-Swirl Inlet Port", SAE 830266 (1983).

3. **Watts, R., and Scott, W.M.**, "Air Motion and Fuel Distribution Requirements in High-Speed DI engines", Proceeding of the Institution of mechanical Engineers, Vol. 184, Paper 17 (1969).

4. **Wigley, G. and Hawkins**, M.G., "Three Dimensional Velocity Measurements by Laser Anemometry in a Diesel Engine Cylinder Under Steady Inlet Flow Conditions", SAE 780060 (1978).

5. **Brandl, F., Reverencic, I., Cartellieri, W., and Dent, J.C.**, "Turbulent Air-Flow in the Combustion Bowl of a DI Diesel Engine and its Effect on Engine Performance", SAE 790040 (1979).

6. **Hatziapostolou, A.**, "Swirling Flows in Direct-Injection Diesel Engines", PhD Thesis, Imperial College of Science, Technology and Medicine, London (1991).

7. **Berals, J.M.**, " Swirl Generation in Motoring Condition using STAR-CD Package", University of Bath, Internal report (July 1999).

CHAPTER 5

Injection conditions and ignition delay

5.1 Introduction

This chapter summarises the results of a detailed analysis of injection conditions and ignition delay based on a series of experimental results obtained with a Ford 1.8 litre automotive direct injection Diesel engine, using a pre-production common rail injection system, operating on the limiting torque curve between 1250 and 4000 rev/min. Table 5.1 provides engine details while the leading operating conditions over the whole of the LTC are summarised in table 5.2.

Table 5.1: Ford HPCR 1.8 litre DI Diesel engine details

Bore	82.5 mm
Stroke	82.0 mm
Displacement	438 cc/cyl
Number of cylinders	4
Compression ratio	19.5
Injection nozzle spec.	5 x 0.15 mm
Rail pressure	540 to 1255 bar, dependent on speed
Engine speed	1250 to 4000 rev/min

Table 5.2: Summary of operating conditions

N_e rev/min	p_{rail} bar	*Power* kW	*Torque* N.m	*bsfc* g/kWh	*Fuel inj.* g/cyl/cycle	*Injection duration* °CA	Ignition delay °CA
1253	540	17.4	132.8	246	0.02830	11.0	1.0
1511	605	25.3	160.2	226	0.03130	14.0	1.6
1755	679	32.2	175.3	216	0.03280	16.0	1.8
2008	750	40.0	190.2	214	0.03520	18.0	2.0
2256	800	46.5	196.8	211	0.03600	20.0	2.4
2511	855	53.5	203.6	213	0.03743	22.0	2.9
3006	1000	62.7	199.2	223	0.03843	26.0	3.2
3543	1110	66.8	180.1	228	0.03552	29.0	3.7
4031	1255	72.2	171.0	248	0.03669	32.0	4.1

The above experimental results also form the basis of the heat release analysis in chapters 6 and 7.

5.2 Injection conditions

5.2.1 Literature survey

Over the last few years numerous studies have revealed that the fuel injection systems of direct injection Diesel engines play a dominant role on the spray development and pollutant formation mechanisms. The demand for well atomised fuel sprays has led to an increase of the injection pressure up to 1500 bar and beyond, to the design of electronic systems, which can accurately control the injection period and injection quantity and to the manufacturing of nozzles with an increased number of smaller holes, which can distribute the fuel more uniformly in the piston bowl.

Recently, common-rail injection systems have been developed [1,2], which allow fuel injection under high and relatively constant pressure independent of engine speed.

This section contains a brief survey of relevant papers dealing in detail with all the complications of flow through the injection nozzle. *Soteriou* et al. [3] describes an investigation of the spray characteristics of entry and exit throttled orifices, and how levels and degrees of opening affect them. For the majority of orifice openings, the issuing jet is significantly different from that produced by conventional sac type or VCO (Valve Covered Orifice) nozzles. They found there are three spray types, which occur in sequence with progressive opening: fan-shaped, horseshoe cross-section and quasi normal, and there is also a wide variation in spray angle and targeting with progressive opening.

A number of studies have provided evidence of the existence of cavitation and its dependence on injection pressure, which affect the velocity and flow field. Most of these studies have been performed on large-scale transparent models since real-size production nozzles have very small dimensions (hole diameters of 0.15-0.18 mm), while operating under very high injection pressure (≥1300 bar) over very short times.

The most recent work by *Arcoumanis* et.al. [4] on multi-hole large-scale transparent nozzles has revealed quite clearly the co-existence of two forms of cavitation initiated in the sac volume and nozzle hole, respectively, independent of nozzle geometry. In addition, velocity measurements using cavitation bubbles as traces have confirmed

that the liquid jet velocities at the nozzle exit are higher than those deduced from volumetric discharge measurements, which implies that the effective hole exit area is smaller than the geometric area due to the presence of cavitation bubbles and structures [5]. These complications will not be dealt with in this thesis in the interests of retaining a degree of simplicity.

5.2.2 Injection velocity, cone angle, penetration, and entrainment during delay period

As has already been stated the velocity profile in the injection nozzle is affected by the wall friction and cavitation. The needle lift, especially for low values, influences in particular the fuel flow velocity [6,7]. Under the assumption that the centre-line velocity is disturbed by neither cavitation nor friction, Bernoulli's law can be directly applied. If the effect of variable needle lift is considered, the injection velocity is given by *Levy* et.al. [8]:

$$v_N = C_n^* \sqrt{\frac{2(p_{inj} - p_{cyl})}{\rho_f}} \tag{5.1}$$

where p_{inj} and p_{cyl} are fuel injection and cylinder pressure respectively, ρ_f is the fuel density and C_n^* characterizes the needle obstruction (C_n^* = 1 when the needle is sufficiently lifted). This coefficient accounts for the liquid acceleration at the needle opening. It also includes the discharge due to boundary layers when geometrical cross section is strongly reduced. C_n^* is modelled by C_n, the effective needle discharge coefficient applied to entire hole area, which can be obtained from equation (5.2):

$$C_n^* = C_n = \min\left(\frac{h}{h_c}, 1\right) \tag{5.2}$$

where h is the needle lift and h_c is the critical lift. In the present simplified treatment C_n = 1 throughout.

The fuel injection rate is then given by:

$$\dot{m}_{inj} = C_d \cdot \rho_f \cdot A_N \cdot v_N \tag{5.3}$$

where A_N is the nozzle hole area and C_d is the discharge coefficient.

Spray development and propagation under both non-evaporative and evaporative conditions has already been dealt with in chapter 3, section 3.2.1. For the purpose of

the present chapter on combusting sprays, it is essential to differentiate between the initial development and propagation of the spray up to initiation of combustion, referred to by *Siebers and Higgins* [9] as "lift-off length", i.e. the ignition delay phase and the subsequent development under combusting conditions.

For the phase of the process up to lift-off, the treatment of *Naber and Siebers* [10], referred to in section 3.2.1 together with that developed in section 3.3.1.3 for the impulsive non-isodense spray, has been selected as the most appropriate.

The relevant equations, repeated here for convenience are:

Spray angle: The spray cone half angle is given by the equation (5.4), *Siebers* [11]:

$$\tan(\theta_{ig}) = C \cdot \left[\left(\frac{\rho_{air}}{\rho_f} \right)^{0.19} - 0.0043 \cdot \sqrt{\frac{\rho_f}{\rho_{air}}} \right] \tag{5.4}$$

where the constant C in equation (5.4) is 0.260 for the 246 μm orifice and 0.255 for the 100 μm orifice. The first density ratio term in the equation with an exponent of 0.19 is for non-vaporising sprays over a large density ratio range, and the second density ratio with an exponent of 0.5 was included to account for the observed vaporisation effects on the spray cone angle *Siebers* [11]. The following equations have already been given in section 3.3.1.3.

Spray velocity at distance x:

$$v = \sqrt{\frac{\rho_f}{\rho_{sp}}} \frac{v_N x_N}{\left(1 + \frac{\rho_{air}}{\rho_{sp}} \frac{C_f}{2} \right)^{1/2} x} \tag{5.5}$$

Penetration, x, may be derived from equation (5.5) with $v = \frac{dx}{dt}$:

$$x = \left\{ 2 \sqrt{\frac{\rho_f}{\rho_{sp}}} \frac{v_N x_N}{\left(1 + \frac{\rho_{air}}{\rho_{sp}} \frac{C_f}{2} \right)^{1/2}} t + x_N^2 \right\}^{\frac{1}{2}} \tag{5.6}$$

Finally, mass entrainment may be calculated by integration of the mass flux at distance x and deducting the original nozzle mass flux, as below:

$$\dot{m}_e = \rho_f \pi v_N x_N \left(\sqrt{\frac{\rho_{sp}}{\rho_f}} \frac{1}{\left(1 + \frac{\rho_{air}}{\rho_{sp}} \frac{C_f}{2} \right)^{1/2}} x - x_N \right) \tan^2 \theta_{ig} \tag{5.7}$$

5.3 Ignition delay

5.3.1 Literature survey

Ignition delay in direct injection Diesel engines is of great interest to researchers and engineers because of its direct impact on the intensity of heat release immediately following auto ignition, as well as its indirect effect on engine noise and pollutant formation. The delay period is composed of a physical delay, encompassing atomisation, vaporisation, and mixing, coupled with a chemical delay, a result of pre-combustion reaction in the fuel/air mixing.

The first paper on ignition delay of diesel fuel sprays is probably the pioneering work by *Wolfer* [12], which appeared in 1938. Since then a number of studies on this subject have appeared. These studies were conducted using single-cylinder test engines (*Yu* et. al. [13], *Henein* and *Bolt* [14], *Stinger* et. al. [15], *Ikegami* et. al. [16], and *Pischinger* et. al. [17]), constant volume combustion apparatus (*Wolfer* [12], *Kadota* et. al. [18], *Hiroyasu* et. al. [19], *Kwon* et. al. [20], *Soon* et. al. [21], *Edwards* and *Siebers* [22], *Aradi* and *Rayan* III [23], and *Siebers* and *Higgins* [9]) rapid compression machines (RCMs) and engines (*Miwa* et. al. [24], *Watson* et. al. [25], *Kobari* et. al. [26], and *Assanis* et. al. [27]).

5.3.2 Empirical ignition delay formulation

As has already been stated numerous empirical steady-state ignition delay correlations have been proposed based on experimental data in constant volume bombs, steady flow reactors, rapid compression machines and engines. Many of those correlations use an Arrhenius expression similar to that proposed by *Wolfer* [12], i.e.:

$$\tau_{id} = A \cdot p^{-n} \cdot \exp\left(\frac{E_a}{R_u \cdot T}\right) \tag{5.8}$$

where p and T are pressure and temperature, respectively, E_a is activation energy, R_u is gas constant, and A, n are adjustable constants.

Watson, et al [25] developed an Arrhenius expression (equation 5.9), using Diesel engine data under steady-state operating conditions.

$$\tau_{id} = 3.454 \cdot \bar{p}^{-1.0218} \cdot \exp\left(\frac{2100}{\bar{T}}\right) \quad \text{(ms)} \qquad (5.9)$$

where $\bar{p}$ and $\bar{T}$ are mean pressure and temperature during ignition delay period in units of bar and Kelvin, respectively.

These correlations for the ignition delay often have limited predictive ability, especially under transient conditions.

Recently *Assanis, et al.* [27] developed an ignition delay correlation that is predictive under both steady state and transient engine operating conditions. They established an Arrhenius expression (equation 5.10), which depends on pressure, temperature and equivalence ratio, based on experimental data was taken on a heavy-duty Diesel engine across the engine speed/load spectrum, under steady state and transient operation.

$$\tau_{id} = 2.4 \cdot \phi^{-0.2} \cdot \bar{p}^{-1.02} \cdot \exp\left(\frac{2100}{\bar{T}}\right) \quad \text{(ms)} \qquad (5.10)$$

Both *Watson* [25] and *Assanis* [27] claimed satisfactory correlation for ignition delay trends and magnitudes, under a wide range of steady-state conditions in modern turbocharged direct injection Diesel engine. Table 5.3 shows the ignition delay predictions from each expression, which is based on the high-speed direct injection Diesel engine with a high-pressure common rail fuel injection system, defined in table 5.1 and the test conditions of table 5.2.

Table 5.3: Comparison of ignition delay

N_e rev/min	p_{ig} kPa	T_{ig} K	ϕ -	τ_{ig}-Assanis ms	D_{ig}-Assanis °CA	τ_{ig}-Watson ms	D_{ig}-Watson °CA
1250	5655	909	0.756	0.4172	3.1293	0.5641	4.2311
1500	7035	917	0.689	0.3333	2.9999	0.4423	3.9809
1750	8100	924	0.633	0.2886	3.0299	0.3764	3.9521
2000	10063	933	0.556	0.2322	2.7868	0.2950	3.5400
2250	1020	937	0.567	0.2278	3.0757	0.2905	3.9217
2500	9956	942	0.597	0.2265	3.3981	0.2919	4.3784
3000	9447	958	0.647	0.2266	4.0781	0.2967	5.3408
3500	9176	967	0.606	0.2317	4.8657	0.2995	6.2893
4000	8940	981	0.652	0.2273	5.4558	0.2982	7.1564

where in Table 5.3, p_{ig}, T_{ig}, N_e, and ϕ are cylinder mean pressure and temperature during the ignition delay, engine speed, and overall equivalence ratio respectively. Also D_{ig} (crank angle of ignition delay) can be obtained from: $D_{ig} = \tau_{ig} \cdot 6N_e$

5.3.3 Ignition delay based on concept of lift off length

More recently *Siebers and Higgins* [9] have developed a more fundamental approach to the determination of the delay period, using the concept of lift off length. Using a high-pressure combustion bomb with optical access they determined the effects of injection pressure and orifice diameter on the lift off length.

The lift-off lengths in figure 5.1 are plotted versus injection velocity for two different orifice diameters, over a range of orifice pressure drops.

The dependence of lift-off length on injection velocity and orifice diameter noted in figure 5.1 is represented by equation (5.11):

$$L_0 = \left(0.0198 - 5.36\times10^{-6} \cdot D_N\right) \cdot v_N + 0.038 \cdot D_N + 2.946 \qquad (5.11)$$

where D_N is orifice diameter in units of millimetre.

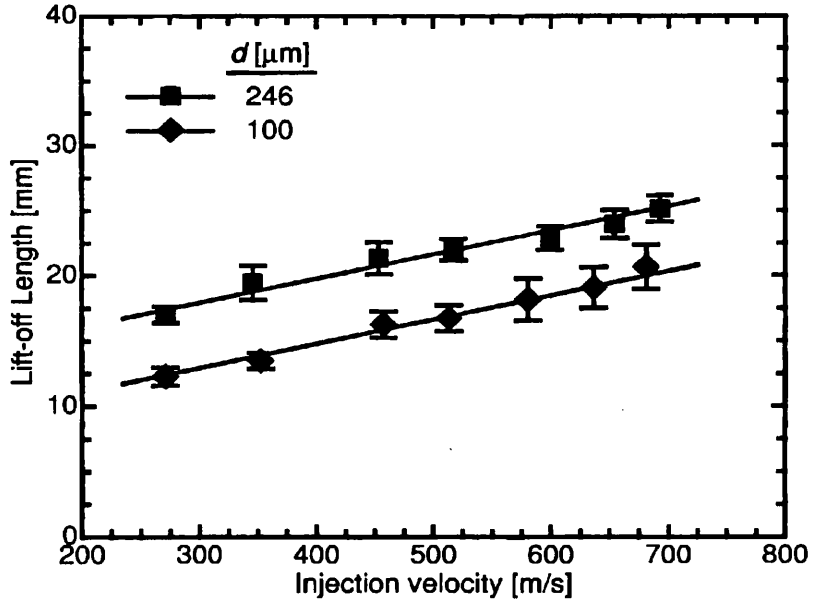

Figure 5.1: Lift-off length versus the injection velocity for the 100 µm and 246 µm diameter orifices. Each lift-off length is the average of lift-off lengths determined from between 5 and 20 images for each condition. The standard deviation in the lift-off length for each condition is given by the bars [9].

The quantity of air entrained prior to lift-off length can be estimated using the expression for the axial variation of cross-sectional average equivalence ratio in the spray, previously developed by *Naber* and *Siebers* [10]. Rearranged, that equivalence ratio relationship gives the air entrained up to the lift-off location as a percentage of the total air required to burn the fuel being injected. This percentage is defined as the percent of stoichiometric air (ζ_{st}), and given by equation (5.12):

$$\zeta_{st}(\%)=\frac{10}{3}\cdot\left[\sqrt{1+16\cdot\left(\frac{L_0}{x^+}\right)^2}-1\right] \tag{5.12}$$

where L_0 is lift-off length and x^+ is the characteristic length scale for spray *Naber and Siebers* [10] defined by:

$$x^+=\sqrt{\frac{\rho_f}{\rho_{air}}}\frac{\sqrt{C_a}\cdot D_N}{0.66\cdot\tan(\theta_{ig})} \tag{5.13}$$

where C_a is the area contraction coefficient; ρ_f and ρ_{air} are the injected fuel and ambient-gas densities, respectively; and θ_{ig} is the measured spray cone half-angle of the spray, which as a function of the ambient gas to injected fuel density ratio (ρ_{air}/ρ_f) can be obtained from equation (5.4).

Note that *Siebers* [9] does not give ignition delay directly, this has been obtained indirectly via equation (5.6) for the evaluation of penetration, i.e.:

$$\tau_{ig}=\left(L_0^2-x_N^2\right)\cdot\frac{\sqrt{1+\frac{\rho_{air}}{\rho_{sp}}\cdot\frac{C_f}{2}}}{2v_N x_N\sqrt{\frac{\rho_f}{\rho_{sp}}}} \tag{5.14}$$

where x_N as a nozzle parameter can be obtained from:

$$x_N=\frac{D_N}{2\tan(\theta_{ig})} \tag{5.15}$$

In equation (5.14) spray density, ρ_{sp} can be obtained from:

$$\rho_{sp}=\frac{m_f+m_a}{V_{sp}} \tag{5.16}$$

where the fuel mass injected up to lift-off length, m_f, is assumed equivalent to a cylinder of nozzle hole diameter D_N and lift-off length L_0:

$$m_f=\frac{\pi}{4}D_N^2\cdot L_0\cdot\rho_f \tag{5.17}$$

And mass of entrained air using the percent of stoichiometric air (ζ_{st}) can be obtained from:

$$m_a = m_f \cdot \zeta_{st}(\%) \times 14.5 \tag{5.18}$$

Spray volume can be calculated as equation (5.19):

$$V_{sp} = \frac{m_a}{\rho_{air}} + \frac{m_f}{\rho_f} \tag{5.19}$$

Values of ignition delay according to lift-off length calculation are summarized in Table (5.4) as below:

Table 5.4: Evaluation of ignition delay according to lift-off length [9]

N_e	p_{rail}	p_{cyl}	p_{ig}	T_{ig}	v_N	ρ_{air}	L_0	$tan(\theta_{ig})$	x^+
rev/min	bar	bar	kPa	K	m/s	kg/m^3	mm	-	-
1250	540	56.29	5655	909	341.404	21.676	15.13	0.1217	1.105e-02
1500	605	70.12	7035	917	359.008	26.731	15.47	0.1276	9.465e-03
1750	679	79.68	8100	924	380.019	30.544	15.86	0.1315	8.573e-03
2000	750	99.22	10063	933	395.998	37.581	16.17	0.1376	7.367e-03
2250	800	99.06	10120	937	410.976	37.632	16.45	0.1376	7.339e-03
2500	855	97.86	9956	942	427.134	36.826	16.76	0.1370	7.433e-03
3000	1000	91.49	9447	958	467.887	34.359	17.53	0.1349	7.768e-03
3500	1110	91.24	9176	967	495.464	33.063	18.06	0.1338	7.940e-03
4000	1255	86.44	8940	981	530.642	31.753	18.73	0.1326	8.127e-03

Table (5.4) continued,

N_e	ζ_{st}	m_f	m_a	V_{sp}	ρ_{sp}	x_N	τ_{ig}	D_{ig}
rev/min	%	kg	kg	m^3	kg/m^3	mm	ms	°CA
1250	15.23	2.22e-07	4.90e-07	2.29e-08	31.127	0.6161	0.1132	0.8488
1500	18.71	2.27e-07	6.15e-07	2.33e-08	36.356	0.5876	0.1276	1.1484
1750	21.57	2.33e-07	7.28e-07	2.41e-08	39.843	0.5705	0.1375	1.4442
2000	26.12	2.37e-07	8.98e-07	2.42e-08	46.942	0.5453	0.1562	1.8746
2250	26.74	2.41e-07	9.36e-07	2.52e-08	46.790	0.5451	0.1557	2.1022
2500	26.92	2.46e-07	9.59e-07	2.64e-08	45.742	0.5477	0.1530	2.2952
3000	26.95	2.57e-07	1.01e-06	2.96e-08	42.700	0.5560	0.1455	2.6193
3500	27.17	2.65e-07	1.04e-06	3.19e-08	41.039	0.5606	0.1417	2.9760
4000	27.57	2.75e-07	1.10e-06	3.49e-08	39.320	0.5656	0.1381	3.3141

Table 5.4 shows that ignition delays predicted by the lift-off length method are well below those based on the *Assanis* [27] and *Watson* [25] predictions in table 5.3.

Comparison of corresponding propagation time τ_{ig} (ignition delay period), from above method with results derived from conventional non-burning spray propagation of *Morgan* [28] are summarized in table5.5.

The *Morgan* [28] correlation for a non-burning spray of the form $x(t) = a \cdot t^b$ used previously by *Verhoeven* [29] was fitted to the experimental data, where $x(t)$ is the spray tip penetration at time t. Adjustable constants a and b were found as follows:

a = 37.00 to 40.80 depend on injection pressure and air pressure

b = 0.376 to 0.414 depend on injection pressure and air pressure

Table 5.5: Comparison of two alternative approaches of propagation time τ_{ig}

N_e	p_{rail}	p_{cyl}	a	b	*Tip penetration*	τ_{ig} *(siebers)*	τ_{ig} *(Morgan)*
rev/min	bar	bar	-	-	mm	ms	ms
1250	540	56.29	40.8	0.414	15.13	0.1132	0.0911
1500	605	70.12	39.0	0.410	15.47	0.1276	0.1048
1750	679	79.68	38.2	0.404	15.86	0.1375	0.1135
2000	750	99.22	37.0	0.387	16.17	0.1562	0.1178
2250	800	99.06	37.5	0.384	16.45	0.1557	0.1170
2500	855	97.86	38.2	0.383	16.76	0.1530	0.1164
3000	1000	91.49	38.9	0.386	17.53	0.1455	0.127
3500	1110	91.24	38.7	0.382	18.06	0.1417	0.136
4000	1255	86.44	38.6	0.376	18.73	0.1381	0.146

Table 5.5 shows that ignition delay calculated by *Siebers and Higgins* [9] and *Morgan* [28] approaches are broadly comparable.

5.4 Discussion of results

Figures 5.2, 5.3, and 5.4 gives rail pressure, p_{rail}, nozzle leaving velocity, v_N, and lift-off length, L_O, as a function of engine speed, N_e, for the experimental conditions summarised in table 5.2.

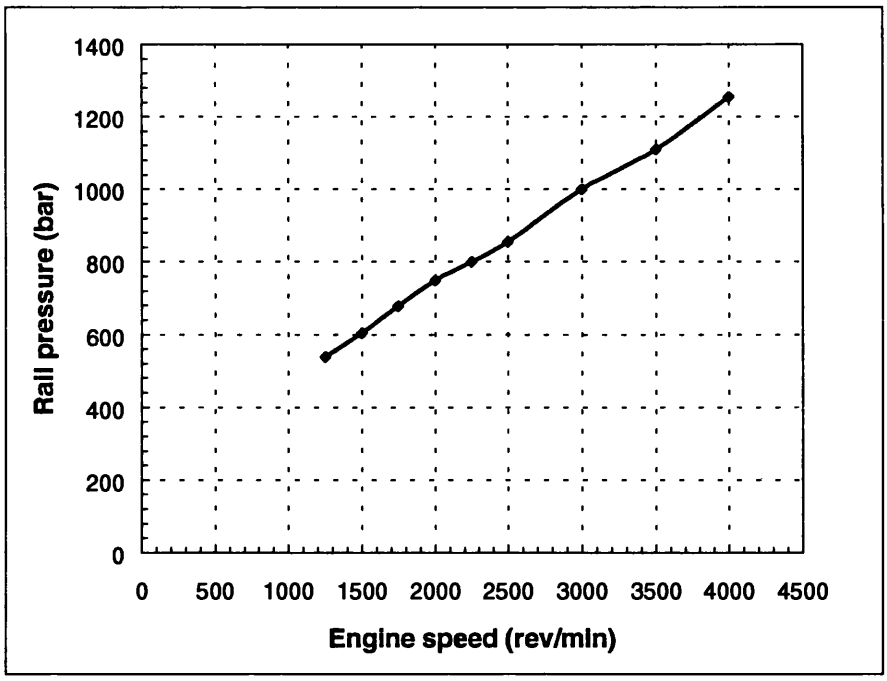

Figure 5.2: Rail pressure versus engine speed

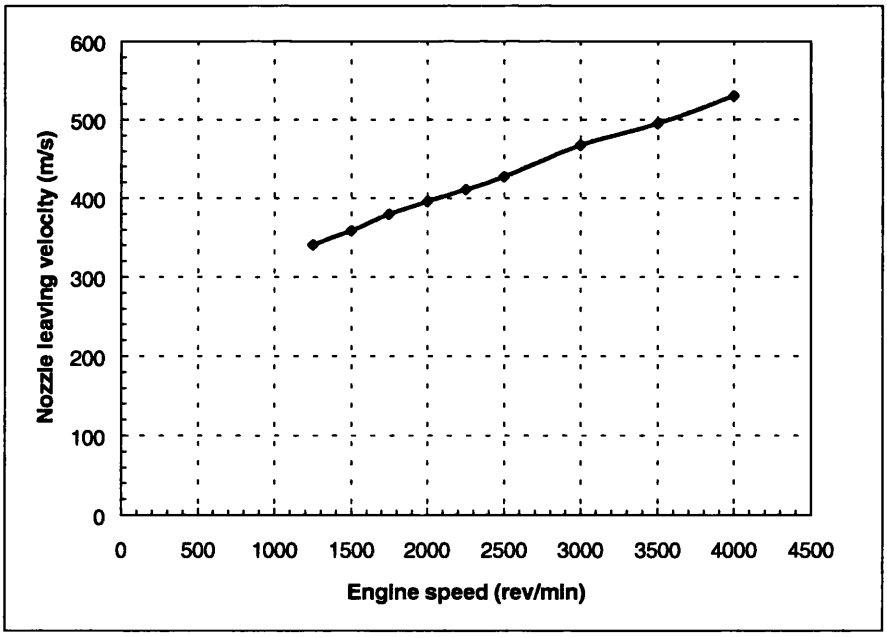

Figure 5.3: Nozzle leaving velocity versus engine speed

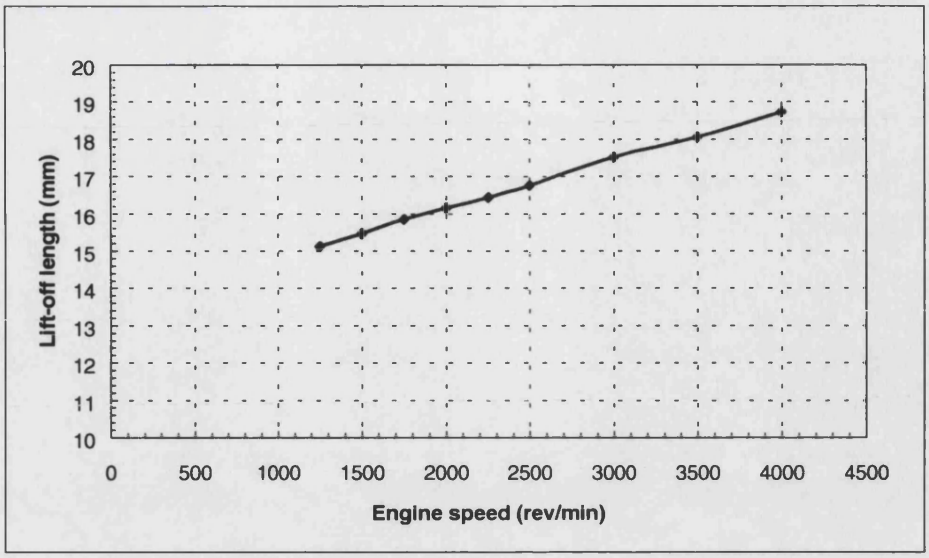

Figure 5.4: Lift-off length versus engine speed

Figure 5.5 compares ignition delay (in °CA) as obtained from the three alternatives approaches (*Watson* [25], *Assanis* [27], and *Siebers* [9]) with the experimental values derived from heat release records using the AVL Concerto software (which will be discussed in detail in chapter 6 and 7).

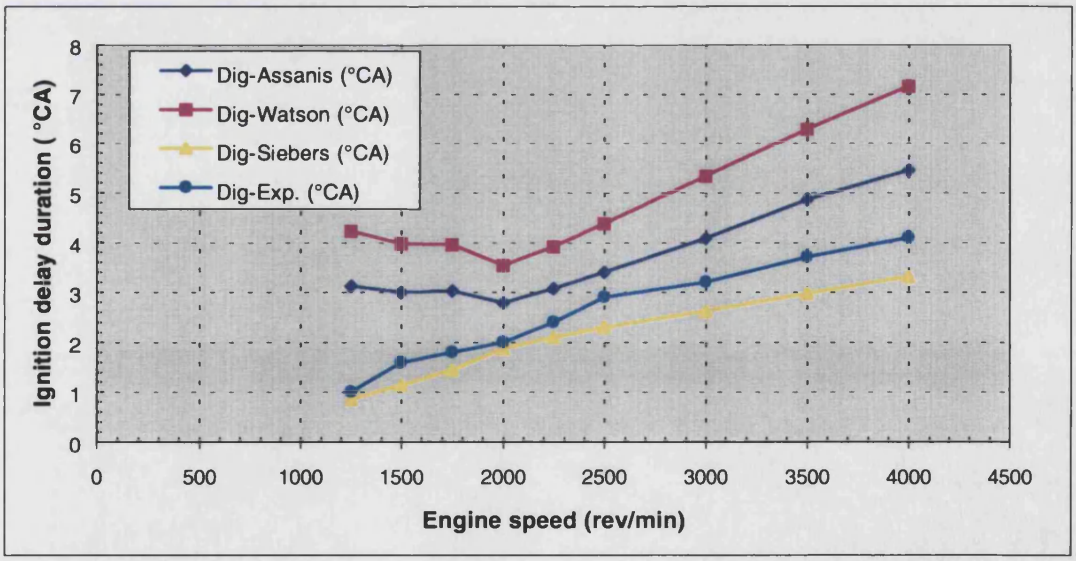

Figure 5.5: Ignition delay versus engine speed

It will be observed that *Watson* [25] and *Assanis* [27] considerably over predict ignition delay while *Siebers* [9] slightly under predicts. It must be remembered that both the *Watson* [25] and *Assanis* [27] correlations refer to pump-line-nozzle systems

with lower injection pressures and different injection characteristics from the nearly constant high-pressure injection conditions associated with the common rail system. Clearly the *Wolfer* [12] prediction would give even longer delay periods (equation 5.8).

5.5 References

1. **Boehner, W., and Hummel, K.**, "Common rail injection system for commercial Diesel vehicles", SAE 970345, (1997).

2. **Guerrasi, N., and Dupraz, P.**,"A common rail injection system for high speed direct injection Diesel engines", SAE 980803, (1998).

3. **Soteriou, C., Andrews, R., Smith, M., Torres, N., and Sankhalpara, S.**, "The flow patterns and sprays of variable orifice nozzle geometries for diesel injection", SAE 2000-01-0943, (2000).

4. **Arcoumanis, C., and Whitelaw, J.**, "Is cavitation important in diesel engine injectors", Proc. THIESEL 2000, pp.259-267, Valencia, September 13-15, (2000).

5. **Chaves, H., and Obermeier, F.**, "Correlation between light absorption signals of cavitating nozzle flow within and outside of the hole of a transparent diesel injection nozzle", Proc. 15th ILASS-Europe 99, pp.224-229, Toulouse, July 5-7, (1999).

6. **Dan, T., Yamamoto, T., Senda, J., and Fujimoto, H.**, "Effect of nozzle configurations for characteristics of non-reacting diesel fuel spray", SAE 970355, (1997).

7. **Kato, M., Kano, K., Date, K., Oya, T., and Niizuma, K.**, "Flow analysis in nozzle hole in consideration of cavitation", SAE 970052, (1997).

8.**Levy, N., Amara, S., and Champoussin, J.-C.**, "Simulation of diesel jet assumed fully atomised at the nozzle exit", SAE 981067, (1998).

9. **Siebers, D.L., and Higgins, B.S.**, "Effects of injector conditions on the flame lift-off length of direct injection diesel sprays", Proc. THIESEL 2000, pp.303-321, Valencia, September 13-15, (2000).

10. **Naber, J.D., and Siebers, D.L.**, "Effect of gas density and vaporization on penetration and dispersion of diesel sprays", SAE 960034, (1996).

11. **Siebers, D.L.**, "Scaling liquid-phase fuel injection system simulation model for diesel engines", SAE 99-01-0528, (1999).

12. **Wolfer, H. H.**, "Der Zundverzug im Dieselmotor" VDI. Forsh.-ht, 392, 15, (1938).

13. **Yu, T.C., Uyehara, O.A., Myers, P.S., Collins, R.N. and Mahadevan, K.**, "Physical and chemical ignition delay in an operating diesel engine using hot-motored technique", SAE Technical Trans., 64, 690, (1956).

14. **Henein, N.A. and Bolt, J.A.**, "Correlation of air charge temperature and ignition delay for several fuels in a diesel engine", SAE 690252 (1969).

15. **Stinger, F.W., Clarke, A.E., and Clarke, J.S.**, "The spontaneous ignition of hydrocarbon fuels in a flowing system", Proc. Instn Mech. Engrs, Vol. 184, pt. 3J. (1969).

16. **Ikegami, M., Shioji, M. and Kimoto, T.**, "Diesel combustion and the pollutant formation as viewed from turbulent mixing concept", SAE 880425 (1988).

17. **Pischinger, F., Reuter, U., and Scheid, E.**, "Self-ignition if diesel sprays and its dependence on fuel properties and injection parameters", ASME journal of Eng. For Gas Turbines and Power, Vol. 110, pp. 339-404, (1988).

18. **Kadota, T., Hiroyasu, H., and Oya, H.**, "Spontaneous ignition delay of fuel droplet in high pressure high temperature gaseous environments", Bulletin of the JSME, Vol. 26, No. 24, Paper 214-12, pp. 569-575, (1976).

19. **Hiroyasu, H., Kadota, T., and Arai, M.**, "Development and use of spray combustion model to predict diesel engine efficiency and pollutant emission", Bulletin of the JSME, Vol. 19, No. 130, Paper 536-46, pp. 437-445, (1983).

20. **Kwon, S-IK, Arai. M., and Hiroyasu, H.**, "Ignition delay of a diesel spray injected into a residual gas mixture", SAE 911841 (1991).

21. **Soon-Ik, K., Masataka, Hiroyasu, H.**, "Ignition delay of a diesel spray injected into residual gas mixture", SAE 911841 (1991).

22. **Edwards, C.F. and Siebers, L.D.**, "A study of the auto-ignition process of a diesel spray via high speed visualization", SAE 920108 (1992).

23. **Aradi, A. and Ryan III, T.**, "Cetane effect on diesel ignition delay times measured in a constant volume combustion apparatus", SAE 952352 (1995).

24. **Miwa, K., Ohmyia, T. and Nishiwaki, T.**, "A study of the ignition delay of diesel fuel spray using a rapid compression machine", Jap. Soc. Mech. Engrs Int. J., Ser. II, Vol. 31(1), Page 166 (1998)

25. **Watson, N., Pilley, A.D. and Marzouk, M.**, "A combustion correlation for diesel engine simulation", SAE 800029 (1980).

26. **Kobari, S. and Kamimoto, T. and Aradi, A.A.**,"A study of ignition delay of diesel fuel sprays", IMechE, Vol. 1, No. 1, JER00499 (2000).

27. **Assanis, D.N., Filipi, Z.S., Fiveland, S.B., and Syrimis, M.**, "A predictive ignition delay correlation under steady-state and transient operation of a direct injection diesel engine", Paper No. 99-ICE-231, ICE-Vol. 33-2, Fall technical conference, ASME, (1999).

28. **Morgan, R.E., Kennaird, D., Heikal, M.R., and Bar, F.**, "Characterisation of a high pressure Diesel fuel spray elevated pressures ", Proc. THIESEL 2000, pp.87-94, Valencia, September 13-15, (2000).

29. **Verhoeven, D., Vanhemelryck, J., and Baritaud, T.**, "Macroscopic and ignition characteristics of high pressure sprays of single-component fuels", SAE 981069 (1998).

CHAPTER 6

Phenomenological heat release model for HPCR engines

6.1 Introduction

The process of heat release in the Diesel engine largely determines its performance and emission characteristics. Due to the complexity of the process there has been a tendency to treat the various subsidiary process separately, in the following manner:

1) Injection of high-pressure liquid fuel through multiple hole nozzles, with or without cavitation [1, 2].
2) Subsequent air-fuel mixing and evaporation of small droplets, followed by propagation of the resultant out fuel/air spray in the combustion chamber under conditions of high turbulence and organised squish and swirl [3].
3) The formation of combustion nuclei within the multiple fuel/air sprays and the spreading of the incipient flame until eventually virtually all the injected fuel injected has given up its chemical energy to the cylinder charge as cumulative heat release [4].

As previously discussed in chapter 3, the literature on sprays is particularly extensive, while that on flame propagation and heat release is comparatively scant.

While the mathematical modelling of the injection process is now very well established [1], heat release has been the subject of empirical formulations based on experimental results from engines rather than closed analytical formulations.

A very widely used empirical formulation incorporated in many cycle simulation codes using shape functions was initially developed by *Wiebe* [5] and later enhanced to represent separately the premixed and diffusion phases by *Marzouk and Watson* [6].

One of the earliest quasi-analytical formulations is that of *Austen and Lyn* [7]. This gave a useful qualitative insight into the rate at which injected fuel is progressively burned both during the initial high intensity, chemically controlled premixed phase and subsequently during the slower mixing controlled diffusion phase [8,9,10,11].

Chmela and Orthaber [12] developed a much more fundamental analytical approach for pure diffusion burning, i.e. mixing controlled burning, as found in high pressure common rail (HPCR) engines at high loads, in which the key constituent elements viz. fuel preparation rate for burning as a function of injection rate and the influence of spray turbulence kinetic energy on the rate of burning are represented by two basic differential equations, leading to a fuel preparation function F_1 and a turbulent kinetic energy dissipation function F_2.

In contradistinction to the closed analytical solutions presented in the present thesis, *Chmela and Orthaber* [12] do not give details of the method of solution of these differential equations, although presumably numerical methods were employed. Nevertheless, their preliminary results were encouraging and allowed the effects of primary parameters such as injection pressure and duration, hole size and number, injected fuel quantity etc., to be assessed.

In the present thesis wholly analytical solutions for the functions F_1 and F_2 are developed. The resultant expressions for heat release represent the effects of:

a) Injection rate as a function of nozzle hole dimensions and the effective applied pressure difference, including the effect of finite rate of needle lift and closure
b) Ignition delay, based on the work of *Siebers* [4]
c) Injection duration and rate
d) Level of turbulent kinetic energy

The calculation schemes have been developed for three cases of increasing complexity:

1) Constant injection rate with negligible ignition delay
2) Constant injection rate with finite ignition delay
3) Effect of a finite period of needle lift assumed to coincide with the ignition delay period, with subsequent constant injection rate.

The associated separate subroutines have been incorporated, as optional alternatives, in the existing ODES cycle simulation code, to replace the original *Marzouk and Watson* [6] shape function routine.

These routines operate in parallel with the NO_x emission subroutine described in appendix A, the new spray models of section 3.3.1.3 and 8.4, and the swirl generation subroutines of section 4.3 and 8.5.

6.2 The model for diffusion burning by *Chmela and Orthaber* [12]

The diffusion-burning model of *Chmela and Orthaber* [12] is a zero-dimensional combustion model that relies on the concept of mixing controlled combustion (MCC Heat Release Rate) avoiding the detailed description of the individual mixture formation and fuel oxidation processes.

For diffusion combustion in today's direct injection Diesel engines it can be shown that the rate of heat release (ROHR) is controlled mainly by two items, i.e. the instantaneous fuel mass present in the cylinder charge and the local density of turbulent kinetic energy.

6.2.1 The fuel preparation function F_1

The starting point of their considerations was the assumption that the heat release rate should, in the first instance, be proportional to the fuel quantity available for combustion. The fuel quantity available can be computed as the difference between the fuel quantity m_f injected up to this moment and the fuel quantity burned at the same time. The latter can be determined from the cumulative heat release Q and the lower calorific value LCV. In equation (6.1), this relation is formulated as function $F_1(m_f,Q)$:

$$F_1(m_f,Q) = m_f - \frac{Q}{LCV} \tag{6.1}$$

Using this definition, the first hypothesis for ROHR is given in equation (6.2):

$$\frac{dQ}{d\theta} = C_{\mathrm{mod}} F_1(m_f,Q) \tag{6.2}$$

For verifying this hypothesis by means of data belonging to the actual heat release rate, the injection rate history will have to be determined first. In order to make sure the data have the required consistency, the actual injection pressure and needle lift histories have to be used instead of an injection rate history measured on an injection pump test bench separately from the engine.

6.2.2 The turbulent kinetic energy dissipation function F_2

As has already been stated the local density of the kinetic energy determines the heat release rate. In a Diesel engine the rate of the fuel oxidation is determined by the rate of mixing of fuel vapour and fresh gas and thus by the local density of the turbulent kinetic energy, *Ryan et al* [13].

The essential sources of the charge turbulence in gas engines are the kinetic energies of the intake flow and possibly the squish flow out of the space between the piston and the cylinder head into the combustion bowl. Here, however, an additional major source is the kinetic energy of the injection sprays. In the following, the contributions of these three energy sources to the total kinetic energy production are estimated.

In equation (6.3), the kinetic energy of the swirling flow, KE_S, is calculated assuming a block swirl flow (bore diameter B) with a swirl number, SR, that will be displaced into the combustion bowl (diameter d) at TDC by maintaining the angular momentum without loss:

$$KE_S = \frac{(B \cdot N_e \cdot SR \cdot \pi)^2}{14400} \cdot \left(\frac{B}{d}\right)^2 \tag{6.3}$$

For computing the kinetic energy of the squish flow, the mass flow m_{Squ} out of the squish volume V_{Squ} through a cylindrical control area A_{Squ} between bowl edge and cylinder head will be determined first by equation (6.4):

$$\frac{dm_{Squ}}{d\theta} = \rho_c \cdot \frac{dV_{Squ}}{d\theta} \tag{6.4}$$

The continuity relation in equation (6.5) will then deliver the velocity of squish flow w_{Squ}:

$$u_{Squ} = \frac{6 \cdot N_e}{A_{Squ}} \cdot \frac{dV_{Squ}}{d\theta} \tag{6.5}$$

This allows computing the kinetic energy of the squish flow, KE_{Squ}, by means of equation (6.6):

$$\frac{dKE_{Squ}}{d\theta} = \frac{(u_{Squ})^2}{2} \cdot \frac{dm_{Squ}}{d\theta} \tag{6.6}$$

The amount of the kinetic energy imparted to the cylinder charge by means of the injection jets can eventually be determined from the injection rate V_f' according to equation (6.7):

$$\frac{dKE_f}{d\theta} = 18 \cdot \rho_f \cdot \left(\frac{N_e}{\mu A}\right)^2 \cdot \left(V_f'\right)^3 \tag{6.7}$$

where, V_f' : volumetric injection rate (m^3/° CA)

ρ_f: fuel density (kg/m^3)

μ : flow coefficient

A : spray hole diameter (m^2)

The contributions of the three energy sources to the total kinetic energy fed into cylinder charge are summarized in table 6.1, for the engine details given in the table 6.2.

Table 6.1: Contributions of Total Kinetic Energy in Cylinder [12]

Engine speed	rev/min	1000	1800
Injection quantity	mm^3/stroke	255	253
Squish flow kinetic energy	J	0.15	0.40
Intake swirl kinetic energy	J	0.20	0.55
Fuel sprays kinetic energy	J	25.3	26.5

Hence, the squish and swirl flows do not play any essential role as regards kinetic energy. As the major part of kinetic energy comes from the fuel jets, they are the only important source of turbulence.

Table 6.2: Technical Data of Single Cylinder Test Engine [12]

Bore	124 mm
Stroke	165 mm
Displacement	2.0 dm^3
Compression Ratio	18:1
Swirl Level	1.8

For computing the instantaneous level of kinetic energy in the cylinder charge, the dissipation has to be taken into account as well. In equation (6.8), a dissipation constant C_{diss} is used for this:

$$\frac{dKE_{diss}}{d\theta} = \frac{dKE_f}{d\theta} - \frac{C_{diss}}{6 \cdot N_e} \cdot KE_{diss} \tag{6.8}$$

Chmela and Orthaber [12] assumed that the kinetic energy of the injection jets fed into the cylinder will first directly be connected with the fuel mass and will then be transferred to the combustion gas during oxidation of the fuel. In this case, the kinetic energy, *KE*, currently available for mixture formation can be described by equation (6.9):

$$KE = KE_{diss} \cdot \frac{F_1(m_f, Q)}{m_f} \tag{6.9}$$

According to this equation, only the share of the dissipation total kinetic energy $KE_{f,diss}$ introduced together with the fuel quantity m_f that is proportional to the currently available fuel quantity $F_1(m_f,Q)$ can be utilised for the mixing process. Then the local turbulent kinetic energy density k, which is given by *KE* divided by just that instantaneous fuel quantity and the amount of fresh gas necessary for approximately stoichiometric diffusion combustion, can be described by means of equation (6.10). In this equation C_{turb} is a measure of the efficiency of the transformation from kinetic energy into turbulent kinetic energy:

$$k = C_{turb} \cdot \frac{KE_{diss}}{m_f \cdot (1 + \lambda_{Diff} \cdot m_{stoich})} \tag{6.10}$$

In order to incorporate the turbulent kinetic energy density into the relation for the heat release rate, it is useful to refer to the study by *Magnussen and Hjertager* [14], in which the oxidation rate for diffusion flames of C_2H_2 in oxygen by means of the k-ε model for turbulence is described using equation (6.11):

$$R_f = A_M \cdot c_f \cdot (\varepsilon / k) \tag{6.11}$$

According to this equation, the reaction rate, R_f, in the considered volume is proportional to the fuel concentration, c_f, and the quotient of the dissipation rate ε and turbulent kinetic energy density, which can, due to its dimension [s^{-1}], be interpreted as mixing rate.

The problem with using equation (6.11) in a zero-dimensional environment is that the dissipation rate, in contrast to the turbulent kinetic energy density, cannot be estimated in a comparably simple way so that the rate term (ε/k) cannot be used like this. Therefore, the attempt was made to describe the effect of the charge turbulence on the fuel oxidation rate by assuming that not only the term (ε/k) could be understood as directly proportional to the reaction rate but also the turbulence level k itself or, more precisely, its square root.

As the collision frequency of molecules at a defined transport velocity will, of course, also depend on the density of the medium, it seems quit obvious to refer this transport velocity to a length derived from the variable cylinder volume V_{cyl}. As it is also necessary to consider the fact that the combustion rate will not become zero even at a low turbulence level, the description of the turbulence density influence on the heat release rate as an exponential function seems appropriate, as is formulated in equation (6.12):

$$F_2\left(k,V_{cyl}\right)=exp\left(C_{Rate}\cdot\frac{\sqrt{k}}{\sqrt[3]{V_{cyl}}}\right) \tag{6.12}$$

Finally, equation (6.13) represents the new formula for the heat release rate describing the influence of the currently available fuel quantity and the local density of the turbulent kinetic energy by means of the two functions $F_1(m_f,Q)$ and $F_2(k,V_{cyl})$ in equations (6.1) and (6.12):

$$\frac{dQ}{d\varphi}=C_{\text{mod}}\cdot F_1\left(m_f,Q\right)\cdot F_2\left(k,V_{cyl}\right) \tag{6.13}$$

Typical plotted results of the two functions $F_1(m_f,Q)$ and $F_2(k,V_{cyl})$ in equations (6.1) and (6.12) and also the new formula for the heat release rate, equation (6.13), for a four stroke direct injection Diesel engine are shown in figure 6.1.

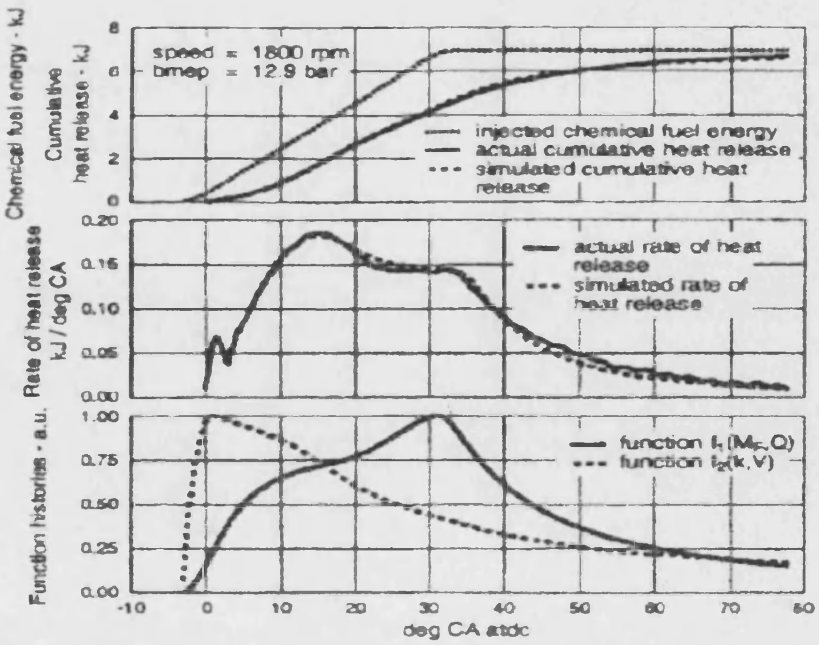

Figure 6.1: ROHR Simulation Using the Mixing Controlled Combustion [12]

6.3 Analytical formulation of the heat release model

6.3.1 Introduction

In developing the basic approach adopted by *Chmela and Orthaber* [12], the introduction of a constant injection rate as a function of injection pressure and fuel quantity as approximated in the common rail system led to wholly analytical solutions both for heat release rate and cumulative heat release.

A simplified analysis led to the formulation of $dQ/d\theta$ corresponding to the F_1 function of *Chmela and Orthaber* [12], and cumulative heat release as exponential functions expressed in terms of a combustion rate factor *WH*, which may be regarded as a mixing constant. Similarly, with the assumption of a constant injection rate the formulation for *Chmela and Orthaber* [12] dissipation function F_2 also leads to an analytical solution in exponential form, in terms of a dissipation constant C_{diss}.

With the total heat release rate expressed as the product of the functions F_1 and F_2, now both expressed in analytical form, the resultant heat release rate is given by:

$$\frac{dQ}{d\theta} = C_{\text{mod}} \cdot F_1(\theta) \cdot F_2(\theta) \qquad \text{(See equation 6.13)}$$

which also becomes a wholly analytical function.

This in turn results in considerable simplification and reduction in computing time compared with the finite difference approach which would have to be adopted in the case of variable injection rates, as found in pump line nozzle (PLN) systems.

Furthermore, it brings the new heat release routine into line with new spray propagation, swirl generation, spray deflection and ignition delay subroutines of chapters 3, 4 and 5, all of which are formulated in analytical rather than finite difference terms.

For diffusion combustion, the rate of heat release (ROHR) is controlled mainly by two items, i.e.,

a) The instantaneous fuel mass present in the cylinder charge,

b) The local density of turbulent kinetic energy.

Therefore, the strategy for the new heat release model is based on the above two items.

As already stated in section 6.1 the assumption of a constant injection rate leads directly to an analytical solution for the two basic processes of fuel/air mixing and turbulent kinetic energy dissipation of the developing spray.

These analytical solutions will be presented in three versions:

1. Simple formulation without ignition delay
2. Modified formulation with ignition delay
3. Complex formulation with ignition delay and effect of a finite period of needle lift.

Figures 6.4 illustrate the variation of the cumulative and rate of heat release functions F_1 for these three cases and will be discussed in the following sections. Similarly figures 6.5 and 6.6 present corresponding results for the kinetic energy dissipation function F_2 and the combined function $C_{mod}F_1F_2$, respectively.

6.3.2 Formulations neglecting ignition delay

6.3.2.1 Derivation of function F_1

The starting point is the assumption that, the heat release rate should be proportional to the fuel quantity available to combustion at the moment of consideration, which can be obtained from:

$$F_1(m_{finj}, m_{fb}) = m_{finj} - m_{fb} \tag{6.14}$$

where, $F_1(m_{finj}, m_{fb})$: The fuel quantity available for burning

m_{fb} : fuel quantity burned up to given crank angle,

$$(m_{fb} = \frac{Q}{LCV} = \frac{\text{The cumulative heat release}}{\text{The lower calorific value}})$$

m_{finj} : Fuel quantity injected up to given crank angle

With the assumption a uniform injection rate, the fuel quantity injected up to this moment, m_{finj}, can be obtained from:

$$m_{finj} = m_{ftot} \cdot \frac{\theta}{D_{inj}} \tag{6.15}$$

where, m_{ftot} : The total amount of fuel injected per cycle per cylinder

θ : crank angle

D_{inj} : crank angle of injection duration

Using this definition, the first hypothesis for the ROHR is given in equation (6.16):

$$\frac{dQ}{d\theta} = C_1 F_1 (m_{finj}, m_{fb}) \qquad \text{(See equation 6.2)}$$

or,
$$\frac{dQ}{d\theta} = C_1 (m_{finj} - m_{fb}) \qquad (6.16)$$

The rate of instantaneous fuel mass burned based on equation (6.16) using $\frac{dm_{fb}}{d\theta} = \frac{1}{LCV} \cdot \frac{dQ}{d\theta}$, can be obtained from:

$$\frac{dm_{fb}}{d\theta} = WH \cdot (m_{finj} - m_{fb}) \qquad (6.17)$$

where WH is combustion rate factor, which may also be regarded as a mixing rate factor.

If the initial conditions are known, i.e., $\theta = 0$ and $m_{fb} = 0$ then, the mathematical solution of this ordinary differential equation during injection period is given by:

$$\alpha_{h1} = \frac{\theta}{D_{inj}} - \frac{1 - \exp(-WH \cdot \theta)}{WH \cdot D_{inj}} \quad , \quad 0 \le \theta \le D_{inj} \qquad (6.18)$$

where, α_{h1} = fuel mass fraction burned relative to total injected fuel mass = $\frac{m_{fb}}{m_{ftot}}$

The rate of instantaneous fuel mass burned during injection period can be derived from the equation (6.18) as given in equation (6.19):

$$\frac{dm_{fb}}{d\theta} = \frac{m_{ftot}}{D_{inj}} [1 - \exp(-WH \cdot \theta)] \quad , \quad 0 \le \theta \le D_{inj} \qquad (6.19)$$

At the end of injection equation (6.18) using $m_{finj} = m_{ftot}$, can be written as:

$$\alpha_{h2} = 1 - \frac{1 - \exp(-WH \cdot D_{inj})}{WH \cdot D_{inj}} \quad , \quad \theta = D_{inj} \qquad (6.20)$$

After $\theta > D_{inj}$, the mathematical solution of the above ordinary differential equation, i.e. equation (6.17), using the additional conditions of $m_{finj} = m_{ftot}$ at $\theta \ge D_{inj}$, and also $m_{fb} = m_{ftot} \cdot \alpha_{h2}$ at $\theta = D_{inj}$, is given in equation (6.21):

$$\alpha_{h3} = 1 - (1 - \alpha_{h2}) \exp[-WH \cdot (\theta - D_{inj})] \quad , \quad \theta > D_{inj} \qquad (6.21)$$

Also, the rate of instantaneous fuel mass burned can be derived from equation (6.21) to give in equation (6.22):

$$\frac{dm_{fb}}{d\theta} = m_{ftot} \cdot WH \cdot (1 - \alpha_{h2}) \exp[-WH \cdot (\theta - D_{inj})] \quad , \quad \theta > D_{inj} \qquad (6.22)$$

The combustion rate factor, *WH*, can be found from equation (6.20) by choosing a value for α_{h2} at the end of injection, based on value derived from experimental cumulative heat release data, or ultimately from fundamental considerations.

6.3.2.2 Derivation of function F_2

As has already been stated the local density of the kinetic energy determines the heat release rate. In a Diesel engine the rate of the fuel oxidation is determined by the rate of mixing of fuel vapour and fresh gas and thus by the local density of the turbulent kinetic energy.

With the assumption of a uniform injection rate and using equation (6.15) the amount of the kinetic energy of the injection jets can eventually be determined by equation (6.23):

$$\frac{dKE_f}{d\theta} = \frac{KE_{f,tot}}{D_{inj}} \tag{6.23}$$

where, D_{inj} : duration of fuel injection (degree CA)

$KE_{f,tot}$: total kinetic energy of injected fuel jets

For computing the instantaneous level of kinetic energy in the cylinder charge, the dissipation has to be taken into account as well. In equation (6.24), a dissipation constant C_{diss} is used for this:

$$\frac{dKE_{diss}}{d\theta} = \frac{KE_{f,tot}}{D_{inj}} - \frac{C_{diss}}{6 \cdot N_e} \cdot KE_{diss} \qquad \text{(see equation 6.8)}$$

or, putting $WK = \frac{C_{diss}}{6 \cdot N_e}$

$$\frac{dKE_{diss}}{d\theta} = \frac{KE_{f,tot}}{D_{inj}} - WK \cdot KE_{diss} \tag{6.24}$$

If the initial conditions are known, i.e., $\theta = 0$ and $KE_{diss} = 0$ then, the mathematical solution of this ordinary differential equation during injection period is given by:

$$\alpha_{k1} = \frac{1}{D_{inj}} \cdot \frac{1}{WK}\left[1 - \exp(-WK \cdot \theta)\right] \quad , \quad 0 \le \theta \le D_{inj} \tag{6.25}$$

where, α_{k1} = fraction of the kinetic energy dissipation relative to total kinetic energy = $\frac{KE_{diss}}{KE_{f,tot}}$

At the end of injection, i.e., $\theta = D_{inj}$ equation (6.25) can be written as:

$$\alpha_{k2} = \frac{1}{D_{inj}} \cdot \frac{1}{WK}\left[1 - \exp\left(-WK \cdot D_{inj}\right)\right] \quad , \quad \theta = D_{inj} \tag{6.26}$$

After $\theta > D_{inj}$ using equation (6.26) as a initial condition, the ordinary differential equation of kinetic energy dissipation with the assumption of a coefficient δ, can be written as equation (6.27):

$$\frac{dKE_{diss}}{d\theta} = \delta \cdot \frac{KE_{f,tot}}{D_{inj}} - WK \cdot KE_{diss} \quad , \quad \theta > D_{inj} \tag{6.27}$$

where δ is adjusted to yield a value such that at the end of heat release $\alpha_{k2} < \alpha_{k3} < 1$

Therefore, the mathematical solution of the above ordinary differential equation, i.e. equation (6.27) is given by equation (6.28):

$$\alpha_{k3} = \alpha_{k2} \cdot \exp\left[-WK\left(\theta - D_{inj}\right)\right] + \frac{\delta}{WK \cdot D_{inj}} \cdot \left\{1 - \exp\left[-WK\left(\theta - D_{inj}\right)\right]\right\} \tag{6.28}$$

The dissipation constant C_{diss}, can be found from equation (6.26) by basing it on experimental values of α_{k2}, found to be in the region of 0.7, or ultimately from fundamental considerations.

The local turbulent kinetic energy density k that is given by KE divided by the instantaneous fuel quantity and the amount of fresh gas necessary for approximately stoichiometric diffusion combustion, can be described by means of equation (6.10), which C_{turb} is a measure of the efficiency of the transformation from kinetic energy into turbulent kinetic energy.

For $0 \le \theta \le D_{inj}$, the local turbulent kinetic energy density k, equation (6.10), using equations $m_{finj} = m_{ftot} \cdot \left(\theta / D_{inj}\right)$ and $\alpha_{k1} = KE_{diss} / KE_{f,tot}$, can be described by equation (6.29):

$$k = \frac{C_{turb} \cdot KE_{f,tot} \cdot D_{inj}}{m_{ftot} \cdot \left(1 + \lambda_{Diff} \cdot m_{stoich}\right)} \cdot \frac{\alpha_{k1}}{\theta} \tag{6.29}$$

Equation (6.29) using the fact that $\frac{C_{turb} \cdot KE_{f,tot} \cdot D_{inj}}{m_{ftot} \cdot \left(1 + \lambda_{Diff} \cdot m_{stoich}\right)} = \text{Constant}$ can be written as:

$$k = \text{Constant} \cdot \frac{\alpha_{k1}}{\theta} \quad , \quad 0 \le \theta \le D_{inj} \tag{6.30}$$

After $\theta \ge D_{inj}$, $m_{finj} = m_{ftot}$, hence, equation (6.30) can be rewritten as equation (6.31):

$$k = \text{Constant} \cdot \frac{\alpha_{k3}}{D_{inj}} \quad , \quad \theta \geq D_{inj} \tag{6.31}$$

As has already been stated the turbulence density influence on the heat release rate can be formulated as an exponential function in equation (6.12), substitution of the local turbulent kinetic energy density, k, using equation (6.30) in equation (6.12) gives:

$$F_2(k, V_{cyl}) = \exp\left(C_{Rate} \cdot \frac{\sqrt{\frac{\alpha_{k1}}{\theta}}}{\sqrt[3]{V_{cyl}}} \right) \quad , \quad 0 \leq \theta \leq D_{inj} \tag{6.32}$$

Similarly for $\theta \geq D_{inj}$, equation (6.32) can be rewritten as:

$$F_2(k, V_{cyl}) = \exp\left(C_{Rate} \cdot \frac{\sqrt{\frac{\alpha_{k3}}{D_{inj}}}}{\sqrt[3]{V_{cyl}}} \right) \quad , \quad \theta \geq D_{inj} \tag{6.33}$$

6.3.2.3 Normalisation of F_1 and F_2, and derivation of complete heat release function

As has already been stated, equation (6.19) gives the rate of instantaneous fuel mass burnt, which has a maximum value at the end of injection. Hence, using a coefficient CF_1 as equation (6.34), a normalised function of $F_1(m_{finj}, m_{fb})$, can be obtained from equation (6.35):

$$CF_1 = \frac{1}{\left(dm_{fb}/d\theta\right)_{\max}} \tag{6.34}$$

$$F_{1N} = \frac{dm_{fb}}{d\theta} \cdot CF_1 \tag{6.35}$$

To normalise the function $F_2(k, V_{cyl})$, firstly, it is necessary to produce a function F_2 varying between a peak value $[F_2]_{max} = 2.0$, and a limiting minimum value $[F_2]_{min} = 1.0$, using C_{Rate} in equation (6.32), from which 1.0 is subtracted to obtain a range of F_2 such that, $0 < F_2 < 1.0$ as a normalised function of F_{2N}, (see figure 6.1).

Equation (6.36) represents the new formula for the heat release rate describing the influence of the currently available fuel quantity and the local density of the turbulent

kinetic energy by means of the two normalised functions $F_{1N}(m_{finj}, m_{fb})$ and $F_{2N}(k, V_{cyl})$:

$$\frac{dQ}{d\varphi} = C_{\text{mod}} \cdot F_{1N}\left(m_{finj}, m_{fb}\right) \cdot F_{2N}\left(k, V_{cyl}\right) \tag{6.36}$$

This new approach for the heat release rate of a direct injection Diesel engine is the description of a purely mixing controlled combustion, in which the chemistry of fuel oxidation plays no role.

6.3.3 Formulation with ignition delay

6.3.3.1 Derivation of function F_1'

In this case derivation of function F_1' is the same as pervious case. The rate of instantaneous fuel mass burned can be obtained from equation (6.17), but the mathematical solution of this ordinary differential equation for $D_{ignd} \le \theta \le D_{inj}$, using some initial condition are known, i.e., $\theta = D_{ignd}$ and $m_{fb} = 0$, is given by:

$$\alpha_{h1} = \frac{\theta}{D_{inj}} - \frac{1-\exp\left[-WH\left(\theta - D_{ignd}\right)\right]}{WH \cdot D_{inj}} - \frac{D_{ignd}}{D_{inj}} \exp\left[-WH\left(\theta - D_{ignd}\right)\right], \quad D_{ignd} \le \theta \le D_{inj} \tag{6.37}$$

The rate of instantaneous fuel mass burned can be derived from the equation (6.37) as given in equation (6.38):

$$\frac{dm_{fb}}{d\theta} = \frac{m_{ftot}}{D_{inj}} \left\{1 - \left(1 - WH \cdot D_{ignd}\right) \cdot \exp\left[-WH\left(\theta - D_{ignd}\right)\right]\right\}, \quad D_{ignd} \le \theta \le D_{inj} \tag{6.38}$$

At end of injection equation (6.37) using $m_{finj} = m_{ftot}$, can be written as:

$$\alpha_{h2} = 1 - \frac{1-\exp\left[-WH\left(D_{inj} - D_{ignd}\right)\right]}{WH \cdot D_{inj}} - \frac{D_{ignd}}{D_{inj}} \exp\left[-WH\left(D_{inj} - D_{ignd}\right)\right], \quad \theta = D_{inj} \tag{6.39}$$

After $\theta > D_{inj}$, the mathematical solution of the above ordinary differential equation, i.e. equation (6.17), using some additional condition of $m_{finj} = m_{ftot}$ at $\theta > D_{inj}$, and also $m_{fb} = m_{ftot} \cdot \alpha_{h2}$ at $\theta = D_{inj}$, is given in equation (6.40):

$$\alpha_{h3} = 1 - \left(1 - \alpha_{h2}\right) \exp\left[-WH \cdot \left(\theta - D_{inj}\right)\right], \quad \theta > D_{inj} \tag{6.40}$$

Also, the rate of instantaneous fuel mass burned can be derived from equation (6.40) to give in equation (6.41):

$$\frac{dm_{fb}}{d\theta} = m_{ftot} \cdot WH \cdot (1-\alpha_{h2}) \exp\left[-WH \cdot (\theta - D_{inj})\right] \quad , \quad \theta > D_{inj} \tag{6.41}$$

6.3.3.2 Derivation of function F_2'

In this case, the assumption of a uniform fuel injection rate leads to the same equations for α_{k1}, α_{k2}, and α_{k3} for determination of fraction of the kinetics energy dissipation as in section 6.3.2.2, and also the local kinetic energy density, k, which can be given by equations (6.25), (6.26), (6.28), (6.30), and (6.31).
Therefore, the turbulence density influence on the heat release rate can be formulated as in the previous section by equation (6.32), and (6.33) for different limit of θ.

6.3.3.3 Normalisation of F_1' and F_2', and derivation of complete heat release function

This follows exactly the same pattern as that described in section 6.3.2.3.

6.3.4 Formulation with ignition delay and effect of a finite period of needle lift

6.3.4.1 Derivation of function F_1''

For the same total fuel mass flow, m_{ftot}, the fuel mass flow rate $\dot{m}_f$, which is constant rate during the injection period in the previous two cases, in the present case choosing a linear increase of fuel mass flow rate coinciding with the ignition delay period, the flow rate during the steady state flow period must be increased to $\dot{m}_f'$ (see figure 6.2).
The ratio of $\dot{m}_f' / \dot{m}_f$, using figure 6.2, can be found as below:

$$RMFR = \frac{\dot{m}_f'}{\dot{m}_f} = \frac{D_{inj}}{D_{inj} - 0.5 D_{ignd}} \tag{6.42}$$

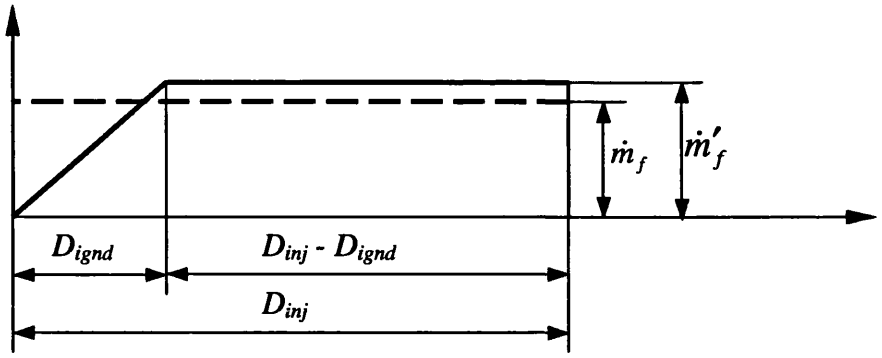

Figure 6.2: Fuel mass flow rate with and without ignition delay

In this case the general equation of m_f in each degree crank angle can be given by:

$$m_f = RMFR \cdot \frac{m_{ftot}}{D_{inj}} \left(\theta - 0.5 D_{ignd}\right) \tag{6.43}$$

Then for the present case the differential equation of burning rate is as below:

$$\frac{dm_{fb}}{d\theta} = WH \cdot \left[RMFR \cdot \frac{m_{ftot}}{D_{inj}} \left(\theta - 0.5 D_{ignd}\right) - m_{fb} \right] \tag{6.44}$$

If the initial conditions are known, i.e., $\theta = D_{ignd}$ and $m_{fb} = 0$ then, the mathematical solution of this ordinary differential equation for $D_{ignd} \le \theta \le D_{inj}$ is given by:

$$\alpha_{h1} = RMFR \left\{ \begin{array}{l} \left(\dfrac{\theta - 0.5 D_{ignd}}{D_{inj}} \right) - \dfrac{1 - \exp\left[-WH\left(\theta - D_{ignd}\right)\right]}{WH \cdot D_{inj}} \\ - \dfrac{0.5 D_{ignd}}{D_{inj}} \exp\left[-WH\left(\theta - D_{ignd}\right)\right] \end{array} \right\} \quad D_{ignd} \le \theta \le D_{inj} \tag{6.45}$$

The rate of instantaneous fuel mass burned can be derived from the equation (6.45) as given in equation (6.46):

$$\frac{dm_{fb}}{d\theta} = RMFR \cdot \frac{m_{ftot}}{D_{inj}} \left\{ 1 - \left(1 - 0.5 D_{ignd} \cdot WH\right) \exp\left[-WH\left(\theta - D_{ignd}\right)\right] \right\} , \quad D_{ignd} \le \theta \le D_{inj} \tag{6.46}$$

At the end of injection, i.e., $\theta = D_{inj}$ equation (6.45) using $m_{finj} = m_{ftot}$, can be written as:

$$\alpha_{h2} = RMFR\left\{\begin{array}{l}\left(\dfrac{D_{inj}-0.5D_{ignd}}{D_{inj}}\right)-\dfrac{1-\exp\left[-WH\left(D_{inj}-D_{ignd}\right)\right]}{WH\cdot D_{inj}} \\ -\dfrac{0.5D_{ignd}}{D_{inj}}\exp\left[-WH\left(D_{inj}-D_{ignd}\right)\right]\end{array}\right\} \quad \theta = D_{inj} \qquad (6.47)$$

After $\theta > D_{inj}$, the mathematical solution of the above ordinary differential equation, i.e. equation (6.44), using the additional conditions of $m_{finj} = m_{ftot}$ at $\theta > D_{inj}$, and also $m_{fb} = m_{ftot} \cdot \alpha_{h2}$ at $\theta = D_{inj}$, is given in equation (6.48):

$$\alpha_{h3} = 1-(1-\alpha_{h2})\exp\left[-WH\cdot(\theta - D_{inj})\right] \quad , \quad \theta > D_{inj} \qquad (6.48)$$

Also, the rate of instantaneous fuel mass burned can be derived from equation (6.48) to give in equation (6.49):

$$\frac{dm_{fb}}{d\theta} = m_{ftot}\cdot WH\cdot(1-\alpha_{h2})\exp\left[-WH\cdot(\theta - D_{inj})\right] \quad , \quad \theta > D_{inj} \qquad (6.49)$$

6.3.4.2 Derivation of function F_2''

The use of a rising injection rate during the ignition delay period will lead to a reformulation of equation (6.23), which was based on a constant injection rate. This will also affect subsequent equations.

For the same total kinetic energy of injected fuel jets, the rate of kinetic energy of the injected fuel jet $\dot{KE}_f$, which is a constant rate during the injection period in the previous two cases, in the present case choosing a linear increase of fuel mass flow rate coinciding with the ignition delay period, leads to a parabolic increase of the kinetic energy of injected fuel jets again coinciding with the ignition delay period. During the steady state period $\dot{KE}_f$ must be increased to $\dot{KE}'_f$ (see figure 6.3).

The rate of $\dot{KE}'_f / \dot{KE}_f$, using figure 6.3, can be found as below:

$$REFR = \frac{\dot{KE}'_f}{\dot{KE}_f} = \frac{D_{inj}}{D_{inj}-(2/3)D_{ignd}} \qquad (6.50)$$

where D_{ignd} : ignition delay period

The general equation of KE_f in each degree of crank angle for $0 \le \theta \le D_{ignd}$ can be given by:

$$kE_f = REFR \cdot KE_{f,tot} \cdot \frac{\theta^3}{3D_{inj} \cdot D_{ignd}^2} \quad , \quad 0 \le \theta \le D_{ignd} \tag{6.51}$$

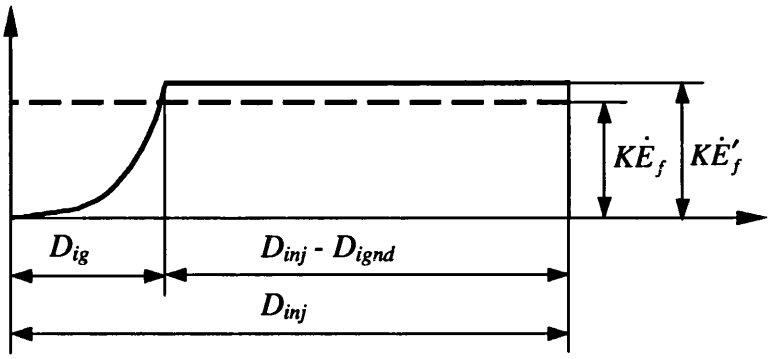

Figure 6.3: The rate of kinetic energy of injected fuel jets with and without the effect of finite period of needle lift coinciding with the ignition delay period

The rate of instantaneous kinetic energy dissipation based on equation (6.8) using equation (6.51), can be obtained from:

$$\frac{dKE_{diss}}{d\theta} = REFR \cdot \frac{KE_{f,tot}}{D_{inj} \cdot D_{ignd}^2} \cdot \theta^2 - \frac{C_{diss}}{6 \cdot n} \cdot KE_{diss} \tag{6.52}$$

If the initial condition are known, i.e., $\theta = 0$ and $KE_{f,tot} = 0$ then, the mathematical solution of this ordinary differential equation for $0 \le \theta \le D_{ignd}$, using $WK = \frac{C_{diss}}{6 \cdot N_e}$, is given by:

$$\alpha'_{kl} = \frac{REFR}{D_{ignd}^2 D_{inj}} \left\{ \frac{\theta^2}{WK} - \frac{2\theta}{WK^2} + \frac{2}{WK^3} \left[1 - \exp(-WK \cdot \theta) \right] \right\} \quad , \quad 0 \le \theta \le D_{ignd} \tag{6.53}$$

where, $\alpha'_{kl} = \frac{KE_{diss}}{KE_{f,tot}}$

During the steady state period the instantaneous level of kinetic energy of injected fuel jets KE_f can be given by:

$$KE_f = REFR \cdot \frac{KE_{f,tot}}{D_{inj}} \cdot \left(\theta - \frac{2}{3} D_{ignd} \right) \quad , \quad D_{ignd} \le \theta \le D_{inj} \tag{6.54}$$

Similarly equation (6.8), using equation (6.54) can be written as:

$$\frac{dkE_{diss}}{d\theta} = REFR \cdot \frac{KE_{f,tot}}{D_{inj}} - \frac{C_{diss}}{6 \cdot N_e} \cdot KE_{diss} \tag{6.55}$$

The mathematical solution of this ordinary differential equation for $D_{ignd} \le \theta \le D_{inj}$, using the initial condition are known, i.e., $\theta = D_{ignd}$ and $KE_{diss} = \alpha'_{k1} \cdot KE_{f,tot}$, is given by:

$$\alpha''_{k1} = \frac{REFR}{D_{inj}} \left\{ \frac{1}{WK} - \frac{2}{D_{ignd} \cdot WK^2} \left(1 - \frac{1}{D_{ignd} \cdot WK} \right) \cdot \exp\left[-WK(\theta - D_{ignd}) \right] - \frac{2}{D_{ignd}^{\,2} \cdot WK^3} \cdot \exp(-WK \cdot \theta) \right\} \quad (6.56)$$

where, $\alpha''_{k1} = \dfrac{KE_{diss}}{KE_{f,tot}}$

At the end of injection, i.e., $\theta = D_{inj}$, equation (6.56) can be written as:

$$\alpha''_{k2} = \frac{REFR}{D_{inj}} \left\{ \frac{1}{WK} - \frac{2}{D_{ignd} \cdot WK^2} \left(1 - \frac{1}{D_{ignd} \cdot WK} \right) \cdot \exp\left[-WK(D_{inj} - D_{ignd}) \right] - \frac{2}{D_{ignd}^{\,2} \cdot WK^3} \cdot \exp(-WK \cdot D_{inj}) \right\} \quad (6.57)$$

After $\theta > D_{inj}$, similarly the mathematical solution of the ordinary differential equation (6.27), using equation (6.57) as an initial condition is given by equation (6.58).

$$\alpha''_{k3} = \alpha''_{k2} \cdot \exp\left[-WK(\theta - D_{inj}) \right] + \frac{\delta}{WK \cdot D_{inj}} \cdot \left\{ 1 - \exp\left[-WK(\theta - D_{inj}) \right] \right\} \quad (6.58)$$

For $0 \le \theta \le D_{ignd}$, the local turbulent kinetic energy density k, equation (6.10), using equations $m_{finj} = m_{ftot} \cdot RMFR \cdot \left(\theta^2 / 2D_{ignd} \cdot D_{inj} \right)$ and $\alpha'_{k1} = E_{kin,F,Diss} / E_{kin,F,tot}$, and also using the fact that $\dfrac{C_{turb} \cdot KE_{f,tot} \cdot D_{inj}}{m_{ftot} \cdot \left(1 + \lambda_{Diff} \cdot m_{stoich} \right)} = \text{Constant}$ can be described by equation (6.59):

$$k = \text{Constant} \cdot \frac{2D_{ignd}}{RMFR} \frac{\alpha'_{k1}}{\theta^2} \quad , \quad 0 \le \theta \le D_{ignd} \quad (6.59)$$

Similarly, for $D_{ignd} \le \theta \le D_{inj}$, the local turbulent kinetic energy density k, eqn. (6.10), using equations $m_{finj} = m_{ftot} \cdot RMFR \cdot \left(\theta - 0.5 D_{ignd} \right)$ and $\alpha''_{k1} = KE_{diss} / KE_{f,tot}$, and also using the fact that $\dfrac{C_{turb} \cdot KE_{f,tot} \cdot D_{inj}}{m_{ftot} \cdot \left(1 + \lambda_{Diff} \cdot m_{stoich} \right)} = \text{Constant}$ can be described by equation (6.60):

$$k = \text{Constant} \cdot \frac{1}{RMFR} \frac{\alpha''_{k1}}{(\theta - 0.5D_{ignd})} \quad , \quad D_{ignd} \le \theta \le D_{inj} \tag{6.60}$$

After $\theta \ge D_{inj}$, $m_{finj} = m_{ftot}$, hence, equation (6.60) can be rewritten as equation (6.61):

$$k = \text{Constant} \cdot \frac{\alpha''_{k3}}{D_{inj}} \quad , \quad \theta \ge D_{inj} \tag{6.61}$$

As has already been stated the turbulence density influence on the heat release rate can be formulated as an exponential function in equation (6.12), substitution of the local turbulent kinetic energy density, k, using equation (6.59) in equation (6.12) gives:

During ignition delay i.e., $0 \le \theta \le D_{ignd}$:

$$F_2(k, V_{cyl}) = \exp\left(C_{Rate} \cdot \frac{\sqrt{\frac{2 \cdot D_{ignd}}{RMFR} \frac{\alpha'_{k1}}{\theta^2}}}{\sqrt[3]{V_{cyl}}} \right) \quad , \quad 0 \le \theta \le D_{ignd} \tag{6.62}$$

Similarly for $D_{ignd} \le \theta \le D_{inj}$, equation (6.62) can be rewritten as:

$$F_2(k, V_{cyl}) = \exp\left(C_{Rate} \cdot \frac{\sqrt{\frac{1}{RMFR} \cdot \frac{\alpha''_{k1}}{(\theta - 0.5D_{ignd})}}}{\sqrt[3]{V_{cyl}}} \right) \quad , \quad D_{ignd} \le \theta \le D_{inj} \tag{6.63}$$

For $\theta > D_{inj}$, equation (6.62) can be rewritten as:

$$F_2(k, V_{cyl}) = \exp\left(C_{Rate} \cdot \frac{\sqrt{\frac{\alpha''_{k3}}{D_{inj}}}}{\sqrt[3]{V_{cyl}}} \right) \quad , \quad \theta \ge D_{inj} \tag{6.64}$$

6.3.4.3 Normalisation of F_1'' and F_2'', and derivation of complete heat release function

This again follows the pattern described in section 6.3.2.3.

6.3.5 Comparison of results of sections 6.3.2, 6.3.3, and 6.3.4

The variation of both the cumulative and rate of heat release functions F_1 for the above three cases are shown in figure 6.4.

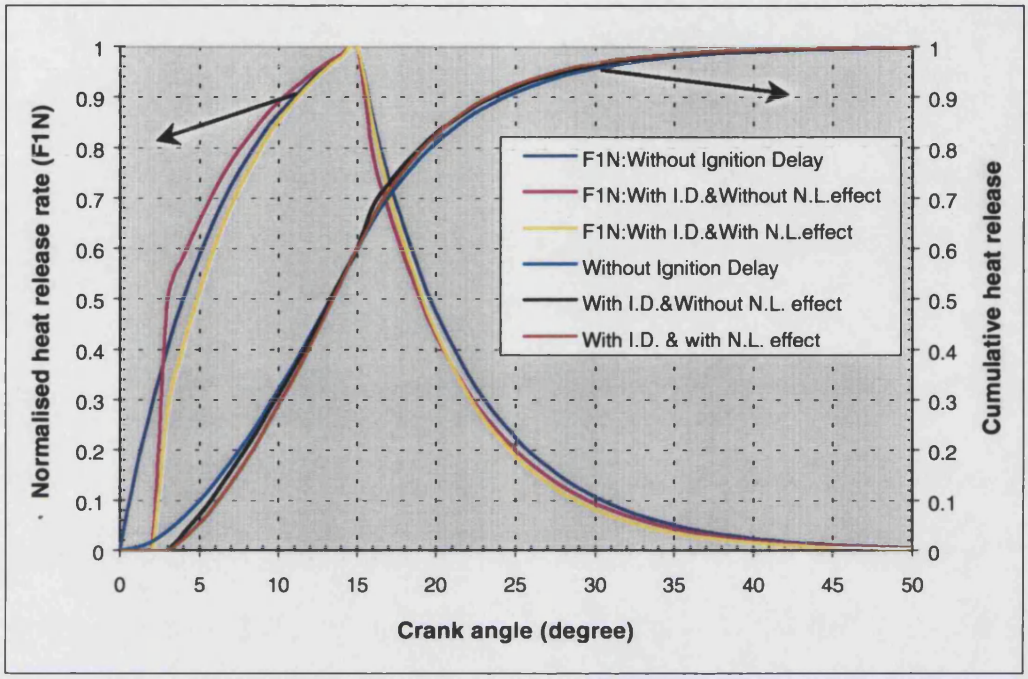

Figure 6.4: Normalised F_1 functions

The case of zero ignition delay (F_{1N}) which does not reflect the true situation, gives a continuous rise both of the cumulative burnt fuel fraction and of the normalised rate of fuel burning, up to the end of injection.

The second case with ignition delay, but neglecting needle lift effect (F'_{1N}), leads to large instantaneous increase in the rate of fuel burning at the end of ignition delay.

The final and most realistic case with ignition delay and finite period of needle lift effect during the delay period leads to an initially lower normalised rate of fuel burning and a lower initial cumulative burnt fuel mass.

The latter case, i.e. the F''_{1N} function was found to be by far the most realistic, as will be shown in chapter 7.

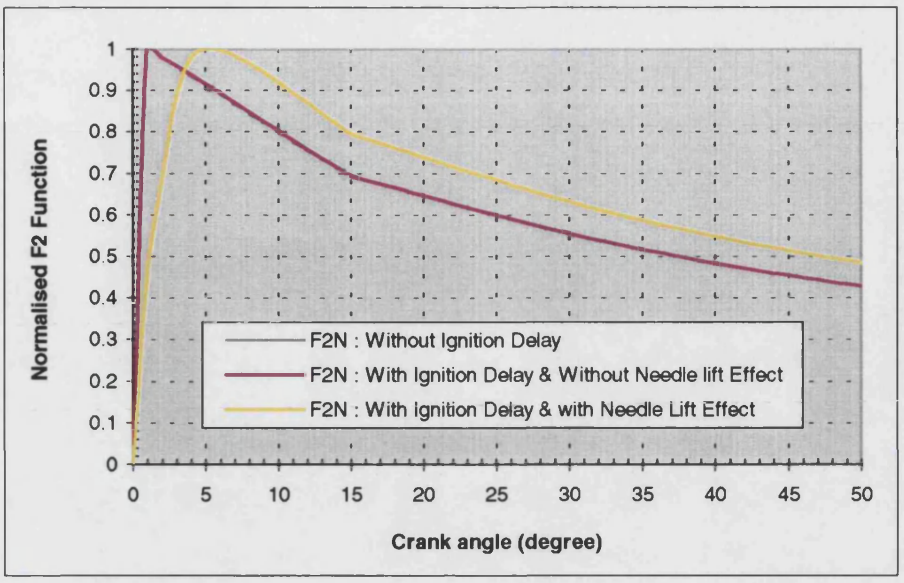

Figure 6.5: Normalised F_2 functions

As already stated the F_{2N} and F'_{2N} cases are identical. With both ignition delay and a finite period of needle lift, i.e. F''_{2N}, the effect on the F_2 function is significant, with a gradual rather than instantaneous rise to the peak value, and considerably altered decay rate (see also figure 6.1).

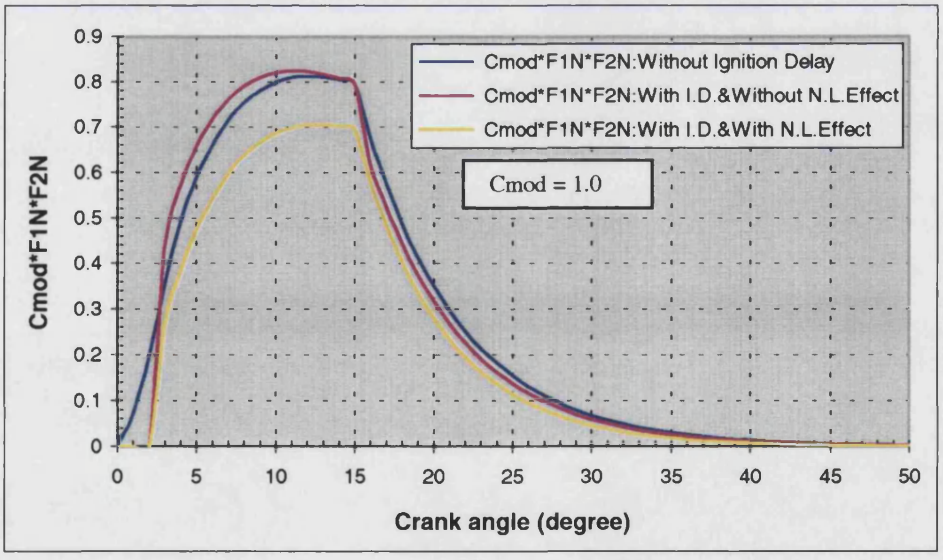

Figure 6.6: Normalised global burnt fuel rate

The resultant change in the normalised heat release rate function is very apparent. Since cumulative fuel burnt at 50° after SoI is assumed to be identical in all cases, the actual ROHR diagram would clearly show higher peak values at the end of injection

for the case with ignition delay and finite rate of needle lift, which was shown to give by far the best approximation to measured rates (see chapter 7).

6.4 References

1. **Russell, M.F.**, " The dependence of diesel combustion on injection rate", paper No. S490/005/97 'Future Engine System Technologies, The Euro IV Challenge' and IMechE Seminar, ISBN 1 86058 166 8 pp.65-81 (1997).

2. **Arcoumanis, C., Gervaises, M., and Nouri, J.M.**, "Effect of Fuel Injection processes on Diesel Injection Sprays", SAE 970080 (1997).

3. **Naber, J. D., and Siebers, D. L.**, "Effect of Gas Density and Vaporization on Penetration and Dispersion of Diesel Sprays", SAE 960034 (1996).

4. **Siebers, D.L., and Higgins, B.S.**, "Effects of Injector Conditions on the Flame Lift-Off Length of DI Diesel Sprays", Proceeding Conference on: Thermofluidynamic Processes in Diesel Engines, Valencia 13-15, September, (2000).

5. **Wiebe, I.**, "Halbempirische Formel dur die Verbrennungsgeschwindigkeit, in krafstoffaufber-eitung und verbrennung bei Dieselmotoren, ed. G. Sitkei, pp. 156-159, Springer-Verlag, Berlin (1964).

6. **Watson, N., Pilley, A.D., and Marzouk, M.**, "A Combustion Correlation for Diesel Engine Simulation", SAE 860029 (1980).

7. **Asten, A.E.W., and Lyn, W.T.**, "Relation Between Fuel Injection and Heat Release in a Direct Injection Engine and Nature of the Combustion Process", Proceedings of the Institution of Mechanical Engineers (1960).

8. **Meguerdichian, M., and Watson, N.**, "Prediction of Mixture Formation and Heat Release in Diesel Engines", SAE 780225 (1978).

9. **Bazari, Z.**, "A DI Diesel Combustion and Emission Predictive Capability for Use in Cycle Simulation", SAE 920462 (1992).

10. **Hiroyasu, H., Kadota, T., and Arai, M.**, "Development and Use of a Spray Combustion Modelling to Predict Diesel Engine Efficiency and Pollutant Emissions: Part1. Combustion Modelling", Bulleting of the JSME, Vol. 26, No. 214, pp. 569-575 (1983).

11. **Shahed, S.M., Chiu, W.S., and Lyn, W.T.**, "A Mathematical Model of Diesel Combustion", Proceeding of the IMechE, C94/75, pp. 119-128 (1975).

12. **Chmela, F.G., and Orthaber, G.C.**, "Rate of Heat Release Prediction for Direct Injection Diesel Engines Based on Purely Mixing Controlled Combustion", SAE 990186 (1999).

13. **Ryan, T. W., et al**, "Homogeneous Charge Compression Ignition of Diesel Fuels", SAE 961160 (1996).

14. **Magnussen, B. F., and Hjertager, B. H.**, "On Mathematical Modelling of Turbulent Combustion with Special Emphasis on Soot Formation and Combustion", 16th International Symposium on Combustion (1976).

CHAPTER 7

Calibration of new heat release model

7.1 Introduction

The calibration of the new heat release formulation of chapter 6 was carried out in two parts:

Part 1: calibration against some results published by *Chmela and Orthaber* [1],

Part 2: calibration against experimental test bed results undertaken at the University of Bath on a HPCR 1.8 l DI Diesel engine under limiting torque condition.

7.2 Calibration against data of Chmela and Orthaber [1]

The results presented in the *Chmela and Orthaber* paper were based on a medium speed direct injection diesel engine with a high-pressure common rail (HPCR) fuel injection system. Leading details are set out in table 7.1.

Table 7.1: Technical Data of Single Cylinder Test Engine [1]

Bore	124 mm
Stroke	165 mm
Displacement	2.0 dm^3
Compression ratio	18:1
Swirl level	1.8
Injection nozzle	8 x 0.18 mm or, 8 x 0.20 mm

As already stated in chapter 6, *Chmela and Orthaber* do not give any details of the method of solution of the basic equations, which has to be assumed to be of a numerical rather than an analytical type.

Three separate sets of cases were:

Case 1 (Figures 7.1 and 7.2):

Figure 7.1 shows the results of the *Chmela* and *Orthaber* analysis, which is a simple validation for one particular operating condition and a single set of injection data, and used to calibrate their own method for further investigation, i.e., determination of C_{mod} (equation 6.13), and C_{Rate} (equation 6.12),

The operating conditions for this case are:

Speed: N_e = 1200 rev/min

Break mean effective pressure: bmep = 12.9 bar

Total fuel chemical energy: Q_{tot} = 7.0 kJ (from figure 7.1)

Total fuel mass injected per cycle: $m_{ftot} = 2.0444 \times 10^{-4}$ kg

Injection nozzle specification: 8 × 0.18 mm

Injection period D_{inj} = 34 °CA

Start of Injection SoI = 3 °BTDC

Injection velocity v_N = 384.33 m/sec, (see chapter 5, equation 5.1)

Fraction of fuel burnt at the end of injection α_{h2} = 0.57 (from figure 7.1, see equation 6.20)

In the absence of detailed information on ignition delay and initial needle lift rate, the simplest of the three alternative formulations of chapter 6, as per section 6.3.2 was used.

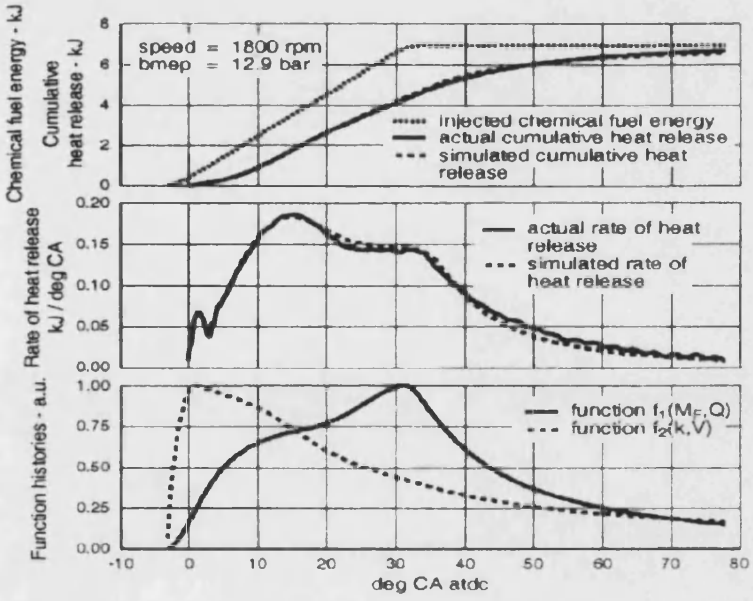

Figure 7.1: ROHR simulation using the "MCC" formula [1]

The results are shown in figure 7.2, representing the final case in a series of iterations on the fraction of energy dissipation at the end of injection, α_{k2} = 0.7.

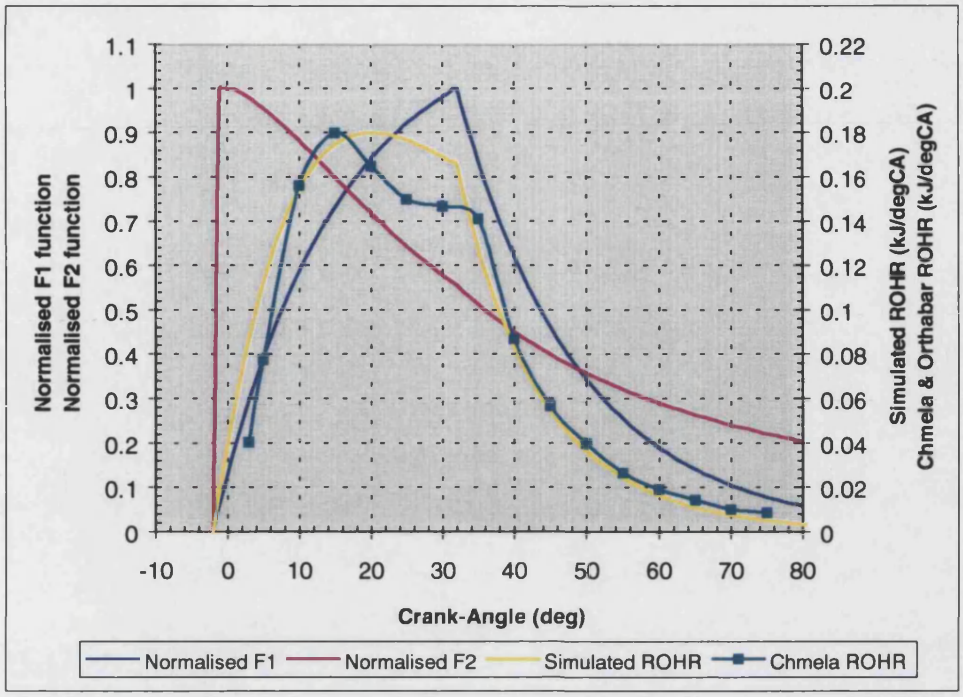

Figure 7.2: Normalised functions of F_1 and F_2, and different types of ROHR

Figure 7.2 shows:

Normalised F_1 function

Normalised F_2 function

Chmela & Orthaber and the simulated rate of heat release kJ/°CA.

The agreement between the simulated ROHRs is not perfect, the major discrepancy being the 'dip' in the *Chmela & Orthaber* ROHR before end of injection. However, the peak rate of heat release, at just over 0.18 kJ /°CA, is well represented, while there is an error of approximately 6°CA in the phasing of the peak rate. The decay of ROHR after end of injection is well represented.

Case 2 (figures 7.3 and 7.4):

Figure 7.3 shows the results of the *Chmela & Orthaber* analysis for a comparison of three different operating conditions with a single injector specification, but different injection durations, implying different derived injection pressures with both speed and bmep varying.

In this case neither information on the heat release fraction α_{h2} at the end of injection nor the total fuel quantity m_{Ftot} was available. Therefore both α_{h2} and α_{k2} had to be obtained by iteration to obtain a best fit, in which the fuel quantity m_{Ftot}, was derived

from the given values of speed and bmep, with an estimated thermal efficiency. The nozzle configuration was 8×0.18 mm hole size.

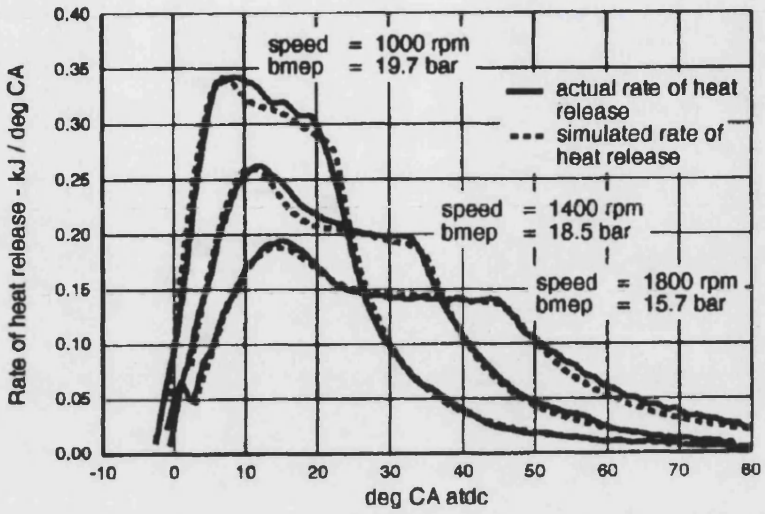

Figure 7.3: *Chmela & Orthaber* and Actual ROHR results [1]

Figure 7.4 shows the *Chmela & Orthaber* ROHR results together with the computed results of simulated rate of heat release for the three operating conditions considered. The inset gives the values of α_{h2} and α_{k2}, as well as C_{mod} for each of the three cases.

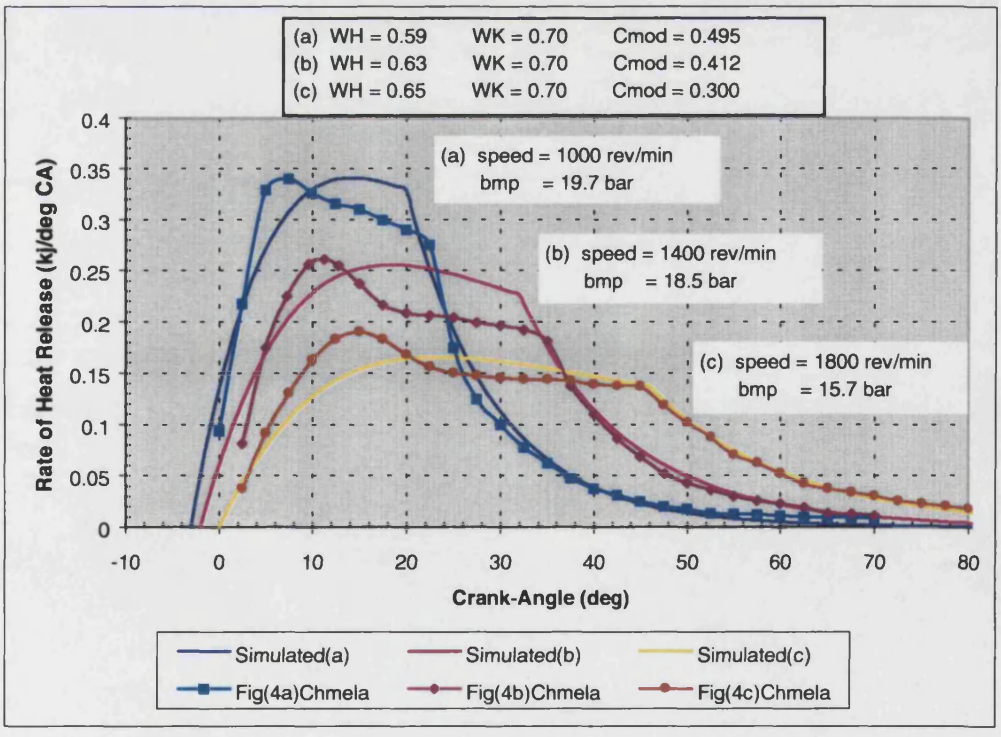

Figure 7.4: *Chmela & Orthaber* and the simulation results of ROHR at different conditions

The agreement between *Chmela & Orthaber* results and the simulated ROHR results is not perfect, again the 'dip' in the *Chmela & Orthaber* ROHR before end of injection is not accounted for. However, the peak rates of heat release in all three cases are well represented, while there is an error of approximately 7°CA in the phasing of the peak rates. The decay of ROHR after end of injection is well represented in each case.

Case 3 (figures 7.5 and 7.6):

Figure 7.5 shows the results of the *Chmela & Orthaber* analysis for a comparison of two different injection pressures for the same injector specification and a single operating condition as indicated.

As in case 2, in the present case neither information on the heat release fraction α_{h2} at the end of injection nor the total fuel quantity m_{ftot} was available. Therefore again both α_{h2} and α_{k2} had to be obtained by iteration to obtain a best fit, in which the fuel quantity m_{Ftot} was derived from the given values of speed and bmep, with an estimated thermal efficiency. The nozzle configuration was 8×0.20 mm hole size.

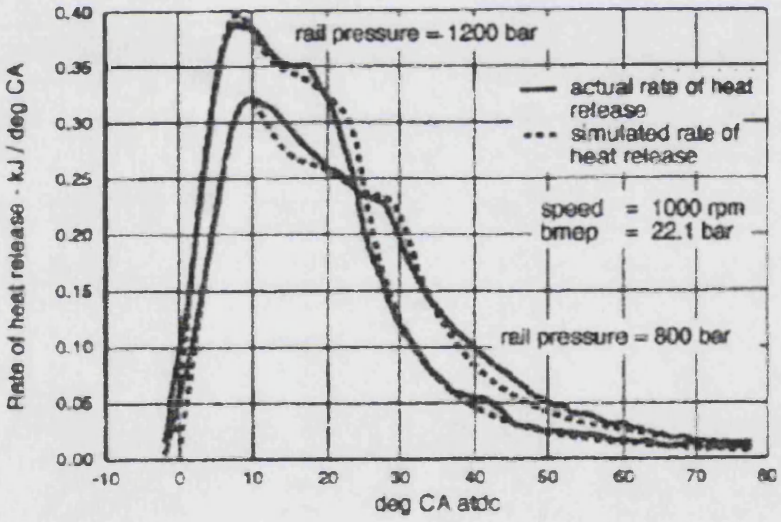

Figure 7.5: *Chmela & Orthaber* simulation results at different fuel rail pressures [1]

Figure 7.6 shows the *Chmela & Orthaber* ROHR results together with the computed results of simulated rate of heat release for two different cases of rail pressure.

The inset gives the values of α_{h2} and α_{k2}, as well as C_{mod} for both cases.

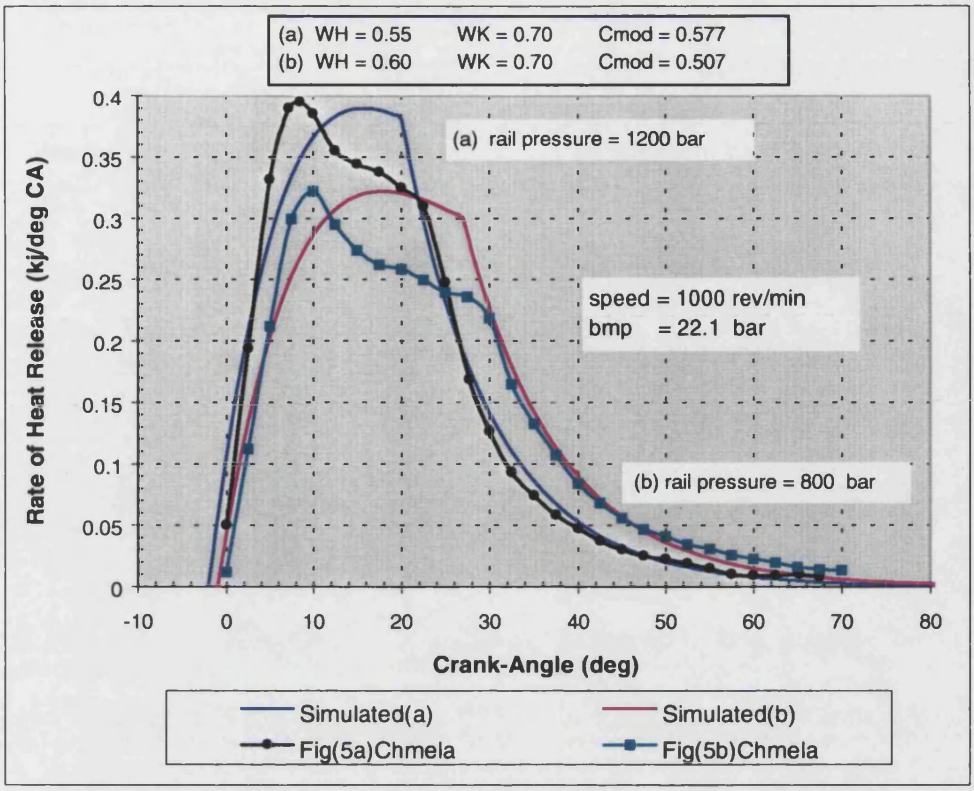

Figure 7.6: *Chmela & Orthaber* and the simulation results of ROHR at different fuel rail pressures

The agreement between *Chmela & Orthaber* results and the simulated ROHR results is not perfect, again the 'dip' in the *Chmela & Orthaber* ROHR before end of injection is not accounted for. However, the peak rates of heat release in both cases are well represented, while there is again an error of approximately 7°CA in the phasing of the peak rates. The decay of ROHR after end of injection is well represented in both cases.

Comment on simulated results

The "dip" in the *Chmela* and *Orthaber* heat release results, which is not reproduced in the simulated results, can only be accounted for by the absence of further detailed information on the former. It is possible that with data on measured needle lift, the rate of fuel delivery could not be constant, as has been assumed in the case of the simulation. Such data on variable fuel delivery rates could readily be dealt with by a numerical method of solution, but not by the analytical method of chapter 6 adapted for the present simulations.

7.3 Calibration against experimental HPCR engine data

7.3.1 Summary of available data

The experimental results were obtained using an AVL heat release data acquisition system together with associated Concerto software. (It is not considered appropriate to give further details, as this thesis is concerned primarily with theoretical analysis.)
The Ford 1.8 litre DI Diesel engine was equipped with a prototype Lucas CAV HPCR system, and an Allied Signal VGT.
Outline details of the engine are given in table 7.2.

Table 7.2: Ford HPCR 1.8 litre DI Diesel engine details

Bore	82.5 mm
Stroke	82.0 mm
Displacement	438 cc per cylinder
Number of cylinders	4
Compression ratio	19.5:1
Injection nozzle specification	5 × 0.15 mm
Rail pressure	540 to 1355 bar, dependent on speed
Engine speed	1250 to 4000 rev/min

All results were obtained at the limiting torque curve with limits set to the following parameters over different speed ranges:
Air-fuel ratio, A/F: ≥ 19.0 for $1250 < N_e < 1500$ rev/min
Maximum cylinder pressure, p_{max}: ≤ 140 bar for $1500 < N_e < 3000$ rev/min
Pre. Turbine temperature, T_{exh}: $\leq 800°C$ for $3000 < N_e < 4000$ rev/min
Rail pressure and injection timing were varied in accordance with a schedule based on a compromise between best bsfc and minimum NOx emissions.
A comprehensive summery of operating conditions is given in table 7.3.

Table 7.3: Summery of operating conditions

ENGINE PERFORMANCE - 1

AVG SPEED (RPM)	CORR TORQUE (Nm)	CORR FACTOR (88/195)	CORR POWER (kW)	CORR BMEP (kPa)	CORR BSFC (g/kWh)	FUEL INJ. (mm3/sht)	BK.TH. EFFY. (%)	RAIL RESSURE (BAR)
1253	132.8	0.997	17.4	952	246	34.1	34	640
1511	160.2	0.998	25.3	1148	226	37.7	37	705
1755	175.3	0.999	32.2	1256	216	39.5	39	779
2008	190.2	1.000	40.0	1363	214	42.4	39	850
2256	196.8	1.000	46.5	1410	211	43.3	40	900
2511	203.6	1.000	53.5	1459	213	45.1	40	955
3006	199.2	1.001	62.7	1427	223	46.3	38	1130
3543	180.1	1.002	66.8	1291	228	42.8	37	1210
4031	171.0	1.002	72.2	1226	248	44.2	34	1355

ENGINE PERFORMANCE - 2

AVG SPEED (RPM)	CORR TORQUE (Nm)	FUEL FLOW (kg/hr)	AIR FLOW (kg/hr)	APPARENT AFR (-)	VOL EFFY (%)	START OF COMB (-BTDC)	COMB. NOISE (dBa)
1253	132.8	4.295	77.4	18.0	82.6	107.7	87.9
1511	160.2	5.733	110.9	19.3	82.0	0.5	89.5
1755	175.3	6.975	146.1	20.9	82.9	0.5	90.7
2008	190.2	8.560	205.3	24.0	88.2	-0.5	90.8
2256	196.8	9.818	231.7	23.6	89.7	-0.5	92.3
2511	203.6	11.390	254.2	22.3	88.8	-1.0	93.7
3006	199.2	13.982	304.6	21.8	90.1	-1.0	94.0
3543	180.1	15.238	348.7	22.9	88.7	-2.0	94.6
4031	171.0	17.880	385.3	21.5	88.0	-2.0	95.3

ENGINE GAS TEMPERATURES

AVG SPEED (RPM)	CORR TORQUE (Nm)	AIR INLET DegC	PRE. COMP DegC	PRE. INT/R DegC	POST INT/R DegC	INLET MAN. DegC	PRE. TURB DegC	POST TURB DegC	EXH D/P DegC
1253	132.8	12	24	54	38	38	564	399	376
1511	160.2	13	24	79	36	38	604	437	419
1755	175.3	13	24	99	38	39	592	431	420
2008	190.2	14	24	124	40	41	567	403	397
2256	196.8	15	24	126	42	42	589	427	419
2511	203.6	15	25	127	43	43	637	473	463
3006	199.2	18	25	128	46	46	701	543	533
3543	180.1	19	26	136	50	50	705	552	544
4031	171.0	18	26	143	50	50	775	608	598

ENGINE FLUID TEMPERATURES

AVG SPEED (RPM)	CORR ORQUE (Nm)	FUEL IN (DegC)	FUEL OUT (DegC)	COOL IN (DegC)	COOL OUT (DegC)	OIL CYL HD. (DegC)	OIL FILTER (DegC)	OIL SUMP (DegC)
1253	132.8	21	30	88	93	89	0	97
1511	160.2	21	31	89	93	88	0	96
1755	175.3	22	32	89	93	88	0	97
2008	190.2	22	33	89	94	87	0	98
2256	196.8	22	34	90	94	88	0	101
2511	203.6	22	36	90	94	88	0	101
3006	199.2	23	38	93	96	86	0	103
3543	180.1	24	40	92	95	88	0	105
4031	171.0	24	42	92	95	91	0	110

Table 7.3: continued,

ENGINE GAS PRESSURES

AVG SPEED (RPM)	CORR TORQUE (Nm)	ABS. BARO (kPa)	PRE. COMP/R (kPa)	PRE. INT/R (kPa)	IN.MAN BOOST (kPa)	MAX CYL (Bar)	PRE. TURBINE (kPa)	EXH D/P (kPa)
1253	132.8	99.7	-0.4	27	27	-4	41	-0.1
1511	160.2	99.7	-0.8	52	52	115	74	0.5
1755	175.3	99.7	-1.4	72	71	121	99	1.2
2008	190.2	99.7	-2.8	100	98	135	156	2.6
2256	196.8	99.7	-3.6	99	97	129	115	3.5
2511	203.6	99.7	-4.3	99	97	127	98	4.6
3006	199.2	99.7	-6.0	98	96	123	100	7.3
3543	180.1	99.7	-7.8	98	96	124	117	9.2
4031	171.0	99.7	-9.4	95	92	117	131	11.5

EXHAUST EMISSIONS - 1

AVG SPEED (RPM)	CORR TORQUE (Nm)	RAW HC (C3ppm)	RAW NOx (ppm)	EXH CO (ppm)	EXH O2 (%)	EXH CO2 (%)	INLET CO2 (%)	AVL 409 SMOKE (Bosch)	AVL 415 SMOKE (FSN)
1253	132.8	76	979	5	3.65	12.00	0.07	3.6	3.89
1511	160.2	55	1145	1156	4.62	11.66	0.07	2.4	3.00
1755	175.3	58	1297	493	6.03	10.76	0.06	1.4	1.80
2008	190.2	50	1299	119	7.83	9.42	0.06	0.8	1.16
2256	196.8	53	1153	239	7.71	9.51	0.05	1.2	1.30
2511	203.6	56	1036	488	6.86	10.15	0.05	2.0	2.42
3006	199.2	44	917	677	5.96	10.76	0.05	2.9	3.30
3543	180.1	42	860	415	6.62	10.29	0.04	2.7	2.80
4031	171.0	27	783	757	5.71	10.94	0.04	3.6	3.90

EXHAUST EMISSIONS - 2

AVG SPEED (RPM)	CORR TORQUE (Nm)	REL. HUMID (%)	NOx C.F. (J177a)	MASS HC (g/hr)	CORR. NOx (g/hr)	MASS PARTIC (g/hr)	AVL EGR (%)	AVL AFR (Spindt)	CORR. SMOKE (Bosch)
1253	132.8	100	1.045	8.9	121.4	40.9	0	0.0	3.3
1511	160.2	100	1.045	9.1	202.8	30.8	0	0.0	2.1
1755	175.3	100	1.044	12.8	301.7	34.1	0	0.0	1.4
2008	190.2	100	1.044	15.3	422.3	17.4	0	0.0	0.8
2256	196.8	100	1.044	18.4	423.4	48.1	0	0.0	1.2
2511	203.6	100	1.044	21.2	418.5	54.4	0	0.0	1.8
3006	199.2	100	1.044	20.2	444.3	115.8	0	0.0	2.8
3543	180.1	100	1.044	21.9	475.6	116.2	0	0.0	2.4
4031	171.0	100	1.043	15.9	479.9	227.0	0	0.0	3.4

SPECIFIC EXHAUST EMISSIONS

AVG SPEED (RPM)	CORR TORQUE (Nm)	SPEC. POWER (kW/l)	SPEC. HC (g/kWh)	SPEC. NOx (g/kWh)	SPEC. PARTIC (g/kWh)
1253	132.8	9.9	0.5	7.0	2.3
1511	160.2	14.5	0.4	8.0	1.2
1755	175.3	18.4	0.4	9.4	1.1
2008	190.2	22.8	0.4	10.6	0.4
2256	196.8	26.5	0.4	9.1	1.0
2511	203.6	30.5	0.4	7.8	1.0
3006	199.2	35.8	0.3	7.1	1.8
3543	180.1	38.1	0.3	7.1	1.7
4031	171.0	41.2	0.2	6.6	3.1

Table 7.3: continued,

TURBOCHARGER PARAMETERS

AVG SPEED (RPM)	CORR TORQUE (Nm)	INTRCLR EFF RAT. (%)	TURBO SPEED (x1000RPM)	VGT VANE POSITION (%shut)
1253	132.8	55	82.2	73
1511	160.2	79	111.3	72
1755	175.3	83	130.3	70
2008	190.2	85	154.1	73
2256	196.8	83	156.2	50
2511	203.6	82	158.7	40
3006	199.2	79	168.9	12
3543	180.1	78	178.1	5
4031	171.0	79	187.4	-5

TURBOCHARGER PERFORMANCE

AVG SPEED (RPM)	CORR TORQUE (Nm)	COMP POWER (kW)	COMP EFFY (%)	COMP P.R.	T/CHGR P.R.	TURB POWER (kW)	TURB EFFY (%)	TURB P.R.
1253	132.8	0.7	71	1.28	1.11	4.5	250	1.41
1511	160.2	1.7	70	1.53	1.15	6.6	157	1.73
1755	175.3	3.0	69	1.75	1.17	8.2	124	1.97
2008	190.2	5.7	69	2.06	1.29	11.5	98	2.50
2256	196.8	6.5	68	2.07	1.09	12.9	116	2.08
2511	203.6	7.2	69	2.08	1.01	14.6	127	1.90
3006	199.2	8.7	70	2.11	1.02	17.1	119	1.87
3543	180.1	10.6	67	2.15	1.11	18.9	105	1.99
4031	171.0	12.5	63	2.15	1.21	23.1	102	2.07

EGR PARAMETERS

AVG SPEED (RPM)	CORR TORQUE (Nm)	VALVE POSITION (%open)	PRE COOLER (DegC)	POST COOLER (DegC)
1253	132.8	0	276	110
1511	160.2	0	307	125
1755	175.3	0	306	132
2008	190.2	0	301	138
2256	196.8	0	310	152
2511	203.6	0	345	162
3006	199.2	0	384	172
3543	180.1	0	365	172
4031	171.0	0	378	184

EUI PARAMETERS

AVG SPEED (RPM)	CORR TORQUE (Nm)	FUEL FILTER (kPa)	FUEL INLET (kPa)	EXHAUST PORT 1 (DegC)	EXHAUST PORT 2 (DegC)	EXHAUST PORT 3 (DegC)	EXHAUST PORT 4 (DegC)
1253	132.8	230	219	502	515	499	510
1511	160.2	229	218	532	558	538	546
1755	175.3	225	213	527	556	533	544
2008	190.2	220	208	518	540	521	530
2256	196.8	226	214	518	548	529	535
2511	203.6	221	209	555	589	571	575
3006	199.2	235	223	615	653	634	637
3543	180.1	229	217	623	662	641	647
4031	171.0	229	217	687	725	711	717

Table 7.3: continued,

MISC. ENGINE PARAMETERS

AVG SPEED (RPM)	CORR TORQUE (Nm)	OIL CYL HD. (kPa)	FORD AIRFLOW (volts)	COOLANT FLOW (kg/min)	FUEL DENSITY (kg/m3)
1253	132.8	177	0.000	2.98	838
1511	160.2	216	0.000	3.12	838
1755	175.3	249	0.000	3.27	838
2008	190.2	282	0.000	3.40	838
2256	196.8	309	0.000	3.48	838
2511	203.6	323	0.000	3.48	838
3006	199.2	345	0.000	3.48	837
3543	180.1	349	0.000	3.48	837
4031	171.0	351	0.000	3.48	837

The heat release data obtained with the aid of the AVL data acquisition system and Concerto software are represented in figures 7.7 to 7.15 for each of the speeds in table 7.3 by the following traces:

1. Cylinder pressure (bar)
2. Apparent rate of heat release, AROHR ($kJ/m^3°CA$)
3. Cumulative apparent heat release (kJ/m^3)
4. Rail pressure (bar)
5. Electrical output of injector needle actuator

The data were obtained at a relatively early stage of the commissioning process of the equipment. Consequently the accuracy both of the AROHR and apparent cumulative heat release traces is somewhat variable.

Since a needle lift transducer was not available, start of injection (SoI) had to be interred from the instant where the raise pressure trace shows its first sharp reduction (subsequent rail pressure variations due to wave action in the system).

Following discussions with Lucas CAV, the pressure at the needle was taken as measured mean rail pressure minus 100 bar.

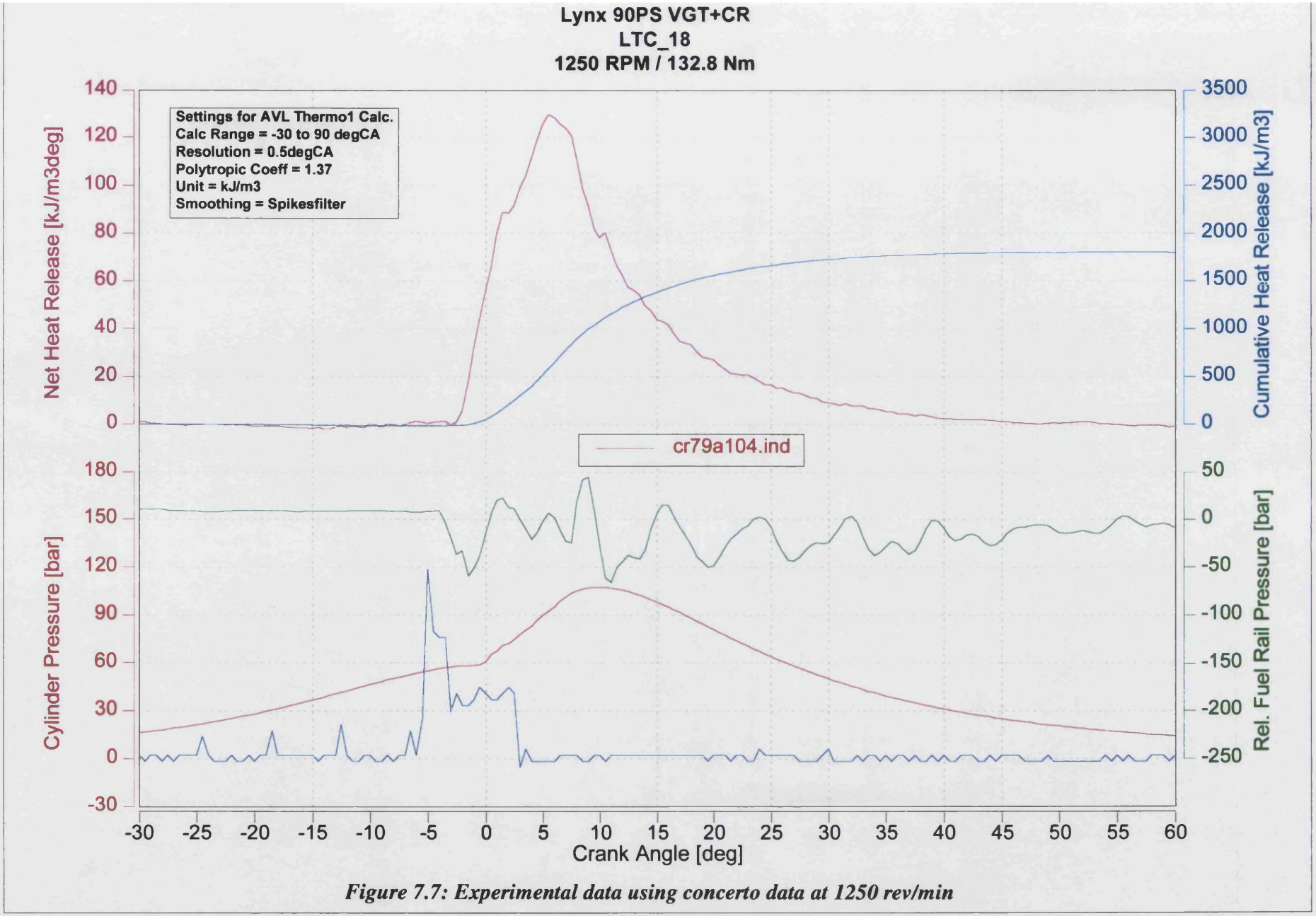

Figure 7.7: Experimental data using concerto data at 1250 rev/min

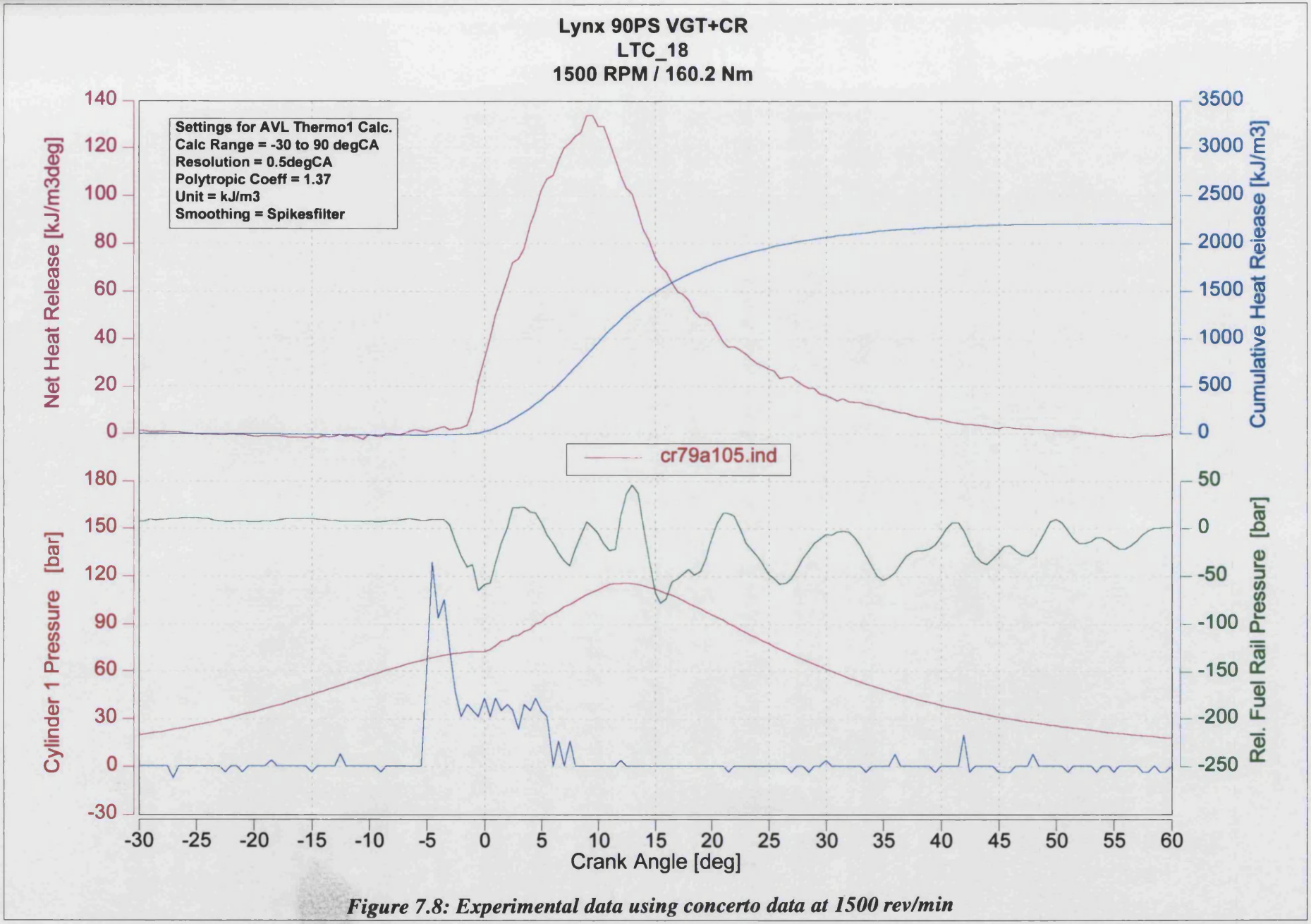

Figure 7.8: Experimental data using concerto data at 1500 rev/min

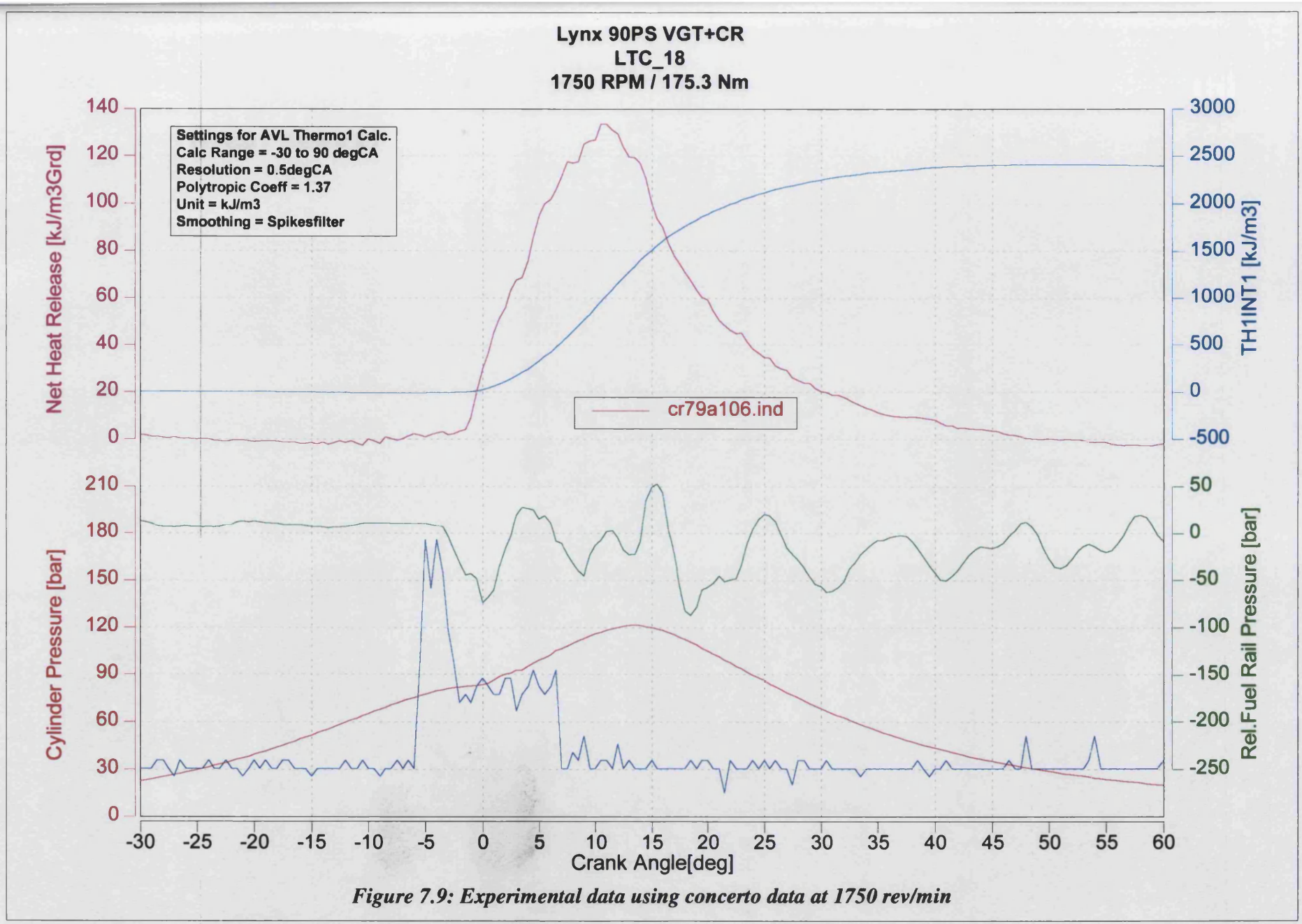

Figure 7.9: Experimental data using concerto data at 1750 rev/min

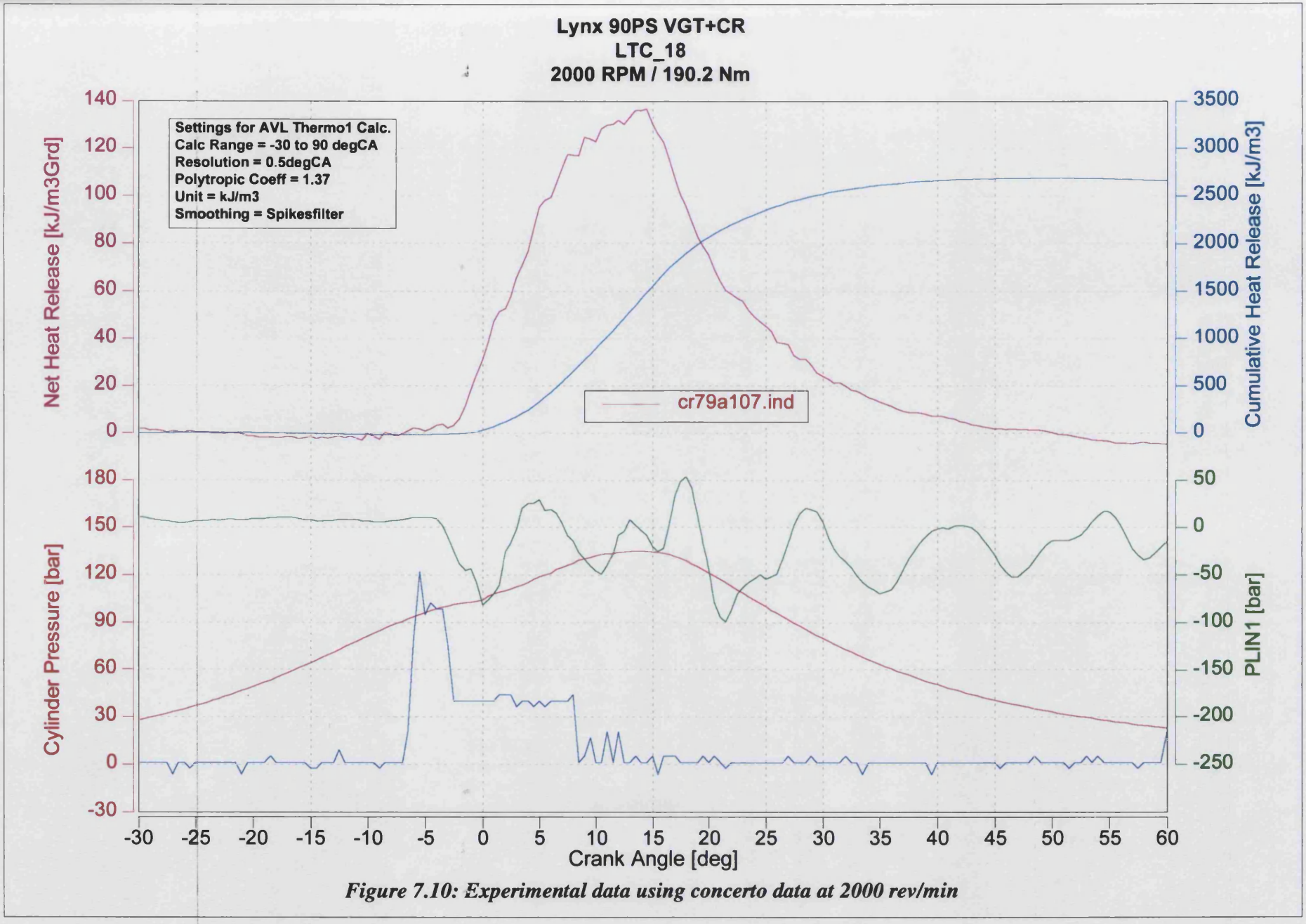

Figure 7.10: Experimental data using concerto data at 2000 rev/min

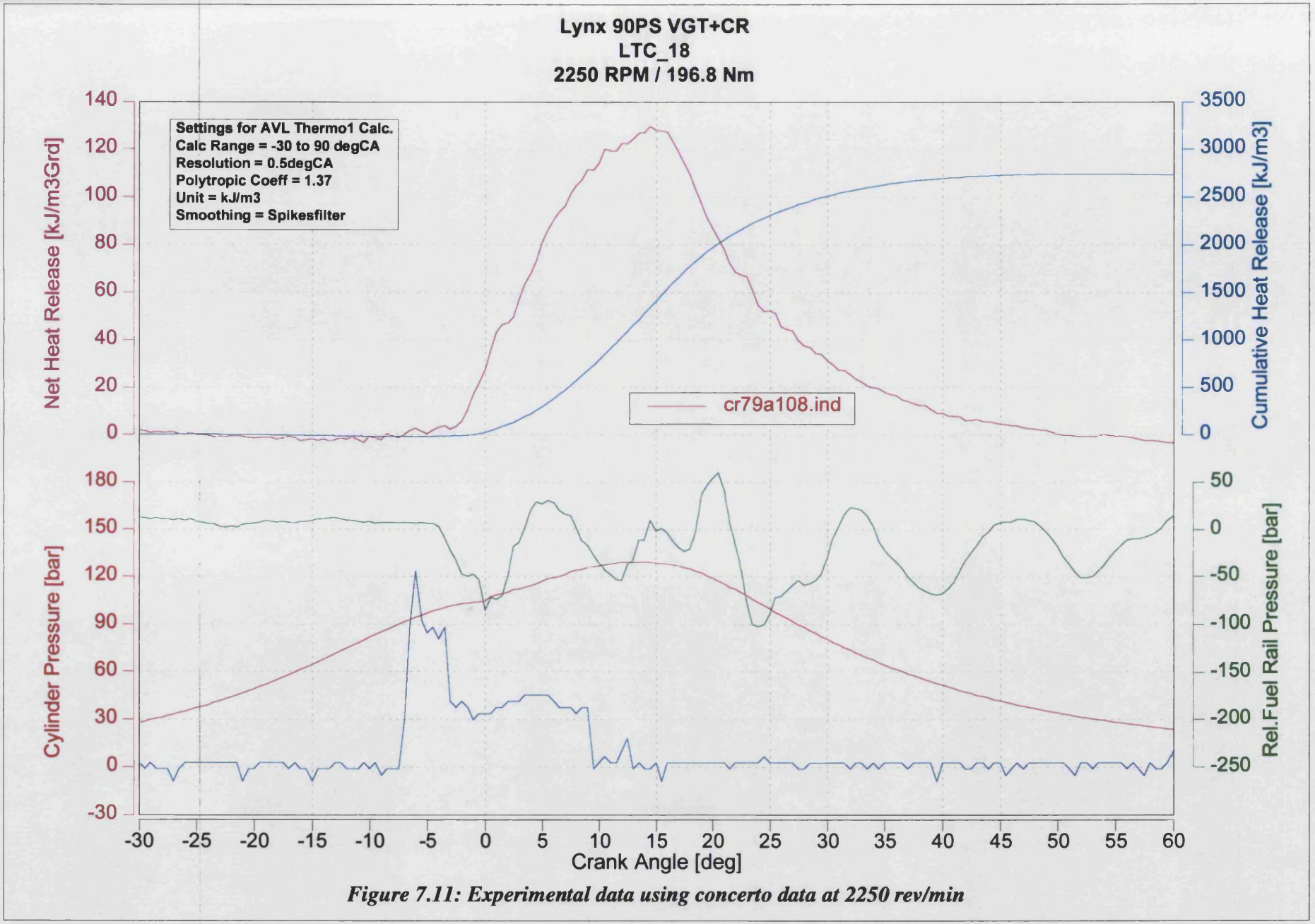

Figure 7.11: Experimental data using concerto data at 2250 rev/min

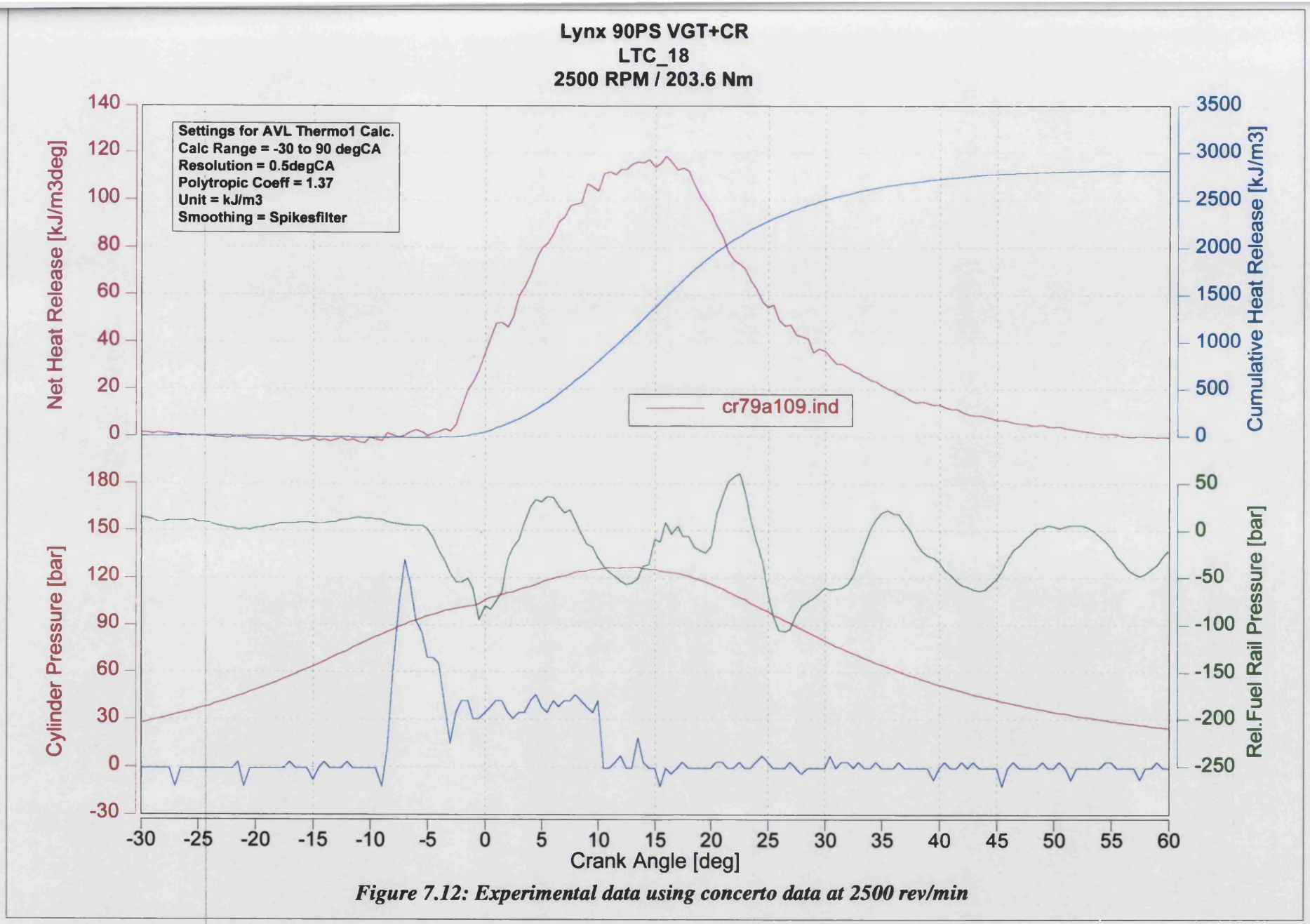

Figure 7.12: Experimental data using concerto data at 2500 rev/min

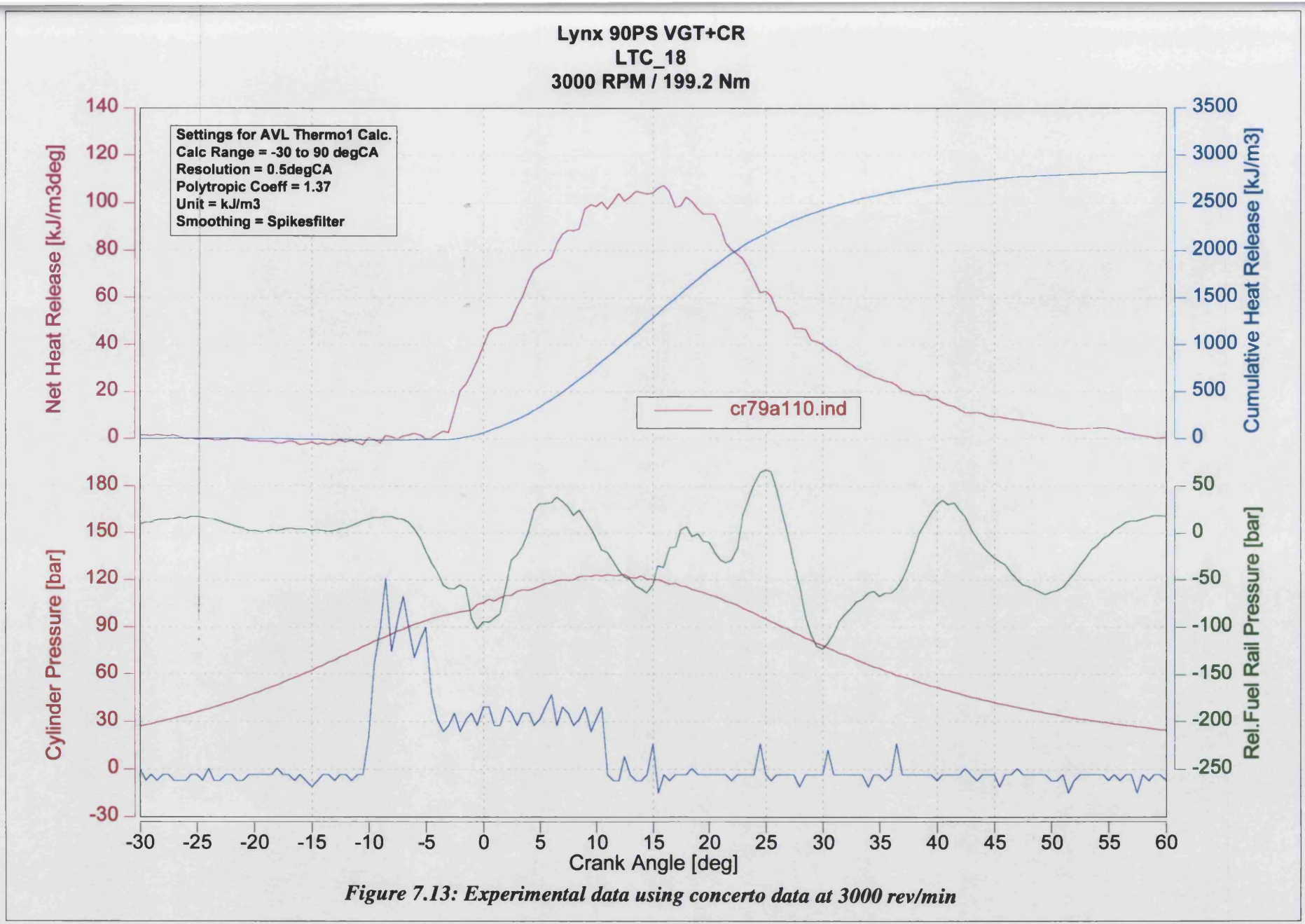

Figure 7.13: Experimental data using concerto data at 3000 rev/min

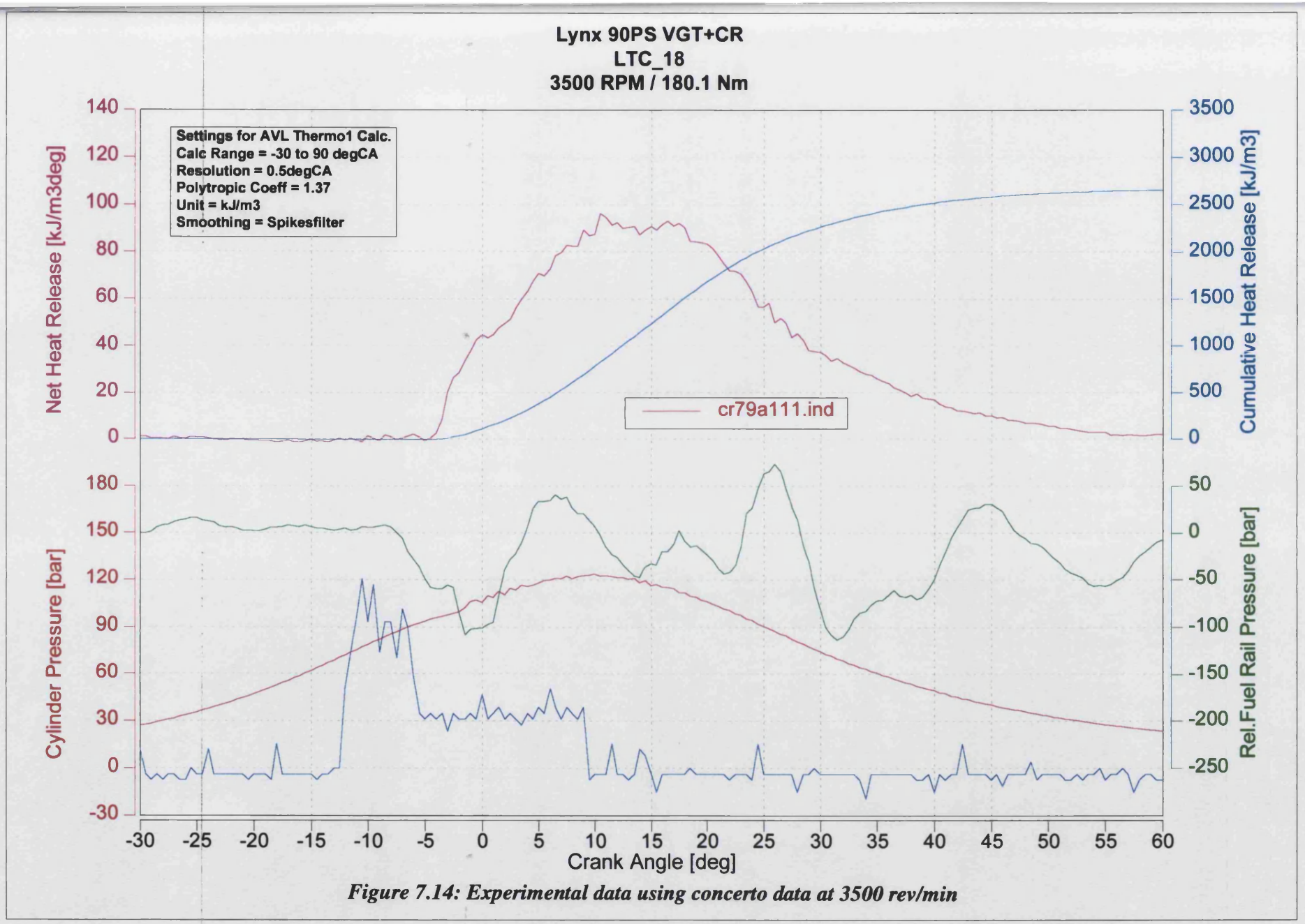

Figure 7.14: Experimental data using concerto data at 3500 rev/min

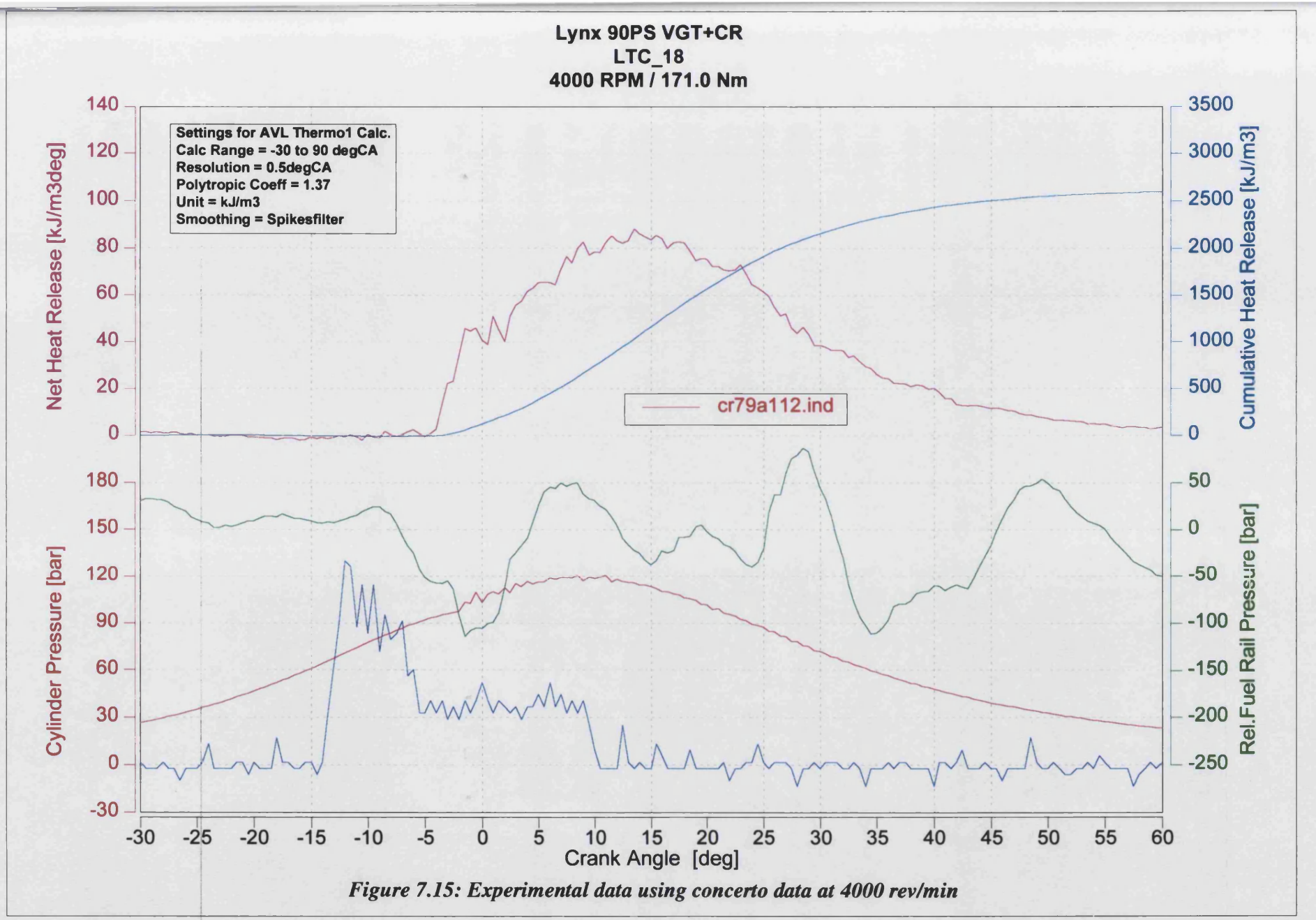

Figure 7.15: Experimental data using concerto data at 4000 rev/min

7.3.2 Calibration against formulation without ignition delay (see section 6.3.2)

The results of this calibration are summarised in tables 7.4a, b and c, and in figures 7.16a, b and 7.17a, b, which refer to cylinder pressure, heat release and cumulative heat release.

Table 7.4a summarises basic running data together with experimental and computed results for engine performance. It will be noted from table 7.4a that the inlet manifold pressure for computational purpose differed slightly from the measured experimental mean value. This was done in order to achieve the best possible correlation with measured cylinder pressure during compression from the computed trapped condition, using the existing ODES as mentioned in chapter 6, section 6.1. Furthermore it was found necessary for the same reason to reduce the geometric compression ratio from the manufacturer's value of 19.5 (table 7.2) to 18.2 to allow for some inferred piston blowby.

Table 7.4b summarises the key heat release data together with α_{h2} and α_{k2} and the derived parameters WH, WK, C_{rate} and C_{mod} (see equations 6.20, 6.26, 6.32 and 6.36). The value of the heat release fraction at the end of injection α_{h2} (equation 6.20) is based on the apparent cumulative heat release at the end of injection (EOI), relative to its final value at 90 °CA after top dead centre (TDC).

Table 7.4c compares the resultant computed heat release parameters with experimental results from figures 7.7 to 7.15.

Figures 7.16a, b and 7.17a, b will now be discussed in turn.

Figure 7.16a and b (2000 rev/min)

The cylinder pressure records, figure 7.16a, show reasonable agreement during compression, but significant differences in the location and the value of peak pressure and the subsequent expansion process, due largely to neglect of ignition delay.

Figure 7.16b gives computed net rate of heat release (ROHR) and the "experimental" net ROHR obtained from the Concerto software. Clearly, neglect of ignition delay is reflected in a corresponding shift in the computed net ROHR up to peak value, which persists during expansion, in figure 7.16b.

Figure 7.16b also gives injected fuel energy as well as computed and experimental net heat release. In the latter case the computed values are initially significantly higher than experimental ones, due to some underestimate of heat transfer to coolant, from the combustion chamber (The *Woschni* [2] heat transfer correlation is used in the program.), and neglect of ignition delay.

Figure 7.17a and b (3000 rev/min)

Figure 7.17a, shows the same substantial effect of neglect of ignition delay on the location of peak pressure and the subsequent expansion process.

Figure 7.17b again shows that the computed values of ROHR initially are significantly higher than experimental ones, due again to the neglect of ignition delay.

The computed cumulative net heat release in figure 7.17b shows again initially significantly higher values than experimental ones.

Overview of results in section 7.3.2

It is obvious that neglect of ignition delay introduces substantial errors, especially in the phasing of cylinder pressure and of ROHR.

These differences are summarised in table 7.4c, which can be explained as follows:

Comparison of computed and experimental cylinder pressure result shows:

- Good agreement during the compression process.
- Reasonable agreement in the location of the peak pressure, which deteriorates with increasing speed due to larger ignition delay in crank angle terms.
- The significant differences in the value of peak pressure and the subsequent expansion process.

Comparison of computed and experimental net ROHR shows:

- There is generally good agreement in the case of maximum net ROHR.
- Due to neglect of ignition delay there is a corresponding shift in the computed net and gross ROHR up to peak value, which persists during expansion.

Comparison of computed and experimental net cumulative heat release shows:

- The growing phase shift in the computed net ROHR is also reflected in the computed cumulative gross and net heat release compared with the values derived from the Concerto software. The result shows that the computed values are initially significantly higher than experimental ones, due to some underestimate of heat transfer to coolant, from the combustion chamber.

Table 7.4a: Summary of basic running data together with experimental and computed results for engine performance using formulation without ignition delay

Initial conditions:

Compression ratio: 18.2:1
Inlet manifold volume: 0.005 m^3
Nozzle hole diameter: 0.15 mm
Number of nozzle holes: 5
Max. cumulative heat release = 0.95 * Total injected fuel energy

N_e	Fuel Inj.	p_{rail}	p_{cyl} At	D_{inj}	v_N	m_f	Torque (N.m)		b.s.f.c (kg/kW-hr)		In.Man.Pr. (bar)	
(rev/min)	(mm^3/sht)	(bar)	Sol (bar)	(°CA)	(m/s)	(kg/s)	Exp.	Comp.	Exp.	Comp.	Exp.	Comp.
1250	34.1	540	56.29	11	341.40	4.01E-03	132.8	130.45	0.246	0.2483	127	118
1500	37.7	605	70.12	13	359.00	4.21E-03	160.2	154.44	0.226	0.2320	152	143
1750	39.5	679	79.68	16	380.02	4.46E-03	175.3	167.00	0.216	0.2248	171	161
2000	42.4	750	99.22	19	396.00	4.66E-03	190.2	183.85	0.214	0.2192	198	198
2250	43.3	800	99.06	20	410.98	4.82E-03	196.8	192.99	0.211	0.2135	197	197
2500	45.1	855	97.86	23	427.13	5.01E-03	203.6	202.03	0.213	0.2120	197	197
3000	46.3	1030	91.49	27	475.55	5.58E-03	199.2	199.93	0.223	0.2199	196	188
3500	42.8	1110	91.24	29	495.46	5.81E-03	180.1	181.16	0.228	0.2242	196	192
4000	44.2	1255	86.44	32	530.64	6.23E-03	171.0	178.85	0.248	0.2345	192	187

Table 7.4b: Summary of the key HR data together with α_{h2} and α_{k2} and the derived parameters WH, WK, C_{rate} and C_{mod}

N_e (rev/min)	SoI °BTDC	SoHR °BTDC	D_{ignd} °CA	α_{h2} based on: F1 func.	α_{h2} based on: Cmod*F1*F2	α_{k2}	δ	WH	WK	C_{rate}	C_{mod}
1250	-4	-4	0	0.343	0.383	0.7	0.04	0.0826	0.06922	0.069179	0.0844
1500	-3	-3	0	0.392	0.439	0.7	0.04	0.0841	0.05857	0.074798	0.0901
1750	-3	-3	0	0.488	0.534	0.7	0.04	0.0957	0.04759	0.082748	0.0899
2000	-3	-3	0	0.566	0.610	0.7	0.04	0.1047	0.03925	0.09093	0.0897
2250	-3	-3	0	0.510	0.569	0.7	0.04	0.0824	0.03807	0.092298	0.0856
2500	-4	-4	0	0.549	0.610	0.7	0.04	0.0817	0.03311	0.099137	0.0814
3000	-4	-4	0	0.565	0.635	0.7	0.04	0.0734	0.0282	0.107705	0.0744
3500	-6	-6	0	0.636	0.690	0.7	0.04	0.0871	0.02626	0.112124	0.0656
4000	-7	-7	0	0.638	0.700	0.7	0.04	0.0796	0.02379	0.118424	0.0624

Table 7.4c: Comparison of the computed and experimental results of heat release

N_e	Loc.of Max.ROHR		Max.Net-ROHR(kJ/m^3deg)		Net Cum.HR (kJ) At 60 ATDC		Loc.of Max.Press.		Max. Press. (bar)		Avg. NOx (ppm)	
(rev/min)	Exp.	Comp.	Exp.	Comp.	Exp.	Comp.	Exp.	Comp.	Exp.	Comp.	Exp.	Comp.
1250	6.0	7	129.83	123.44	0.833	0.850	10.0	10	107.10	100.7	967	1676
1500	9.5	10	133.89	135.42	1.021	1.010	12.5	11	115.77	110.7	1143	1364
1750	11.0	11	133.57	130.21	1.105	1.100	13.5	12	121.50	117.3	1303	1180
2000	14.5	11	136.70	129.13	1.233	1.214	13.5	11	135.23	133.1	1346	1013
2250	14.5	13	129.53	120.43	1.267	1.271	14.0	11	129.15	126.5	1148	917
2500	16.0	13	118.56	113.66	1.304	1.333	13.0	10	126.89	128.2	1031	968
3000	16.5	13	104.91	102.51	1.310	1.387	11.0	9	123.32	122.2	915	957
3500	10.5	11	96.33	94.59	1.230	1.290	11.0	8	123.70	126.2	857	854
4000	13.5	12	88.29	89.90	1.205	1.342	8.5	8	120.78	124.4	783	896

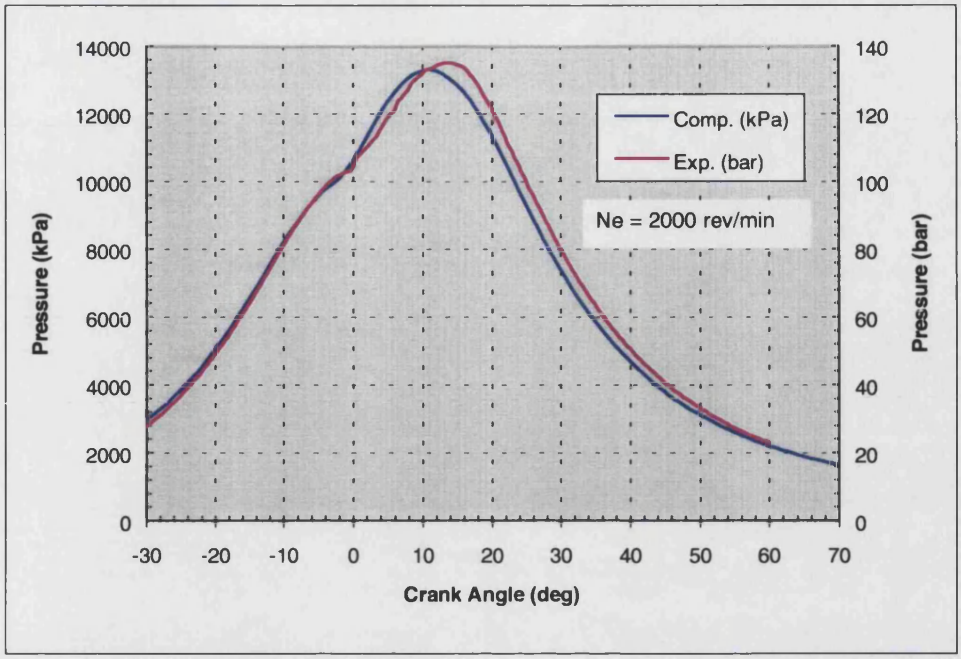

Figure 7.16 (a): Cylinder pressure vs. crank angle degree (2000 rev/min)

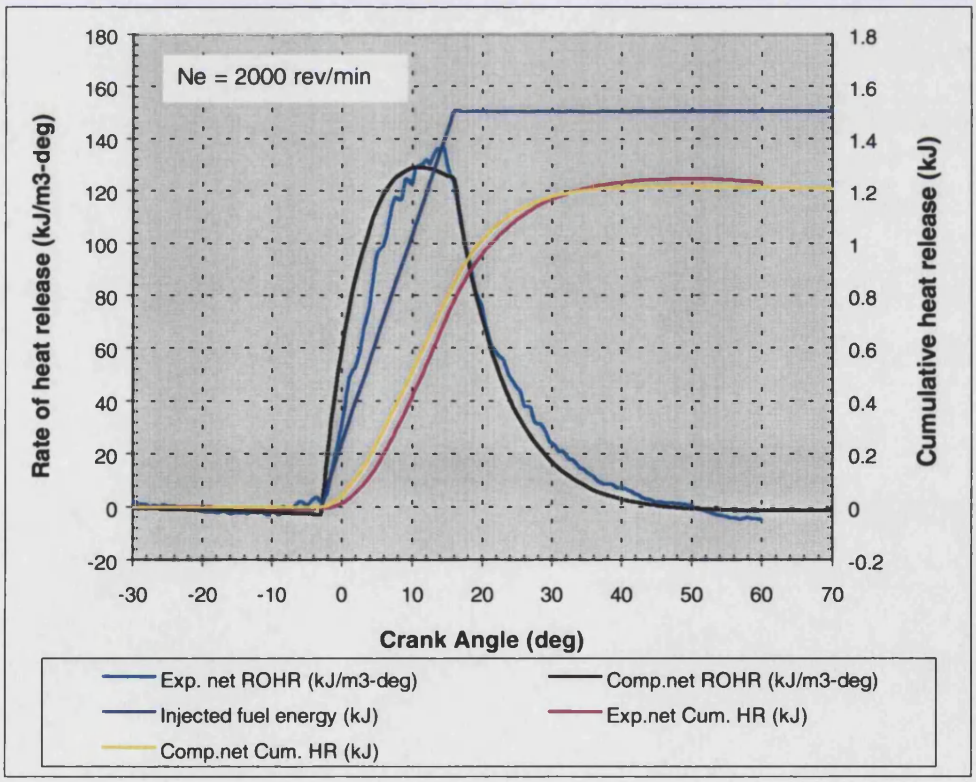

Figure 7.16 (b): ROHR and cumulative HR vs. crank angle degree (2000 rev/min)

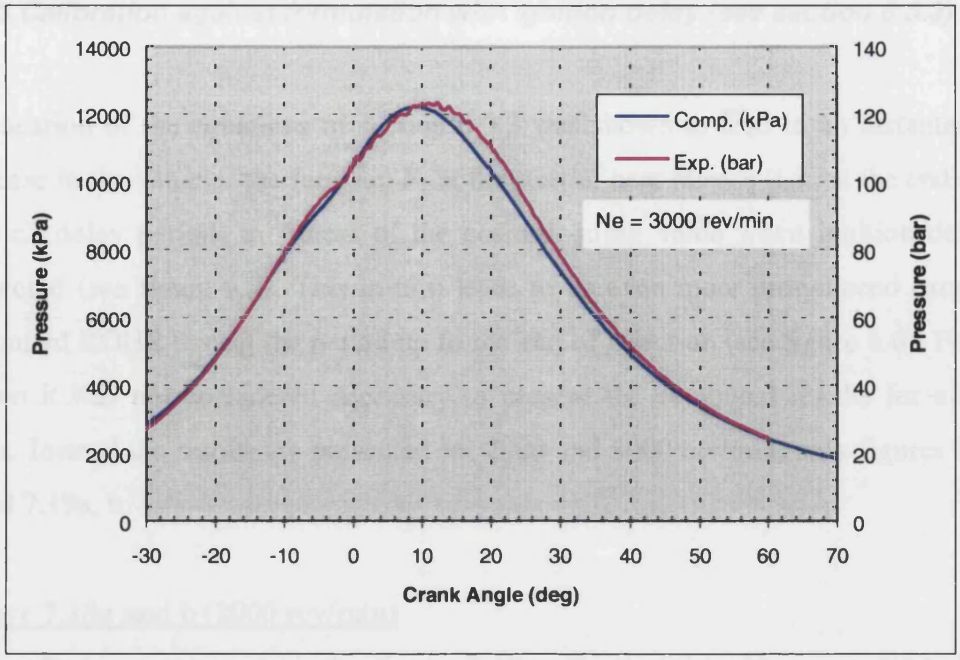

Figure 7.17 (a): Cylinder pressure vs. crank angle degree (3000 rev/min)

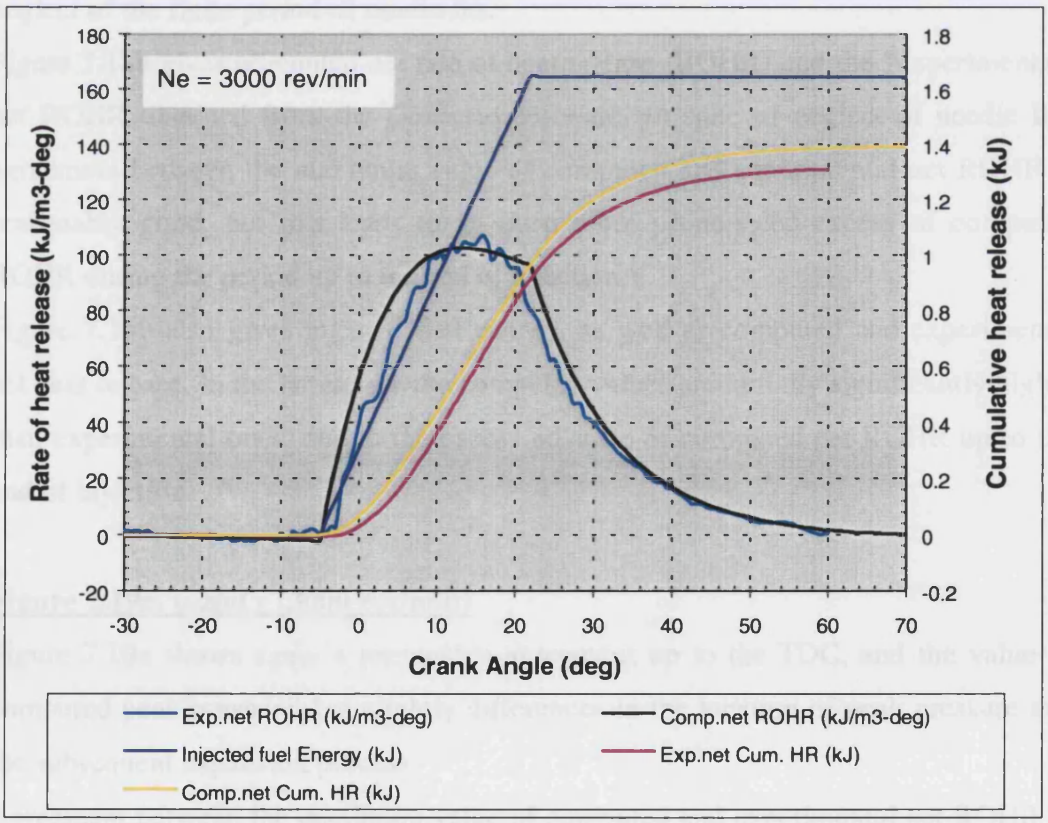

Figure 7.17 (b): ROHR and cumulative HR vs. crank angle degree (3000 rev/min)

7.3.3 Calibration against formulation with ignition delay (see section 6.3.3)

Application of the equations of section 6.3.3 was shown to lead to an instantaneous increase in the value of the function F_1 at the start of heat release (i.e., at the end of the ignition delay period) in excess of the corresponding value when ignition delay is neglected (see figure 6.4). This in turn leads to an even more pronounced excess of computed ROHR during the period up to the end of injection (see figure 6.6). For this reason it was not considered necessary to present the computed results for all nine cases. Instead the results are presented for 2000 and 3000 rev/min, only figures 7.18a, b and 7.19a, b.

Figure 7.18a and b (2000 rev/min)

The cylinder pressure records, figure 7.18a, show reasonable agreement during compression, but slight differences in the location and the value of peak pressure, as well as significant differences in the subsequent expansion process, due largely to neglect of the finite period of needle lift.

Figure 7.18b gives computed net rate of heat release (ROHR) and the "experimental" net ROHR obtained from the Concerto software. In spite of neglect of needle lift, agreement between the maximum value of computed and experimental net ROHR is reasonably good, but this leads to an even more pronounced excess of computed ROHR during the period up to the end of injection.

Figure 7.16b also gives injected fuel energy, as well as computed and experimental net heat release. In the latter case the computed values are initially significantly higher than experimental ones, due to the excess advance of computed net ROHR up to the end of injection.

Figure 7.19a, b and c (3000 rev/min)

Figure 7.19a shows again a reasonable agreement up to the TDC, and the value of computed peak pressure, but slightly differences in the location of peak pressure and the subsequent expansion process.

Agreement between the maximum value of computed and experimental net ROHR in figure 7.19b is reasonably good, but the results again shows an pronounced excess of the computed net ROHR during the period up to the end of injection.

The computed cumulative net heat release in figure 7.19b shows again initially significantly higher than experimental ones.

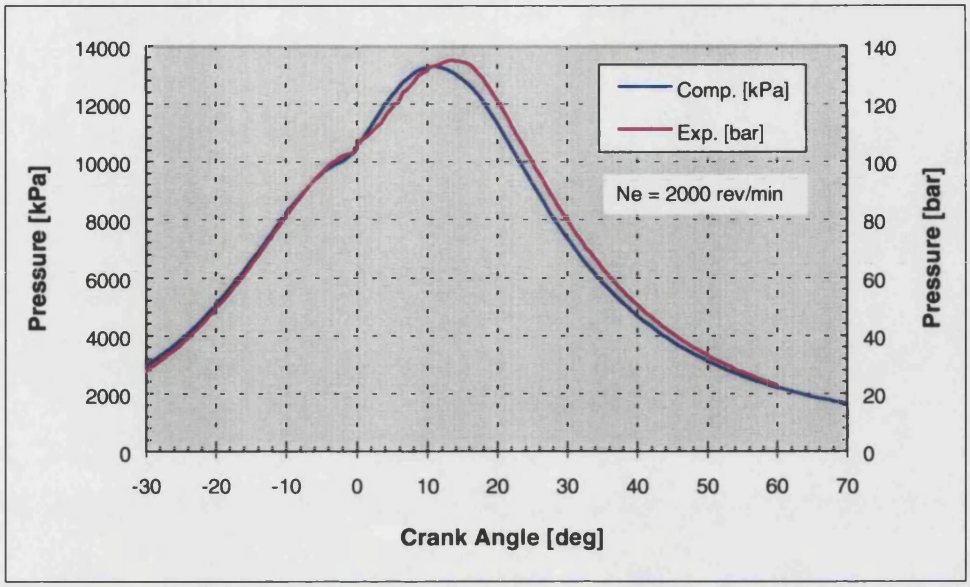

Figure 7.18 (a): Cylinder pressure vs. crank angle degree (2000 rev/min)

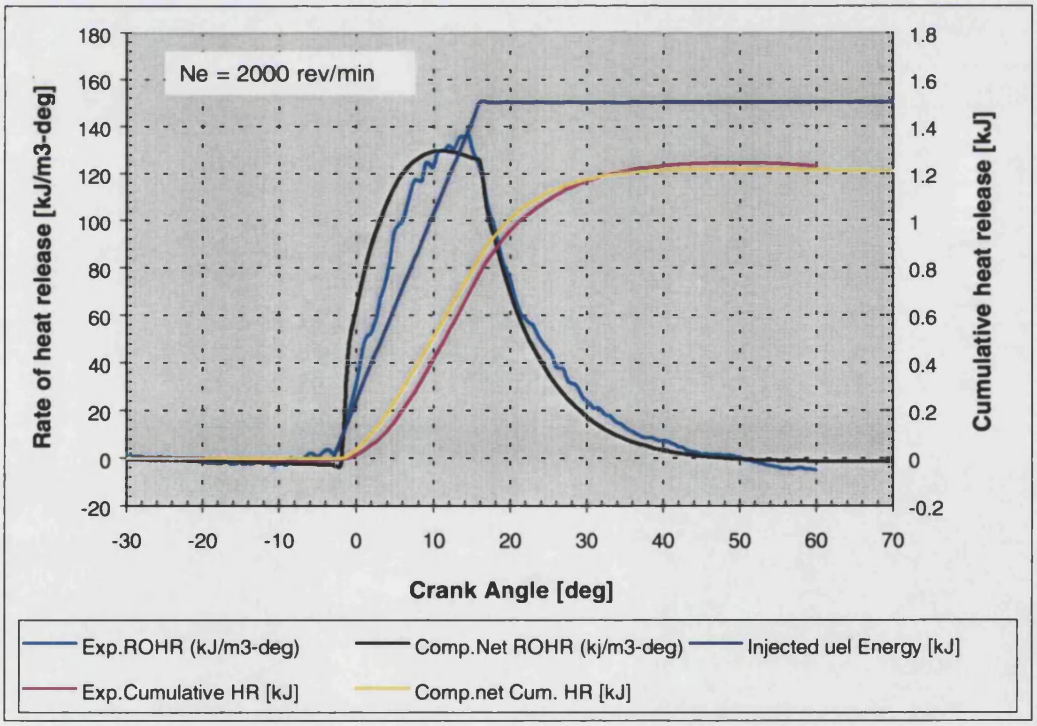

Figure 7.18 (b): ROHR and cumulative HR vs. crank angle degree (2000 rev/min)

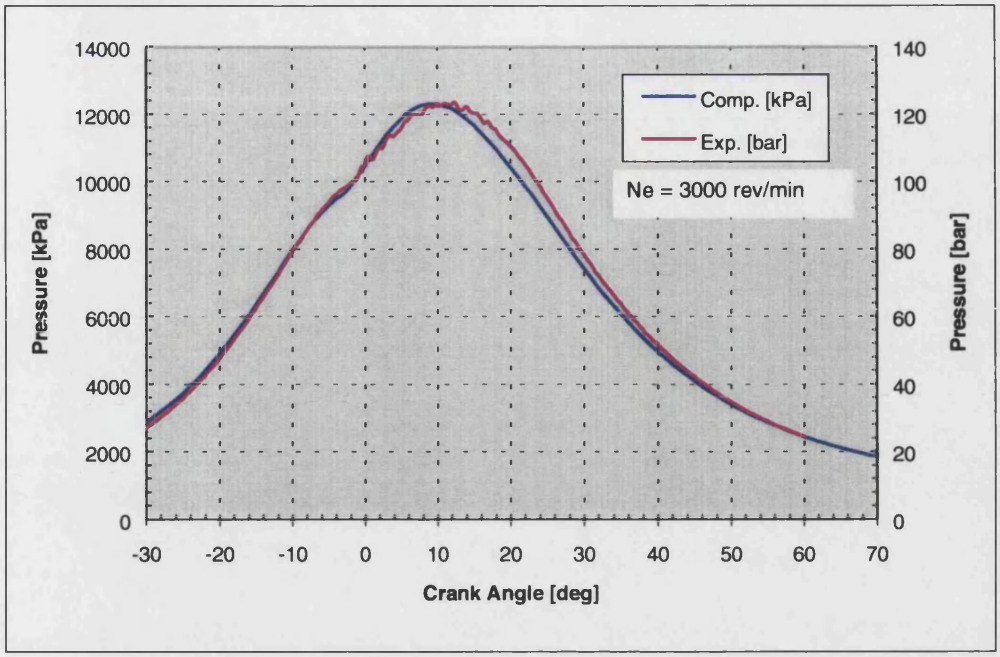

Figure 7.19 (a): Cylinder pressure vs. crank angle degree (3000 rev/min)

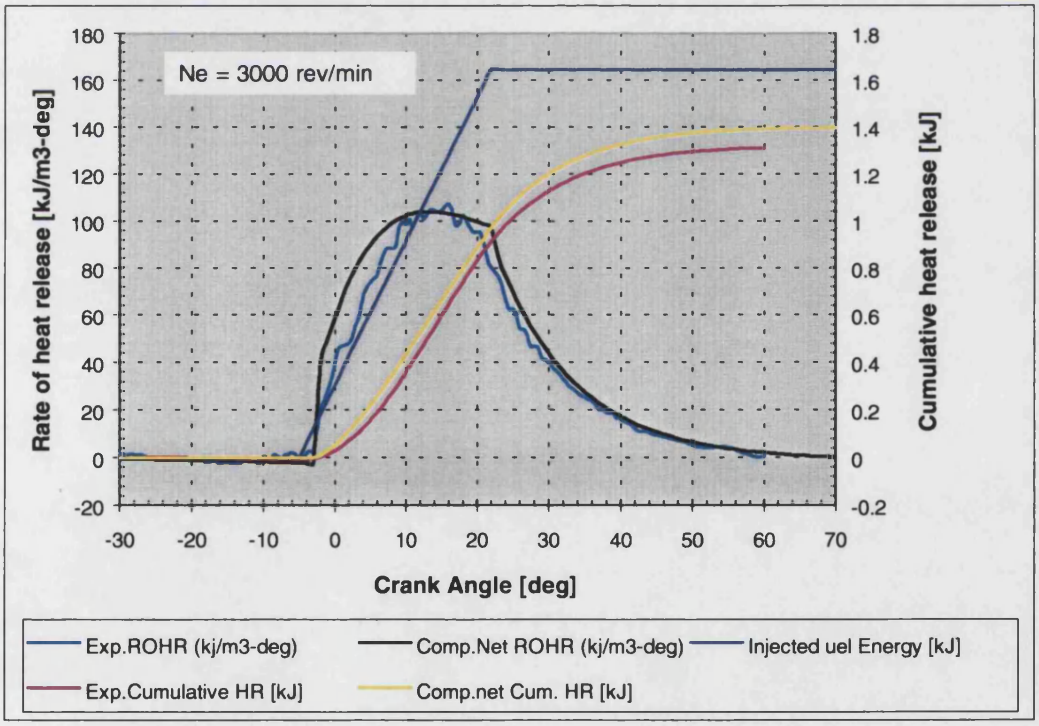

Figure 7.19 (b): ROHR and cumulative HR vs. crank angle degree (3000 rev/min)

7.3.4 Calibration against formulation with ignition delay and linear rate of needle lift during ignition delay period (see section 6.3.4, figure 6.2)

The assumption of a finite rate of needle lift during the initial phase of the injection process is intended to reproduce a real physical situation. Unfortunately the injectors used in the experimental programme did not incorporate a needle lift transducer, so that inevitably assumptions concerning both the duration of the initial needle lift period and the rate of increase of fuel flow had to be made. The simplest set of assumption was to equate the needle lift period to the ignition delay period and to assume a linear increase of the fuel flow rate.

The results of two separate calibrations are summarised in tables 7.5a, b, c and in figures 7.20a, b to 7.28a, b, and tables 7.6a, b, c and figures 7.29a, b to 7.37a, b.

Table and figures follow the same patterns as that adopted in section 7.3.2.

The difference between the two sets of results in section 7.3.4.1 and 7.3.4.2 is that in the first case the parameter α_{h2} was adjusted to gives the best possible agreement of the computed and experimental cylinder pressure traces while in the second case, values of α_{h2} based broadly on experimental results for cumulative heat release derived from the Concerto software, were used. This gave much better agreement of heat release data with experimental results, but inevitably led to significant differences between experimental and computed cylinder pressure traces in the lower speed range.

Both sets of results are based on the modified form of function F_2 described in section 6.3.4, equations 6.62, 6.63 and 6.64.

7.3.4.1 Optimisation with respect to cylinder pressure

Throughout these calculations best agreement between computed and experimental cylinder pressure was achieved by the deliberate choice of a higher value of α_{h2} than that based on the experimental cumulative net heat release.

Figure 7.20a and b (1250 rev/min)

Figure 7.20a, shows excellent agreement between the computed cylinder pressure and the experimental ones.

Figure 7.20b shows that the computed values of ROHR initially are significantly higher than experimental ones, due to the choice of a higher value of α_{h2} than experimental derived values to give the best possible agreement between computed and experimental cylinder pressure traces.
However, this leads to a deficit during the later part of heat release.
Figure 7.20b also shows that the computed values of net heat release are initially significantly higher than experimental ones, due possibly to some underestimate of heat transfer to coolant, from the combustion chamber, and adjusted of the higher value of α_{h2}.

Figure 7.21a, b and c (1500 rev/min)

Figure 7.21a, shows very good agreement between the computed cylinder pressure and the experimental ones.
In figure 7.21b computed net ROHR values are again in advance of experimental values up to the end of injection, and then falls below experimental values over the remainder of the heat release process.
The results for computed and experimental cumulative net heat release in figure 7.21b reflects the corresponding differences between computed and experimental ROHR in figure 7.21b already noted above.

Figure 7.22a and b (1750 rev/min)

Figure 7.22a again shows very good agreement of the cylinder pressure traces.
In figure 7.22b computed net ROHR is again substantially in advance of experimental ROHR up to the end of injection, and conversely again shows a deficit beyond that point.
Figure 7.22b shows very similar trend for cumulative net heat release to those observed earlier.

Figure 7.23a and b (2000 rev/min)

Figure 7.23a shows very good agreement for the two cylinder pressure traces, with a slight phase advance of the computed peak pressure.

Figure 7.23b again reflects the excess calculated net ROHR up to the end of injection, and the corresponding later deficit, resulting in the corresponding discrepancies between computed and experimental cumulative net heat release.

Figure 7.24a and b (2250 rev/min)

Figure 7.24 shows a phase advance of approximately 2°CA of the computed over the experimental peak cylinder pressure.

The discrepancies between computed and experimental ROHR in figure 3.24b are now less than those already noted for the four lower speeds, and this is reflected in the better agreement between computed and experimental net cumulative heat release.

Figure 7.25a and b (2500 rev/min)

Agreement between computed and experimental cylinder pressure traces in figure 7.25a is excellent. However, the discrepancies between computed and experimental ROHR, and also between computed and experimental net heat release in figure 7.25b are now somewhat greater than the previous results in figure 7.24b, for 2250 rev/min.

Figure 7.26a and b (3000 rev/min)

Figure 7.26a shows again an excellent agreement between computed and experimental cylinder pressure traces.

Agreement between the maximum value of computed and experimental net ROHR in figure 7.26b is reasonably good, but the results shows a slight excess of the computed net ROHR during the period up to the end of injection, and this is reflected in the discrepancies between computed and experimental net heat release.

Figure 7.27a and b (3500 rev/min)

Agreement between computed and experimental cylinder pressure traces in figure 7.27a is excellent. However, the discrepancies between computed and experimental ROHR, and also between computed and experimental net heat release in figure 7.27b are now somewhat greater than the previous results in figure 7.26b for 3000 rev/min.

Figure 7.28a and b (4000 rev/min)

Figure 7.28a shows again an excellent agreement between computed and experimental cylinder pressure traces.

In figure 7.28b computed net ROHR values are in advance of experimental values up to the end of injection, which persists during the initial part of expansion process and then falls below experimental values over the remainder of the heat release process.

The results for computed and experimental cumulative net heat release in figure 7.28b reflects the corresponding differences between computed and experimental ROHR already noted above.

Overview of results in section 7.3.4.1

Compared with the results of section 7.3.2, the incorporation both of ignition delay and a finite period of needle lift assumed to coincide with the ignition delay period (see figures 6.2 and 6.3) has led to a marked reduction in the previous overestimate of ROHR in the early phase of the heat release process. Unfortunately the adoption of a higher value of the heat release function α_{h2} in the function F_1, than that derived from experimental values in order to achieve the best possible agreement of the computed and experimental cylinder pressure traces, to some extent cancels the effect of inclusion of both ignition delay and finite initial rate of needle lift, already noted above.

The results of section 7.3.4.1 are summarised in table 7.5c, which can be explained as follows:

Comparison of computed and experimental cylinder pressure result shows:

- Excellent agreement between both results.

Comparison of computed and experimental net ROHR shows:

- Due to the higher values of α_{h2} than those used in section 7.3.2, peak values of computed net ROHR are now generally in excess of experimental values.
- Again due to the choice of higher values of α_{h2}, there is a consistent excess of computed net ROHR up to the end of injection, followed by a consistent deficit beyond end of injection.

Comparison of computed and experimental net cumulative heat release shows:

- The respective excess and deficit in computed net ROHR up to and beyond the end of injection noted above are reflected in the corresponding results for net cumulative heat release.

Table 7.5a: Summary of basic running data together with experimental and computed results for engine performance using formulation with ignition delay and linear needle lift based on the best pressure runs

Initial conditions:

Compression ratio: 18.2:1
Inlet manifold volume: 0.005 m^3
Nozzle hole diameter: 0.15 mm
Number of nozzle holes: 5
Max. cumulative heat release = 0.95 * Total injected fuel energy

N_e	Fuel Inj.	p_{rail}	p_{cyl} At	D_{inj}	v_N	m'_f	Torque (N.m)		b.s.f.c (kg/kW-hr)		In.Man.Pr. (bar)	
(rev/min)	(mm^3/sht)	(bar)	Sol (bar)	(°CA)	(m/s)	(kg/s)	Exp.	Comp.	Exp.	Comp.	Exp.	Comp.
1250	34.1	540	57.16	10	341.097	4.00E-03	132.8	129.27	0.246	0.2506	127	118
1500	37.7	605	70.17	13	358.991	4.21E-03	160.2	154.23	0.226	0.2323	152	143
1750	39.5	679	81.63	17	379.400	4.45E-03	175.3	169.29	0.216	0.2218	171	163
2000	42.4	750	101.40	19	395.334	4.64E-03	190.2	186.38	0.214	0.2162	198	200
2250	43.3	800	100.70	21	410.495	4.82E-03	196.8	195.20	0.211	0.2111	197	200
2500	45.1	855	99.92	23	426.552	5.01E-03	203.6	204.41	0.213	0.2095	197	198
3000	46.3	1030	93.04	27	475.156	5.58E-03	199.2	202.70	0.223	0.2169	196	191
3500	42.8	1110	91.23	29	495.466	5.81E-03	180.1	182.23	0.228	0.2229	196	192
4000	44.2	1255	86.44	32	530.642	6.23E-03	171.0	179.35	0.248	0.2338	192	187

Table 7.5b: Summary of the key HR data together with α_{h2} and α_{k2} and the derived parameters WH, WK, C_{rate} and C_{mod}

N_e (rev/min)	SoI °BTDC	SoHR °BTDC	D_{ignd} °CA	α_{h2} based on: F1 func.	Cmod*F1*F2	α_{k2}	δ	WH	WK	C_{rate}	C_{mod}
1250	-3	-1	2	0.3981	0.4221	0.7	0.62	0.1180	0.08155	0.06938	0.0987
1500	-3	-1	2	0.4411	0.4748	0.7	0.62	0.1091	0.06519	0.08043	0.0948
1750	-2	0	2	0.6395	0.6590	0.7	0.62	0.1602	0.04857	0.09135	0.0933
2000	-2	0	2	0.6564	0.6790	0.7	0.62	0.1512	0.04307	0.09621	0.0921
2250	-3	-1	2	0.5893	0.6300	0.7	0.62	0.1077	0.03869	0.10056	0.0842
2500	-3	0	3	0.6314	0.6676	0.7	0.62	0.1159	0.03623	0.10694	0.0835
3000	-5	-2	3	0.6126	0.6630	0.7	0.62	0.0915	0.03044	0.11462	0.0745
3500	-6	-2	4	0.6571	0.6990	0.7	0.62	0.1011	0.02889	0.11992	0.0658
4000	-7	-3	4	0.6529	0.7020	0.7	0.62	0.0896	0.02595	0.1253	0.0628

Table 7.5c: Comparison of the computed and experimental results of heat release

N_e	Loc.of Max.ROHR		Max.Net-ROHR(kJ/m^3deg)		Net Cum.HR (kJ) At 60 ATDC		Loc.of Max.Press.		Max. Press. (bar)		Avg. NOx (ppm)	
(rev/min)	Exp.	Comp.	Exp.	Comp.	Exp.	Comp.	Exp.	Comp.	Exp.	Comp.	Exp.	Comp.
1250	6.0	7	129.83	156.57	0.833	0.825	10.0	10	107.71	107.1	967	1870
1500	9.5	10	133.89	149.88	1.0206	0.993	12.5	12	115.77	115.5	1143	1465
1750	11.0	10	133.57	143.59	1.105	1.087	13.5	13	121.50	120.7	1303	1211
2000	14.5	10	136.70	140.85	1.233	1.213	13.5	12	135.23	134.4	1346	1010
2250	14.5	12	129.53	123.08	1.267	1.268	14.0	11	129.15	128.3	1148	934
2500	16.0	12	118.56	125.18	1.304	1.336	13.0	12	126.89	126.2	1031	928
3000	16.5	13	104.91	107.72	1.310	1.39	11.0	10	123.32	122.7	915	943
3500	10.5	12	96.33	99.00	1.230	1.296	11.0	10	123.70	122.0	857	780
4000	13.5	12	88.29	92.52	1.205	1.348	8.5	9	120.78	119.6	783	810

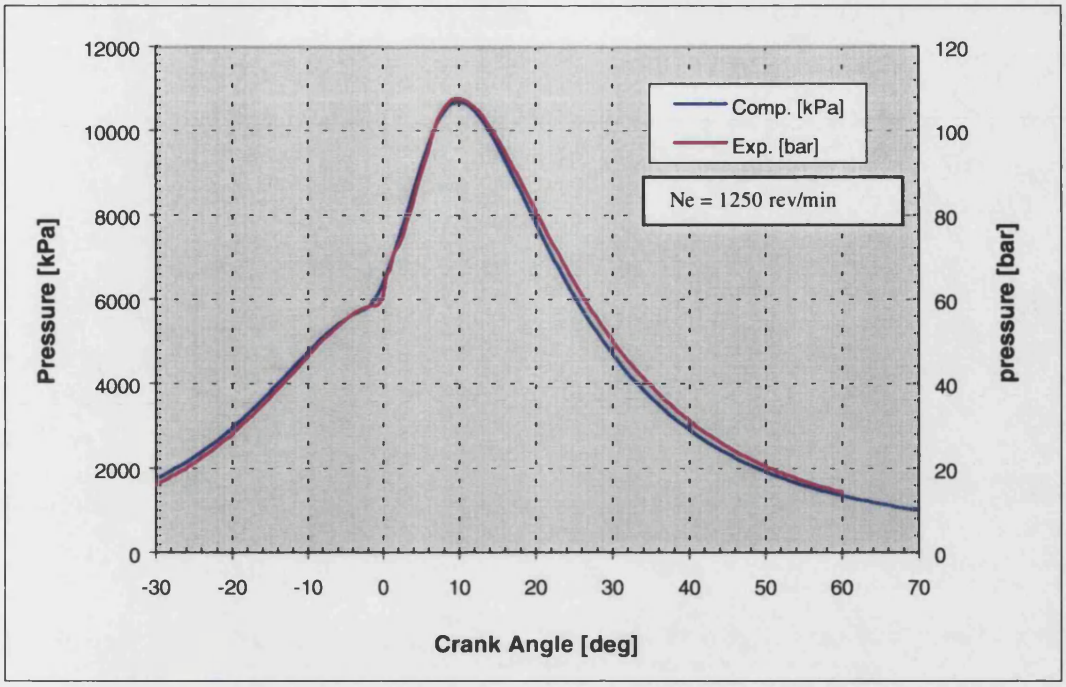

Figure 7.20 (a): Cylinder pressure vs. crank angle degree (1250 rev/min)

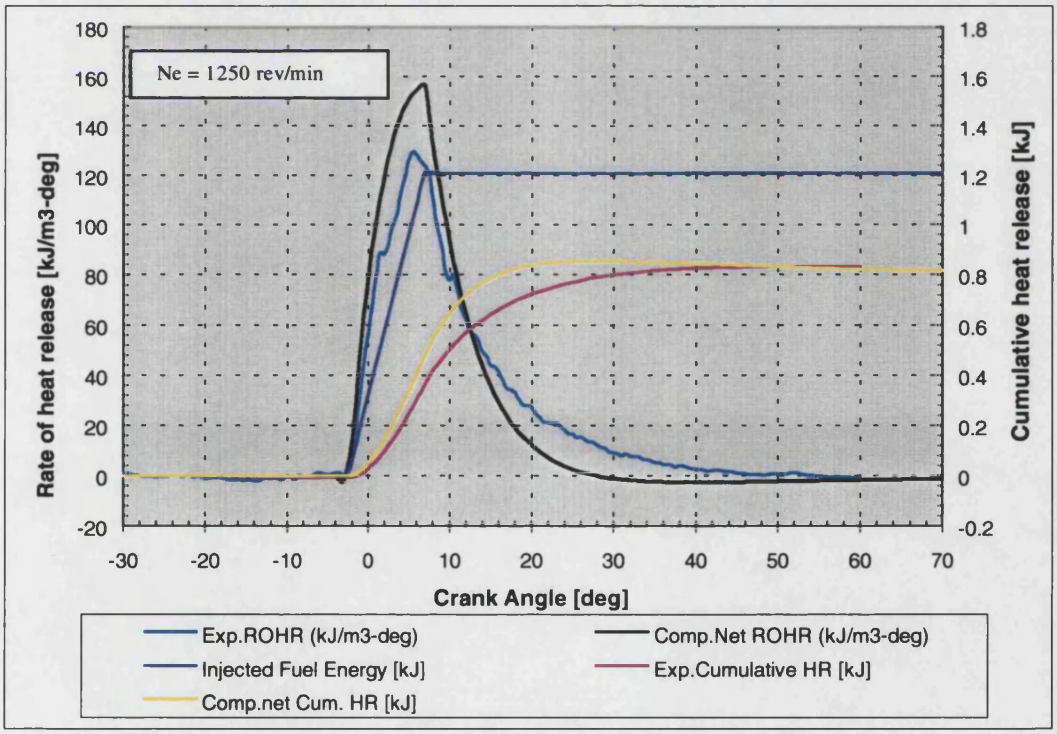

Figure 7.20 (b): ROHR and cumulative HR vs. crank angle degree (1250 rev/min)

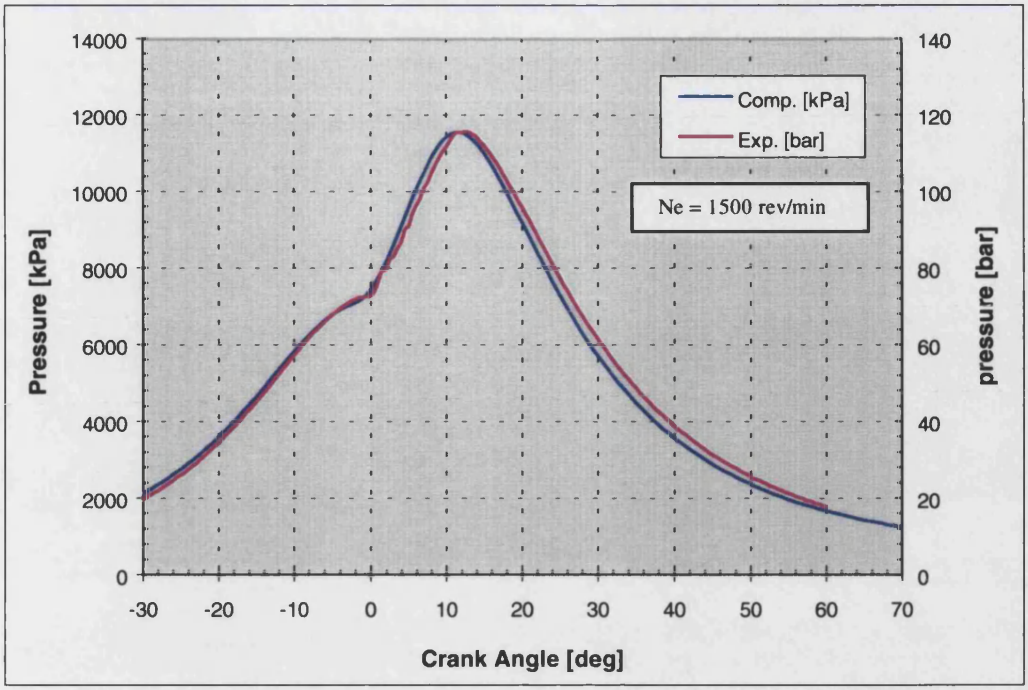

Figure 7.21 (a): Cylinder pressure vs. crank angle degree (1500 rev/min)

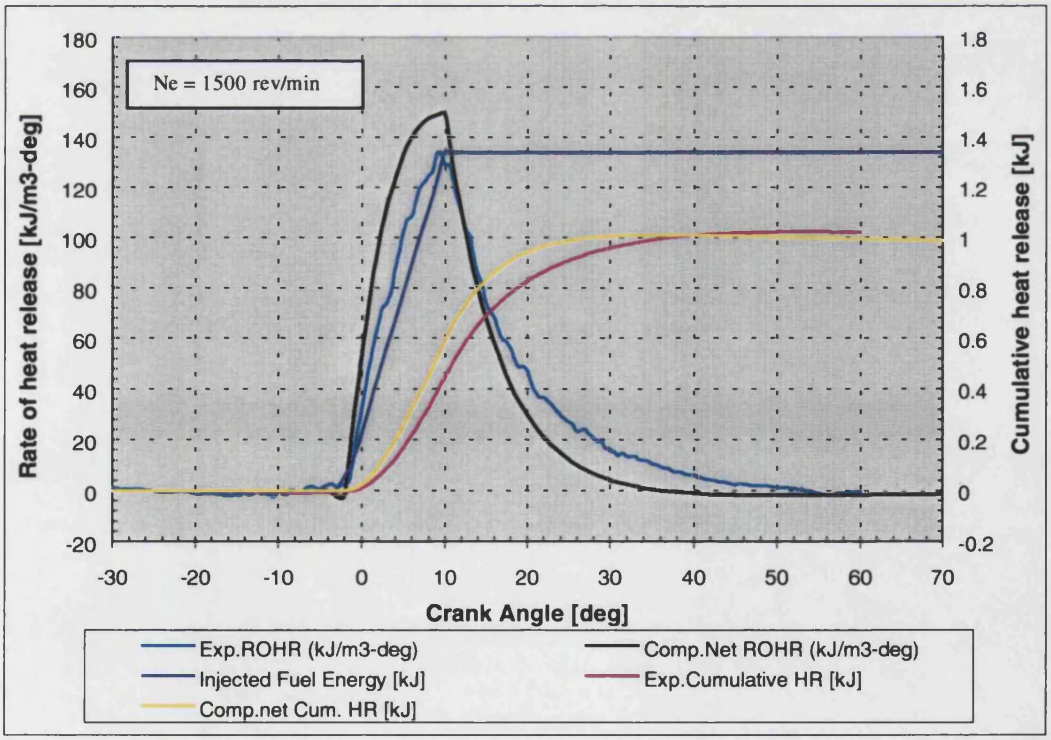

Figure 7.21 (b): ROHR and cumulative HR vs. crank angle degree (1500 rev/min)

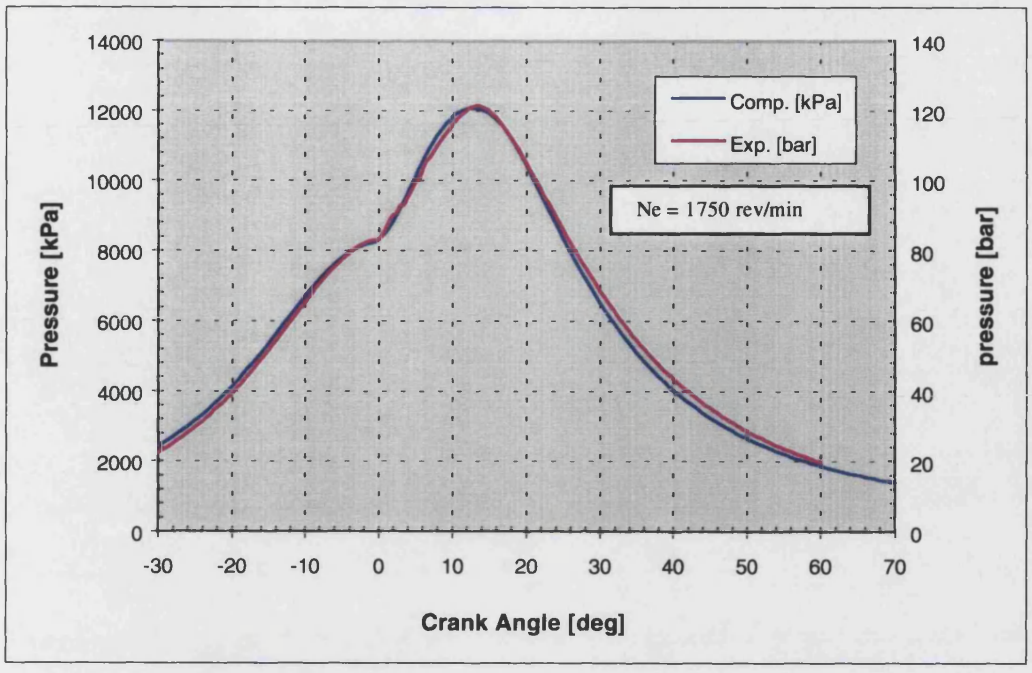

Figure 7.22 (a): Cylinder pressure vs. crank angle degree (1750 rev/min)

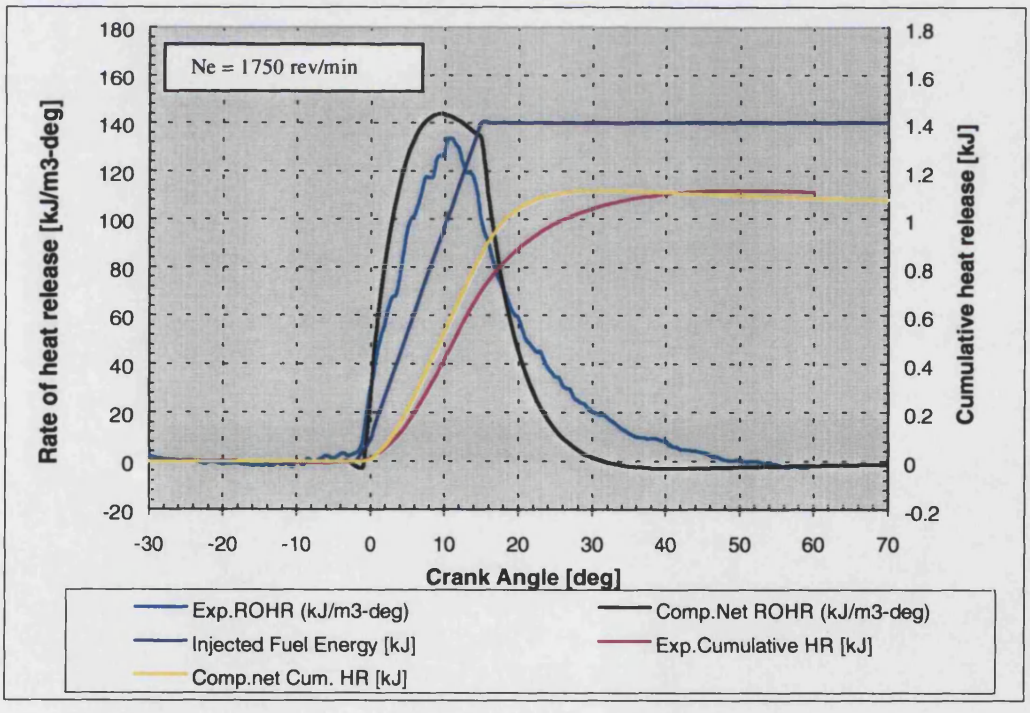

Figure 7.22 (b): ROHR and cumulative HR vs. crank angle degree (1750 rev/min)

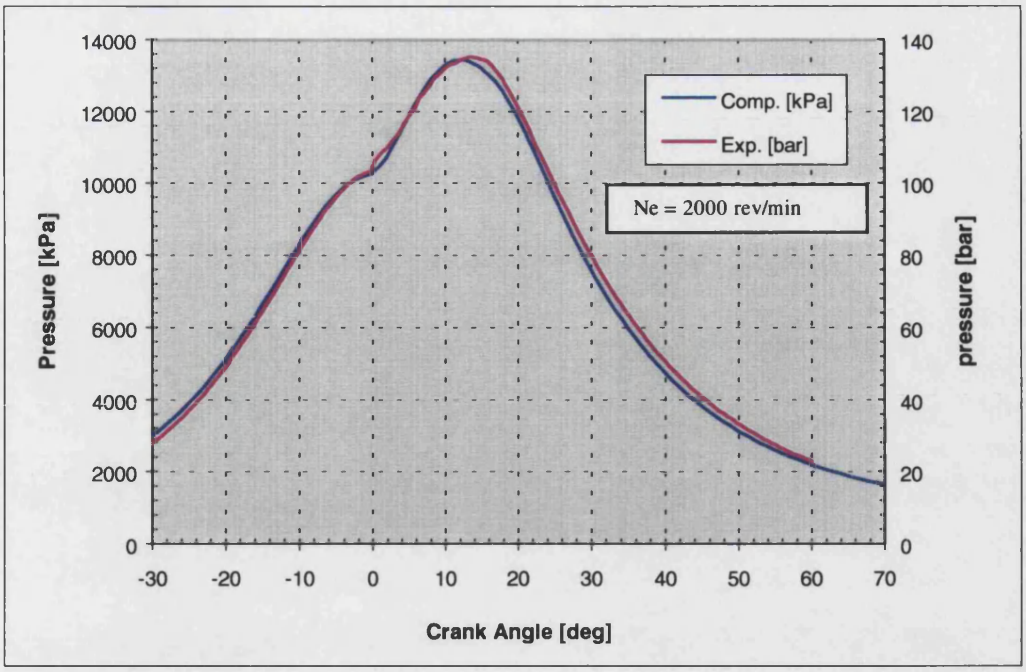

Figure 7.23 (a): Cylinder pressure vs. crank angle degree (2000 rev/min)

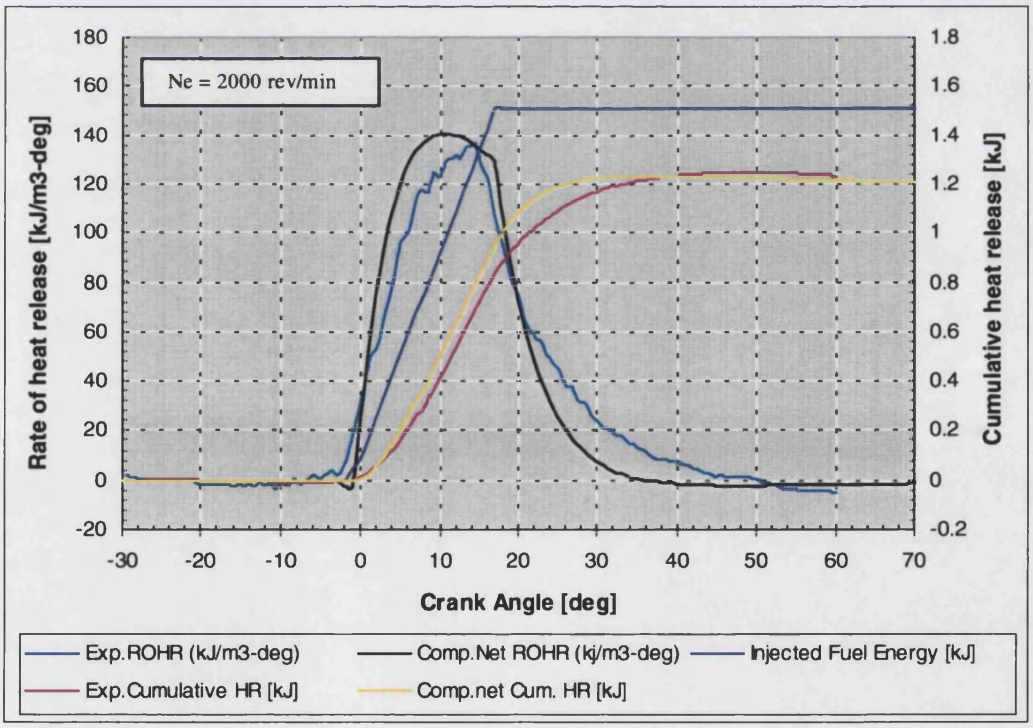

Figure 7.23 (b): ROHR and cumulative HR vs. crank angle degree (2000 rev/min)

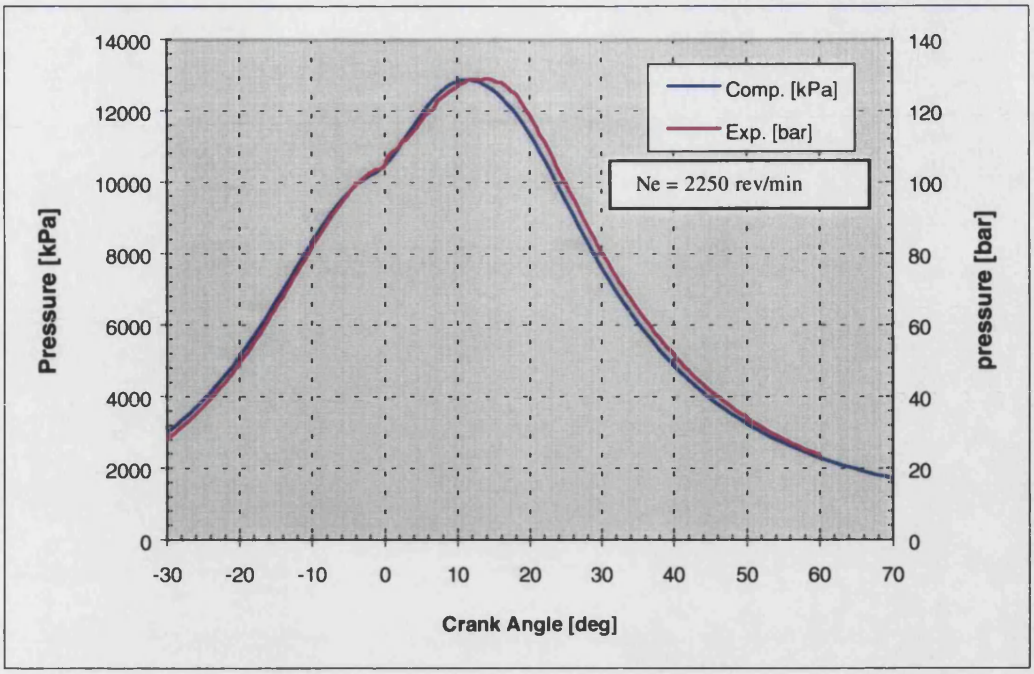

Figure 7.24 (a): Cylinder pressure vs. crank angle degree (2250 rev/min)

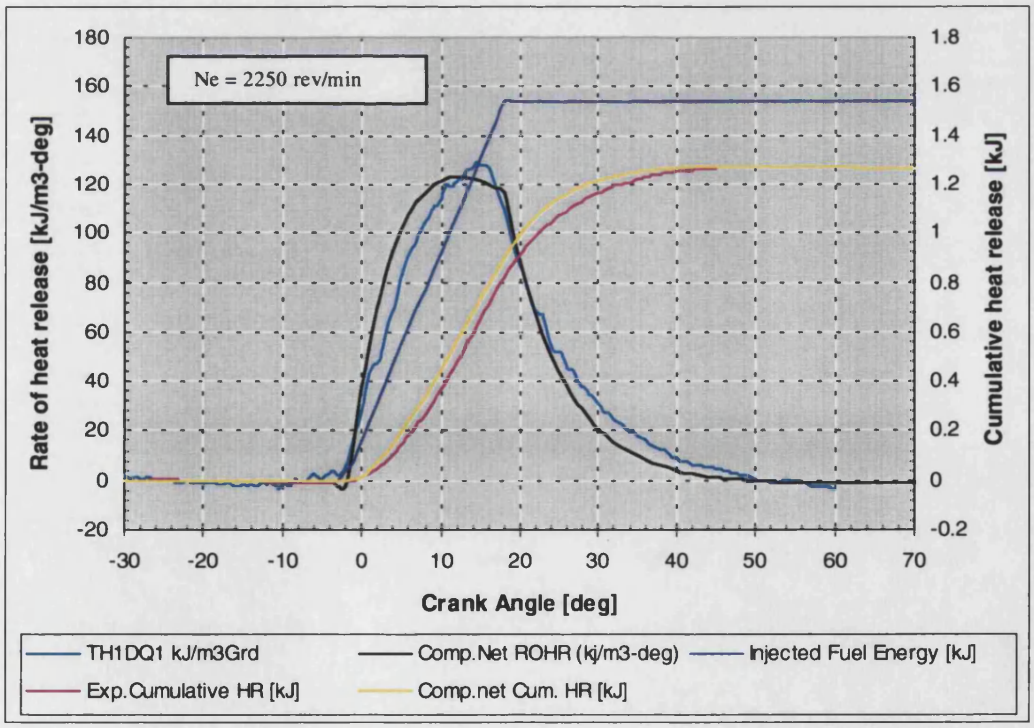

Figure 7.24 (b): ROHR and cumulative HR vs. crank angle degree (2250 rev/min)

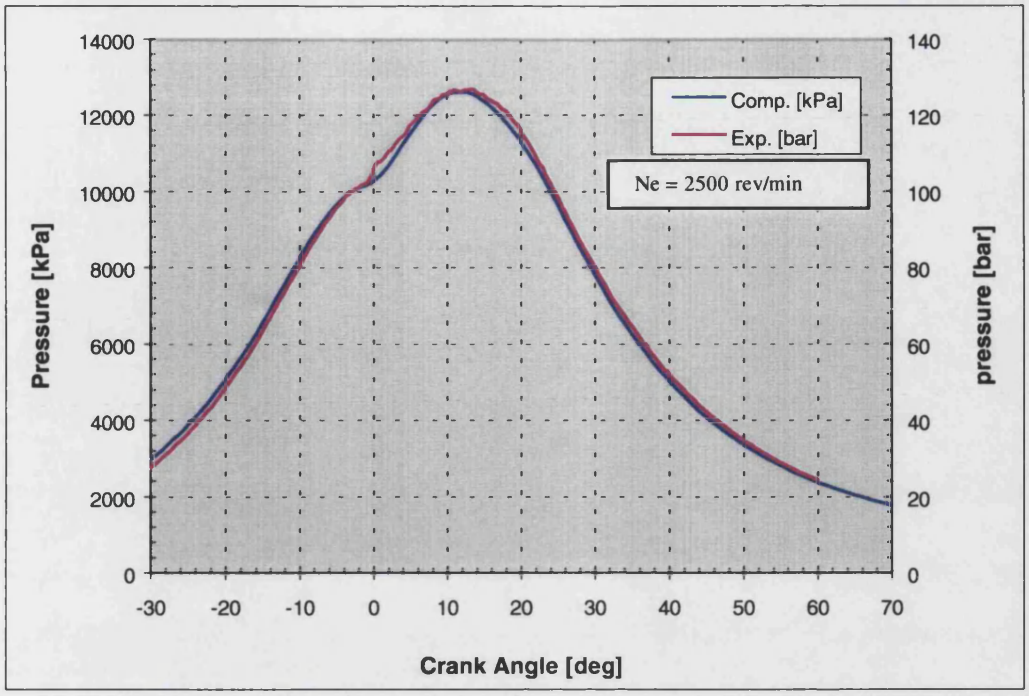

Figure 7.25 (a): Cylinder pressure vs. crank angle degree (2500 rev/min)

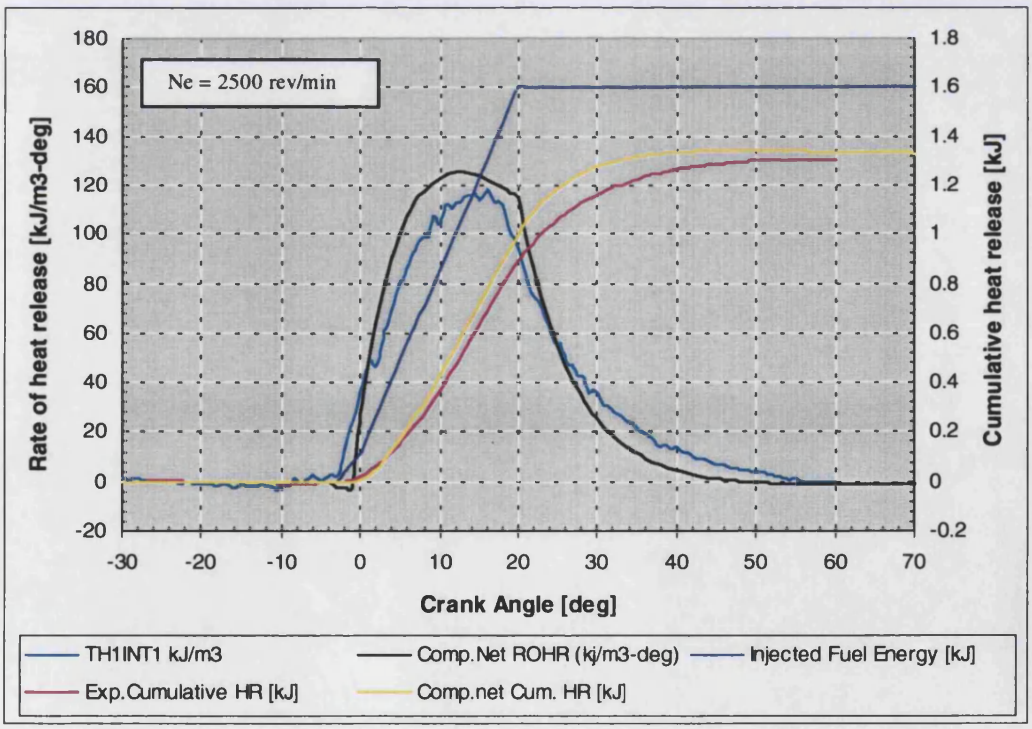

Figure 7.25 (b): ROHR and cumulative HR vs. crank angle degree (2500 rev/min)

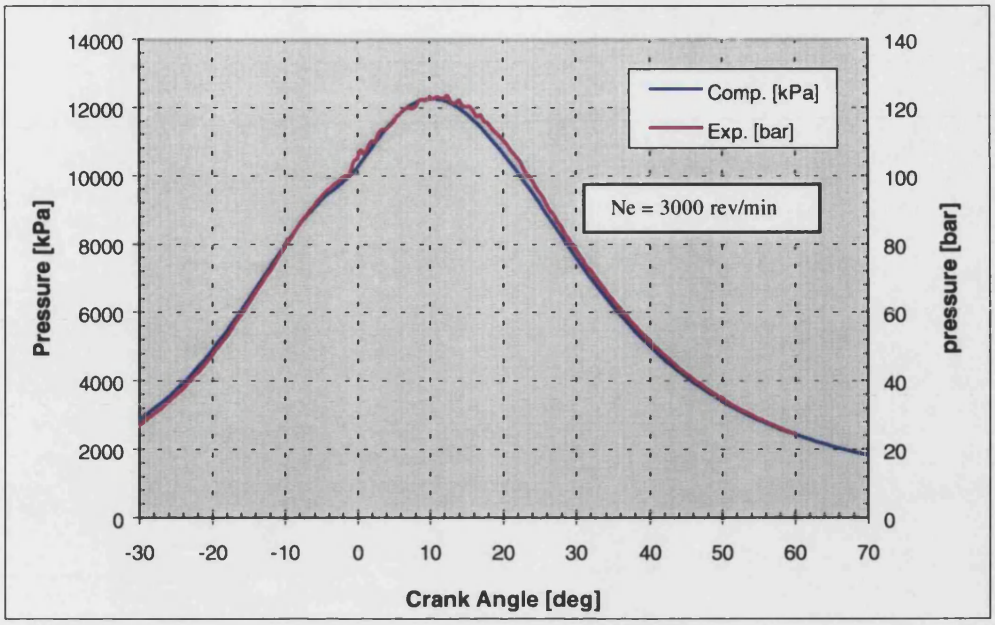

Figure 7.26 (a): Cylinder pressure vs. crank angle degree (3000 rev/min)

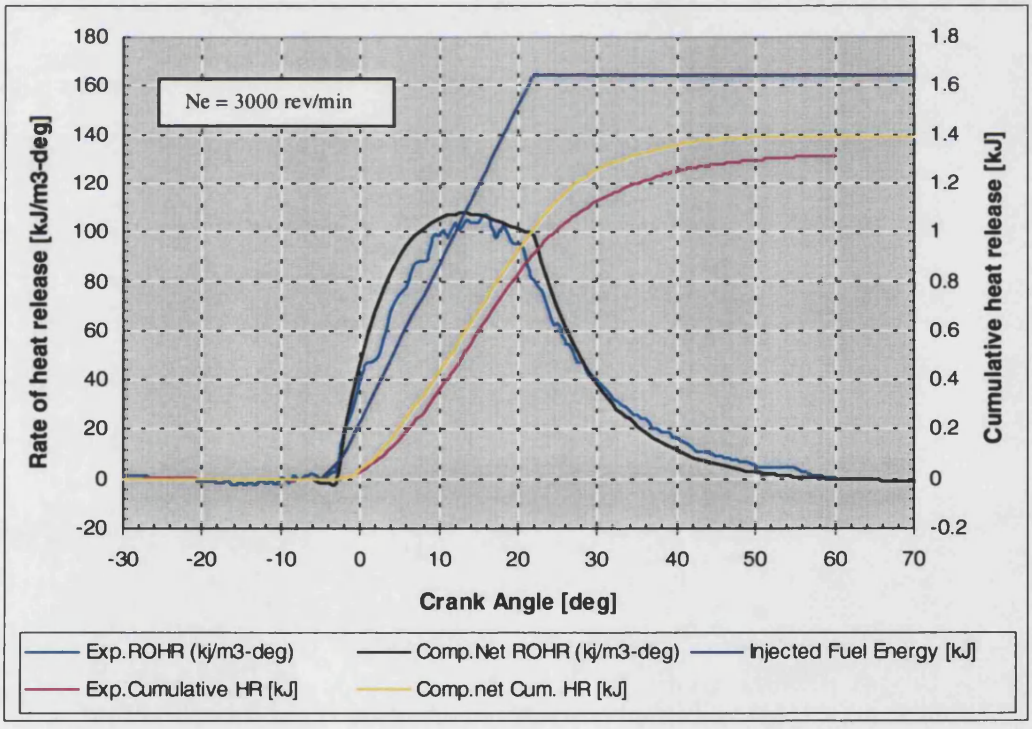

Figure 7.26 (b): ROHR and cumulative HR vs. crank angle degree (3000 rev/min)

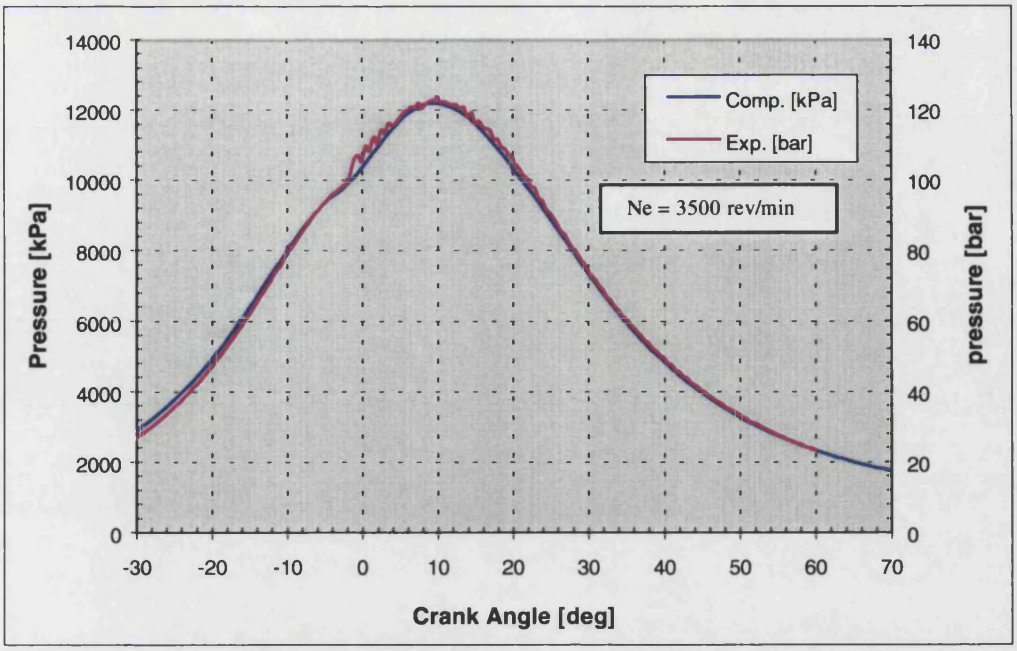

Figure 7.27 (a): Cylinder pressure vs. crank angle degree (3500 rev/min)

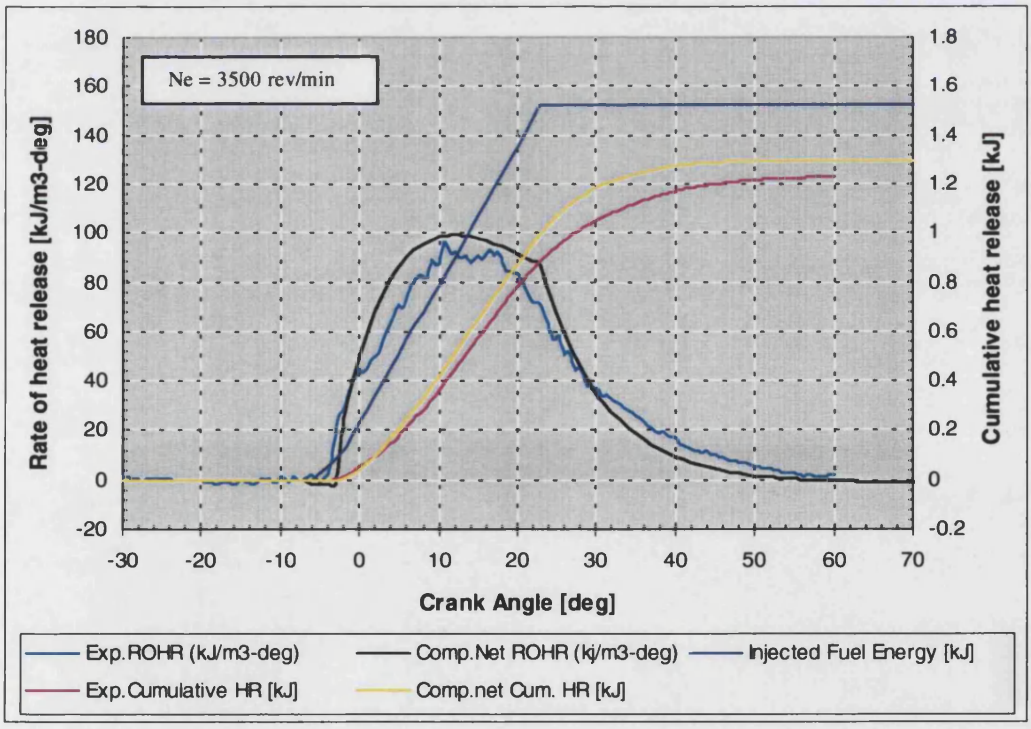

Figure 7.27 (b): ROHR and cumulative HR vs. crank angle degree (3500 rev/min)

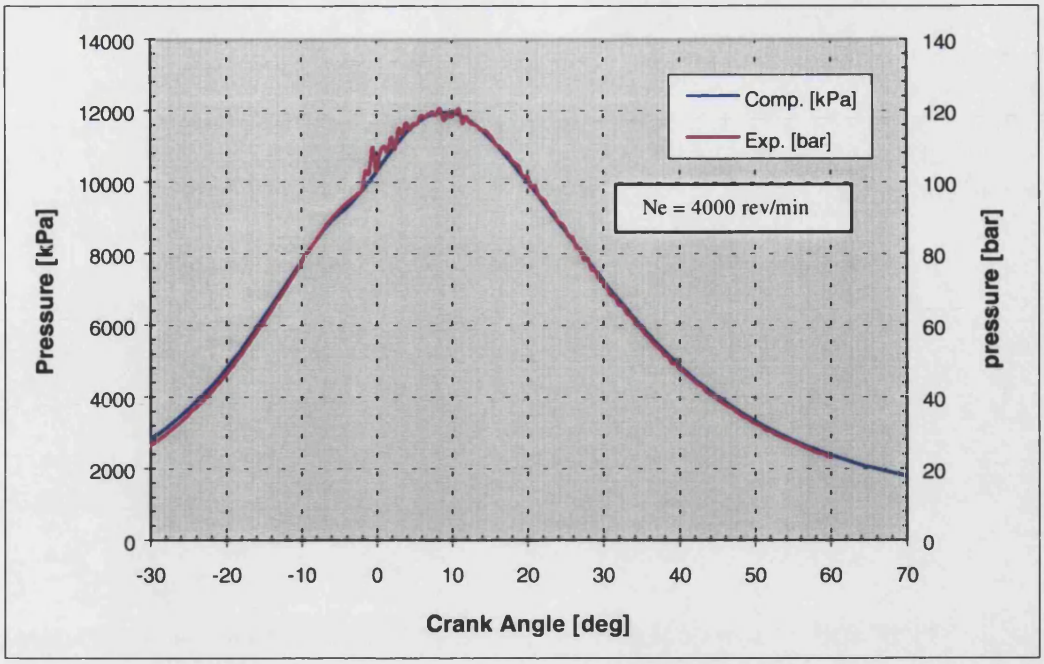

Figure 7.28 (a): Cylinder pressure vs. crank angle degree (4000 rev/min)

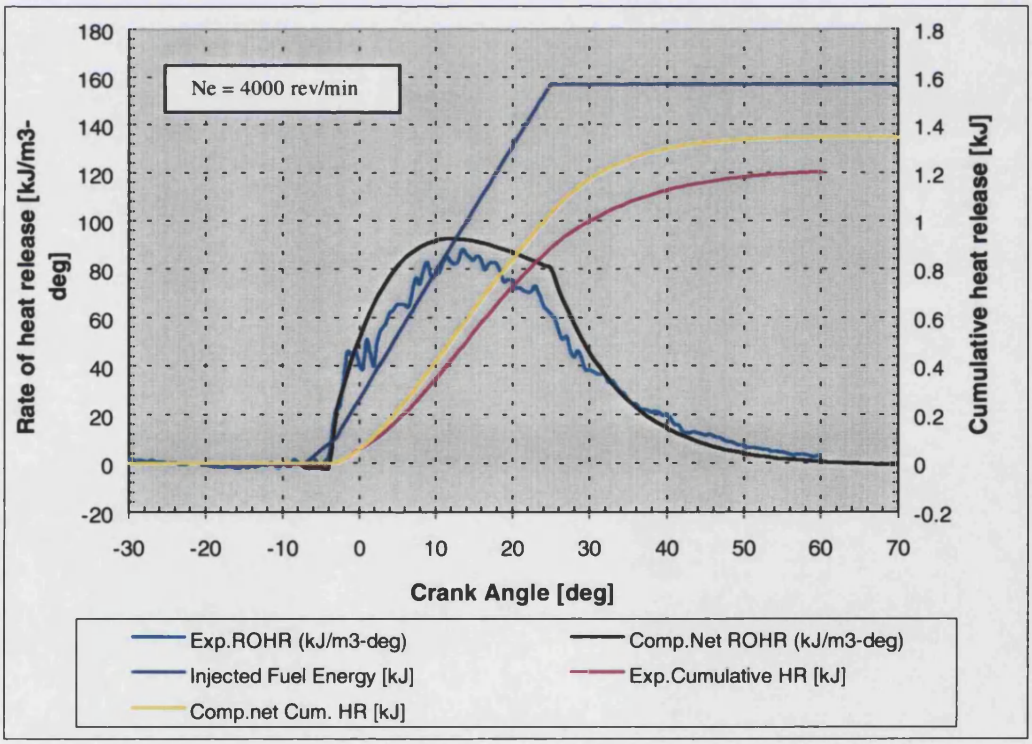

Figure 7.28 (b): ROHR and cumulative HR vs. crank angle degree (4000 rev/min)

7.3.4.2 Optimisation with respect to rate of heat release

As has already been stated, throughout these calculations the parameter α_{h2} was adjusted based on the experimental cumulative heat release.

Figure 7.29a and b (1250 rev/min)

The cylinder pressure records, figure 7.29a, show reasonable agreement during compression, and the location of peak pressure, but significant differences in the value of peak pressure and the subsequent expansion process.

Figure 7.29b shows very good agreement between computed net rate of heat release and experimental ones.

The computed cumulative heat release in figure 7.29b shows initially slightly higher values than experimental ones.

Figure 7.30a and b (1500 rev/min)

Figure 7.30a, shows excellent agreement during the compression process, and the location of peak pressure, but the computed value of peak pressure is about 6 percent less than experimental ones, which persists during expansion.

Figure 7.30b shows reasonable agreement between computed and experimental net rate of heat release.

Agreement between computed and experimental net cumulative heat release traces in figure 7.30b is reasonably good.

Figure 7.31a and b (1750 rev/min)

Figure 7.31a again shows very similar trends for cylinder pressure to those of the earlier results.

Agreement between computed and experimental net rate of heat release in figure 7.38b is very good.

Also figure 7.31b shows an excellent agreement between computed and experimental net cumulative heat release traces.

Figure 7.32a and b (2000 rev/min)

Again figure 7.32a shows excellent agreement during the compression process, but significant differences in the location and the value of peak pressure and during the subsequent expansion.

Figure 7.32b shows again reasonable agreement between computed and experimental net rate of heat release traces.

The computed net cumulative heat release traces in figure 7.32b shows again an excellent agreement with experimental ones.

Figure 7.33a and b (2250 rev/min)

Figure 7.33a shows a reasonable agreement during compression and the value of peak pressure, but slight differences in the location of peak pressure and the subsequent expansion process.

In figure 7.33b computed net ROHR values are slightly in advance of experimental ones up to the end of injection, and then fall below experimental values over the remainder of the heat release process.

Also figure 7.33b shows excellent agreement between computed and experimental net cumulative heat release traces.

Figure 7.34a and b (2500 rev/min)

Figure 7.34a shows an excellent agreement during compression and the value of peak pressure, but slightly differences in the location of peak pressure and the subsequent expansion process.

Agreement between the maximum value of computed and experimental net ROHR in figure 7.34b is very good, but the results shows a slight excess of the computed net ROHR during the period up to the end of injection, and this is reflected in the discrepancies between computed and experimental net heat release.

Figure 7.35a and b (3000 rev/min)

Figure 7.35a shows again an excellent agreement between computed and experimental cylinder pressure traces.

Agreement between computed and experimental ROHR traces in figure 7.35b is reasonably good, but the computed net cumulative heat release values are now

somewhat greater than the experimental ones, due either to an underestimate of cylinder heat transfer to coolant or inaccuracies in the Concerto heat release record.

Figure 7.36a and b (3500 rev/min)

Agreement between computed and experimental cylinder pressure traces in figure 7.36a is excellent.

Agreement between the location and maximum value of computed and experimental net ROHR in figure 7.36b is very good, but the results shows significant excess of the computed net ROHR during the period up to the end of injection, and this is reflected in the discrepancies between computed and experimental net heat release. The reasons are similar to those for figure 7.35b.

Figure 7.37a and b (4000 rev/min)

Again figure 7.37a shows an excellent agreement between computed and experimental cylinder pressure traces. However, the discrepancies between computed and experimental ROHR, and also between computed and experimental net heat release in figure 7.37b are now somewhat greater than the previous results in figure 7.36b, for 3500 rev/min, again for the reasons noted above.

Overview of results in section 7.3.4.2

As has already been stated, compared with the results of section 7.3.2, the incorporation both of ignition delay and a finite period of needle lift assumed to coincide with the ignition delay period (see figures 6.2 and 6.3) has led to a marked reduction in the previous overestimate of ROHR in the early phase of the heat release process.

The results of section 7.3.4.2 are summarised in table 7.6c, which can be explained as follows:

Comparison of computed and experimental cylinder pressure result shows:

- Excellent agreement during the compression process.
- Good agreement in the location of cylinder peak pressure at low speeds, but slight differences at high speeds.
- Significant differences in the value of cylinder peak pressure and during the subsequent expansion process at low speeds, but good agreement at high speeds.

- Very good agreement between both results at high speeds.

Comparison of computed and experimental net ROHR shows:

- There is generally very good agreement in the location and maximum values of net ROHR.
- Reasonable agreement between computed and experimental net ROHR traces, except for the last case, i.e. 4000 rev/min, which for the computed net ROHR shows higher values than experimental ones.

Comparison of computed and experimental net cumulative heat release shows:

- There is a good agreement between both results, which however deteriorates somewhat with increasing speed due to some underestimate of heat transfer to coolant or inaccuracies in the Concerto heat release record.

Table 7.6a: Summary of basic running data together with experimental and computed results for engine performance using formulation with ignition delay and linear needle lift based on the best heat release runs

Initial conditions:

Compression ratio: 18.2:1
Inlet manifold volume: 0.005 m^3
Nozzle hole diameter: 0.15 mm
Number of nozzle holes: 5
Max. cumulative heat release = 0.95 * Total injected fuel energy

N_e	Fuel Inj.	p_{rail}	p_{cyl} At	D_{inj}	v_N	m'_f	Torque (N.m)		b.s.f.c (kg/kW-hr)		In.Man.Pr. (bar)	
(rev/min)	(mm^3/sht)	(bar)	SOI (bar)	(°CA)	[m/s]	(kg/s)	Exp.	Comp.	Exp.	Comp.	Exp.	Comp.
1250	34.1	540	56.33	11	341.390	4.01E-03	132.8	130.20	0.246	0.2488	127	118
1500	37.7	605	70.12	14	359.010	4.21E-03	160.2	154.86	0.226	0.2314	152	143
1750	39.5	679	80.71	16	379.692	4.46E-03	175.3	168.27	0.216	0.2231	171	163
2000	42.4	750	100.30	18	395.669	4.64E-03	190.2	184.50	0.214	0.2184	198	200
2250	43.3	800	100.70	20	410.495	4.82E-03	196.8	194.53	0.211	0.2118	197	200
2500	45.1	855	98.38	22	426.987	5.01E-03	203.6	203.19	0.213	0.2108	197	198
3000	46.3	1030	93.03	26	475.159	5.36E-03	199.2	202.23	0.223	0.2174	196	191
3500	42.8	1110	88.71	29	496.079	5.82E-03	180.1	181.20	0.228	0.2242	196	192
4000	44.2	1255	86.42	32	530.646	6.22E-03	171.0	178.40	0.248	0.2351	192	187

Table 7.6b: Summary of the key HR data together with α_{h2} and α_{k2} and the derived parameters WH, WK, C_{rate} and C_{mod}

N_e (rev/min)	SoI °BTDC	SoHR °BTDC	D_{ignd} °CA	α_{h2} based on: F1 func.	α_{h2} based on: Cmod*F1*F2	α_{k2}	δ	WH	WK	C_{rate}	C_{mod}
1250	-4	-2	2	0.3450	0.3798	0.7	0.62	0.0923	0.07863	0.07439	0.0852
1500	-3	-1	2	0.4176	0.4601	0.7	0.62	0.0927	0.06005	0.08327	0.0867
1750	-3	-1	2	0.4945	0.5342	0.7	0.62	0.1046	0.05188	0.08857	0.0887
2000	-3	-1	2	0.5124	0.5572	0.7	0.62	0.0979	0.04566	0.09354	0.0882
2250	-3	-1	2	0.5309	0.5800	0.7	0.62	0.0932	0.04077	0.09827	0.0845
2500	-4	-1	3	0.5448	0.5956	0.7	0.62	0.0906	0.03804	0.10440	0.0823
3000	-5	-2	3	0.5729	0.6301	0.7	0.62	0.0832	0.03171	0.11260	0.0754
3500	-7	-3	4	0.6126	0.6648	0.7	0.62	0.0865	0.02889	0.11970	0.0645
4000	-7	-3	4	0.6260	0.6830	0.7	0.62	0.0815	0.02594	0.12530	0.0626

Table 7.6c: Comparison of the computed and experimental results of heat release

N_e	Loc.of Max.ROHR		Max.Net-ROHR(kJ/m^3deg)		Net Cum.HR (kJ) At 60 ATDC		Loc.of Max.Press.		Max. Press. (bar)		Avg. NOx (ppm)	
(rev/min)	Exp.	Comp.	Exp.	Comp.	Exp.	Comp.	Exp.	Comp.	Exp.	Comp.	Exp.	Comp.
1250	6.0	7	129.83	139.27	0.833	0.843	10.0	10	107.71	101.9	967	1694
1500	9.5	11	133.89	133.87	1.021	1.012	12.5	12	115.77	108.8	1143	1319
1750	11.0	13	133.57	132.70	1.105	1.096	13.5	13	121.50	118.2	1303	1162
2000	14.5	12	136.70	130.88	1.233	1.220	13.5	12	135.23	131.4	1346	963
2250	14.5	13	129.53	122.94	1.267	1.271	14.0	12	129.15	127.2	1148	905
2500	16.0	12	118.56	121.38	1.304	1.333	13.0	12	126.89	127.3	1031	941
3000	16.5	14	104.91	108.17	1.310	1.390	11.0	10	123.32	122.0	915	930
3500	10.5	12	96.325	95.10	1.230	1.291	11.0	9	123.70	123.1	857	795
4000	13.5	13	88.29	90.51	1.205	1.348	8.5	9	120.78	117.8	783	769

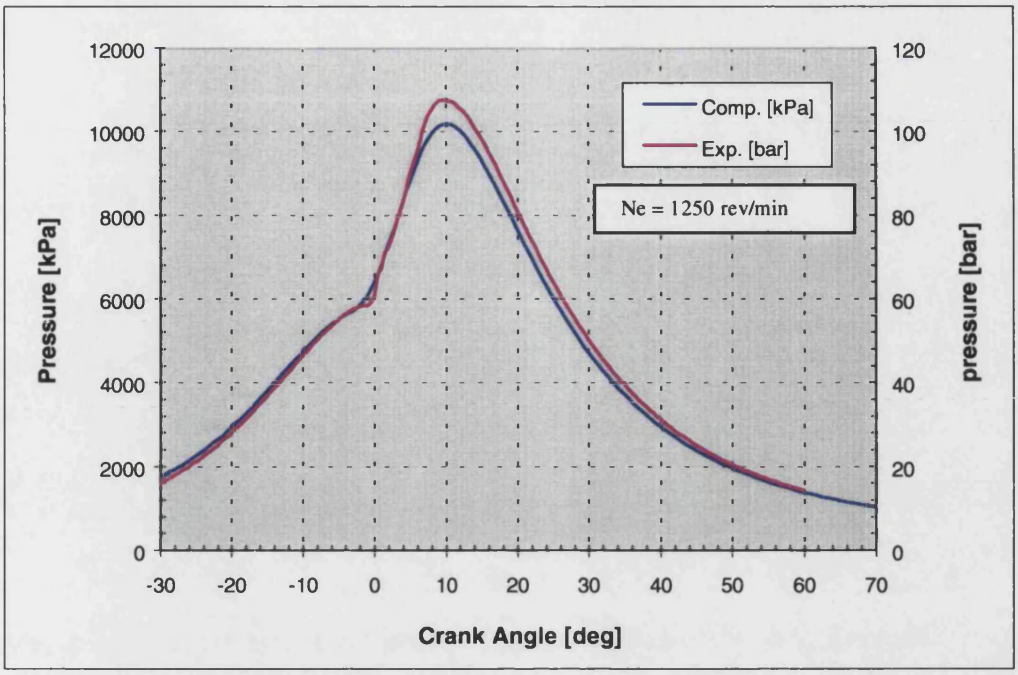

Figure 7.29 (a): Cylinder pressure vs. crank angle degree (1250 rev/min)

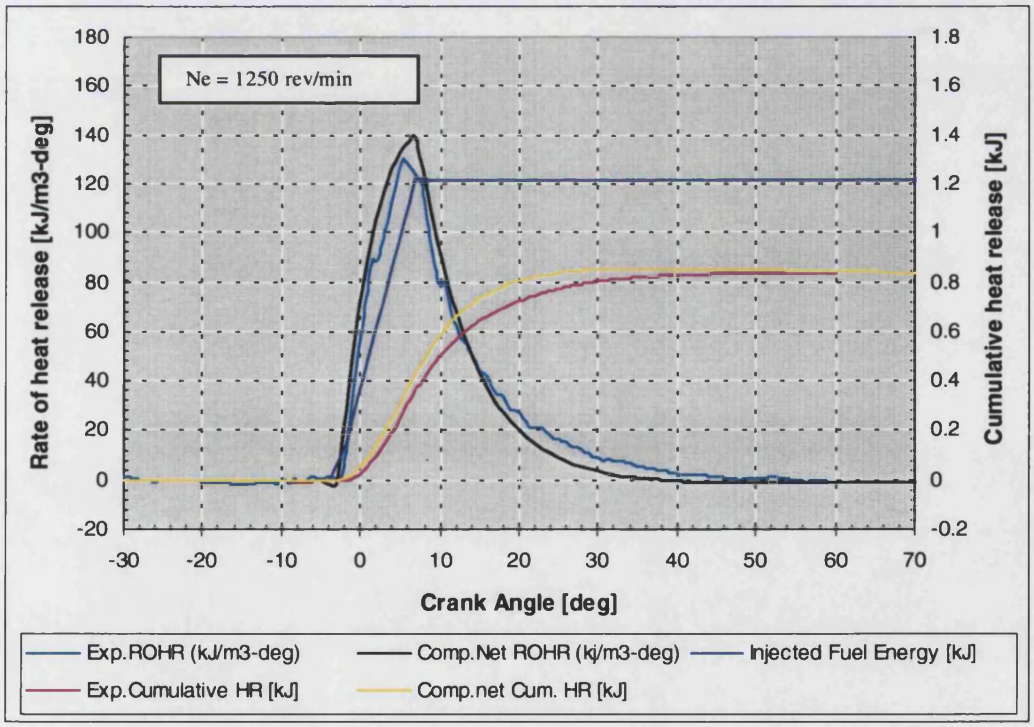

Figure 7.29 (b): ROHR and cumulative HR vs. crank angle degree (1250 rev/min)

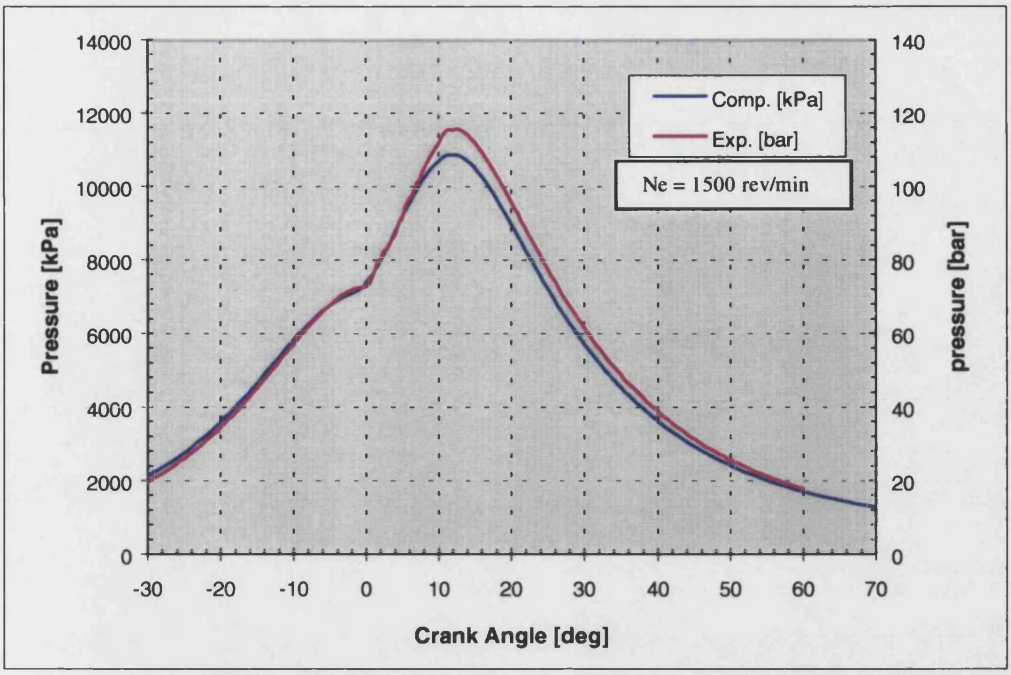

Figure 7.30 (a): Cylinder pressure vs. crank angle degree (1500 rev/min)

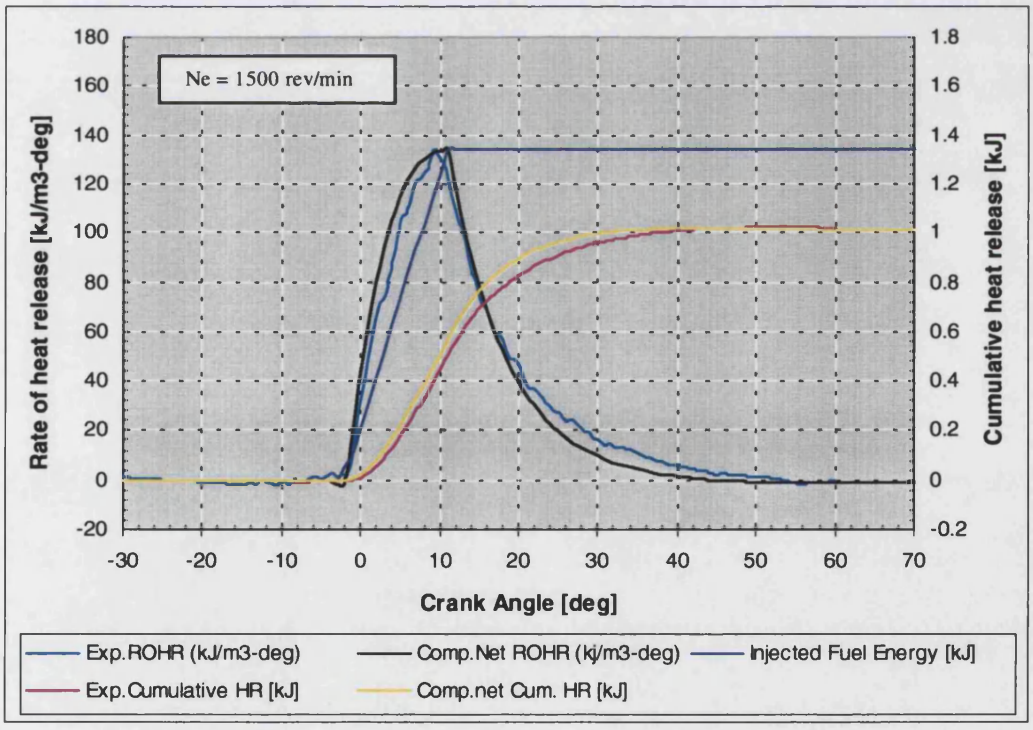

Figure 7.30 (b): ROHR and cumulative HR vs. crank angle degree (1500 rev/min)

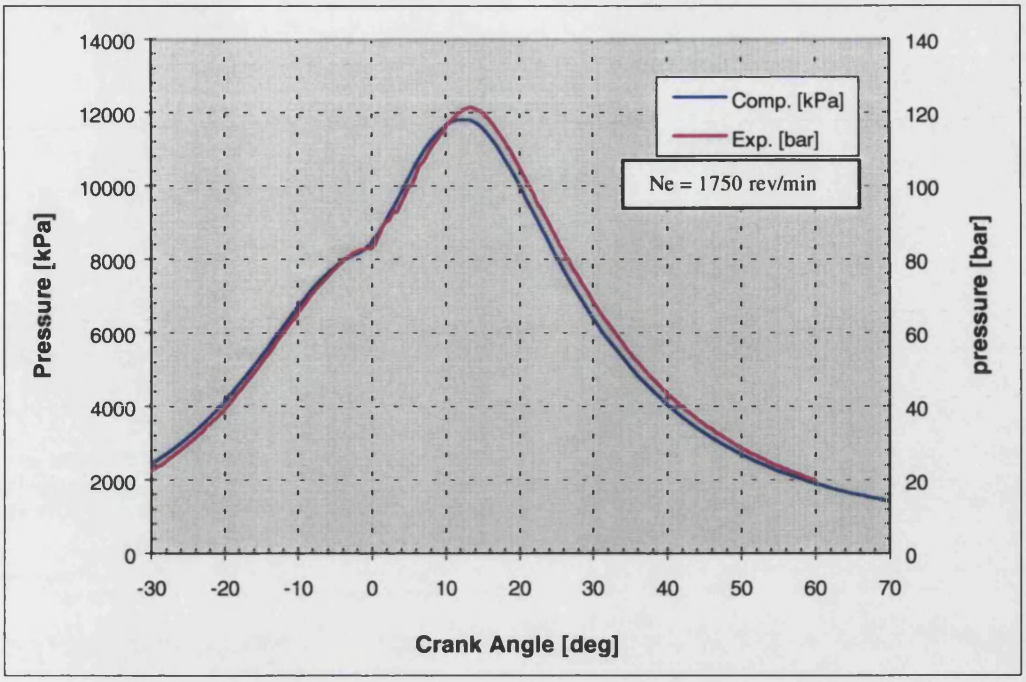

Figure 7.31 (a): Cylinder pressure vs. crank angle degree (1750 rev/min)

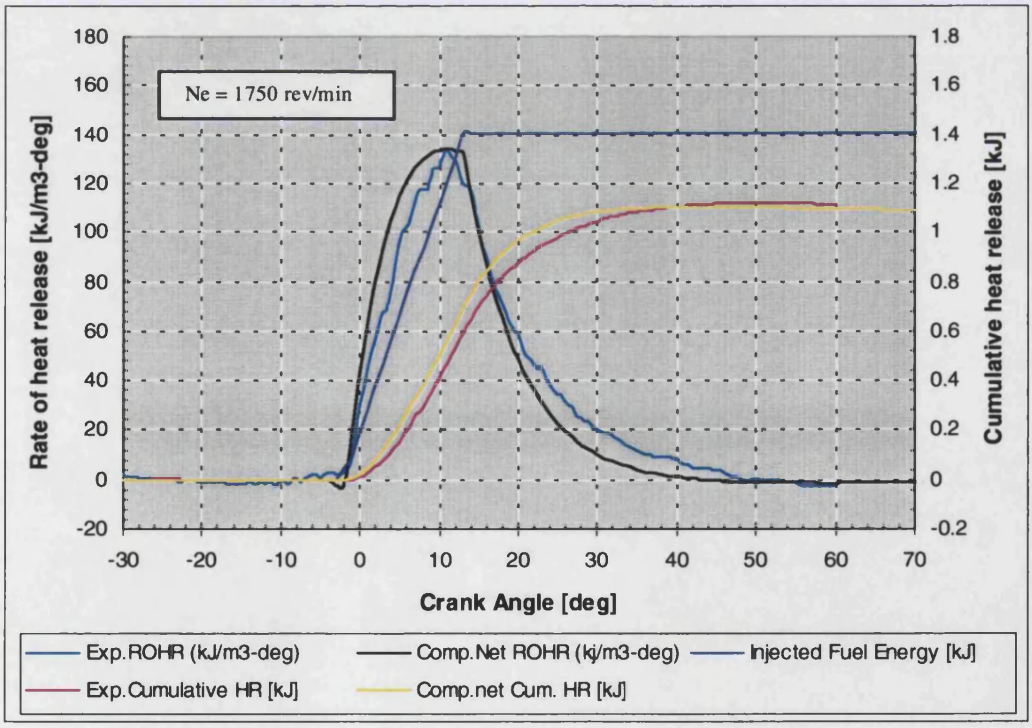

Figure 7.31 (b): ROHR and cumulative HR vs. crank angle degree (1750 rev/min)

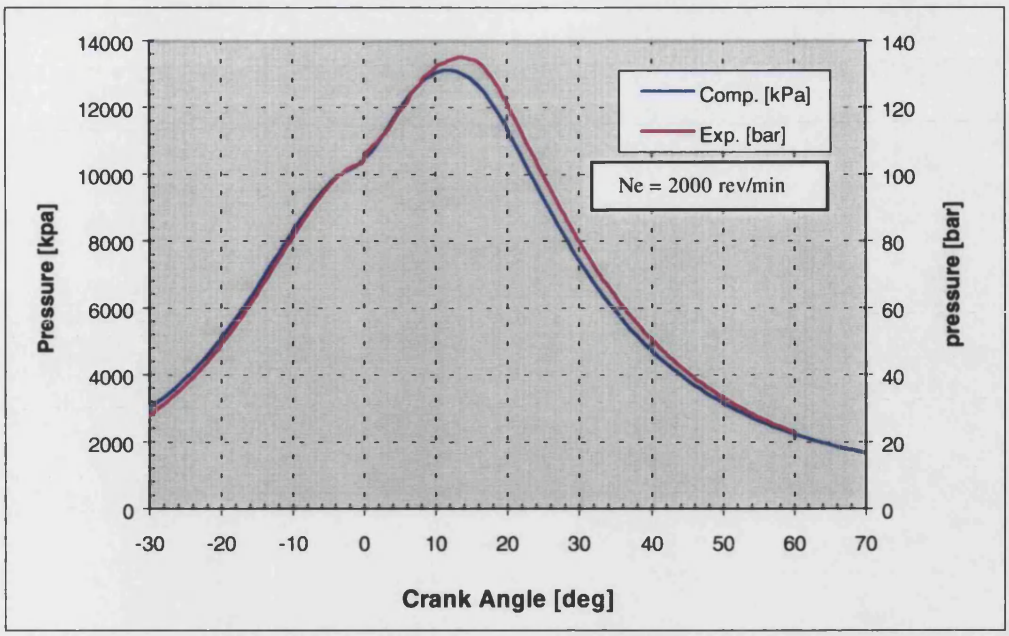

Figure 7.32 (a): Cylinder pressure vs. crank angle degree (2000 rev/min)

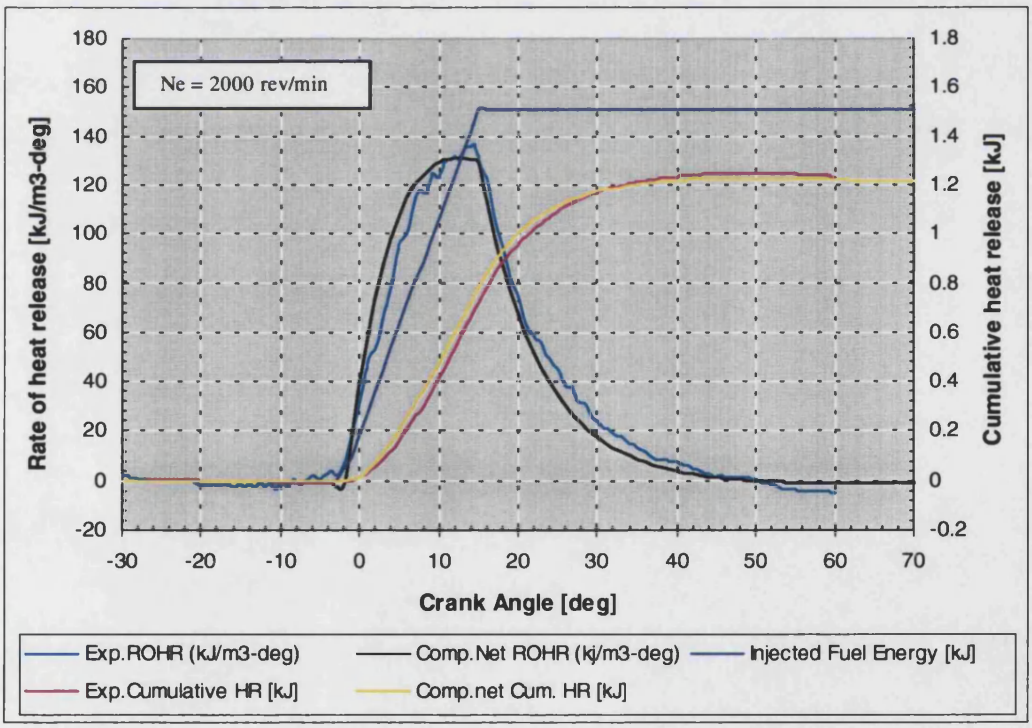

Figure 7.32 (b): ROHR and cumulative HR vs. crank angle degree (2000 rev/min)

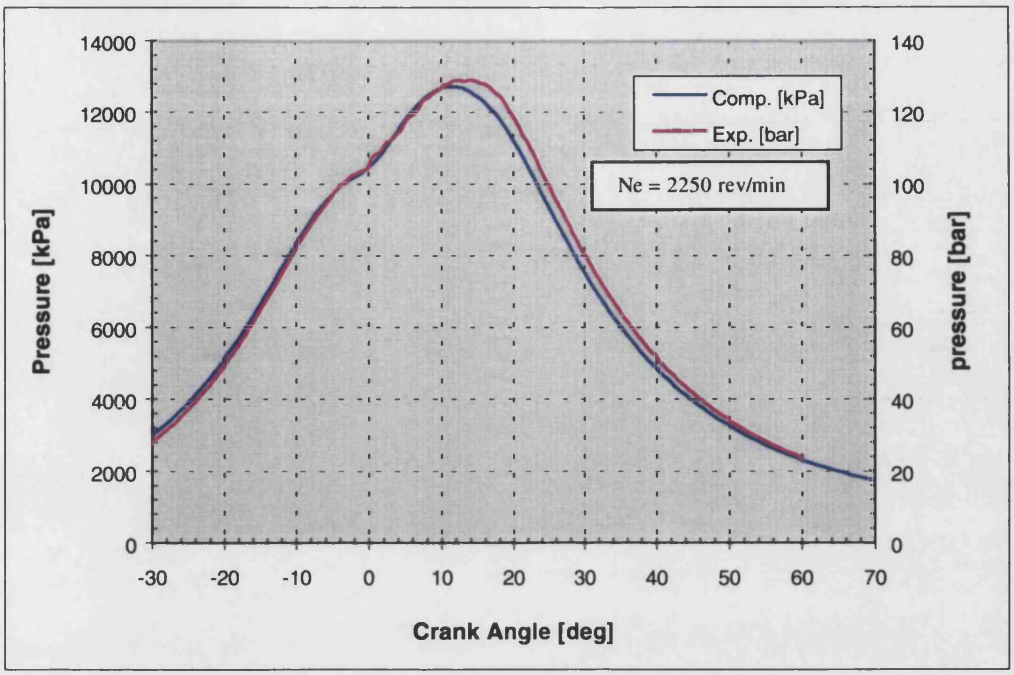

Figure 7.33 (a): Cylinder pressure vs. crank angle degree (2250 rev/min)

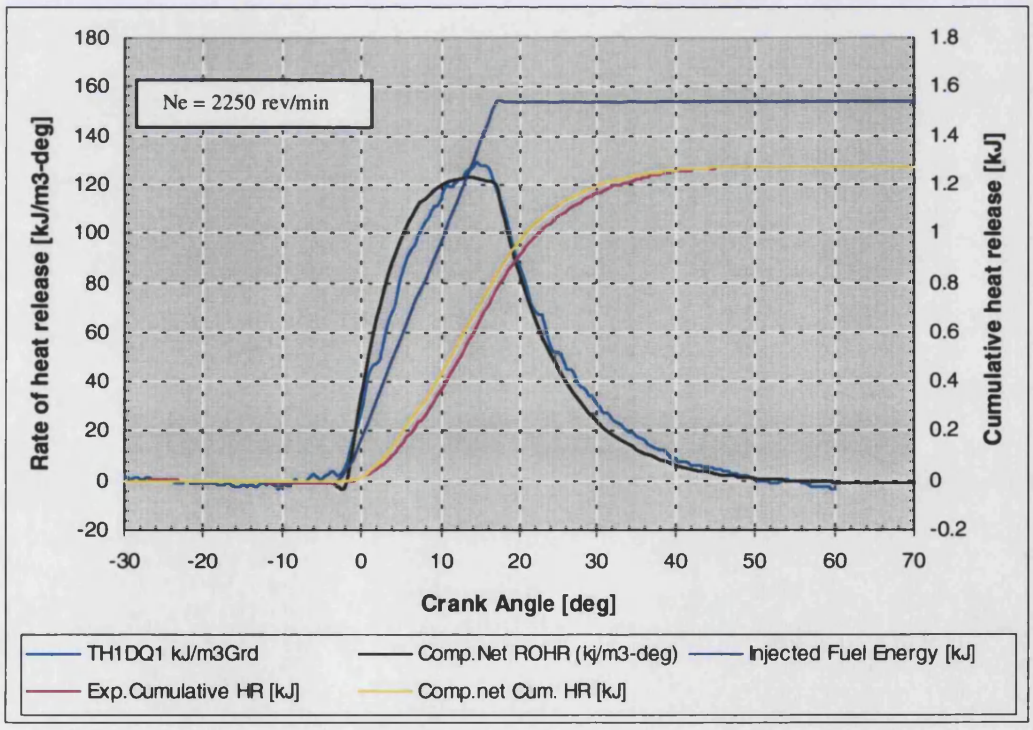

Figure 7.33 (b): ROHR and cumulative HR vs. crank angle degree (2250 rev/min)

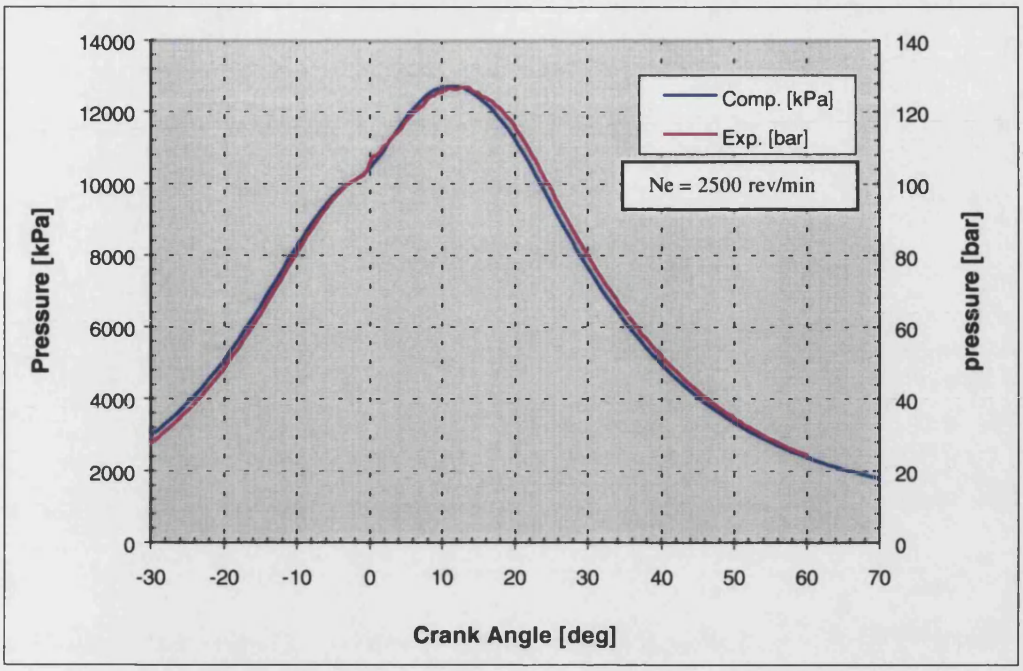

Figure 7.34 (a): Cylinder pressure vs. crank angle degree (2500 rev/min)

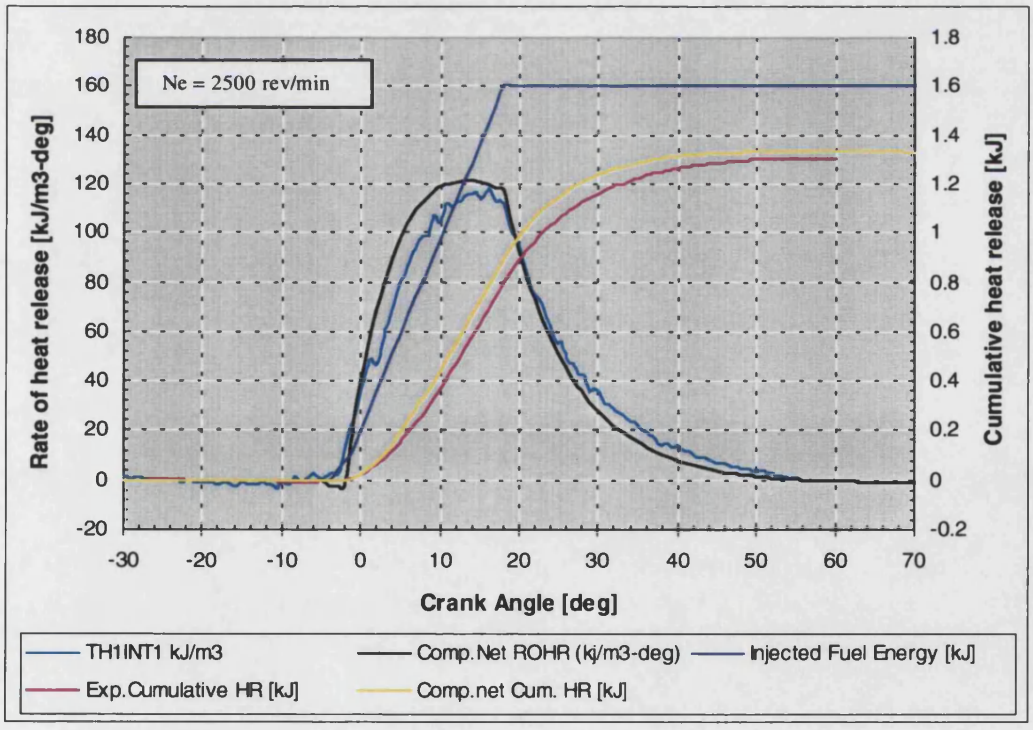

Figure 7.34 (b): ROHR and cumulative HR vs. crank angle degree (2500 rev/min)

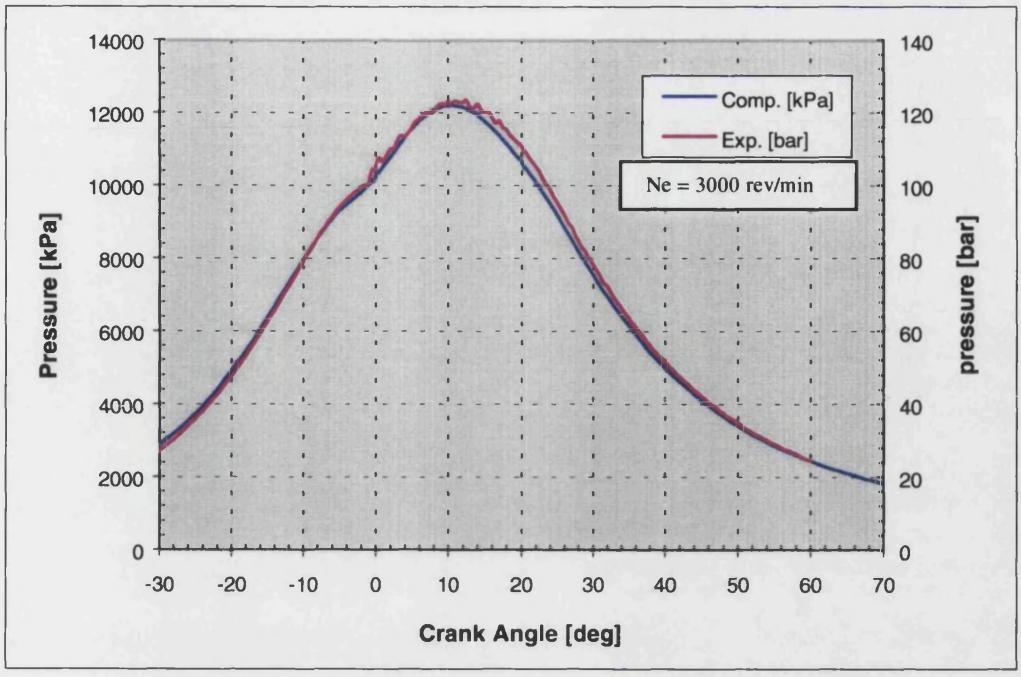

Figure 7.35 (a): Cylinder pressure vs. crank angle degree (3000 rev/min)

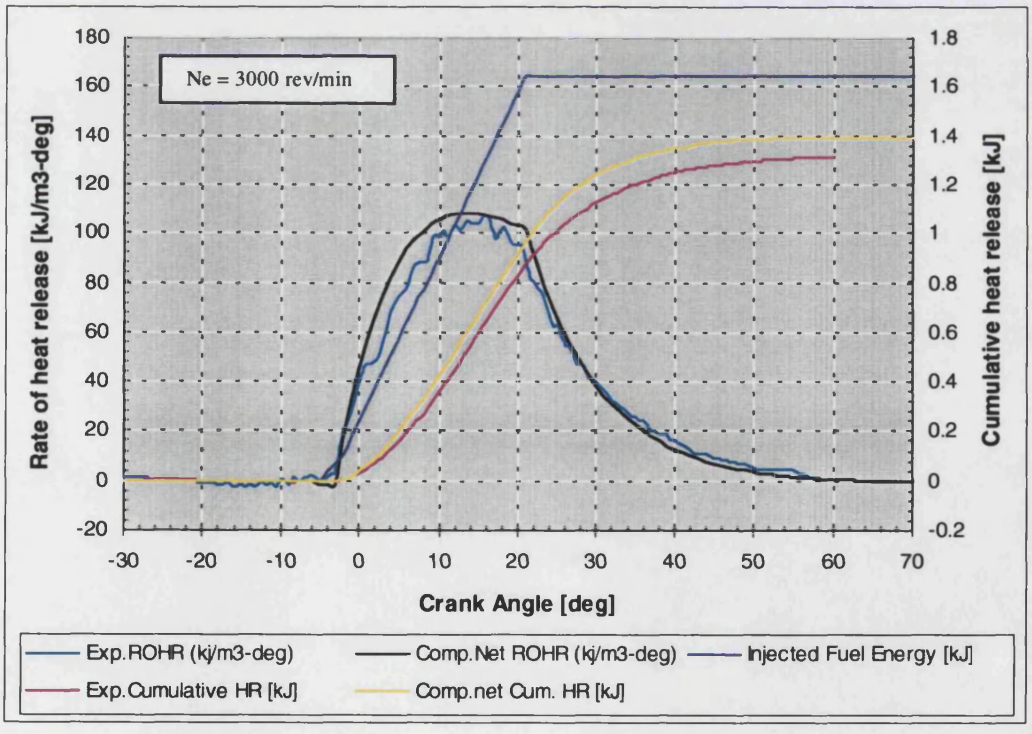

Figure 7.35 (b): ROHR and cumulative HR vs. crank angle degree (3000 rev/min)

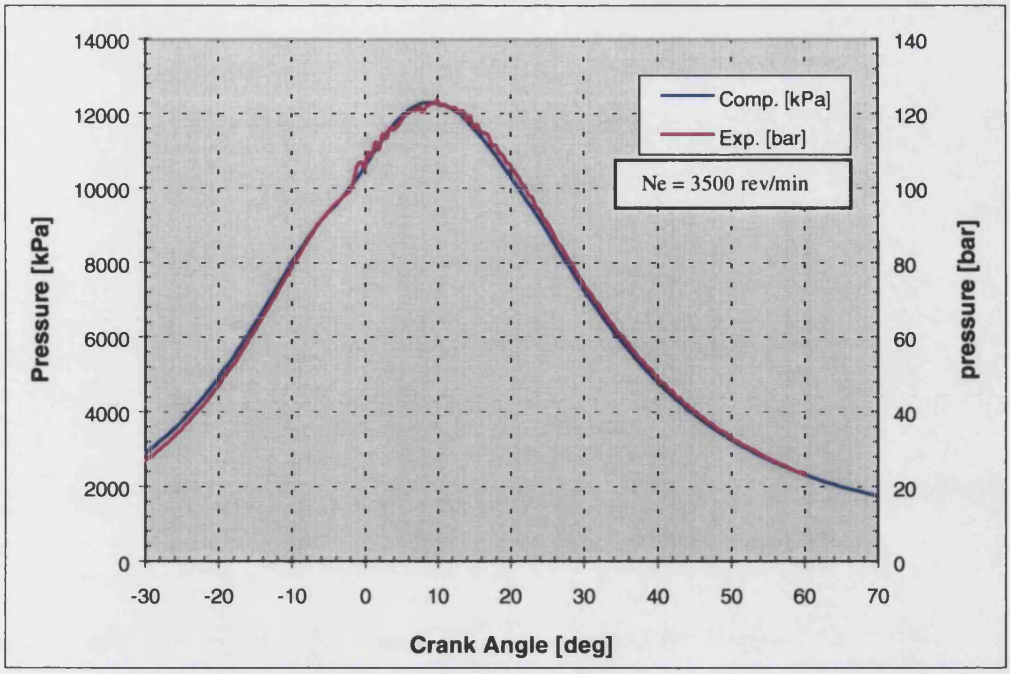

Figure 7.36 (a): Cylinder pressure vs. crank angle degree (3500 rev/min)

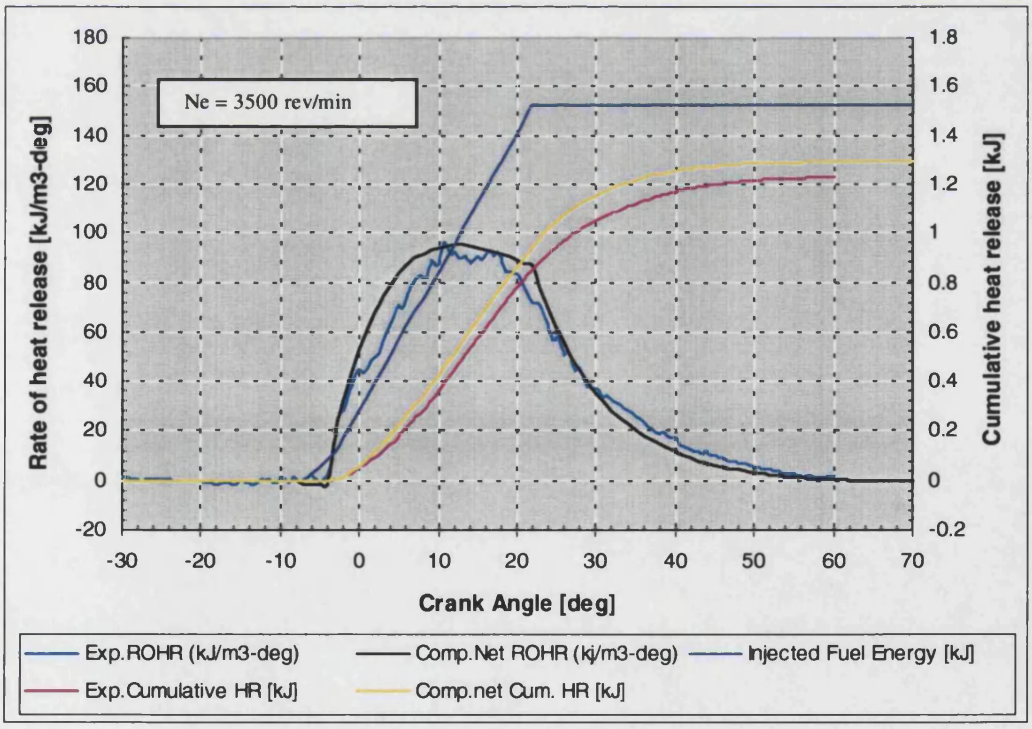

Figure 7.36 (b): ROHR and cumulative HR vs. crank angle degree (3500 rev/min)

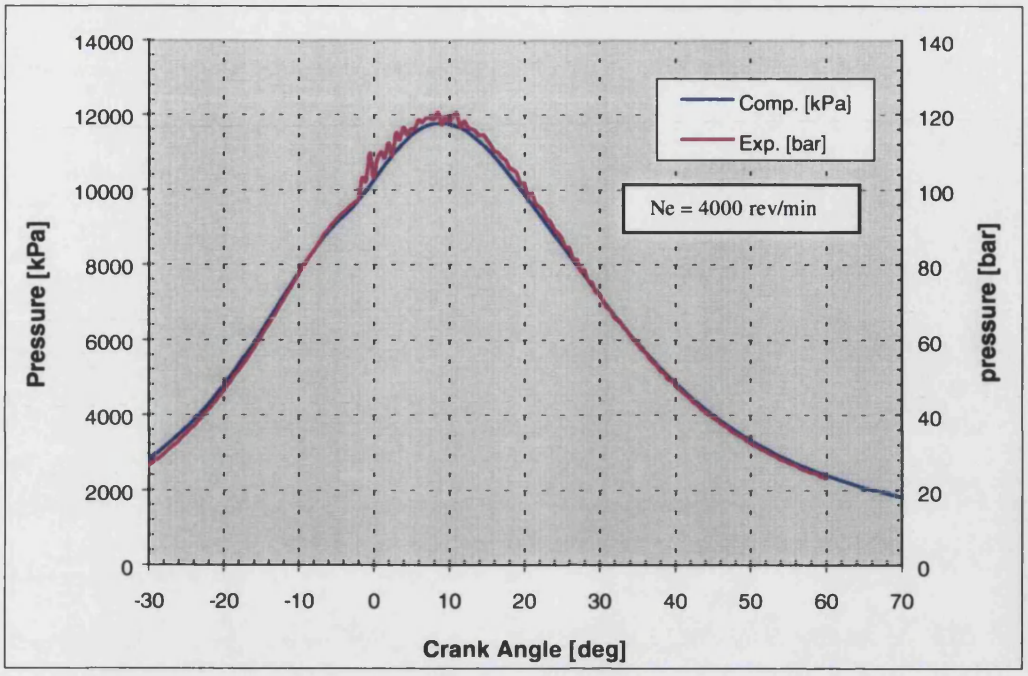

Figure 7.37 (a): Cylinder pressure vs. crank angle degree (4000 rev/min)

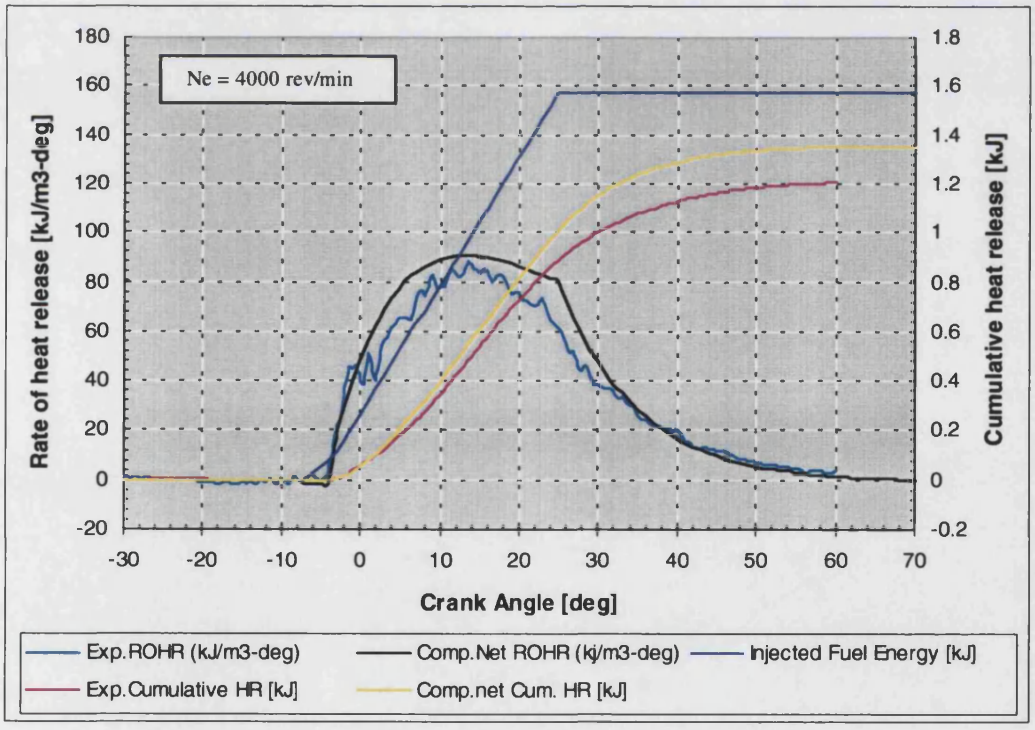

Figure 7.37 (b): ROHR and cumulative HR vs. crank angle degree (4000 rev/min)

7.4 Correlation of mixing rates factor WH (eqation 6.17), with engine speed and rail pressure

The analysis of the Concerto derived heat release rate and cumulative heat release curves utilised experimental data on injection duration and, in the first instance, the fraction α_{h2} of fuel burnt at the end of the injection period.

The results obtained, especially in the final section 7.3.4.2 in which the best possible approximation to experimental heat release rates was aimed at, are considered very satisfactory.

However, in order to improve the predictive ability of the analytical approach, it is desirable to establish a possible correlation of the mixing rate factor *WH* with the basic operating variables of effective rail pressure expressed as injection rate or injection velocity, and engine speed.

This attempted correlation is based on the assumption that the mixing rate constant *WH*, expressed in equation (6.17) on a crank angle basis, when alternatively expressed on a time basis, i.e. $(WH)_{time}$, (where $(WH)_{time} = 6N_e\ (WH)_{crank\text{-}angle}$) can be regarded as describing the fundamental fuel/air mixing process which, as shown in section 6.2.2, equation 6.7 and table 6.1, is dominated by the kinetic energy of the injected fuel which in turn is proportional to the square of the injection velocity.

Table 7.7 and figures 7.38a, b, c, and d show the results of a smoothing operation performed on:

a) The α_{h2} values of section 7.3.4.1 and table 5.5b (figure 7.38a)
b) The injection duration D_{inj} (figure 7.38b)
c) The rail pressure p_{rail} (figure 7.38c)

The table 7.7 gives the above smoothed values together with the derived injection velocity and *WH* values based on both crank angle and time.

The column RVSP represents the ratio of $\left[\frac{(v_N)_{Ne}}{(v_N)_{1250}}\right]^2$ to express the proportionality of mixing rate to that ratio, and represented by the column $(WH)_{equ}$ Where:

$$(WH)_{equ} = [(WH)_{time}]_{250} \cdot RVSP$$

The close correspondence between the columns $(WH)_{time}$ and $(WH)_{equ}$ shows that injection velocity does indeed lead to the excellent correlation shown in figure 7.38d, which also given the 2nd order polynomial in speed for this new value of *WH*.

An alternative correlation based on a slightly different set of smoothed values of α_{h2} (based on values of section 7.3.4.2 and table 7.6b), D_{inj} and p_{rail} is summarised in table 7.8, and figure 7.39 a, b, c, and d.

In view of the previously established smooth curve for p_{rail} as a function of speed, it is not surprising that a direct correlation of $(WH)_{\text{time}}$ with engine speed only via the new ratio $(RVSP)' = \frac{(N_e)_n}{1250}$ again gives excellent correlation, as seen in figure 7.39b.

The only disadvantage is that the dependence of WH on injection velocity is now no longer explicit.

Table 7.7: Summary of smoothed values of α_{h2}, D_{inj} and p_{rail} for calculation of WH (correlation based on injection velocity)

N_e rev/min	p_{rail} bar	p_{cyl} bar	v_N m/s	D_{inj} °CA	α_{h2} -	WH (CA based)	RVSP -	WH (time based)	WH (equ.)	FMFR kg/s
1250	540	56.3	341.4	11	0.42	0.11	1	825.007	825.007	0.00401
1500	605	70.1	359.01	13	0.45	0.1034	1.106	930.461	912.281	0.00421
1750	679	79.7	380.02	16	0.49	0.0963	1.239	1011.11	1022.19	0.00446
2000	750	99.2	396	18	0.515	0.0931	1.345	1117.38	1109.96	0.00465
2250	800	99.1	410.98	20	0.54	0.0911	1.449	1230.25	1195.51	0.00482
2500	865	97.9	429.95	22	0.563	0.0895	1.586	1342.39	1308.42	0.00505
3000	995	91.5	466.6	26	0.602	0.0864	1.868	1555.56	1541.01	0.00548
3500	1120	91.2	497.89	29	0.628	0.0848	2.127	1779.98	1754.63	0.00584
4000	1255	86.4	530.64	32	0.65	0.083	2.416	1992.46	1993.07	0.00623

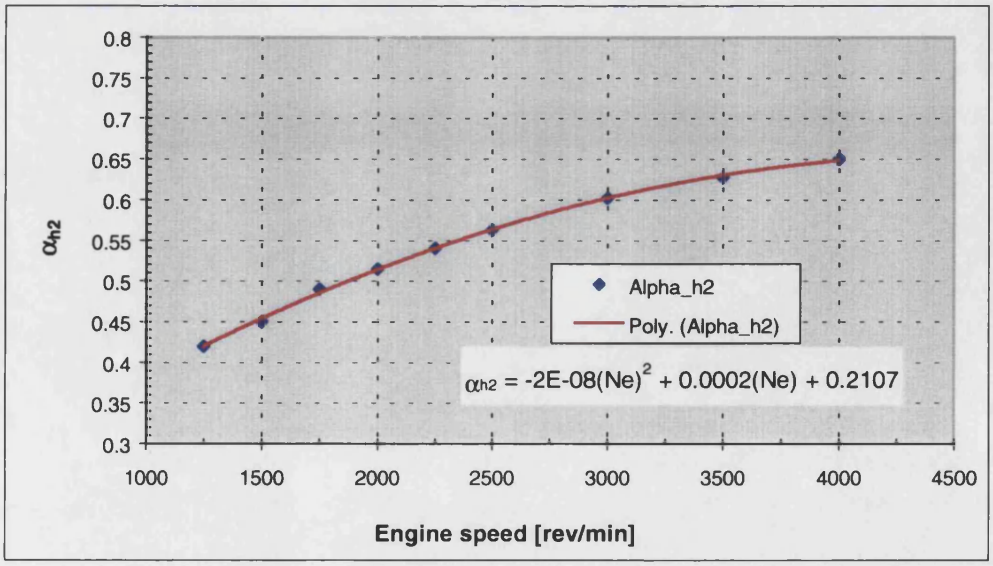

Figure 7.38a: Smoothed values of α_{h2} vs. engine speed

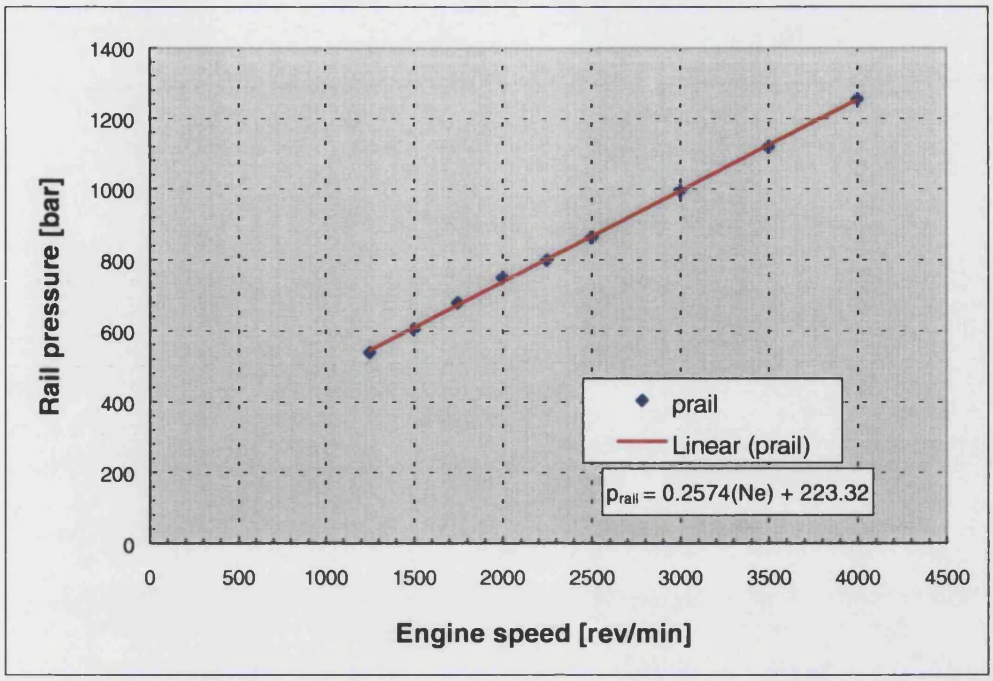

Figure 7.38b: Rail pressure vs. engine speed

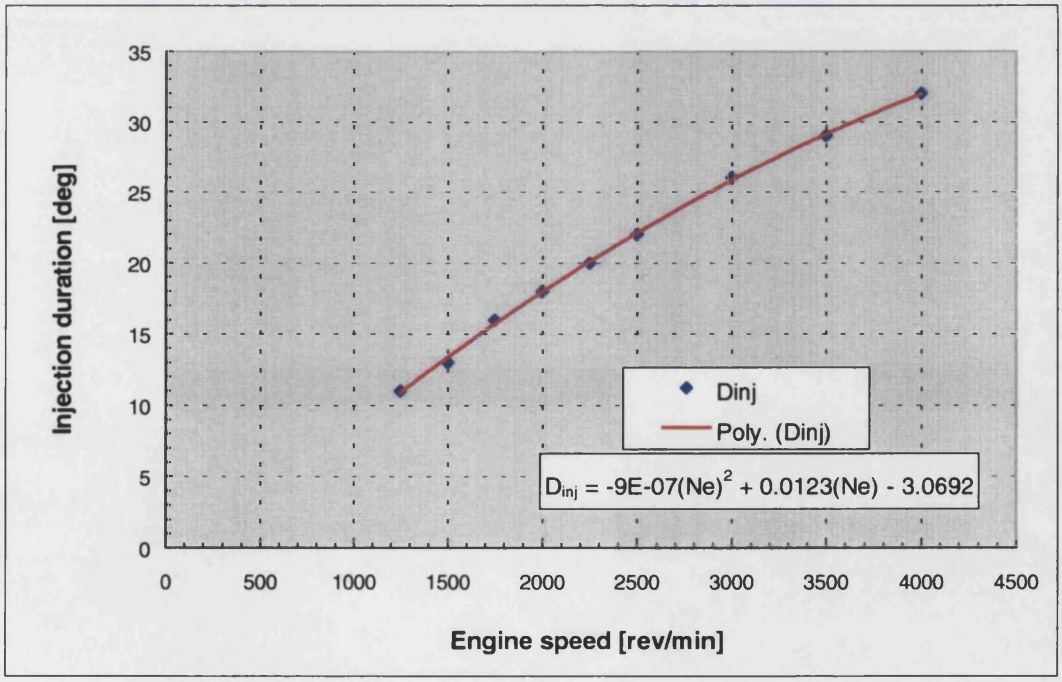

Figure 7.38c: Duration of fuel injection vs. engine speed

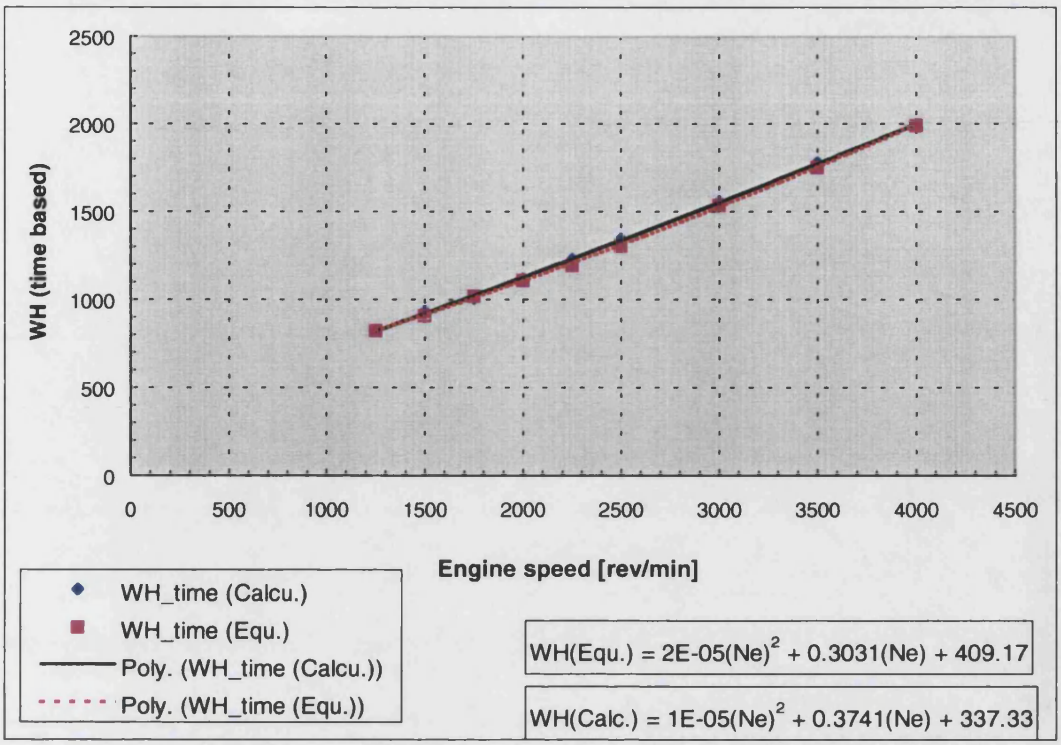

Figure 7.38d: Comparison of WH vs. engine speed

Table 7.8: Summary of smoothed values of α_{h2}, D_{inj} and p_{rail} for calculation of *WH* (correlation based on engine speed)

N_e rev/min	p_{rail} bar	p_{cyl} bar	v_N m/s	D_{inj} °CA	α_{h2} -	*WH* CA based	(RVSP) -	*WH* Time based	*WH* (equ.)	FMFR kg/s
1250	540	56.3	341.4	11	0.38	0.0951	1	713.536	713.536	0.00401
1500	605	70.1	359.01	13	0.43	0.0964	1.2	867.811	856.243	0.00421
1750	679	79.7	380.02	16	0.49	0.0963	1.4	1011.11	998.951	0.00446
2000	750	99.2	396	18	0.53	0.0979	1.6	1175.02	1141.66	0.00465
2250	800	99.1	410.98	20	0.56	0.0975	1.8	1315.63	1284.37	0.00482
2500	865	97.9	429.95	22	0.58	0.0948	2	1421.57	1427.07	0.00505
3000	995	91.5	466.6	26	0.63	0.0952	2.4	1713.67	1712.49	0.00548
3500	1120	91.2	497.89	29	0.66	0.095	2.8	1994.19	1997.9	0.00584
4000	1255	86.4	530.64	32	0.69	0.0962	3.2	2307.84	2283.32	0.00623

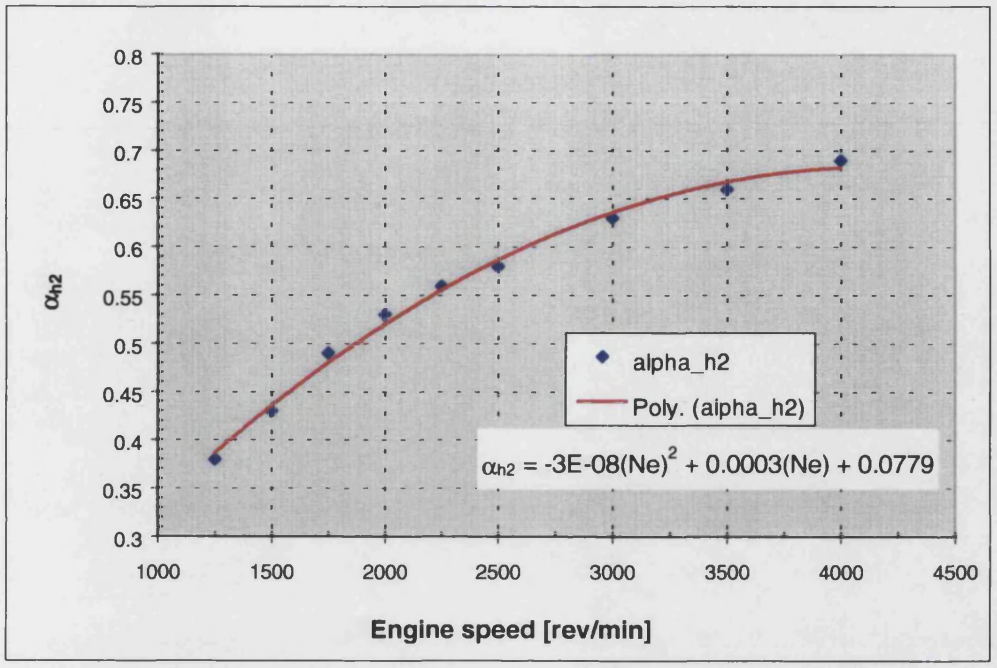

Figure 7.39a: Smoothed values of α_{h2} vs. engine speed

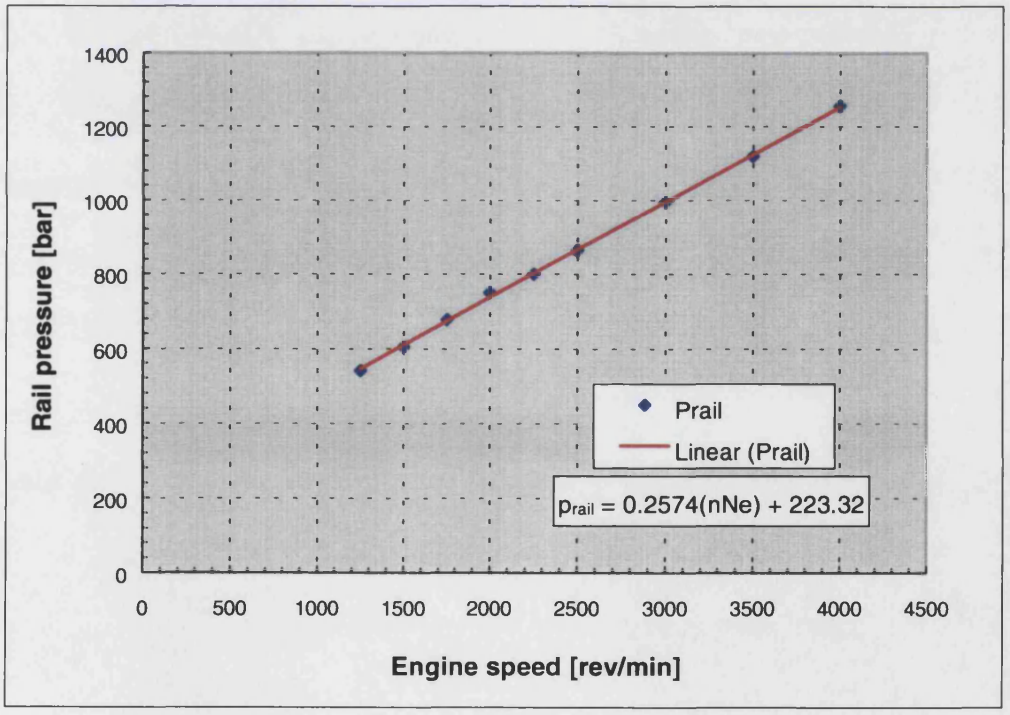

Figure 7.39b: Rail pressure vs. engine speed

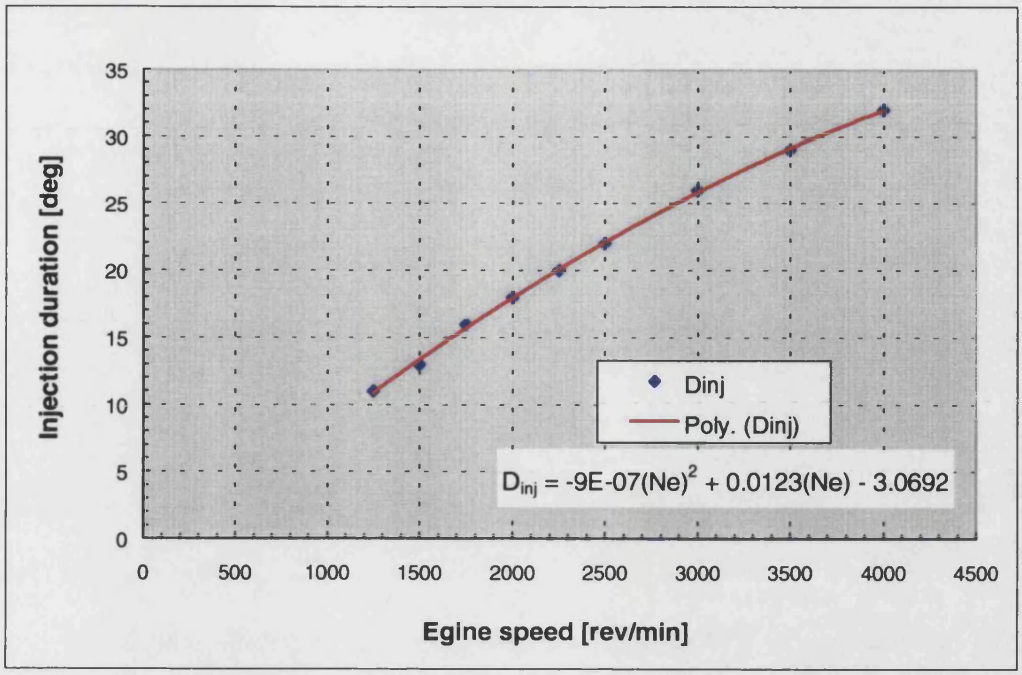

Figure 7.39c: Duration of fuel injection vs. engine speed

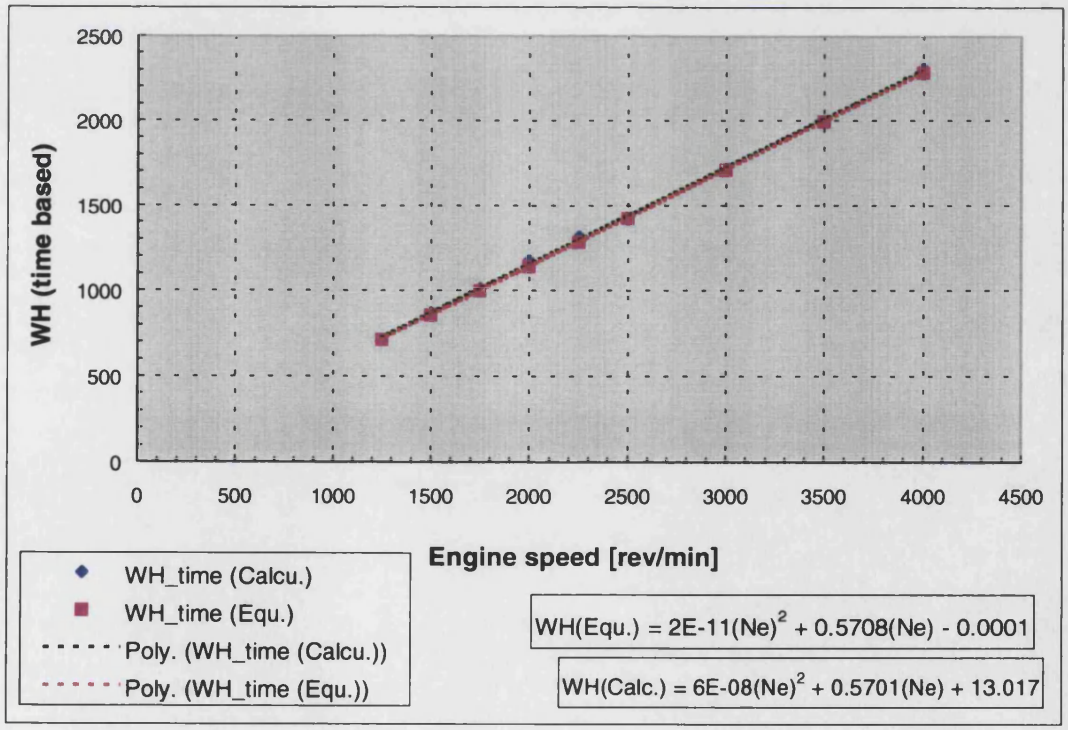

Figure 7.39d: Comparison of WH vs. engine speed

7.5 Conclusions

1. The initial formulation of heat release conditions under pure diffusion burning, presented by *Chmela and Orthaber* [1], has been greatly extended resulting in a series of analytical expressions for both heat release rate and cumulative heat release.

2. The simplest of those formulations, neglecting ignition delay and assuming instantaneous needle lift overestimates heat release rate (ROHR) up to the end of injection.

Inclusion of ignition delay, still with instantaneous needle lift, also results in overestimate of ROHR up to end of injection.

The final formulation, which includes both ignition delay and a finite rate of needle lift, assumed to coincide with the ignition delay period, gives very good agreement with experimental ROHR's.

3. There is some evidence for the existence of premixed burning at low engine speeds (see also section 9.3), which has deliberately been neglected in order to facilitate the formulation of a wholly analytical heat release model based on *Chmela and Orthaber* approach of pure diffusion burning

4. A well known difficulty when attempting to adjust the various parameters in the final formulation, above, to obtain the best possible agreement of the cylinder pressure traces, is that this leads to significant differences in ROHR.

Hence the alternative approach of adjusting these parameters to obtain the best possible agreement of the ROHR traces was adopted.

5. To extend the predictive ability of the analytical approach, correlations of the mixing rate factor *WH* with the basic engine operating variables of rail pressure expressed as injection velocity, and engine speed, were established.

While the resulting expression are still only applicable to the 1.8 litre Ford DI HPCR Diesel engine, the method nevertheless has a high degree of generality.

7.6 Reference

1. **Chmela, F.G., and Orthaber, G.C.**, "Rate of Heat Release Prediction for Direct Injection Diesel Engines Based on Purely Mixing Controlled Combustion", SAE 990186 (1999).

2. **Woschni, G.**, "Universally Applicable Equation for the Instantaneous heat Transfer Coefficient in the Internal Combustion Engine", SAE 670931 (1967).

CHAPTER 8

Spray development under combusting conditions

8.1 Introduction

Spray development under combusting conditions has been much less extensively investigated than under non-combusting conditions, as previously discussed in chapter 3. Clearly, experimental and theoretical investigations of combusting sprays require far more sophisticated techniques than is the case for non-combusting sprays.

The literature survey of section 8.2 is divided into two sections as follows:

8.2.1 Experimental investigations

8.2.2 Analytical approaches.

The original work described in sections 8.4 and 8.5 is based on a relatively simple phenomenological approach developed from that in chapter 3 for non-combusting sprays, but drawing also on the multi-zone combustion model incorporated in the submodel for NO_x formation previously developed at the University of Bath by *D.Dang* and revised by *F.J.Wallace* [1].

This provides a basis for defining successive elements of the developing combusting spray, which in turn is combined with the swirl generation models of chapter 4 and the spray deflection model of chapter 3.

8.2 Literature survey

8.2.1 Experimental investigation

In the early studies of the spray combustion phenomena, the majority of researches such as *Agnew* [2], *Faeth* [3] and *Kuo* [4], focused on steady spray combustion in furnaces and gas turbines, since direct measurement of combustion phenomena under

real engine conditions was impossible due to its considerable complexity in addition to technical problems related to experimental measurement.

Over the past decade, researchers have used laser-based planar imaging diagnostics to provide the detailed measurement needed to better understand the diesel combustion process. A wide variety of these diagnostics have been applied to direct injection diesel combustion using a specially designed optically accessible research engine. These laser-imaging measurements have an abundance of new information about the details of diesel combustion and emission formation.

Single-point Rayleigh scattering was used by *Arcoumanis* et al. [5-7]. To avoid the interference of droplets, his group simulated the evaporating diesel jet by injection of gaseous Freon-12. *Scheid* et al. [8] and later *Heinze* et al. [9] applied spontaneous Raman spectroscopy to obtain measurements of the local fuel-air ratio in a diesel combustion chamber. Both types of diagnostics are quantitative, but both techniques were exclusively applied as point measurements in these works. However the diesel fuel spray is a highly turbulent jet, thus point measurements can provide only local statistical information of the phenomena.

Over the past ten years, a wide variety of laser-sheet-imaging and other optical diagnostics have been applied to diesel combustion by *Dec* and co-workers [10-13], at the Sandia Combustion Research Facility in Livermore, California. They carried out an extremely extensive experimental investigation on a large four-stroke low speed optical Diesel engine (figure 8.1) operating at 1200 rev/min, under somewhat unrepresentative operating conditions relative to those in HSDI engines with common rail injection, including a substantial amount of premixed burning. The engine specification and operating conditions are summarised in table 8.1.

Although the effects of wall interaction and swirl flow which are very important in small-sized high-speed DI Diesel engines, were not considered, the work of *Dec* and co-workers [10-13] provides a framework for interpreting experimental measurements and thus a guide to the development of numerical modelling of a combusting diesel fuel jet.

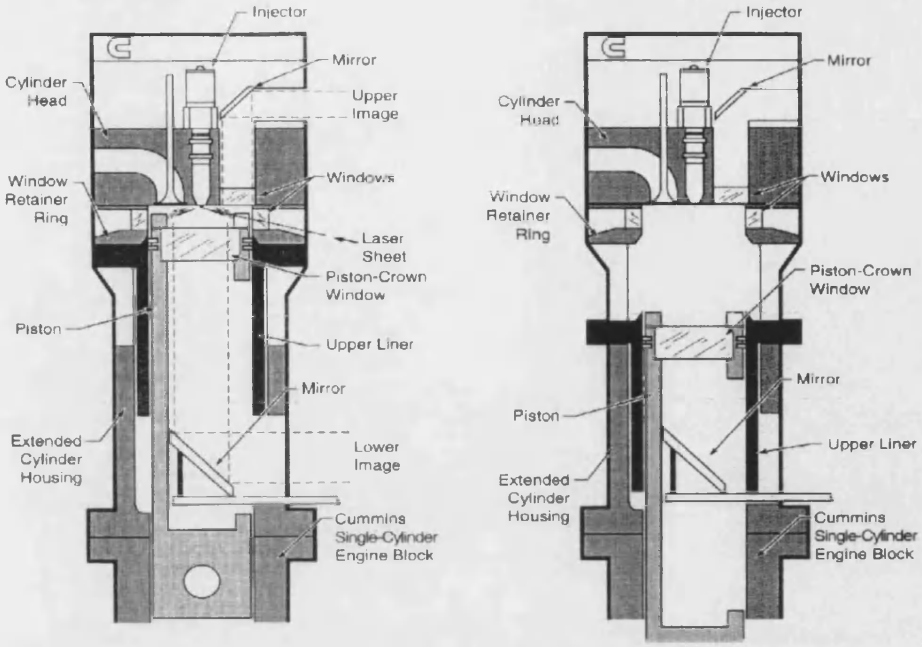

a) The upper liner in operating position b) The upper liner in cleaning position

Figure 8.1: Schematic of optical-access Diesel engine [11]

Table 8.1: Specification and operating conditions of the optical-access Diesel engine [11]

Bore	139.7 mm
Stroke	152.4 mm
Displacement	2.34 litre
Compression ratio	10:1 or 11:1
Injection nozzle spec.	8 × 0.194 mm
Rail pressure	68 to 86 MPa, dependent on fuel load
Fuel injected per cycle	0.0960 and 0.1554 ml dependent on fuel
Engine speed	1200 rev/min

Figure 8.2 gives a useful conceptual model of the entire combustion process, although again it is not wholly applicable to the HSDI situation.

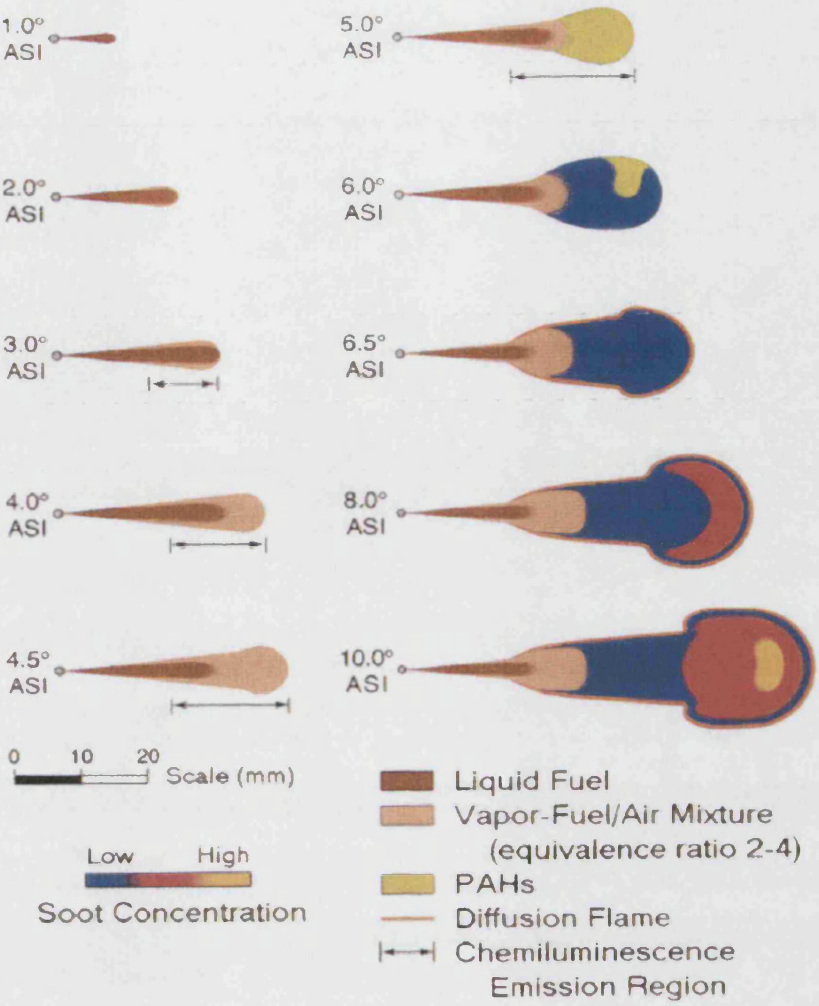

Figure 8.2: Schematic of early flame images from laser measurements [13]

Figure 8.2 shows a sequence of the early stages of the diesel combustion event. The sequence begins shortly after the start of fuel injection and continues through the premixed burn and into the start of quasi-steady combustion.

The pictures start immediately after the beginning of injection and show the development of liquid jet. As penetration increases, more and more hot air is entrained into the jet, causing its temperature to rise. As the liquid fuel is heated, it vaporises and a sheath of vaporised heated fuel/air mixture forms around the jet's periphery and at the leading edge of the jet. The vaporising fuel jet grows until about 5 °CA after the start of injection when the temperature in the plume reaches approximately 750 K. At these temperatures, reactions typical of the breakdown of high cetane fuels begin to occur. As these reactions take place and additional hot air is entrained into the jet, temperatures within the jet reach approximately 825 K, increasing the rate of these

oxidation reactions. As figure 8.2 indicates, between 5.5 °CA and 6.5 °CA after start of injection (ASI), a diffusion flame forms at the jet periphery between the products of the fuel-rich premixed burn (which contain a significant quantity of unconsumed fuel) and the surrounding air. By 6.5 °CA ASI this thin diffusion flame completely encircles the downstream portion of the jet. It extends back toward the injector to a point just upstream of the tip of the liquid fuel penetration. As depicted in the schematic, the liquid-fuel length becomes about 2 to 3 mm shorter as the diffusion flame forms, presumably due to local heating by the flame. By 9.0 °CA ASI to end of injection, as the combustion transitions to being purely mixing-controlled, the overall appearance of the jet shows only moderate changes. This is probably because the jet was already almost in a mixing-controlled-burn mode as the last of the premixed fuel was burning out. As shown in the 10 °CA ASI schematic, the jet has penetrated further, and the head vortex is becoming well formed.

8.2.2 Analytical approaches

The models used for the analysis and prediction of the spray combustion behaviour can be divided into two categories of multi-zone and multi dimensional models.
Several multi-zone models have been developed to analyse combustion in DI Diesel engines. Most of these models use experimental and theoretical correlations for the fuel jet penetration, and divide the chamber into burning and non-burning zones. The effects of swirl on the spray deflection can be empirically introduced into the models.
The simplest form of multi-zone model is the two-zone model, *Whitehouse and Sareen* [14]. The cylinder charge is divided into a burning and non-burning zone, with air entrainment from the latter to the former. However, it makes the unrealistic assumption of a uniform mixture composition in the burning zone. True multi-zone models simulate a much more realistic process.
A general study of the available literature has revealed two different types of zoning method. The first method separates the fuel into individual packets, which have trajectories depending on their radial position relative to the axis of the jet, such as *Meguerdichian & Watson* [15], or *Bazari* [16], which has already been fully explained in chapter 2 sections 2.2.4.2a. The other method of zoning, as used by *Shahed, Chiu, and Lyn* [17, 18], has a system of expanding zones with iso-equivalence ratio

boundaries. Again the main principle of this model has been described in section 2.2.4.2b.

The application of computational fluid dynamics (CFD) to spray combustion allows the fundamentals of single-droplet behaviour to be combined with fluid mechanics to predict fuel preparation effects in practical spray combustors. For combustion applications the mechanism of spray vaporisation and mixing is of primary importance. Application of heat and mass transfer theory allows models to predict vaporisation histories for a single, undeformed droplet of pure fuel. Some of these CFD codes, which are used by many researchers in order to simulate spray formation, will be presented in this section.

One of the first codes developed for transient, variable volume, chemically reactive flow fields was KIVA [19]. Since its inception, improvements to KIVA have resulted in KIVA-2 [20] and KIVA-3 [21] versions which, include more recent spray and combustion submodels in addition to the inclusion of moving boundaries, i.e. valves or ports. *Tanner* [22] performed both non-reactive and reactive calculations on a Cray-YMP with CRI/Turbokiva 2.2, an enhanced version of the KIVA-3 code developed at Los Alamos National Laboratory, New Mexico, U.S.A. The computations were performed for reacting and non-reacting, solid-cone hexadecane diesel sprays, injected at a constant injection rate, axially from the top centre into a constant-volume cylindrical chamber whose air was subject to uniform turbulent kinetic energy.

Rutland et al [23] used a computer model based on the KIVA-2 and KIVA-3 computer codes but with some submodels being improved. The submodels that were updated were: spray atomisation; drop drag with distorting and breaking up of drops, multi-step kinetics ignition and laminar-turbulent characteristic time combustion.

They performed calculations for a 2.44 l Caterpillar single cylinder engine at 1600 rev/min and 15:1 compression ratio. Diesel fuel was injected through a 6-hole nozzle of 0.26 mm hole diameter into compressed air after induction and compression calculations were performed by using KIVA-3. The main findings of this study were:

- After an ignition delay 4 °CA (with start of injection at 11 °CA BTDC), the flame extended back to the injector nozzle.
- Excellent agreement was obtained between the predicted and measured cylinder pressure and heat release data.

- Using the standard KIVA-2 ignition and combustion models, combustion was predicted to be too fast initially, resulting in lower levels of cylinder pressure and consequently in large discrepancies between measured and predicted values.

Ikonomou [24] developed the EPISO engine code (*Watkins et al* [25]) to attain a better understanding of in-cylinder processes of fuel-air interactions, ignition & combustion in the combustion chamber of DI Diesel engines. In his application, calculations are made of ignition and combustion of a small Ford designed direct injection turbocharged intercooled Diesel engine. The engine was equipped with an 'omega' shaped piston bowl and a five-hole injector. Three different studies were carried out of the effects of using different fuel loads and two different engine speeds.

The specifications of the modelled engine and operating conditions are summarised in table 8.2.

Table 8.2: Specification and operating conditions of the engine used in the demonstration calculations [24]

Bore	82.5 mm
Stroke	82.0 mm
Displacement	1.8 litre
Clearance gap	0.9551 mm
Compression ratio	19.1:1
Bowl diameter	40.0 mm
Injection nozzle spec.	5 × 0.18 mm
Fuel injected	11.75 and 23.5 mm^3/cyc/cyl
Engine speed	1200 and 2400 rev/min

The specific contributions of his work are as follows:

- Incorporation of modelling of spray atomisation for the engine calculations.
- Incorporation of modelling of diesel ignition.
- Incorporation of modelling of diesel combustion.
- Validation of the spray calculation method by comparison with data from experiments.
- Predictions of the spray-air interaction, ignition and combustion for a production engine.

Figures 8.3 and 8.4 show typical results of spray development for an operating condition of 2400 rev/min and 11.75 mm^3, based on size in plan and side view respectively.

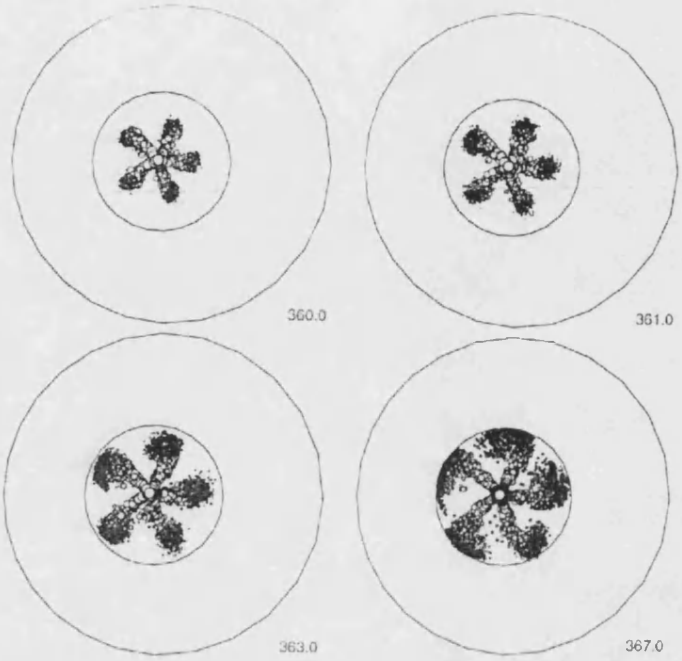

Figure 8.3: Typical result of spray development based on size from 360to 367 °CA [24]

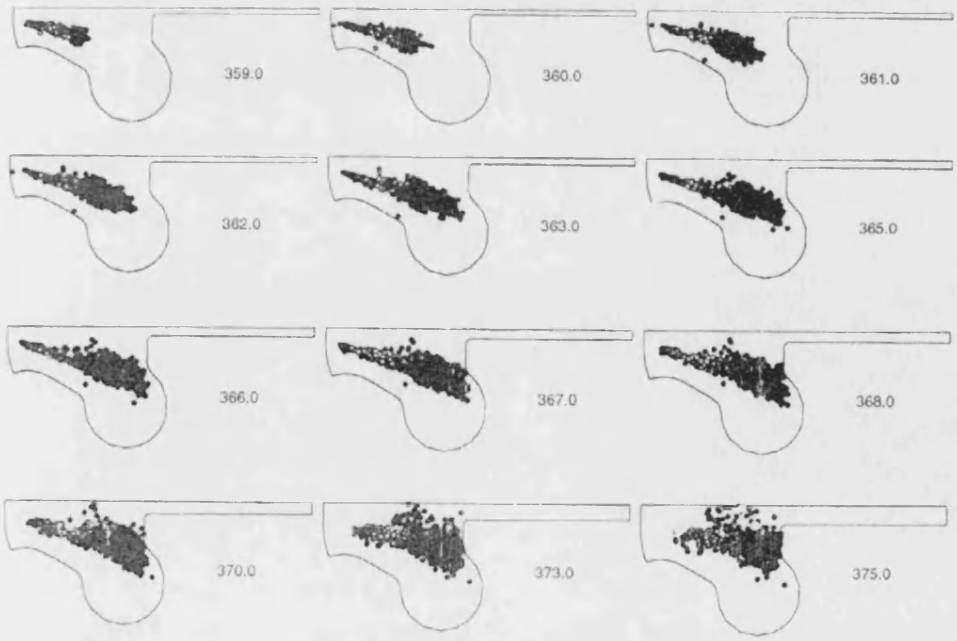

Figure 8.4: Schematic of spray development based on size from 359 to 375 °CA [24]

The main features, which have been revealed by the engine calculations, are the following:

i) The gas flow is significantly disturbed the spray: it is entrained into them and accelerated in the direction of the injection. Also turbulence generation results from the high relative velocities between the gas and spray droplets (spray-induced turbulence) and form the spray- wall impingement process;

ii) If the swirl is strong enough, then the sprays are deflected from their original directions. Small droplets are carried by the swirl close to the edge of the downstream spray, thus delaying the wall impingement and reducing the droplet penetration. This droplet deflection by the swirl results in better fuel-air mixing and consequently more efficient burning and higher temperatures;

iii) The first ignition site occurred near the nozzle, at the edge of the vapour plume in a region of small hot droplets. Slow pre-ignition reaction, though, extended over the five sprays;

iv) If swirl and turbulent mixing are insufficient to substantially extract the fuel vapour from the spray plumes, then fast burning conditions are not promoted;

v) The burning zone develops along the vapour zone periphery towards the bowl wall. Reverse squish, enhanced by the pressure expansion due to combustion, drives the flame into the squish region, resulting in high-temperature zones in there;

vi) Poor mixing results in incomplete burning with some percentage of the fuel vapour (5%) left unburned even by 60 °CA ATDC;

vii) Due to strong evaporation under burning conditions, more small droplets evaporate completely, thus leaving the relatively large droplets in the chamber;

8.3 Evaporation/mixing phase during delay period

Spray development and propagation under both non-evaporative and evaporative conditions has already been dealt with in chapter 3, section 3.2.1. For the purpose of the present chapter on combustion sprays, it is essential to differentiate between the initial development and propagation of the spray up to initiation of combustion, i.e. the ignition delay and the subsequent development under combustion conditions.

The first element of spray, which simply represents the non-burning phase during the delay period, is referred to by *Siebers* and *Higgins* [26] as "lift-off length".
As has already been stated in chapter 5, section 5.3.3, the dependence of lift-off length on injection velocity v_N and orifice diameter D_N can be obtained from equation (5.11). The corresponding ignition delay (ms or °CA) is calculated using equation (5.14).

8.4 Development of Undeflected burning spray based on NO_x subroutine

The NO_x subroutine, which was developed by *Dang* [1] is essentially a multi-zone combustion model coupled with the equations of the Zeldovich mechanism for NO_x formation, but unlike models such as *Meguerdichian & Watson* [15] or *Bazari* [16] does not require spatial definition of the combustion zones. The output of the subroutine which is discussed in detail in appendix A consists of the following zonal parameters, in which zone 1 always represents the air zone, with subsequent zones representing successive combustion zones:

Zonal mass: m_z

Zonal volume: V_z

Zonal temperature: T_z

Zonal equivalence ratio: ϕ_z

NO concentration: $[NO]_z$

With changing in the spray cone half-angle from θ_{ig} (from equation 5.4) during the ignition delay period to θ (based on the literature review) during the combustion zones, and with adjustment for some remaining liquid fuel in combustion zones the first combustion zone element of undeflected spray proceed as follows:
1) Since the NO_x routine gives the value of fuel burnt (m_{fb}) at θ_{HR} (crank angle at start of heat release), i.e. $(m_{fb})_{HR}$, the mass of fuel actually burnt during the chosen interval $\Delta\theta$ of 1 °CA can be obtained from:

$$\Delta m_{fb} = (m_{fb})_{\theta_{HR}+\Delta\theta} - (m_{fb})_{\theta_{HR}} \tag{8.1}$$

2) Similarly the quantity injected during the interval becomes:

$$\Delta m_{finj} = (m_{finj})_{\theta_{HR}+\Delta\theta} - (m_{finj})_{\theta_{HR}} \tag{8.2}$$

3) The instantaneous spray mass and volume are calculated by respectively subtracting the air zone mass m_{zl} or volume V_{zl} from the total cylinder mass m_{cyl} or volume V_{cyl} as follows:

$$(m_{sp})_{\theta_{HR}} = (m_{cyl})_{\theta_{HR}} - (m_{Z1})_{\theta_{HR}} \tag{8.3a}$$

$$(m_{sp})_{\theta_{HR}+\Delta\theta} = (m_{cyl})_{\theta_{HR}+\Delta\theta} - (m_{Z1})_{\theta_{HR}+\Delta\theta} \tag{8.3b}$$

$$\therefore \quad \Delta m_{sp} = (m_{sp})_{\theta_{HR}+\Delta\theta} - (m_{sp})_{\theta_{HR}} \tag{8.3c}$$

4) Mass of unburnt fuel in the first combustion element can be obtained from:

$$m_{fub} = \Delta m_{finj} - \Delta m_{fb} \tag{8.4}$$

5) The evaluation of spray volume proceed as follow:

Volume of air zone at θ_{HR} is:

$$(V_{z1})_{\theta_{HR}} = \left(\frac{m_{z1} \cdot R \cdot T_{z1}}{p}\right)_{\theta_{HR}} \tag{8.5a}$$

Volume of spray at θ_{HR} is:

$$(V_{spray})_{\theta_{HR}} = (V_{cyl})_{\theta_{HR}} - (V_{z1})_{\theta_{HR}} \tag{8.5b}$$

then volume increment of spray during the first interval can be obtained from:

$$\therefore \quad \Delta V_{spray} = (V_{spray})_{\theta_{HR}+\Delta\theta} - (V_{spray})_{\theta_{HR}} \tag{8.5c}$$

It also follows from equation (8.5a) that the volume increment for the air zone becomes:

$$\Delta V_{z1} = (V_{z1})_{\theta_{HR}+\Delta\theta} - (V_{z1})_{\theta_{HR}} \tag{8.5d}$$

so that the associated mass of air entrained into the spray as a whole becomes:

$$\Delta m_e = -\Delta m_{z1} = \Delta V_{z1} \rho_{z1} \tag{8.5e}$$

where,

$$\rho_{z1} = \frac{p_{cyl}}{R \cdot T_{z1}} \tag{8.5f}$$

Numerical calculations show that the spray mass increment Δm_{sp} for the spray as a whole always exceeds the mass of the new element formed, i.e. $\Delta V_{sp} \cdot \rho_{sp}$, indicating that air entrainment is distributed over the whole spray rather than being limited to the new element formed. This also accords with the phenomenological model.

6) The spray mean density during the first interval becomes:

$$\rho_{sp} = \frac{\Delta m_{sp} + m_{fub}}{\Delta V_{sp}} \tag{8.6}$$

7) The first burning spray propagation distance, Δx_1, may now be calculated based on assumed simple shape of the spray envelope, initially a plain cone of given divergence angle $2\theta_{ig}$ changing to 2θ as figure 8.5 together with spray volume from equation (8.5c) as follow:

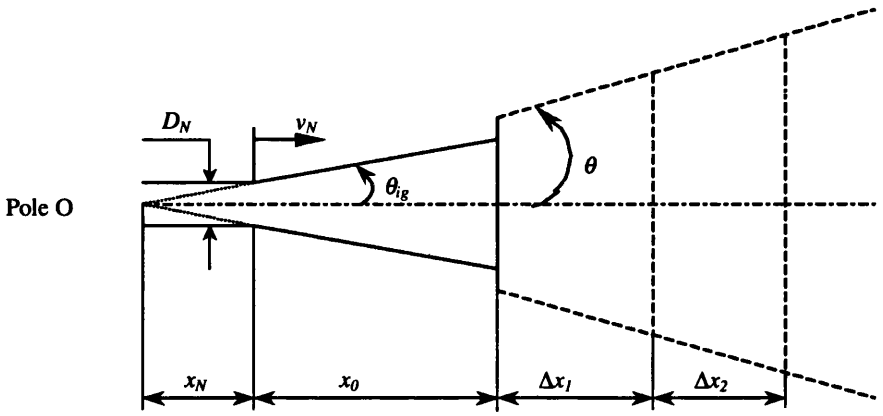

Figure 8.5: Undeflected plain cone spray

$$\Delta V_{sp} = \frac{\pi}{3}\left[(x_N + x_0 + \Delta x_1)^3 - (x_N + x_0)^3\right]\tan^2\theta \qquad (8.7)$$

where $x_N = D_N / 2\tan\theta_{ig}$, and x_0 is the spray propagation distance during the delay period, which can be obtained from equation (5.11) as lift-off length. With an estimated spray half angle, θ, based on the literature review in chapter 3 section 3.2.1, together with spray volume from equation (8.5c), equation (8.7) can be solved with the spray volume increment ΔV_{sp} from equation (8.5c), for the spray propagation distance Δx_1 as the first element of combustion zone.

8) The propagation mean velocity during the step can be obtained from:

$$v_1 = \frac{\Delta x}{\Delta t} \qquad (8.8)$$

where Δt is the chosen time increment becomes:

$$\Delta t = \frac{\Delta\theta \times 60}{360 \times N_e} \qquad (8.9)$$

where N_e is the engine speed (rev/min)

9) Finally, v_1 can be compared with the velocity calculated from equ. (8.10), based on the phenomenological model of section 3.3.1.3, and repeated in section 5.2.2.

$$v_2 = \sqrt{\frac{\rho_f}{\rho_{sp}}} \frac{v_N D_N}{\left(1+\frac{\bar{\rho}_{air}}{\rho_{sp}}\frac{C_f}{2}\right)^{1/2} 2\bar{x}_1 \tan\theta} \tag{8.10}$$

where, mean spray propagation distance and mean air density can be obtained from equations (8.10a) and (8.10b) respectively:

$$\bar{x}_1 = x_0 + \frac{\Delta x_1}{2} \tag{8.10a}$$

$$\bar{\rho}_{air} = \left[\left(\frac{p}{R \cdot T_{z1}}\right)_{\theta_{HR}} + \left(\frac{p}{R \cdot T_{z1}}\right)_{\theta_{HR}+\Delta\theta}\right] \Big/ 2 \tag{8.10b}$$

The above procedure for the evaluation of the various spray propagation parameters for the first combustion element is then repeated for all subsequent spray elements up to the point of spray impingement on the combustion chamber wall. After impingement two wall jets are represented as two semi cones, their combined volume should be calculated as before.

Typical results for the engine speed of 2000 rev/min as given by table 7.5a, chapter 7 namely,

Engine speed	Fuel Injection	Injection pressure	Cylinder pressure at SOI	Injection Duration	Compression ratio	Nozzle diameter	No. of nozzle hole	Swirl ratio at IVC
N_e (rev/min)	(mm^3/sht)	(bar)	(bar)	(° CA)	(-)	(mm)	(-)	(-)
2000	42.4	750.0	100.3	18.0	18.2:1	0.15	5	3.0

for a spray with half angle of 10 degrees are shown in figure 8.6, which gives the comparison of the two alternative methods.

The two methods of evaluating spray velocity decay with propagation distance are seen to give very similar results, particularly in the combusting phase. This confirms that the procedure based on the zone formation analysis of the NO_x subroutine with its implied rate of entrainment is broadly consistent with the physically based impulse model of chapter 3, using established conservation laws of mass and momentum.

The results of this spray analysis are fully discussed in chapter 9, section 9.2.3.

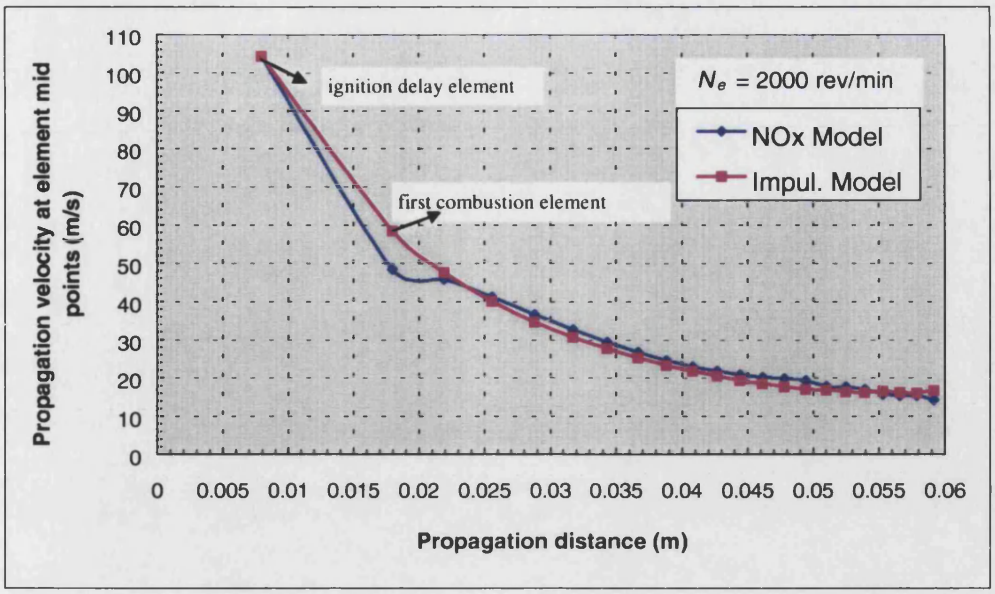

Figure 8.6: Results of the undeflected plain cone spray

8.5 Development of burning deflected spray

8.5.1 Development of basic equations

Following the development of the simplified deflection equations for the isodense spray in section 3.4, the following equations are now developed for the non-isodense (fuel vapour-liquid or combusting) spray.

Considering first the transfer of momentum flux normal to the spray centre line (see figure 8.7):

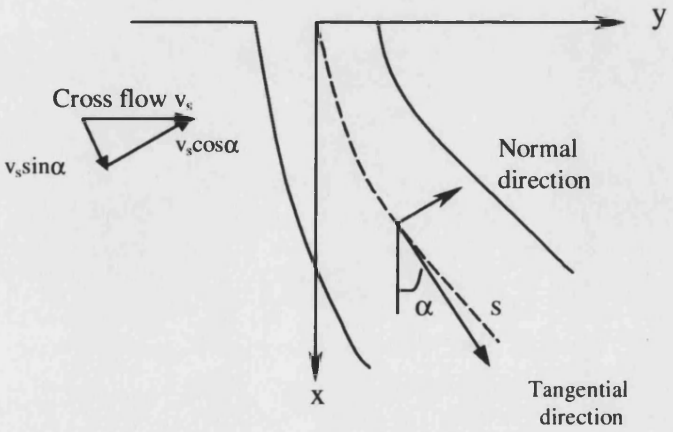

Figure 8.7: Deflected spray in a cross-flow field

Rate of mass entrainment, in terms of the spray properties derived from NO_x subroutine (see section 8.4) may be expressed as,

$$\frac{d\dot{m}_{e_D}}{ds} = \frac{\Delta(v \cdot \rho_{sp} \cdot A)_n}{(\Delta s)_n} \tag{8.11}$$

where suffix n refer to the n^{th} spray element

The local swirl velocity $(v_s)_n$, for the element of entrained air, instead of being reduced to zero, as for a spray of zero inclination, $\alpha_n = 0$, will be reduced to $\bar{v}_n \sin\bar{\alpha}_n$, so that the entrained momentum flux becomes, normal to the spray axis

$$\dot{M}_n = \frac{\Delta(v \cdot \rho_{sp} \cdot A)_n}{(\Delta s)_n}(v_s - \bar{v}\sin\bar{\alpha})_n \cdot (\Delta s)_n \cdot \cos\bar{\alpha}_n \tag{8.12}$$

where α_n is the local inclination of the spray axis (figure 8.7).

Next considering the drag force on the element due to the swirl flow over it, again normal to the spray axis,

$$(F_D)_n = \frac{1}{2} C_f \cdot \rho_{air} (v_s)_n^2 \cos^2\bar{\alpha}_n \cdot \bar{D}_n \cdot (\Delta s)_n \tag{8.13}$$

where C_f drag coefficient

$(v_s)_n$ cross flow velocity (m/s)

$\bar{D}_n$ local spray means diameter (m)

The sum of the entrained momentum flux and spray drag effects (equations 8.12 and 8.13) is balanced by the centrifugal force on the spray element *n* travelling along its moved path which is given by, assuming a circular curve section of diameter $\bar{D}_n$ by,

$$F_{cent} = \frac{\frac{\pi}{4}\bar{D}_n^2 \cdot \rho_{sp}(\Delta s)_n \bar{v}_n^2}{R_n} \tag{8.14}$$

where R_n is the local radius of curvature of the spray trajectory, $R_n = \dfrac{\left[1 + (dy/dx)_n^2\right]^{3/2}}{(d^2y/dx^2)_n}$

where $(dy/dx)_n = \tan\bar{\alpha}_n$ and then

$$\left[1 + (dy/dx)_n^2\right]^{3/2} = (1 + \tan^2\bar{\alpha}_n)^{3/2} = (\sec^2\bar{\alpha}_n)^{3/2} = \cos^{-3}\alpha_n \tag{8.15}$$

so that F_{cent} reduces to:

$$F_{cent} = \frac{\pi}{4}\bar{D}_n^2 \cdot \rho_{sp}(\Delta s)_n \bar{v}_n^2 (d^2y/dx^2)_n \cos^3\bar{\alpha}_n \tag{8.16}$$

With equation (8.16) = equation (8.12) + equation (8.13)

$$\frac{\pi}{4}\rho_{sp}\bar{v}_n^2\bar{D}_n^2\left(\frac{d^2y}{dx^2}\right)_n(\Delta s)_n\cos^3\bar{\alpha}_n=\left[\frac{\Delta(v\rho_{sp}A)_n}{(\Delta s)_n}\left(1-\frac{\bar{v}_n\sin\bar{\alpha}_n}{(v_s)_n}\right)+\frac{1}{2}C_f\cdot\rho_{air}(v_s)_n\bar{D}_n\cos\bar{\alpha}\right]\cdot(v_s)_n\cdot(\Delta s)_n\cos\bar{\alpha}_n \tag{8.17}$$

With a simple numerical method for evaluation of d^2y/dx^2, (see figure 8.8), using equation (8.18):

$$\left(\frac{d^2y}{dx^2}\right)_n=\frac{(y)_n-2(\bar{y})_n+(y)_{n-1}}{2(\Delta x/2)_n^2} \tag{8.18}$$

where, $(\Delta x)_n=(\Delta s)_n\cdot\cos\bar{\alpha}_n$

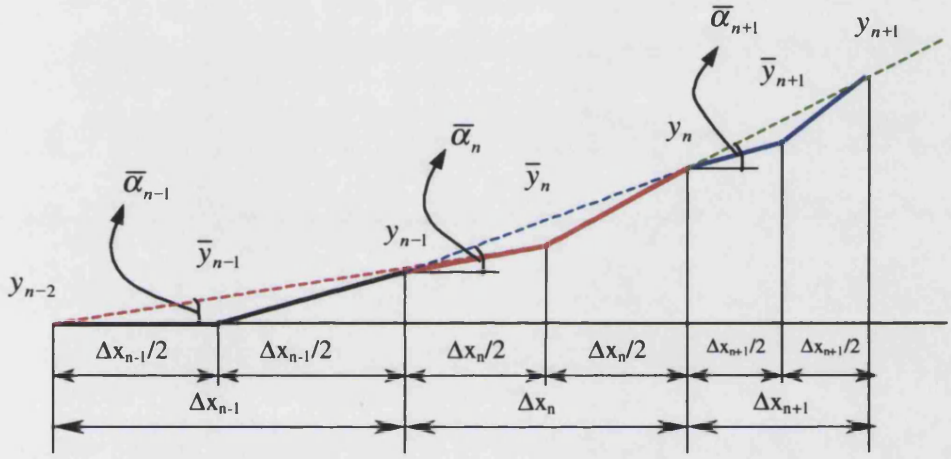

Figure 8.8: Deflected spray in a cross-flow field

The transverse deflection $(y)_n$ of spray element n may finally be expressed as:

$$(y)_n=\left(\frac{2(\Delta s)^2}{\pi\rho_{sp}\bar{v}_n^2\bar{D}_n^2}\right)\cdot\left[\frac{\Delta(v\rho_{sp}A)}{(\Delta s)_n}\cdot\left(1-\frac{\bar{v}_n\sin\bar{\alpha}_n}{(v_s)_n}\right)+\frac{1}{2}C_f\cdot\rho_{air}(v_s)_n\bar{D}_n\cos\bar{\alpha}_n\right]\cdot(v_s)_n+2(\bar{y})_n-(y)_{n-1} \tag{8.19}$$

where $(\bar{y})_n$ is the mean deflection over the interval $(\Delta s)_n$, and can be obtained from:

$$(\bar{y})_n=(y)_{n-1}+\frac{1}{2}(\Delta s)_n\sin\bar{\alpha}_{n-1} \tag{8.20}$$

$$\bar{D}_n=2\left(\left(x_n+\sum_{k=1}^{n-1}(\Delta s)_k\right)+\frac{(\Delta s)_n}{2}\right)\tan\theta \tag{8.21}$$

$$\bar{\alpha}_n = \sin^{-1}\left[\frac{(y)_n - (y)_{n-1}}{(\Delta s)_n}\right] \tag{8.22}$$

$$(v_s)_n = \bar{x}_n \cdot \omega_n \tag{8.23}$$

$$\bar{x}_n = \sum_{k=1}^{n-1}(\Delta x)_k + \frac{(\Delta x)_n}{2} \tag{8.24}$$

Typical results of above equations for deflection of a plain cone spray with half angle of 10-degree in large diameter Mexican Hat configuration and for the same conditions as section 8.3 are shown in figure 8.9.

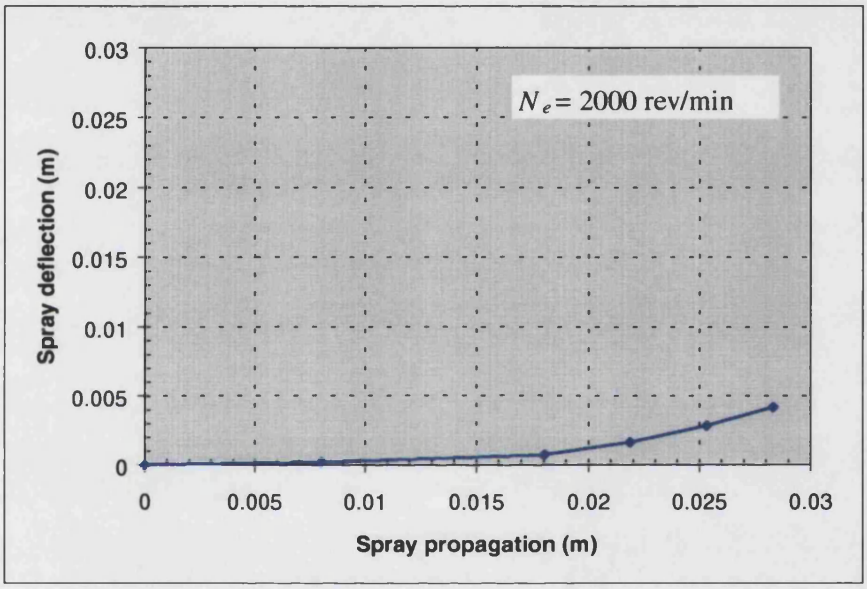

Figure 8.9: Typical deflected spray in a cross-flow field

8.5.2 Deflection in compact bowl-in-piston combustion chamber for low injection pressures

The complete picture of build up and decay of swirl in the compact bowl-in-piston combustion chamber under motoring conditions is discussed in chapter 4, section 4.3.1. In this section due to interaction between swirling air and spray and also due to combustion the situation is much more complicated.

Combustion increases the rate of loss of mass and loss of angular momentum from bowl to cylinder under firing conditions. Rate of entrained linear momentum in direction of swirl becomes:

$$\frac{d\dot{m}_{eD}}{ds}(v_s - \bar{v}\sin\bar{\alpha})$$

Expressed in terms of angular momentum

$$\frac{d\dot{M}}{ds} = \frac{d\dot{m}_{eD}}{ds}(v_s - \bar{v}\sin\bar{\alpha})\bar{r}$$

Where $\bar{r}$ is the local radius,

or
$$\frac{dM}{dt} = \frac{dm_{eD}}{dt}(v_s - \bar{v}\sin\bar{\alpha})\bar{r} \qquad (8.25)$$

This equation can be equated to loss of angular momentum of remaining air in bowl

i.e.
$$\frac{d(I_b\omega_b)}{dt} = \omega_b\frac{dI_b}{dt} + I_b\frac{d\omega_b}{dt} \qquad (8.26a)$$

Where, $I_b = m_b\frac{R_b^2}{2}$,

$$\therefore \quad \frac{d(I_b\omega_b)}{dt} = \frac{R_b^2}{2}\omega_b\frac{dm_b}{dt} + \frac{R_b^2}{2}m_b\frac{d\omega_b}{dt} \qquad (8.26)$$

Conservation of rate of angular momentum in bowl:

$$\frac{d(I_b\omega_b)}{dt} = (Mom_{in})_b - (Mom_{out})_b - (Mom_{fr})_b \qquad (8.27)$$

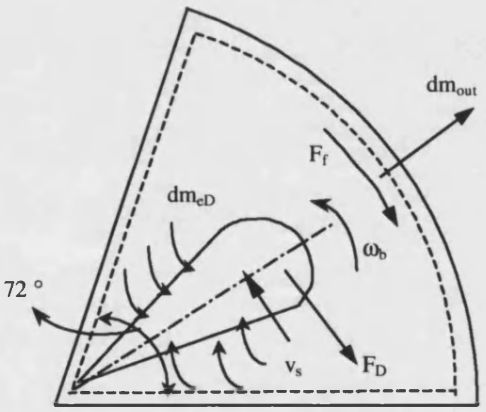

Figure 8.10: Control volume and control surface surrounding one of five sprays

Figure 8.10 shows a 72° segment of the combustion bowl with one of the five sprays, together with its control surface. Starting from equation 8.27 there are two momentum outflow terms, the first by loss of mass from the swirling air to the spray and the second by outflow from the bowl to the main cylinder. Similarly the friction term is made up of two terms viz. the drag exerted by the spray on the swirling air, F_D, from equation 8.13 and the wall friction drag F_f from equation 4.16. The latter corresponded to the first and second the R.H.S. of equation 8.17. Hence,

$$(Mom_{out})_b = \frac{dm_{eD}}{dt} \cdot (v_s - \bar{v}\sin\bar{\alpha}) \cdot \bar{r} + \frac{dm_{out}}{dt}\frac{R_b^2}{2}\omega_b \quad \text{(where, } dm_{out} = -dm_b\text{)} \quad (8.28)$$

$$(Mom_{fr})_b = \frac{1}{2}C_f \rho_a v_s^2 \cos^2\bar{\alpha} \cdot \bar{D} \cdot ds \cdot \bar{r} + \frac{1}{2} f \rho_a R_b^2 \omega_b^2 [\pi R_b (2e + R_b)] R_b \quad (8.29)$$

With $(Mom_{in})_b = 0$ (no inflow), substitution of equations (8.28) and (8.29) in equation (8.27) gives,

$$\frac{R_b^2}{2} m_b \frac{d\omega_b}{dt} + \frac{R_b^2}{2}\omega_b \frac{dm_b}{dt} = -\sum_1^5 \frac{dm_{eD}}{dt}(v_s - \bar{v}\sin\bar{\alpha}) \cdot \bar{r} - \frac{dm_{out}}{dt}\frac{R_b^2}{2}\omega_b - \sum_1^5 \frac{1}{2} C_f \rho_a v_s^2 \cos^2\bar{\alpha}\bar{D} ds \cdot \bar{r} - \frac{1}{2} f \rho_a R_b^2 \omega_b^2 [\pi R_b (2e + R_b)] R_b \quad (8.30)$$

or expressed in finite difference form:

$$\frac{R_b^2}{2} m_b \frac{\Delta\omega_b}{\Delta t} = -\sum_1^5 \frac{\Delta m_{eD}}{\Delta t}(v_s - \bar{v}\sin\bar{\alpha}) \cdot \bar{r} - \sum_1^5 \frac{1}{2} C_f \rho_a v_s^2 \cos^2\bar{\alpha}\bar{D} \cdot \Delta s \cdot \bar{r} - \frac{1}{2} f \omega_b^2 \pi \rho_a R_b^4 e\left(2 + \frac{R_b}{e}\right) \quad (8.31)$$

This should give a solution for $(\omega_b)_{n+1}$ as equation (8.32),

$$(\omega_b)_{n+1} = (\omega_b)_n - \frac{2}{(m_b)_n \cdot R_b^2}\left\{\sum_1^5 (\Delta m_{eD})_n (v_s - \bar{v}\sin\bar{\alpha})_n \cdot \bar{r}_n - \sum_1^5 \frac{1}{2} C_f \rho_a v_s^2 \cos^2\bar{\alpha}\bar{D}\Delta s \cdot \bar{r}\Delta t - \frac{1}{2} f (\omega_b)_n^2 \pi \rho_a R_b^4 e\left(2 + \frac{R_b}{e}\right) \cdot \Delta t\right\} \quad (8.32)$$

N.B. m_b is the mass of remaining air (zone1) in bowl, not total mass of gas in bowl.

Figure 8.11, shows angular velocity in main cylinder, ω, and in the combustion bowl, ω_b, versus crank-angle degree from IVC to EVO again for motoring and also from TDC to EVO based on firing condition.

The above equations cover the processes in the combustion bowl only. For mass and momentum transfer from the combustion bowl to the main cylinder, mass transfer is given by the reduction in "free air", $\frac{dm_{air}}{d\theta}$, derived from the NO_x routine (see appendix A), as also used for the calculation of spray development (see chapter 8, section 8.4). Momentum transfer to the main cylinder will be given by an equation similar to equation (4.23), but substituting $\frac{dm_{air}}{d\theta}$ from the NO_x routine for $\frac{dm_m}{d\theta}$ from equation (4.9).

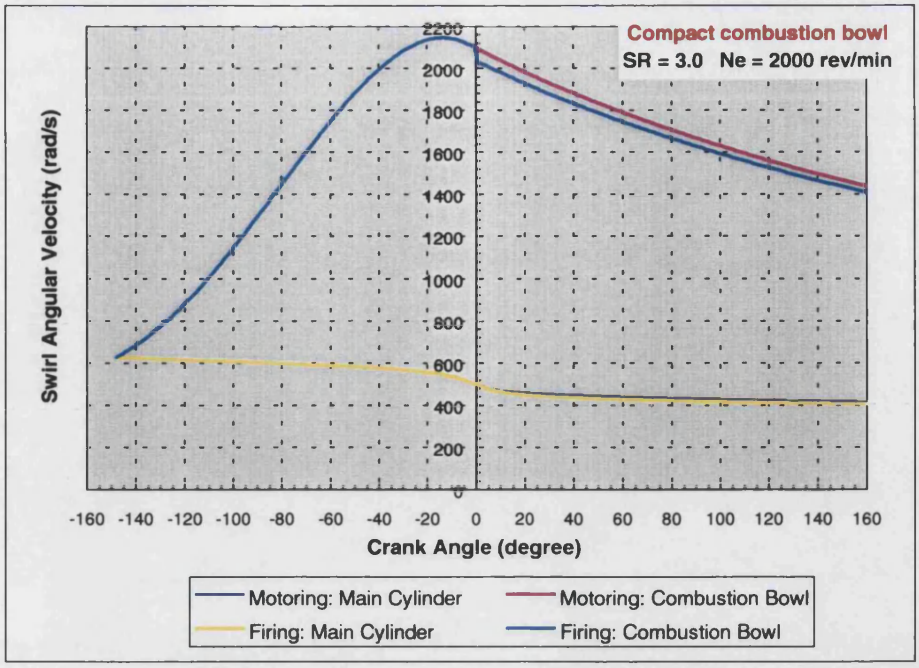

Figure 8.11: Typical swirl velocity in the main cylinder and combustion bowl

The calculations for spray deflection and swirl-spray interaction terminate at the point of impingement of the spray on the wall. The subsequent process of further transfer of mass and momentum to the wall jet is not covered by the present treatment which now proceeds as the previous basis for motoring conditions as outlined in chapter 4.

Figure 8.12 shows spray deflection based on the variable swirl rate under firing conditions predicted in the above section.

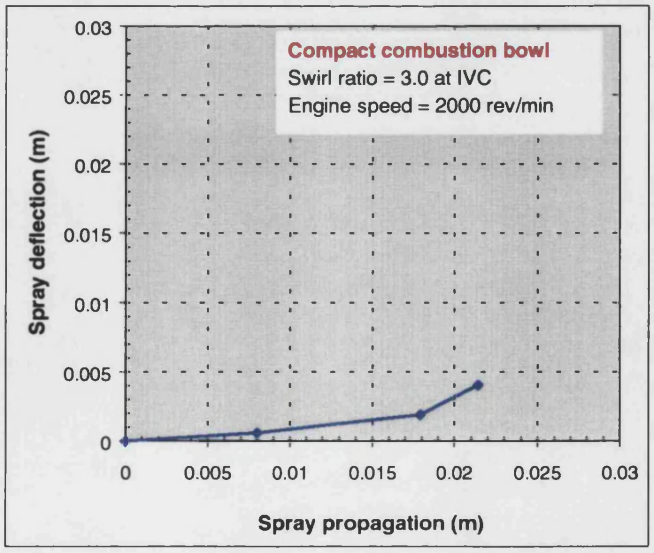

Figure 8.12: Typical deflected spray in a cross-flow field

8.5.3 Deflection in large diameter Mexican Hat configuration for high pressure injection systems in HPCR engines

The basic formulation for this case is still represented by equation (8.25) to (8.29). However, the expression for bowl inertia and also the linear area of the combustion bowl for calculation of the rate of friction momentum has to be changed to reflect the new geometry, as expressed by equations (4.28) and (4.30), in chapter 4, section 4.3.2, i.e.

$$I_b = m_b \cdot \frac{R_b^2}{2} \cdot \left(\frac{3}{5} \cdot \frac{4e_1 + e_2}{2e_1 + e_2} \right) \tag{8.33}$$

$$A_b = 2\pi R_b e_1 + \pi R_b^2 \frac{\sqrt{R_b^2 + (e_1 - e_2)^2}}{R_b} \tag{8.34}$$

$$\therefore \quad \begin{aligned} \left(Mom_{fr}\right)_b = & \sum_1^5 \frac{1}{2} C_f \rho_a v_s^2 \cos^2 \bar{\alpha} \bar{D} \cdot \Delta s \cdot \bar{r} + \\ & \frac{1}{2} f \rho_a R_b^2 \omega_b^2 \left[\pi R_b \left(2e_1 + \sqrt{R_b^2 + (e_1 - e_2)^2} \right) \right] R_b \end{aligned} \tag{8.35}$$

Substitution of above equations in the equation of conservation of rate of angular momentum in bowl i.e. equation (8.27) gives,

$$\begin{aligned} & \frac{R_b^2}{2} \cdot \left(\frac{3}{5} \cdot \frac{4e_1 + e_2}{2e_1 + e_2} \right) m_b \frac{\Delta \omega_b}{\Delta t} = -\sum_1^5 \frac{\Delta m_{eD}}{\Delta t} \cdot (v_s - \bar{v} \sin \bar{\alpha}) \bar{r} \\ & -\sum_1^5 \frac{1}{2} C_f \rho_a v_s^2 \cos^2 \bar{\alpha} \bar{D} \cdot \Delta s \cdot \bar{r} - \frac{1}{2} f \rho_a R_b^2 \omega_b^2 \left[\pi R_b \left(2e_1 + \sqrt{R_b^2 + (e_1 - e_2)^2} \right) \right] R_b \end{aligned} \tag{8.36}$$

This should give a solution for $(\omega_b)_{n+1}$ as equation (8.37),

$$\begin{aligned} (\omega_b)_{n+1} = & (\omega_b)_n + \frac{2 \cdot \Delta t}{(m_b)_n R_b^2} \left(\frac{5}{3} \cdot \frac{2e_1 + e_2}{4e_1 + e_2} \right) \left\{ -\sum_1^5 \frac{(\Delta m_{eD})_n}{\Delta t} (v_s - \bar{v} \sin \bar{\alpha})_n \cdot \bar{r}_n - \right. \\ & \left. \sum_1^5 \frac{1}{2} C_f \rho_a v_s^2 \cos^2 \bar{\alpha} \bar{D} \cdot \Delta s \cdot \bar{r} - \frac{1}{2} f (\omega_b)_n^2 \pi \rho_a R_b^4 \left(2e_1 + \sqrt{R_b^2 + (e_1 - e_2)^2} \right) \right\} \end{aligned} \tag{8.37}$$

Figure 8.13, shows angular velocity in main cylinder, ω, and in the combustion bowl, ω_b, versus crank-angle degree from IVC to EVO again for motoring and also from TDC to EVO based on firing condition.

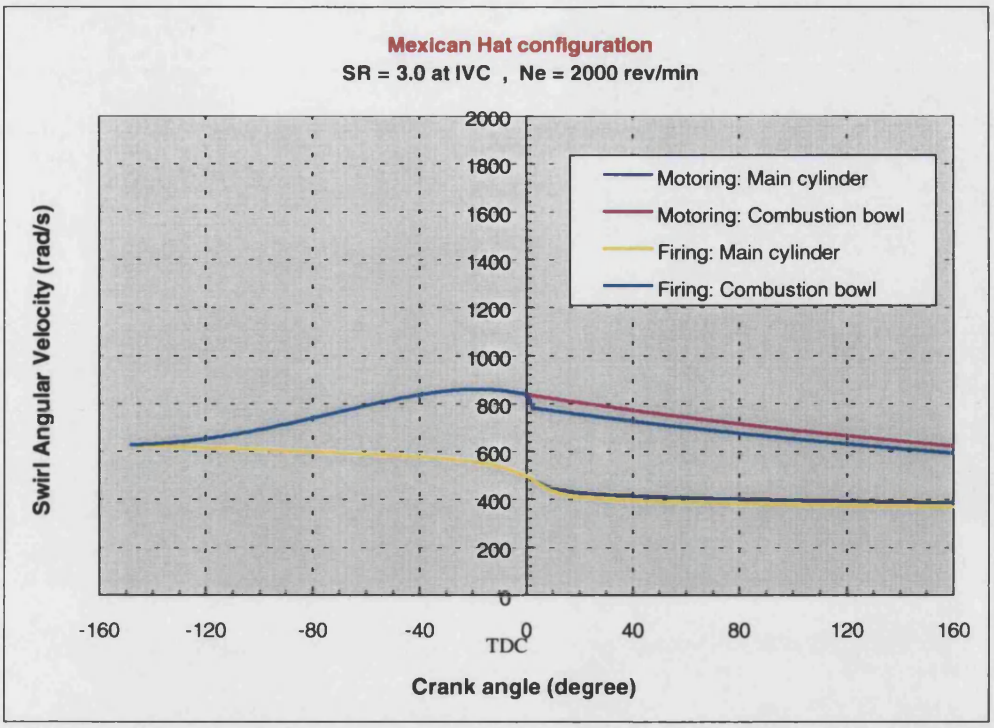

Figure 8.13: Typical swirl velocity in the main cylinder and combustion bowl

Figure 8.14 shows spray deflection based on the variable swirl rate under firing conditions predicted in the above section.

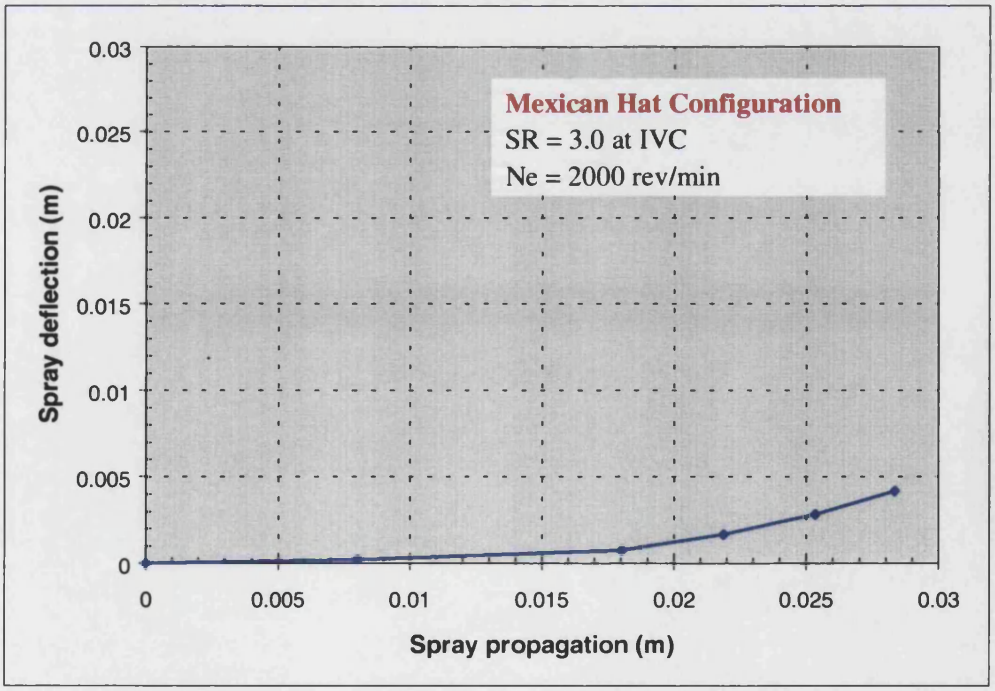

Figure 8.14: Typical deflected spray in a cross-flow field

8.6 Discussion

Chapter 8 provides analytical solutions to three key aspects of spray development, i.e.

a) Spray propagation
b) Spray deflection
c) Spray swirl interaction

The analysis of spray propagation, section 8.4 gives satisfactory results supported by the parallel impulse approach based on established conservation laws for mass and momentum.

The spray deflection results, although unfortunately not supported by direct experimental evidence, give entirely credible results for two alternative combustion chamber geometries, viz. compact (bowl diameter 40 mm) and "Mexican Hat", (bowl diameter 60 mm), the former giving higher deflections due to the higher swirl rates following start of injection, SoI, for identical assumed injection conditions and swirl ratios of 3.0 at inlet valve closing, IVC, (see figure 8.15).

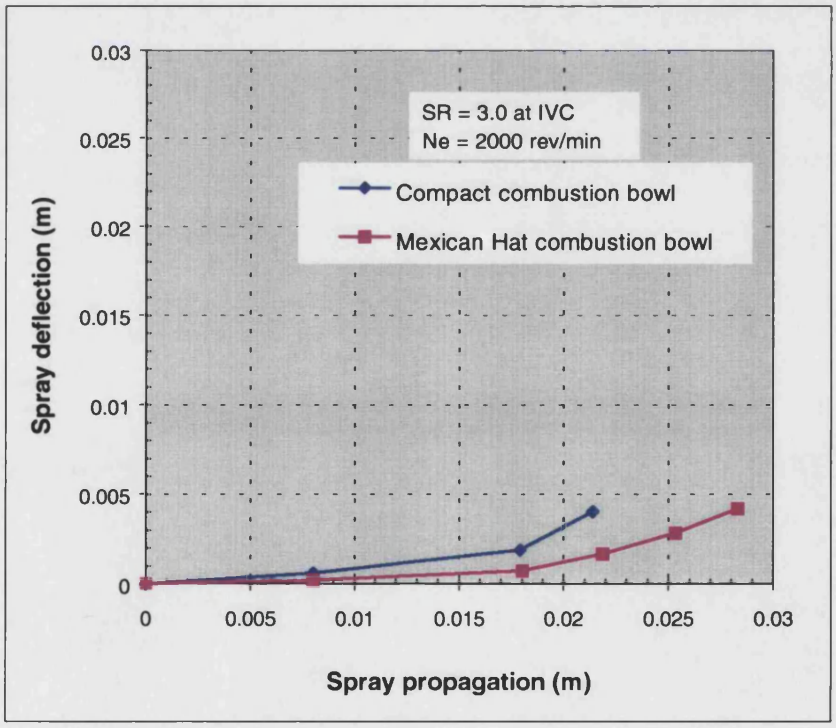

Figure 8.15: Comparison of deflected spray in a cross-flow field for two alternative combustion chamber geometries

Finally, the calculations for spray-swirl interaction based on the use of the fully integrated program presented in chapter 9, again for the two alternative combustion chambers, with identical injection conditions show interesting trends.

The angular momentum exchange analysis between spray and swirl (equation 8.27) in the swirl direction suggests that with given injection conditions, i.e. broadly similar spray centre line velocities v (equation 8.25), similar rates of entrainment, and rates of change of spray angle of similar order, the rate of increase of momentum of the spray in the direction of swirl will be broadly similar for the two configurations. However, since this momentum gain is at the expense of momentum loss of the swirling mass of air, then with the much lower level of swirl in the Mexican Hat configuration at SoI, the proportional effect will be greater than for the compact chamber, as shown clearly in figure 8.13 compared with figure 8.11.

8.7 References

1. **Wallace, F.J.**, "Presentation of Simulation Package ODES at University Internal Combustion Group (UNICEG) meeting", University College London, December 1993.

2. **Agnew, W.G.**, "Room at the piston top: Contributions of combustion science to engine design", Twentieth Symposium (International) on Combustion, pp. 1-17, 1984.

3. **Faeth, G.M.**, "Current status of droplet and liquid combustion", Prog. Energy Combust. Sci., Vol. 3, pp. 191-224, (1977).

4. **Kuo, K.K.**, "Principle of Combustion", Wiley & Sons, New York, pp. 589-594, (1986).

5. **Arcoumanis, C., Green H.G., and Whitelaw, J.H.**, "The application of laser Rayleigh scattering to a reciprocating model engine", SAE 840376, (1984).

6. **Arcoumanis, C., Green H.G., and Whitelaw, J.H.**, "Velocity and concentration measurements in a model Diesel engine", Experience in fluids 3, pp. 270-276, (1985).

7. **Arcoumanis, Whitelaw, J.H., and Wong, K.Y.**, "Gaseous simulation of diesel-type sprays in a motored engine", SAE 890793, (1989).

8. **Scheid, E., Pischinger, F., Knoche, K.F., Daams, H. -J., Hassel, E.P., and Reuter, U.**, "Spray combustion chamber with optical access, ignition zone visualization and first Raman measurements of local air-fuel ratio", SAE 861121, (1986).

9. **Heinze, T., and Schmidt, T.**, "Fuel-air ratios in a spray, determined between injection and autoignition by pulsed spontaneous Raman spectroscopy", SAE 892102, (1989).

10. **Espey, C., and Dec, J.E.**, "Diesel engine combustion studies in a newly designed optical-access engine using high-speed visualization and 2-D laser imaging" SAE 930971, (1993).

11. **Espey, C., Dec, J.E., Litziger, T.A., and Santavicca, D.A.**, "Quantitative 2-D fuel concentration imaging in a firing DI Diesel engine using planar laser-induced Rayleigh scattering", SAE 940682, (1994).

12. **Dec, J.E.**, "A conceptual model of DI diesel combustion based on laser-sheet imaging", SAE 970873, (1997).

13. **Flynn, P.F., Durrett, R.P., Hunter, G.L., Loye, A.O., Akinyemi, O.C., Dec, J.E., and Westbrook, C.K.**, "Diesel combustion: an integrated view combining laser diagnostics, chemical kinetics, and empirical validation", SAE 1999-01-1180, (1999).

14. **Whitehouse, N.D., and Sareen, B.k.**, "Prediction of Heat Release in a quiescent Chamber Diesel Engine Allowing for Fuel/Air Mixing", SAE 740084 (1979).

15. **Meguerdichian, M., and Watson, N.**, "Prediction of Mixture Formation and Heat Release in Diesel Engines", SAE 780225 (1978).

16. **Bazari, Z.**, "A DI Diesel Combustion and Emission Predictive Capability for Use in Cycle Simulation", SAE 920462 (1992).

17. **Chiu, W. S., Shahed, S. M., and Lyn, W. T.**, "A Transient Spray Mixing Model of Diesel Combustion, SAE 760128 (1976).

18. **Shahed, S. M., Chiu, W. S., and Lyn, W. T.**, "A Mathematical Model of Diesel Combustion", Proceeding of the IMechE, C94/75, pp. 119-128 (1975).

19. **Amsden, A. A., Butler, T. D., O'Rourke, P. J., and Ramshaw, J. D.**, "KIVA – A comprehensive model for 2-D and 3-D engine simulations", SAE 850554, 1985.

20. **Amsden, A. A., O'Rourke, P. J., and Butler, T. D.**, "KIVA-II: A computer program for chemically reactive flow with sprays", U.S. Department of Commerce Report, Los Alamos National Laboratory, May 1989.

21. **Amsden, A. A.**, "KIVA-III: A KIVA program with block-structured mesh for complex geometries", Los Alamos National Laboratory, March 1993.

22. **Tanner, F. X.**, "Numerical Simulation of diesel sprays and diesel combustion: A case study", 21st CIMAC Congress 1995, Interlaken: CRFD and Laser Diagnostic Workshop.

23. **Rutland, C. J., Eckhause, J., Hampson, G. J., Hessel, R., Kong, S., Patterson, M., Pierpont, D., Sweetland, P., Tow, T., and Reitz, R. D.**, "Toward predictive modelling of Diesel engine intake flow, Combustion and Emission", SAE 941897 (1994).

24. **Ikonomou, E.**, "A Computational Study of Diesel Sprays and Combustion", PhD Thesis, Imperial College of Science, Technology and Medicine, London (1995).

25. **Watkins, A.P., Gosman, A.D., and Tabrizi, B.S.**, "Calculation of three dimensional spray motion in engines", SAE 860468, (1986).

26. **Siebers, D.L., and Higgins, B.S.**, "Effects of injector conditions on the flame lift-off length of direct injection diesel sprays", Proc. THESEL 2000, pp.303-321, Valencia, September 13-15, (2000).

CHAPTER 9

Overall results using integrated program

9.1 Introduction

This chapter presents both performance results and detailed results under the headings:

a) Engine performance and NO_x emission
b) Ignition delay (already covered in chapter 5)
c) Spray propagation and deflection
d) Swirl generation and decay

over the full operating range of the engine from 1250 to 4000 rev/min.
In the case of (a) and (b), the corresponding experimental results are presented in full to provide validation of the new integrated program.
In the case of (c) and (d), experimental results are not available (optical methods have not, so far, been used at the University of Bath) but it is considered useful to present general trends for these phenomena. Very limited additional evidence on spray formation and deflection using CFD methods by *Ikonomou* [1] on a similar 1.8 litre Ford HSDI Diesel engine is also presented for completeness. Although *Ikonomou* presented the very light operating conditions compared with the high LTC conditions presented here, but it is the only evidence, which shows the short time of spray propagation before impingement.

9.2 Overall results

9.2.1 Performance results

To validate the model with regards to engine performance a variety of parameters were considered. The results of two separate performance sets are summarised in table 9.1 and in figures 9.1 to 9.5, and table 9.2 and figures 9.6 to 9.10.

As has already been stated in chapter 7, the difference between the two sets of performance results is that in the first case the parameter α_{h2} was adjusted to give the best possible agreement of the computed and experimental cylinder pressure trace while in the second case values of α_{h2} based broadly an experimental results for cumulative heat release derived from the Concerto software, were used.

a) Maximum cylinder pressure optimised runs

Table 9.1: Summary of performance results based on the best pressure runs

Engine Speed	Torque (N.m)		bsfc (g/kW-hr)		Max. Press. (bar)		Avg. NOx (ppm)		Max.Net ROHR (kJ/m^{3}deg)		Mass Airflow (kg/s)	
(rev/min)	Exp.	Comp.	Exp.	Comp.	Exp.	Comp.	Exp.	Comp.	Exp.	Comp.	Exp.	Comp.
1250	132.8	129.27	246	250.6	107.7	107.1	967	1870	129.8	156.57	0.0054	0.0055
1500	160.2	154.23	226	232.3	115.8	115.5	1143	1465	133.9	149.88	0.0077	0.0081
1750	175.3	169.29	216	221.8	121.5	120.7	1303	1211	133.6	143.59	0.0102	0.0107
2000	190.2	186.38	214	216.2	135.2	134.4	1346	1010	136.7	140.85	0.0142	0.0149
2250	196.8	195.2	211	211.1	129.2	128.3	1148	934	129.5	123.08	0.0161	0.0169
2500	203.6	204.41	213	209.5	126.9	126.2	1031	928	118.6	125.18	0.0177	0.0186
3000	199.2	202.7	223	216.9	123.3	122.7	915	943	104.9	107.72	0.0212	0.0212
3500	180.1	182.23	228	222.9	123.7	122	857	780	96.33	99	0.0242	0.0243
4000	171	179.35	248	233.8	120.8	119.6	783	810	88.29	92.52	0.0268	0.0267

Figure 9.1 shows both the experimental and computed results for torque and bsfc. It can be seen that very good agreement between the computed and experimental results is obtained.

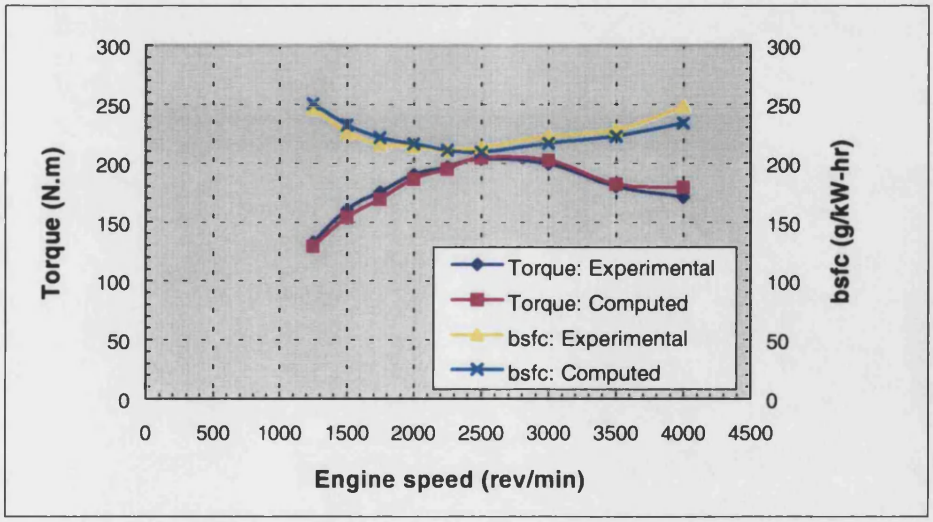

Figure 9.1: Comparison of experimental and computed results of torque and bsfc.

Figure 9.2 shows an excellent agreement between computed and experimental mass airflow traces.

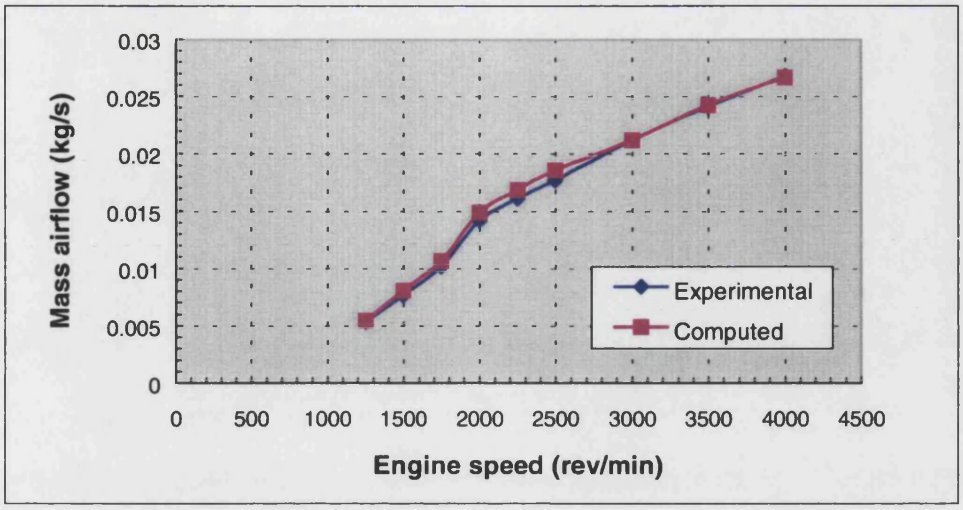

Figure 9.2: Comparison of experimental and computed results of mass airflow

Agreement between the maximum value of the computed and experimental cylinder pressure in figure 9.3 is excellent.

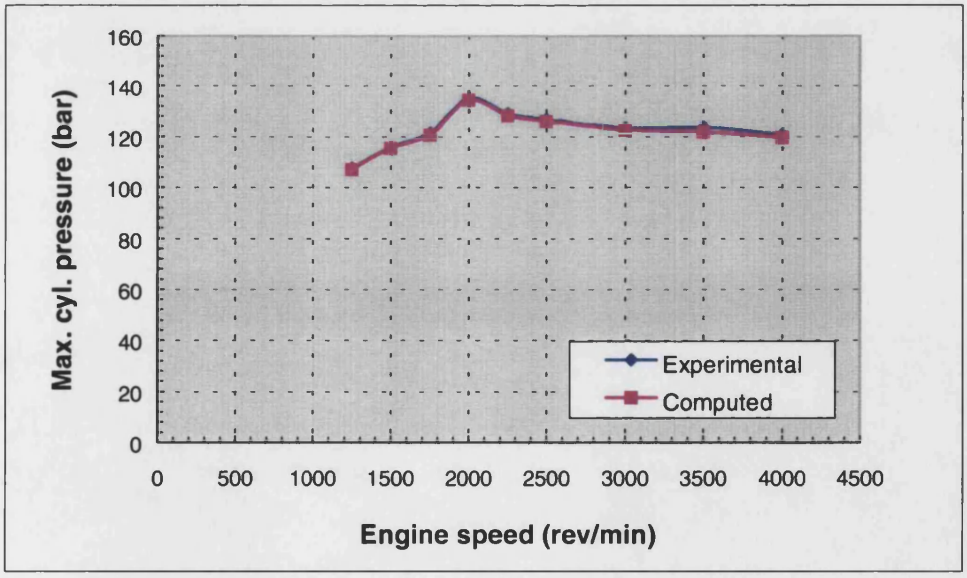

Figure 9.3: Comparison of experimental and computed results of maximum cylinder pressure

Figure 9.4 shows the experimental and computed results for the maximum value of rate of net heat release.

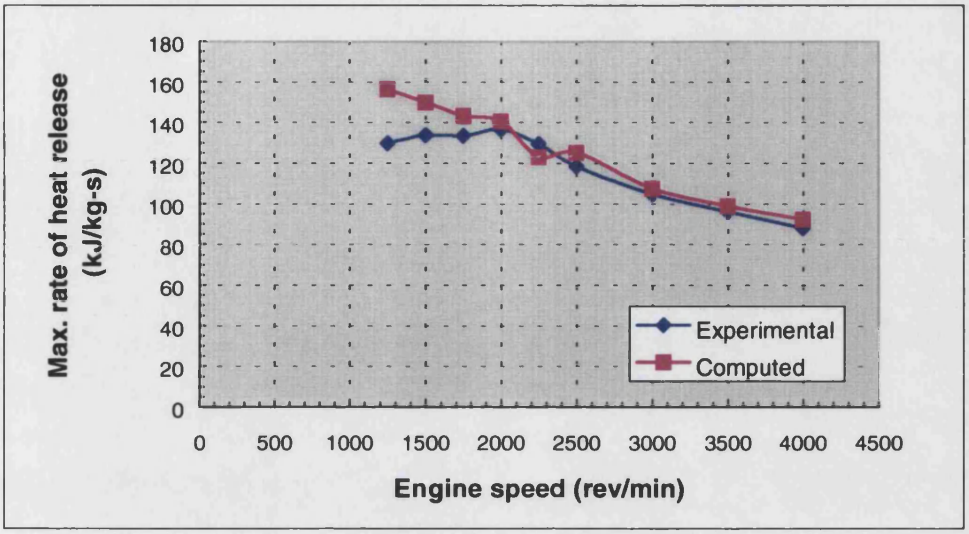

Figure 9.4: Comparison of experimental and computed results of maximum rate of net heat release

The experimental and computed results for the average value of NO_x in figure 9.5, show reasonable agreement at high speeds, but significant differences at low speeds. This discrepancy, together with the similar discrepancy shown in figure 9.10 will be commented on at the end of this section.

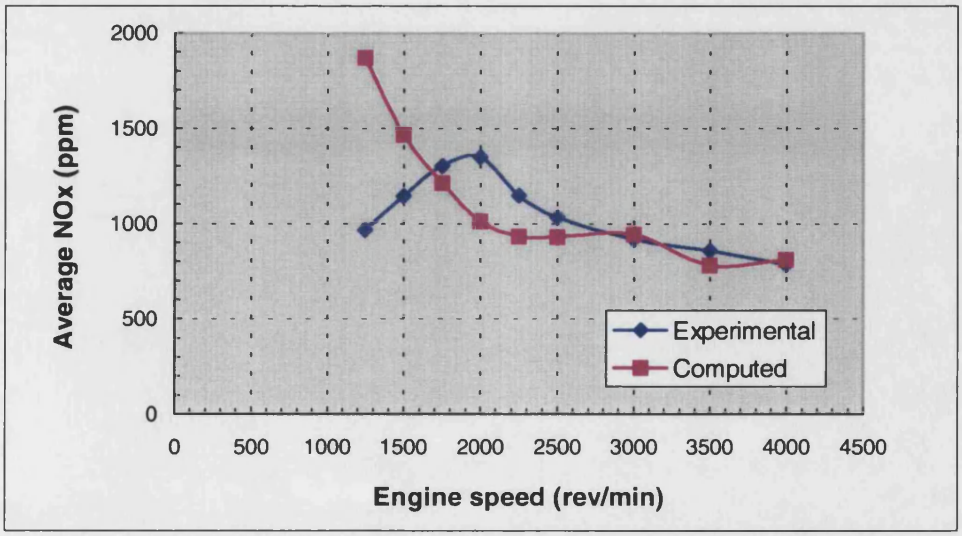

Figure 9.5: Comparison of experimental and computed results of average NO_x

b) Heat release optimised runs

Table 9.2: Summary of performance results based on the best heat release runs

Engine Speed	Torque (N.m)		Bsfc (g/kW-hr)		Max. Press. (bar)		Avg. NOx (ppm)		Max.Net ROHR (kJ/m^3deg)		Mass Airflow (kg/s)	
(rev/min)	Exp.	Comp.	Exp.	Comp.	Exp.	Comp.	Exp.	Comp.	Exp.	Comp.	Exp.	Comp.
1250	132.8	130.2	246	248.8	107.7	101.9	967	1694	129.8	139.27	0.0054	0.0055
1500	160.2	154.86	226	231.4	115.8	108.8	1143	1319	133.9	133.87	0.0077	0.0081
1750	175.3	168.27	216	223.1	121.5	118.2	1303	1162	133.6	132.7	0.0102	0.0107
2000	190.2	184.5	214	218.4	135.2	131.4	1346	963	136.7	130.88	0.0142	0.0149
2250	196.8	194.53	211	211.8	129.2	127.2	1148	905	129.5	122.94	0.0161	0.0169
2500	203.6	203.19	213	210.8	126.9	127.3	1031	941	118.6	121.38	0.0177	0.0186
3000	199.2	202.23	223	217.4	123.3	122	915	930	104.9	108.17	0.0212	0.0212
3500	180.1	181.2	228	224.2	123.7	123.1	857	795	96.33	95.1	0.0242	0.0243
4000	171	178.4	248	235.1	120.8	117.8	783	769	88.29	90.51	0.0268	0.0267

Figure 9.6 shows both the experimental and computed results for torque and bsfc. Again it can be seen that very good agreement between the computed and experimental results is obtained.

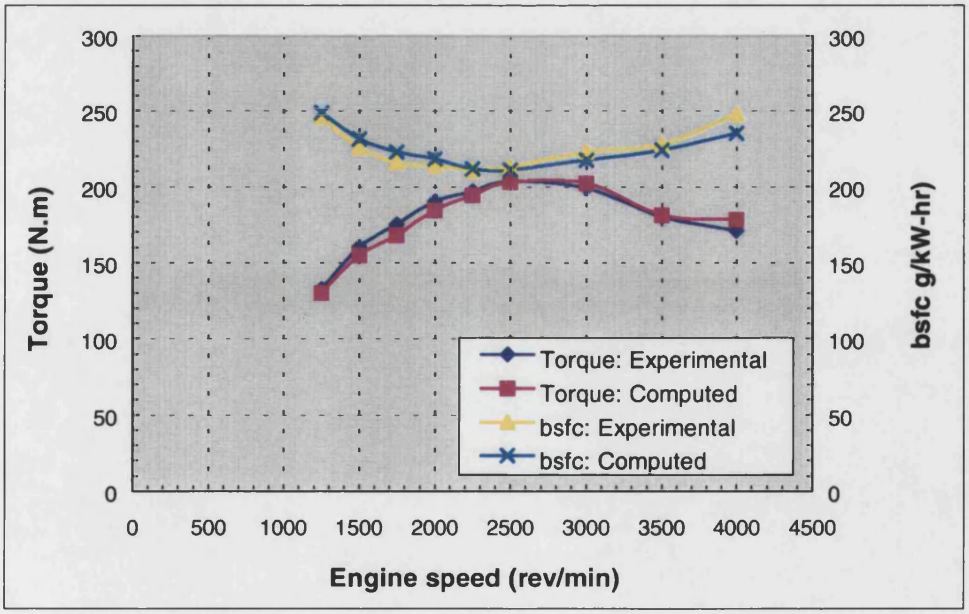

Figure 9.6: Comparison of experimental and computed results of torque and bsfc.

Figure 9.7 shows again an excellent agreement between computed and experimental mass airflow traces.

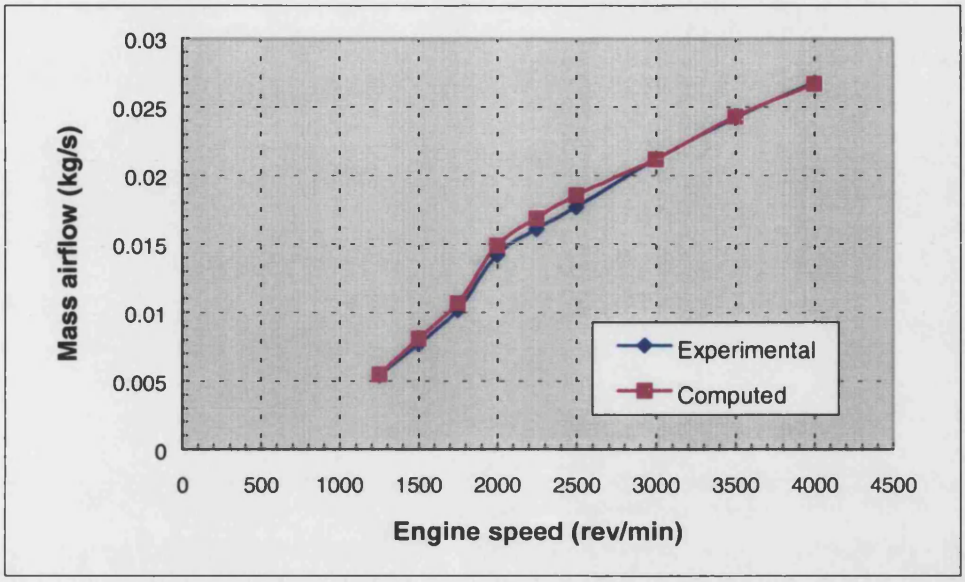

Figure 9.7: Comparison of experimental and computed results of mass airflow

Agreement between the maximum value of the computed and experimental cylinder pressure in figure 9.8 is still very good.

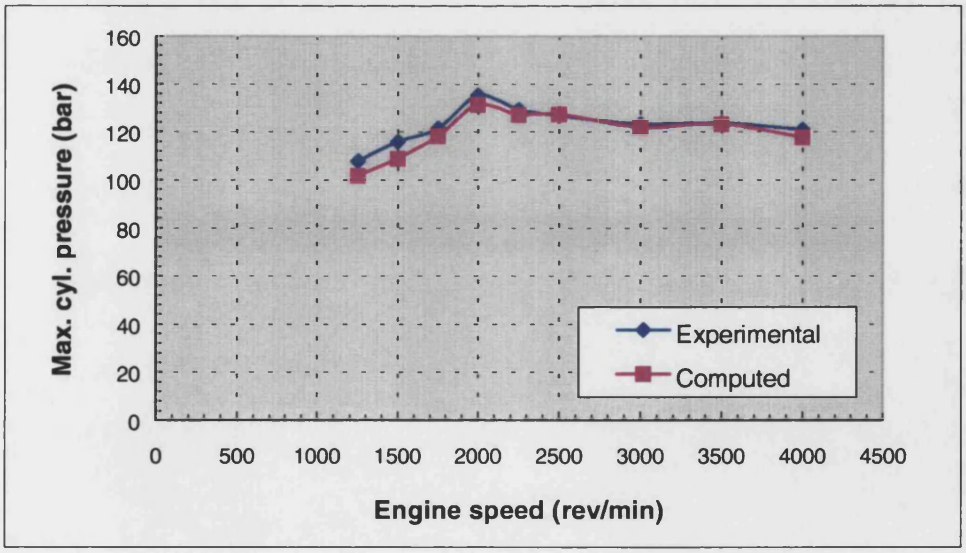

Figure 9.8: Comparison of experimental and computed results of maximum cylinder pressure

Figure 9.9 shows very good agreement between experimental and computed results for the maximum value of rate of net heat release.

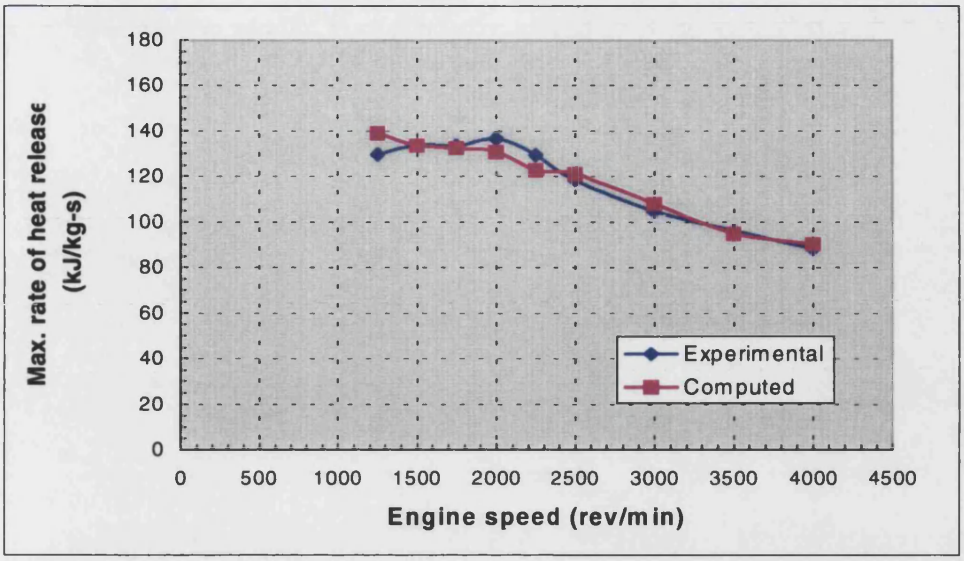

Figure 9.9: Comparison of experimental and computed results of maximum rate of net heat release

The experimental and computed results for the average value of NO_x in figure 9.10, again show reasonable agreement at high speeds, but significant differences at low speeds.

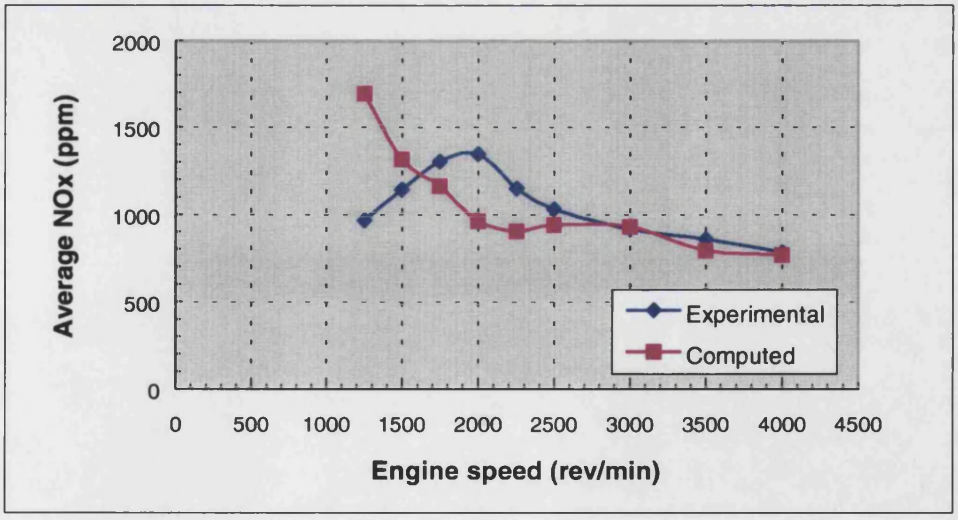

Figure 9.10: Comparison of experimental and computed results of average NO_x

The marked discrepancy between experimental and predicted NO_x at low engine speeds is due in large measure to neglect in the model of premixed burning with its associated low NO_x emission characteristics. It is also noteworthy that the

experimental curve peaking at 2000 rev/min closely follow the trends for maximum cylinder pressure as described by *M.F.Russell* [2] as a common feature on engine with high pressure common rail systems.

9.2.2 Ignition delay correlation

As has already been stated, the purpose of the ignition delay submodel is to calculate the duration of ignition delay, which is fully discussed in chapter 5, section 5.3.
Figure 9.11 compares ignition delay (in °CA) as obtained from the three alternative approaches (*Watson* [3], *Assanis* [4], and the new correlation) with the experimental values derived from heat release records using the AVL Concerto software, were used.

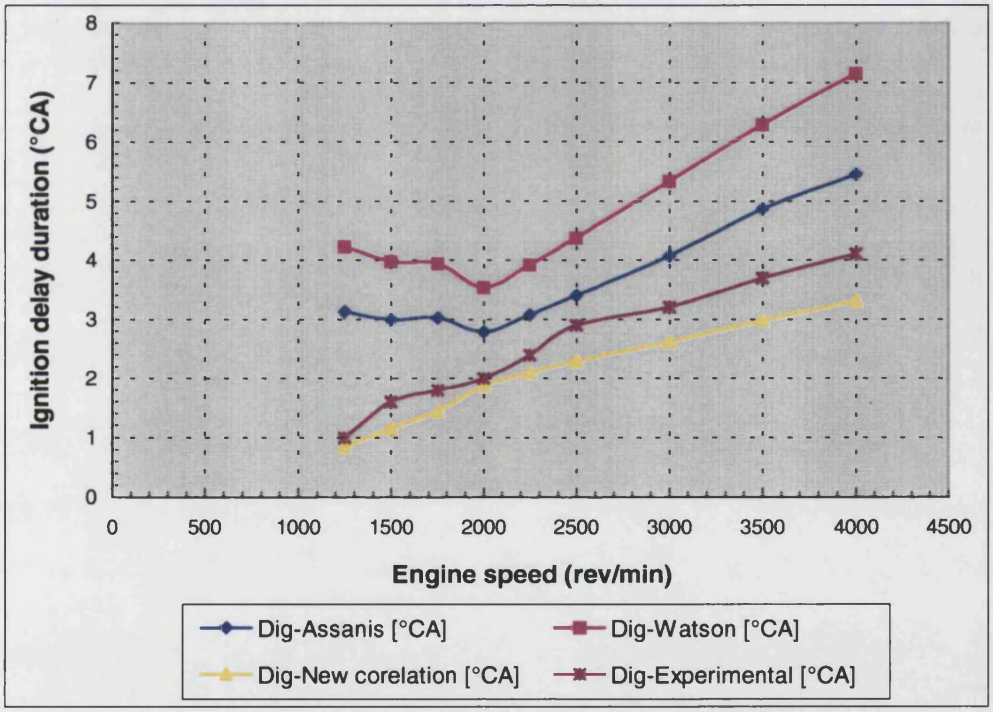

Figure 9.11: Ignition delay versus engine speed

It will be observed that *Watson* [3] and *Assanis* [4] considerably over predict ignition delay while the new correlation slightly under predicts. It must be remembered that both the *Watson* [3] and *Assanis* [4] correlations refer to pump-line-nozzle systems with lower injection pressures and different injection characteristics from the nearly constant high-pressure injection conditions associated with the common rail system.

9.2.3 Spray formation and deflection

As has already been stated, the purpose of the spray submodel is to calculate the spray trajectory for a free jet under combusting conditions based on relations discussed in chapter 8, section 8.4, and also calculation of spray penetration and deflection in swirling air based on relations discussed in section 8.5.

9.2.3.1 Undeflected spray

The undeflected spray tip penetration distances vs. time from start of injection as a function of engine speed are plotted in figure 9.12.

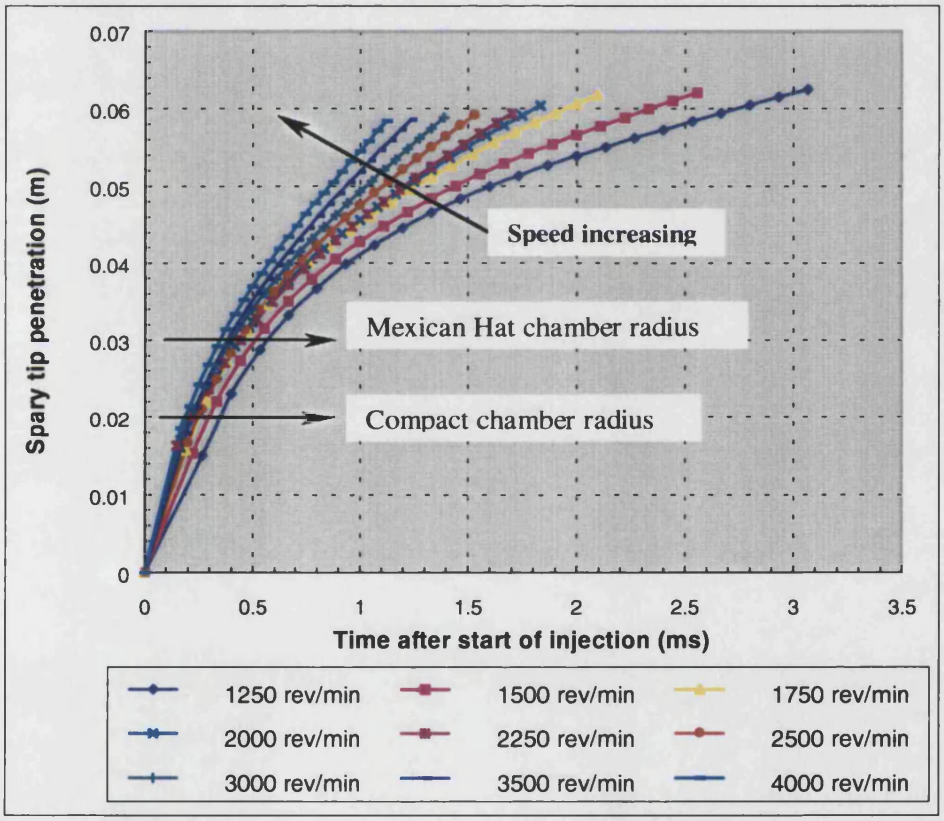

Figure 9.12: Spray tip penetration distance vs. time

Figure 9.12 shows the fact that the low injection pressures at low speeds lead to low injection velocity and hence low penetration on a time basis.

When tip penetration is replotted on a crank angle basis, and taking changes to start of injection into account (figure 9.13), for any given crank angle, differences in penetration are relatively small. Hence a given combustion bowl shape, optimised experimentally or analytically for a particular condition, will tend to be reasonably satisfactory over a wide range of operating conditions.

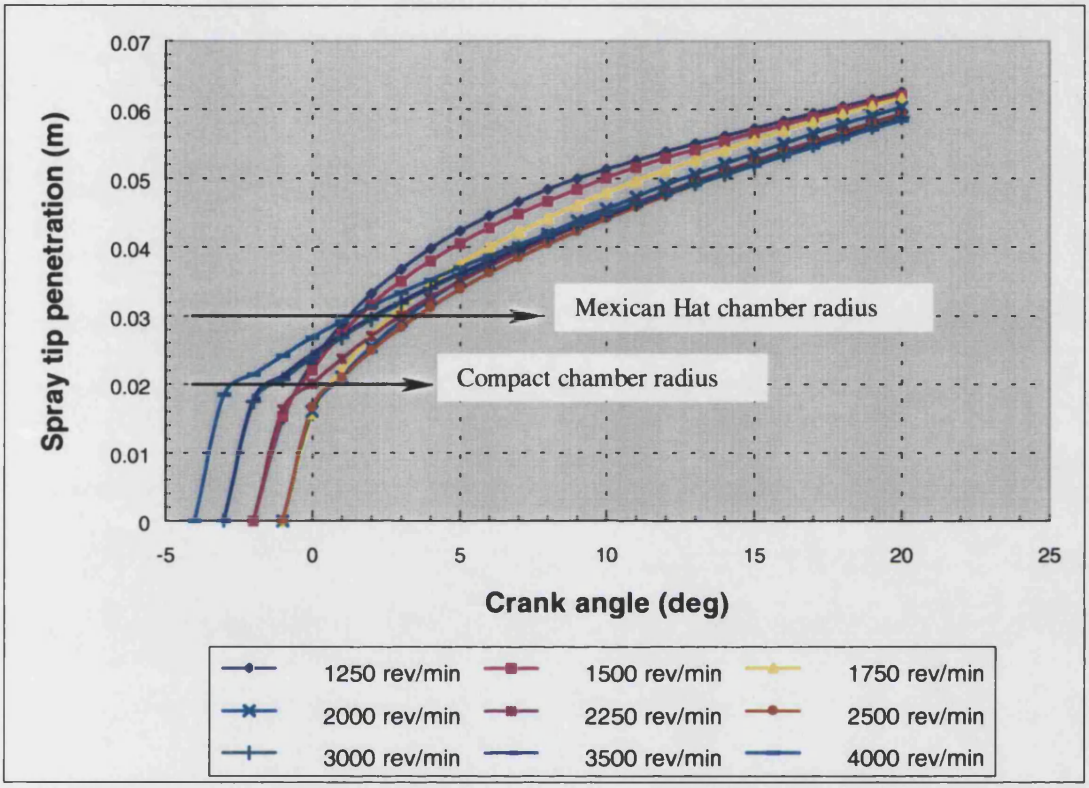

Figure 9.13: Spray tip penetration distance vs. crank angle

9.2.3.2 Deflected spray

As has already been stated in section 8.4.1, pressure forces and viscous action in a cross flow field deflect the spray. The results of the spray trajectory of the centreline for two alternative combustion chamber geometries, viz. compact (bowl radius 20 mm) and "Mexican Hat" (bowl radius 30 mm), are shown in figures 9.14 and 9.15 respectively.

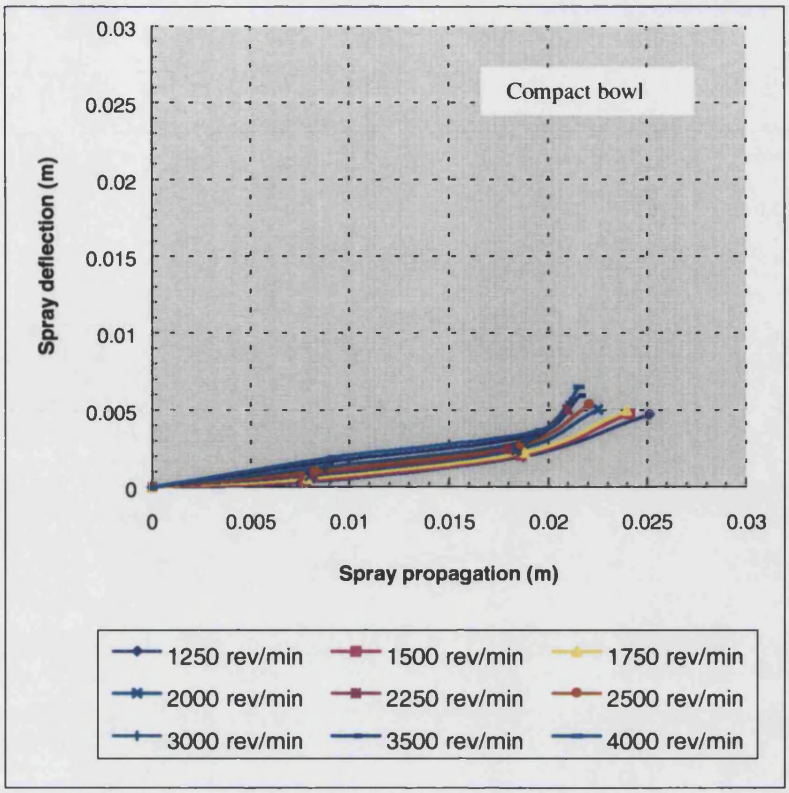

Figure 9.14: Spray deflection vs. spray propagation in compact bowl shape

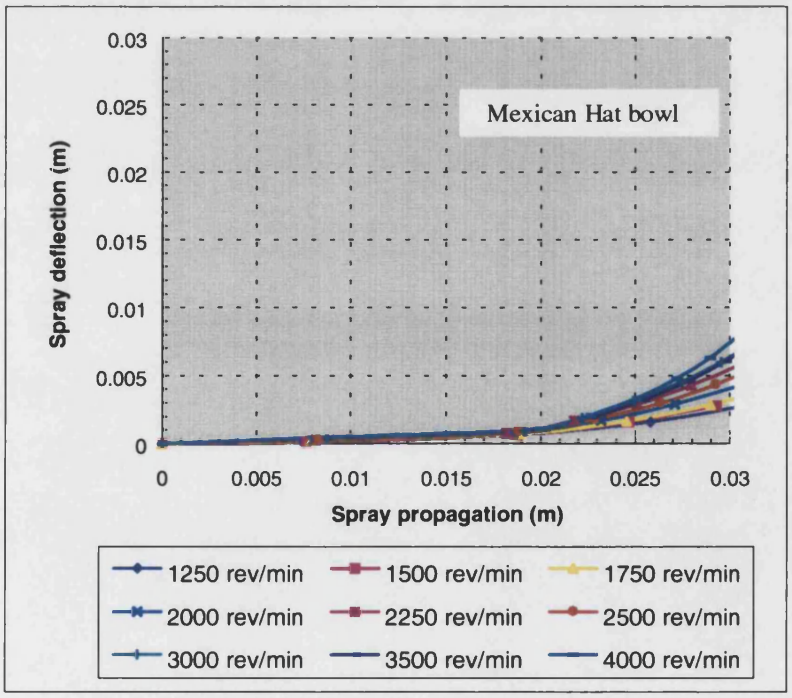

Figure 9.15: Spray deflection vs. spray propagation in Mexican Hat bowl shape

Figures 9.14 and 9.15 show that:

a) As expected deflections for all speeds are greater in the high swirl compact chamber than in the Mexican Hat configuration.

b) In both deflections are higher at high speed and the associated higher swirl rates.

9.2.4 Swirl formation and destruction

As has already been stated, the purpose of the swirl submodel is to calculate the swirl generation and decay in the main cylinder and the combustion bowl based on a given swirl rate in the main cylinder at inlet valve closing (IVC), see section 8.5.3.

The swirl results in firing conditions for both compact and Mexican Hat configuration for a drag coefficient $C_f = 0.45$, under the assumed swirl ratio of 3.0 at IVC are shown in figures 9.16, and 9.17, respectively.

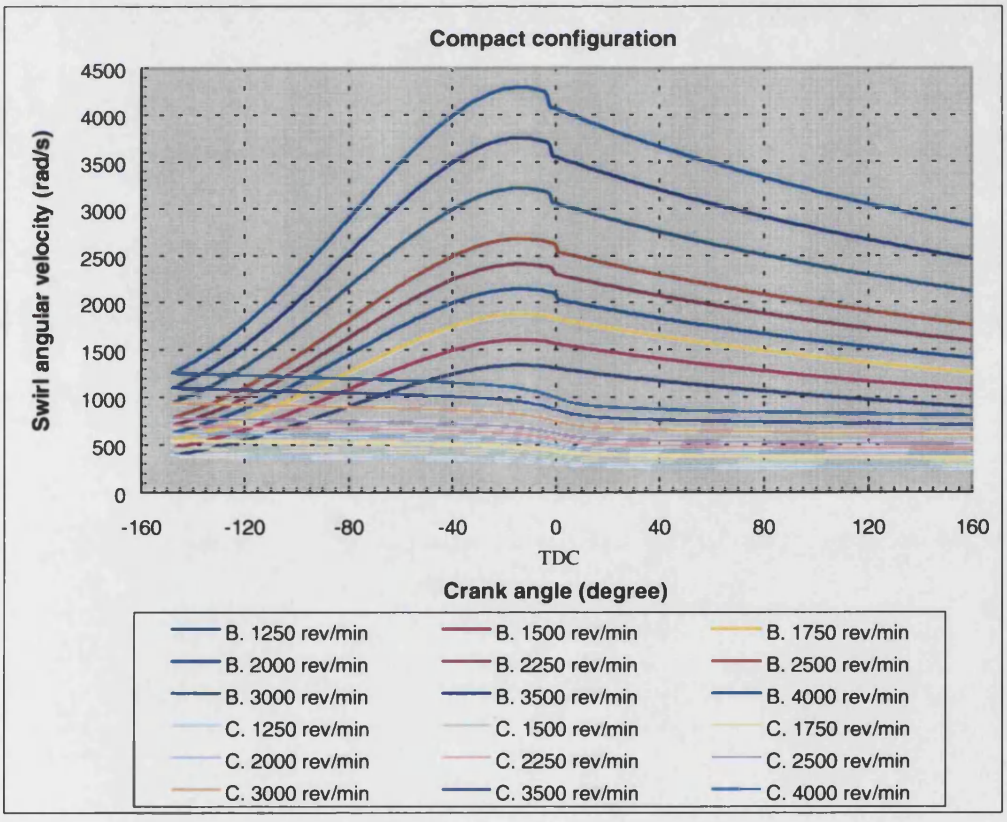

Figure 9.16: Variation of swirl angular velocity in the main cylinder and the compact combustion bowl vs. crank angle for all engine speeds

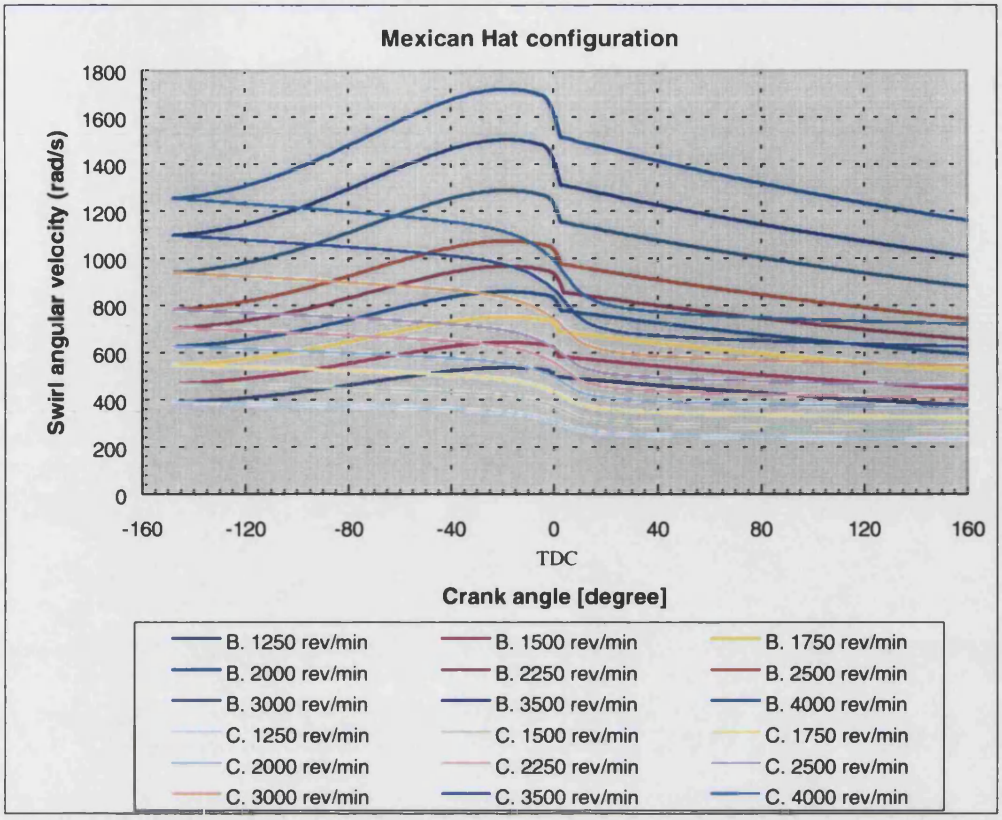

Figure 9.17: Variation of swirl angular velocity in the main cylinder and Mexican Hat combustion bowl vs. crank angle for all engine speeds

Figures 9.16 and 9.17 show the following:

a) As expected higher engine speeds result in a continuous increase of maximum swirl angular velocity in the combustion chamber from approximately 1342 rad/s at 1250 rev/min to 4296 rad/s at 4000 rev/min for the compact chamber and from 538 rad/s at 1250 rev/min to 1721 rad/s at 4000 rev/min for the Mexican Hat configuration.

b) However, when converted to a ratio $\frac{\text{Maximum swirl speed [rev/min]}}{\text{Engine speed [rev/min]}}$, this ratio remain almost constant at 10.26 for the compact chamber and at 4.11 for the Mexican Hat configuration, implying that absolute swirl rates in the compact chamber are approximately 2.5 times higher than in the Mexican Hat configuration.

This is in line with the fact that the higher spray kinetic energies associated with the HPCR system require lower swirl rates for good fuel/air mixing than those associated

with the lower pressure pump-line-nozzle (PLN) system, which led to the almost universal adoption of the high swirl compact chamber.

9.3 Conclusions

The results presented in chapter 9 for performance, ignition delay, spray propagation, deflection and swirl generation and dissipation, taken together with the heat release results of chapter 7, show that the new integrated program yields predictions which, where applicable, are in good agreement with experimental results and in the case of spray and swirl formation provide valuable insights into the interdependence of these parameters and engine operating conditions.

However, a shortcoming of the analysis in its present form is the neglect of premixed burning in the analytical heat release formulation of chapter 6, based on the *Chmela and Orthaber* [5] model for wholly diffusion burning. There is some evidence in the experimental cylinder pressure diagrams, 7.7a (1250 rev/min) to 7.12a (2500 rev/min) of the occurrence of the well known premixed "spike" which is in turn attributable to the combustion of relatively low injection velocities and a cool cylinder air charge.

There is further indirect evidence for this in the cylinder pressure diagrams, figure 7.20a to 7.28a and 7.29a to 7.37a in which agreement between computed and experimental values becomes progressively better with increase in engine speed.

9.4 References

1. **Ikonomou, E.**, "A Computational Study of Diesel Sprays and Combustion", PhD Thesis, Imperial College of Science, Technology and Medicine, London (1995).

2. **Russell, M.F.**, " The dependence of diesel combustion on injection rate", paper No. S490/005/97 'Future Engine System Technologies, The Euro IV Challenge' and IMechE Seminar, ISBN 1 86058 166 8 pp.65-81 (1997).

3. **Watson, N., Pilley, A.D. and Marzouk, M.**, "A combustion correlation for diesel engine simulation", SAE 800029 (1980).

4. **Assanis, D.N., Filipi, Z.S., Fiveland, S.B., and Syrimis, M.**, "A predictive ignition delay correlation under steady-state and transient operation of a direct injection diesel engine", Paper No. 99-ICE-231, ICE-Vol. 33-2, Fall technical conference, ASME, (1999).

5. **Chmela, F.G., and Orthaber, G.C.**, "Rate of Heat Release Prediction for Direct Injection Diesel Engines Based on Purely Mixing Controlled Combustion", SAE 990186 (1999).

CHAPTER 10

Conclusions and suggestions for further work

This last chapter of the thesis is divided into two sections. Section 10.1 highlights the main results of the present study, and section 10.2 is a series of forward suggestions for further research based on the findings and experience acquired from this work.

10.1 Review of results obtained

The detailed results of the present computational study have been extensively discussed in the previous chapters. In the following, the most important conclusions are summarised.

- A wide literature survey has been conducted relevant to each of the main arias investigated to arrive at the mathematical models presented in the thesis. Although much of the early work on certain topics, e.g. spray formation, ignition delay and heat release, was not considered directly applicable to HPCR systems, it was important to include these references in arriving at the final choice of particular recent model, e.g. *Siebers et al* [1,2] for spray formation and ignition delay and *Chmela and Orthaber* for heat release [3].
- Engine performance results obtained from the new integrated program are in good agreement with the experimental results. These results are torque, bsfc, and mass airflow, which cover the full limiting-torque-curve (LTC) for a Ford 1.8 litre high-pressure common rail, direct injection Diesel engine, for engine speeds of 1250 rev/min to 4000 rev/min.
- Results of the computational pressure traces are in very good agreement with the experimental results, particularly at higher engine speeds.
- Results of the new computational heat release submodels, which include rate of heat release and cumulative heat release are in good agreement with the

experimental results based on Concerto software, again particularly at higher engine speeds.

- As already pointed out, neglect of premixed burning in the analytical heat release model of chapter 6, based on the pure diffusion burning model of *Chmela and Orthaber* [3], does lead to some discrepancies between predicted and experimental cylinder pressure traces, particularly at low engine speeds. This also accounts for over predictions of NO_x formation at low engine speeds where premixed burning would contribute significantly to lower emission levels.
- In the case of the new spray propagation submodel, experimental results are not available, but the results are validated with the physically based impulse model using established conservation laws of mass and momentum.
- The spray deflection results although unfortunately not supported by direct experimental evidence, give entirely credible results for two alternative combustion chamber geometries.
- Finally, the calculations for swirl formation and spray-swirl interaction, again for the two alternative combustion chambers, based on the fully integrated program provide valuable insights into the interdependence of these parameters and engine operating conditions.

10.2 Suggestions for further work

In this section, some proposals are made for possible further research, which could be considered as two categories, i.e., experimental and theoretical works.

10.2.1 Experimental work

It is expected that the results of theoretical investigations supported by experimental studies, will further assist the understanding of the flow, combustion and emission characteristics in the design of more efficient and clean engines with reduced development times.

The exact level of swirl and the mean velocity distribution within the cylinder were not examined experimentally. However, measurements could be obtained with laser anemometry equipment used in conjunction with an optical head. Results obtained in this way would also be more useful when used with information obtained from films.

10.2.2 Theoretical work

- The final version of the analytical heat release model of section 6.3.4, with allowance for both ignition delay and a finite period for needle lift assumed to coincide with ignition delay would be significantly improved by incorporating data now available for the shape and duration of the needle lift ramp.
- The heat release model could be further improved by the incorporation of a submodel for premixed burning under conditions of low engine speed. This would also enhance the potential of the model for application to part load conditions.
- Spray wall impingement becomes increasingly important in HSDI Diesel engines with high injection pressure, since the spray penetration is increased, and some engines have intense impingement. Further extensions to the current spray model would be modelling of the wall jet, which is formed after impingement of the spray on the wall of the in-piston combustion bowl.
- The present NO_x submodel assumes that the entrainment constant, C, and zonal number, z, are pre-set. A minor modification required is the ability to vary these two constants. Change in the entrainment constant, C, could reflect the effect of both variation in injection pressure as well as enhanced entrainment associated with high swirl rates, wile large values of z would improve the resolution of the multi-zone combustion process.
- At present the only existing submodel for emissions is that for NO_x (Appendix A). Other new submodels for the prediction of hydrocarbons and particulate emissions could also be included.

10.3 References

1. **Naber, J.D., and Siebers, D.L.**, "Effect of gas density and vaporization on penetration and dispersion of diesel sprays", SAE 960034, (1996).

2. **Siebers, D.L., and Higgins, B.S.**, "Effects of injector conditions on the flame lift-off length of direct injection diesel sprays", Proc. THIESEL 2000, pp.303-321, Valencia, September 13-15, (2000).

3. **Chmela, F.G., and Orthaber, G.C.**, "Rate of Heat Release Prediction for Direct Injection Diesel Engines Based on Purely Mixing Controlled Combustion", SAE 990186 (1999).

APPENDIX A

NO_X emission submodel

Summary

It has already been shown that the multi-zone models of *Watson et al* [1], *Bazari* [2], and *Shahed et al* [3, 4], based on division of the spray into a large number of zones inevitably lead to large numbers of equations which have to be solved, without necessarily representing the full mathematical description of the burning process. The main simplification of the multi-zone sub-program in ODES originally intended for the prediction of NO_x emissions, but now also used to provide data for spray formation, propagation, and interaction with swirl (chapter 8) is that no attempt is made to locate the successively formed heat release zones spatially. Furthermore these zones are formed successively, rather than concurrently. This leads to considerable mathematical simplification and much more rapid computation.

A.1 Introduction

In order to develop a spray formation model, such as the spray trajectory and growth due to the combined effects of burning and entrainment, using the result of a quasi-dimensional model is inevitable. For this purposes a practical multi-zone [NO] prediction model for diesel engines developed by *D.Dang* and revised by *F.J.Wallace* [5] is used.

The model itself can be considered as an evolution based on the combustion model proposed by *Shahed* [3, 4]. This model uses input of fuel burn rate, pressure, bulk temperature and bulk equivalence ratio, from the zero-dimensional version of *ODES* in order to create a relatively simple quasi-dimensional model, which does not require spatial definition of the developing spray trajectory or growth by air entrainment etc., but rather relives on the creation of successive notional heat release zones each receiving, over a period defined by the number of separate zones to be created, a mass

of fuel derived from the known single-zone burning rate. The implementation of the present model is described in the next section.

A.2 General description of the model

The model draws the state of cylinder charge, heat release rate and heat transfer rate from the main program. Prior to heat release, a single-zone is assumed and the state of the charge in the sub-module is the same as that in the main program. Zone formation commences at the start of heat release. There are two types of zones, viz. an air zone, i.e., a mixture of fresh air and residuals, having the composition of the cylinder gases at IVC, and the rest product zones. Combustion takes place in only one zone at any time, designated as a heat addition zone. A new zone begins when the mass of fuel input to the present heat addition zone has reached a predetermined value and the new zone becomes the next heat addition zone. Simultaneously, gas from the 'air' zone continues to be entrained into the previous product zones. As time progresses, fuel energy is released; the zone numbers increases and the mass of the product zone increases while that of the 'air' zone diminishes. Combustion is assumed to take place at stoichiometric conditions. No unburned fuel is taken into consideration and heat release is instant. The amount of fuel burned (from the main program) is mixed with the correct quantity of charge from the 'air' zone and these forms a combustion sub-zone. For each step, the NO formation calculation is performed for each zone and the combustion sub-zone, and the combustion sub-zone is mixed with the heat addition zone afterwards.

A drastic simplification is effected in the process of determining zone states. Instead of rigorously solving the differential conservation equations for each zone, a simplified scheme is applied taking the cylinder pressure from the main program as the pressure that also applies to the multi-zone case. Since this pressure is common to all zones, a first estimate of the initial zone temperature at the beginning of the step is based on an assumed isentropic relationship, i.e., a compression of the zones from the pressure of the previous step to that of the present step. This temperature is then corrected for heat transfer and energy balance. This is followed by entrainment and combustion calculations. The final stage in the calculation sequence is, with the zone states and volumes obtained, the determination of chemical equilibrium and of the rate of formation of NO in each zone.

In the absence of spray formation equations, it is not possible to create zone divisions, and ultimately to calculate air entrainment to the product zones and zone states, through an assumed fuel concentration distribution as proposed by *Shahed* [4], since the boundary for integration is unknown. An alternative solution has to be sought. The present model uses an entrainment constant, C, which defines the rate of change of equivalence ratio in terms of the instantaneous equivalence ratio, and which in turn allows the instantaneous rate of entrainment to be calculated. There is no mixing between zones. However at EVO, the zones collapse to form a single-zone.

A.3 Model formulation

A.3.1 Zone division

The zone formation process is relatively straightforward. Before heat release, a single-zone is assumed (figure A.1). Thereafter, the procedure is as follows:

a) At each calculation step, a single combustion sub-zone is first formed in which a mass of fuel corresponding to that obtained from the main program is burned stoichiometrically.

b) This combustion sub-zone is now absorbed into the current heat addition zone, N+1, by mixing with it, while at the same time gas from the 'air' zone is entrained.

c) a and b continue simultaneously until the cumulative mass of fuel burnt has reached the total zone number.

d) The sequence a to c is then repeated for the next zone N+2.

e) Air entrainment takes place all the time once a zone starts to form until the equivalence ratio in that zone is equal to the trapped equivalence ratio derived from the single-zone main program.

No attempt has been made to ensure that the fuel input to each zone is precisely the same. This means that the fuel quantity, and eventually the total mass, in each zone will not be the same; as will be clear later the composition for every zone will be equal when entrainment is accomplished. Usually, the fuel mass will be more than for an even distribution among the zones, and the fuel in the last zone will have a smaller

share. The quantity of fuel in the heat addition zone is calculated in each step, rather than saved in memory, as follows:

$$m_{fh} = m_{zh} f_s \frac{f_{zh} - f_{za}}{1 + f_s f_{zh}} \tag{A.1}$$

where f_s stoichiometric fuel-air ratio

f equivalence ratio

m mass

and suffix z zonal

h heat addition zone

f fuel

a air zone

A.3.2 Initial calculation step

At the beginning of each step, the state of each zone is determined from the known state of the previous step. With the known cylinder pressure taken from the main program, the temperature is calculated through an isentropic relationship:

$$T_2 = T_1 \left(\frac{p_2}{p_1} \right)^{\frac{\gamma - 1}{\gamma}} \tag{A.2}$$

where T temperature

p pressure

γ specific heat ratio

and suffix 1 previous step

2 present step

Note that γ is the average between the two steps. In arriving at the cylinder pressure, the main program has taken the heat transfer, work transfer and heat release into account in the solution of the energy equation.

A.3.3 Correction for heat transfer

Owing to the single-zone nature of the main program, the heat transfer is distributed uniformly over the whole mass, while in a multi-zone case, due to non-uniform temperature among the zones; the amount of heat transfer varies for each zone. For this reason, it is considered that a correction to the initial zone temperatures would be appropriate. The method adopted is that by *Shahed* [3], i.e., assuming the amount of heat transfer from each zone is proportional to the product of its mass and temperature. It is implemented as follows:

First, the heat lost by the cylinder gases as a whole is 'recovered' for each zone as an increase in enthalpy proportional to its mass. In the second step, the heat transferred from each zone is then taken as a decrease in enthalpy proportional to the product of mass and temperature for each zone.

$$m_z h_{zc} \equiv h_{zo} m_z - \frac{dQ}{\sum m_z} m_z + dQ \frac{T_z m_z}{\sum T_z m_z}$$

$$\therefore \quad h_{zc} \equiv h_{zo} + dQ \left(\frac{T_z}{\sum m_z T_z} - \frac{1}{\sum m_z} \right) \tag{A.3}$$

where h specific enthalpy

dQ heat transfer

and suffix $_c$ corrected

$_o$ uncorrected

It can be seen that this correction procedure serves to redistribute the heat transfer over each zone.

A.3.4 Correction for energy balance

As mentioned earlier, heat release has been taken into account in the main program to obtain the cylinder pressure and temperature, which is then used in deriving the individual zone temperatures. However, for the multi-zone module, heat release has not taken place at this stage. Therefore a further correction is necessary from the point of view of energy balance. Clearly the sum of the enthalpy over all the zones should be equal to the total enthalpy of the cylinder charge, which in turn equals the total enthalpy determined by the main program but reduced by an amount equal to the

energy released from the fuel at that step. This gives an enthalpy adjustment in each zone such that:

$$h_z \equiv h_{zc} \frac{H - dHr}{\sum h_{zc}} \tag{A.4}$$

where H total cylinder enthalpy inc. dHr

dHr heat release during the step

h_{zc} 'corrected' from equ.(3)

The use of enthalpy instead of internal energy is due to the fact that in these processes, the cylinder pressure is fixed.

From the known enthalpy and pressure, zone temperature can be obtained, i.e., the state of the gas in each zone is completely determined.

A.3.5 Entrainment

A proper entrainment description is essential for the success of a multi-zone model to reflect the non-uniformity of the cylinder charge in both a spatial and temporal sense. In the real process, fuel concentration covers the entire range from zero to infinity (pure fuel). The composition of the cylinder charge may vary from a low equivalence ratio corresponding to the trapped condition, to pure product. In the *Shahed* [4] model, a fuel concentration distribution of a hyperbolic type along the spray axis and a gaussian type over the spray cross-section, is superimposed on a transient spray defined by entrainment can be evaluated.

In the present model, this assumption of a given distribution cannot be applied. Instead, a prescribed function is adopted. The idea is to allow zone composition represented by equivalence ratio to vary and from the variation of composition, the degree of entrainment to be determined. The key point is to exercise an effective and sensible control. The approach is to reduce the equivalence ratio incrementally step by step. The trapped equivalence ratio, i.e., that calculated at the trapped condition when all the intended fuel is put in, is taken as the reference value. Clearly this is also the value after combustion has been completed while the cylinder charge is considered as a uniform mixture. This value is designated as the minimum for the product zones, since the ultimate result of entrainment and mixing is a uniform charge over the entire cylinder. As time marches on, the zone equivalence ratio approaches the reference

value. Entrainment begins as soon as a zone starts to develop. Since combustion is always assumed stoichiometric, for each zone, equivalence ratio starts from unity. The entrainment is treated as consisting of two phases, viz. the combustion phase and a pure entrainment phase. During the first phase, the equivalence ratio as follows:

$$f_{z2} \equiv f_{z1} - \frac{f_{z1} - f_t}{C} \tag{A.5}$$

where f_t reference value

C prescribed constant

And suffix z_1 previous step

z_2 present step

During this period, entrainment reduces equivalence ratio and temperature, while subsequent mixing with the stoichiometric product from the combustion sub-zone does the opposite. During the second phase, the following relationship is applied:

$$f_{z2} \equiv f_{z1} - \frac{f_{ze} - f_t}{C} \tag{A.6}$$

where suffix e denotes the value at the end of zone heat addition

This means that, at each step, the equivalence ratio is reduced by a fixed amount, until at the last step, the reference value is reached. Thereafter, the zone composition is fixed. Mass and energy transfer are calculated as follows:

$$dm_z \equiv m_{z1} \frac{(1 + f_s f_{za})(f_{z2} - f_{z1})}{(1 + f_s f_{z1})(f_{z2} - f_{za})} \tag{A.7}$$

$$m_{z2} \equiv m_{z1} + dm_z \tag{A.8}$$

$$h_{z2} \equiv \frac{h_{z1} m_{z1} + h_a dm_z}{m_{z2}} \tag{A.9}$$

where dm_z mass entrainment

A.3.6 Combustion

As noted briefly earlier, combustion is always assumed to take place at stoichiometric condition, by taking the correct amount of charge from the 'air' zone (mixture of fresh air and residual) corresponding to the fuel that is taken from the heat release in the main program. This stoichiometric product will subsequently be mixed to the heat addition zone. In arriving at the combustion temperature, it is assumed that the initial

specific fuel enthalpy is the same as that in the air zone. The following relations are applied:

$$dm_{ab} \equiv dm_f \frac{1+f_{za}f_s}{f_s(1-f_{za})} \tag{A.10}$$

$$m_b \equiv dm_{ab} + dm_f \tag{A.11}$$

$$h_b \equiv h_a + \frac{dHr}{m_b} \tag{A.12}$$

where dm_{ab} mass for combustion draw from 'air' zone

dm_f fuel input

and suffix b combustion

From the product enthalpy, the temperature can be solved. The air zone mass will be updated below:

$$dm_a \equiv \sum dm_z + dm_{ab} \tag{A.13}$$

$$m_{a2} \equiv m_{a1} - dm_a \tag{A.14}$$

A.3.7 Zone volume determination

The zone volume is determined at this juncture because it is at this point that NO formation is to be evaluated. This evaluation is carried out within each zone. Further, the heat addition zone and the combustion sub-zone are treated separately before they finally mix. Therefore the volumes for these two zones will be determined separately similar to the rest.

Since for each zone, temperature and pressure are known, the volume can be obtained readily. However, one constraint has to be satisfied, i.e., the sum of the zone volumes equals the total cylinder volume. Therefore, instead of applying the state equation to separate zones, the zone volume is allocated in an overall perspective. Since the pressure for each zone is the same, and also, from the equation of state, under a constant pressure the volume is proportional to the product $m \cdot R \cdot T$. Hence, the zone volumes can be calculated as follows:

$$V_z \equiv V_c \frac{m_z R_z T_z}{\sum (m_z R_z T_z) + m_b R_b T_b} \tag{A.15}$$

$$V_b \equiv V_c \frac{m_b R_b T_b}{\sum (m_z R_z T_z) + m_b R_b T_b} \tag{A.16}$$

where V_z zone volume

V_c total cylinder volume

V_b combustion sub-zone volume

R specific gas constant

Finally, the heat addition zone and combustion sub-zone are mixed and the zone-state determined after performing the NO formation calculations described in section A.3.8:

$$f_{zh2} \equiv \frac{\frac{m_{h1} f_{zh1}}{1 + f_{zh1} f_s} + \frac{m_b}{1 + f_s}}{\frac{m_{h1}}{1 + f_{zh1} f_s} + \frac{m_b}{1 + f_s}} \tag{A.17}$$

$$m_{h2} \equiv m_{h1} + m_b \tag{A.18}$$

$$h_{h2} \equiv \frac{h_{h1} m_{h1} + h_b m_b}{m_{h2}} \tag{A.19}$$

It is worth noting that at this point, having completed the heat release and unifying the heat addition zone, another energy balance calculation similar to the previous one (section A.3.4) is carried out. This further fine-tunes the zone temperatures.

A.3.8 NO formation

The well known extended Zeldovich kinetic scheme is applied. The chemical reactions concerned are:

$$N + NO \overset{K1}{\rightleftharpoons} N_2 + O$$

$$N + O_2 \overset{K2}{\rightleftharpoons} NO + O$$

$$N + OH \overset{K3}{\rightleftharpoons} NO + H$$

Defining:

$$R_1 \equiv K_1 [N]_e [NO]_e \tag{A.20}$$

$$R_2 \equiv K_2 [N]_e [O_2]_e \tag{A.21}$$

$$R_3 \equiv K_3[N]_e[OH]_e \tag{A.22}$$

$$\beta \equiv \frac{[NO]}{[NO]_e} \tag{A.23}$$

where K_i equilibrium constant

[ ] concentration

and suffix $_e$ equilibrium value

Then (6),

$$\frac{d[NO]}{dt} \equiv \frac{2R_1(1-\beta^2)}{1+\dfrac{\beta R_1}{R_2+R_3}} \tag{A.24}$$

$$[NO]_2 \equiv [NO]_1 + \left(\frac{d[NO]}{dt}\right)dt \tag{A.25}$$

The equilibrium concentration is calculated according to *Olikara and Borman* [6], taking 11 species into account.

Further, the averaged NO concentration is calculated:

$$[NO]_a \equiv \frac{\sum([NO]_z m_z)}{\sum m_z} \tag{A.26}$$

A.4 Model discussion

As compared with the *Shahed* [3,4] model, the present one involves considerable simplification. Firstly, entrainment is presented through a simple relationship rather than using a complex transient spray together with the assumed fuel concentration distribution within it, avoiding the rather complicated iterative integration. Secondly, no attempt is made to solve the usual set of differential equations for each zone to determine the zone states, for which, again, iteration is necessary, whereas algebraic expressions are adopted, relying on certain information from the main program. Clearly, considerable-computing effort can be saved. However, the inevitable drawback is some deviation from the physical process. The justification is from the *Shahed* [3] model where a limited number of zones is employed and the average property values for each zone are used in the analysis, which should be regarded as a substantial deviation from the real process. Bearing this in mind, it is considered that the error incurred in the present model would be nevertheless acceptable.

The number of zones and the entrainment rate constant largely defines the model. It is expected that the entrainment rate constant will play a major role in fine-tuning to fit a specific type of engine.

The analysis of the practical multi-zone NO prediction model that was developed by *D.Dang* [5] provides the means of defining the mass, volume, and mean density of the spray by difference between the cylinder total volume and volume of the air-zone, with spray cone half angle based on the literature.

As has already been stated, incorporation of the ODES code and NO_x sub-program leads to the creation of the successive notional heat release zones with respective volumes, equivalence ratios, temperature and mass at any given crank-angle. The zonal results of the ODES code such as NO_x concentration, temperature, equivalence ratio, and mass are summarized in results files called, 'EMIS1', 'EMIS2', 'EMIS3', and 'EMIS4' respectively.

Typical plotted results of 'EMIS1', 'EMIS2', 'EMIS3', and 'EMIS4' for a four-stroke direct injection diesel engine are shown in figures A.2 to A.5. In applying the model, an arbitrary 11 zones, i.e. 1 air zone and 10 product zones, and an entrainment rate constant of 10 are adopted. The details of the engine configuration and operating conditions are illustrated in chapter 5, tables 1 and 2.

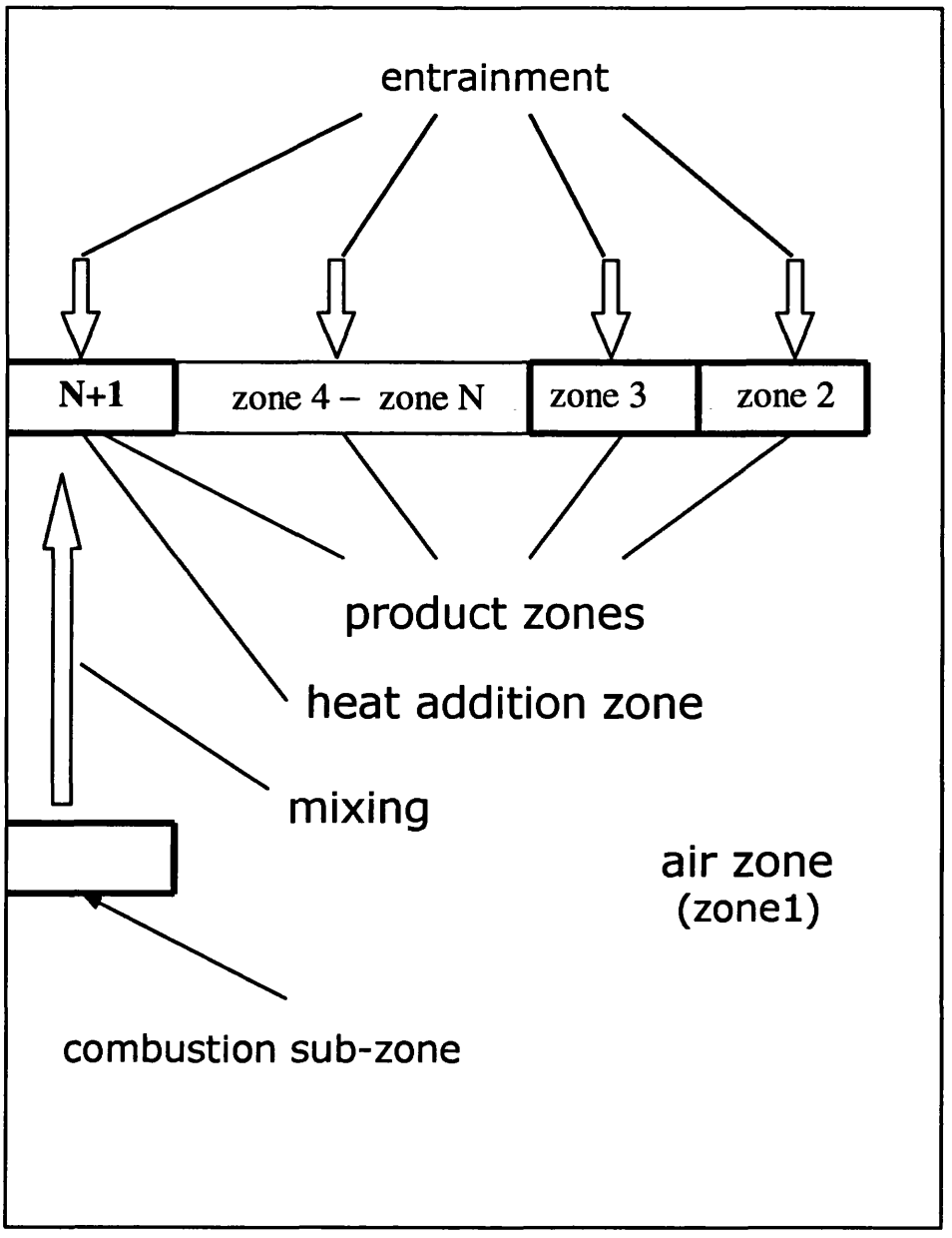

Figure A.1: The schematic of zone formation

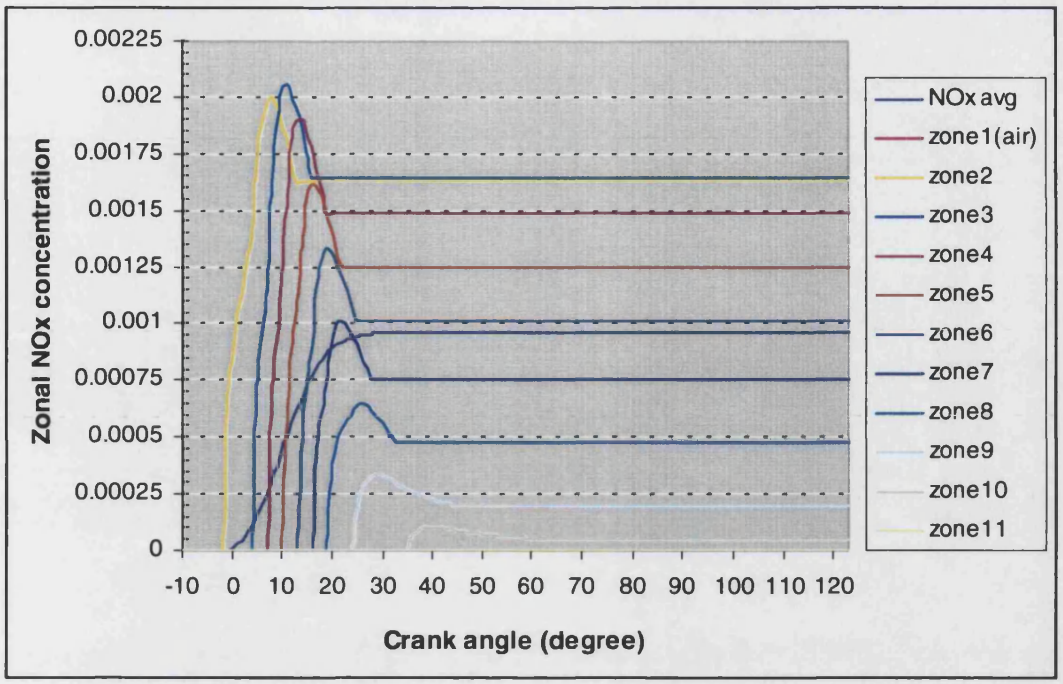

Figure A.2: Typical plotted results of EMIS1.RES

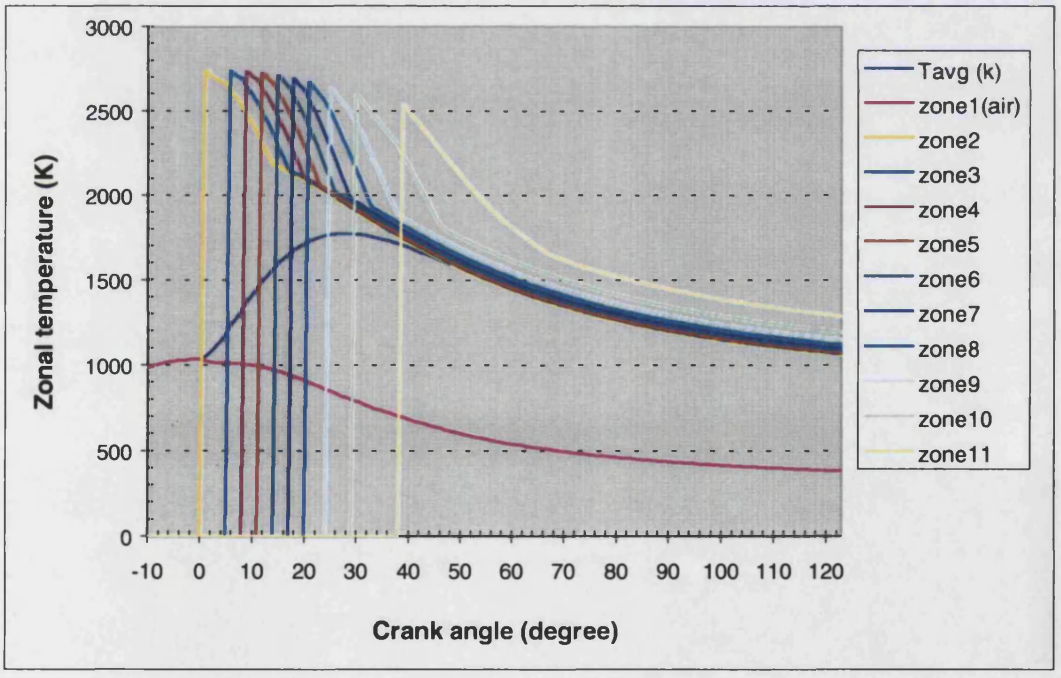

Figure A.3: Typical plotted results of EMIS2.RES

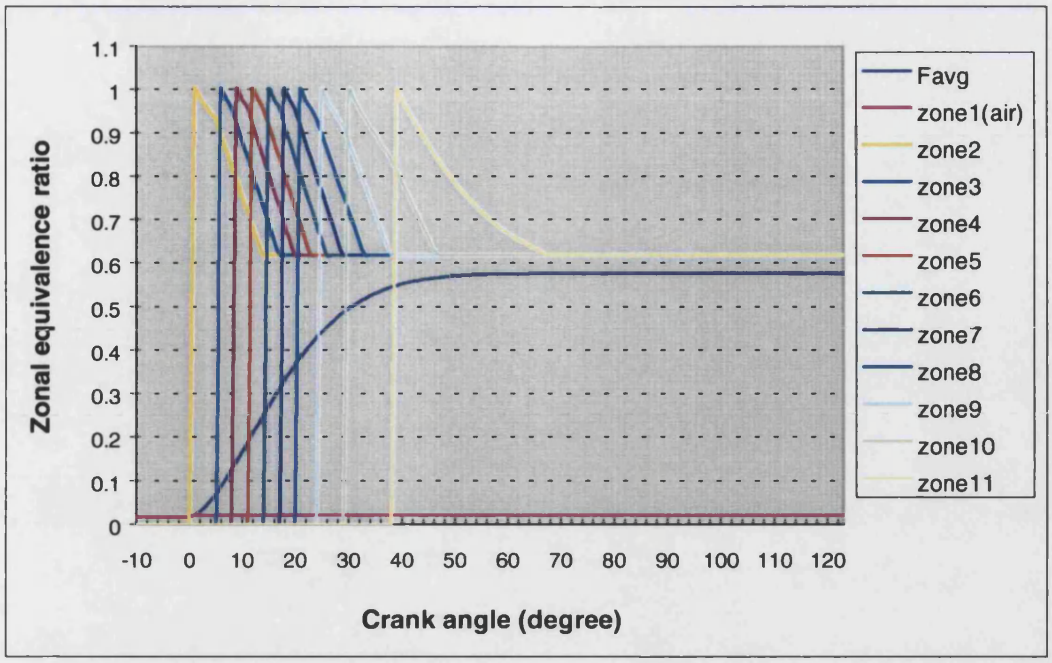

Figure A.4: Typical plotted results of EMIS3 .RES

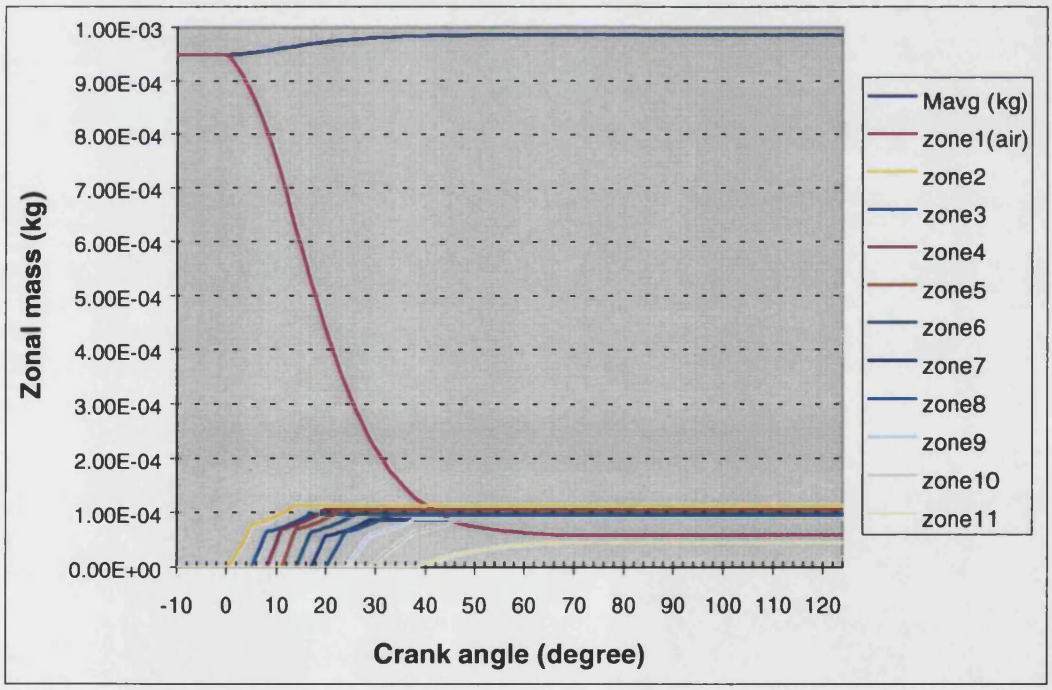

Figure A.5: Typical plotted results of EMIS4.RES

A.5 References

1. **Watson, N., Pilley, A.D., and Marzouk, M.**, "A Combustion Correlation for Diesel Engine Simulation", SAE 860029 (1980).

2. **Bazari, Z.**, "A DI Diesel Combustion and Emission Predictive Capability for Use in Cycle Simulation", SAE 920462 (1992).

3. **Shahed, S. M., Chiu, W. s., and Lyn, W. T.**, "A Mathematical Model of Diesel Combustion", Proceeding of the IMechE, C94/75, pp. 119-128 (1975).

4. **Chiu, W. s., Shahed, S. M., and Lyn, W. T.**, "A Transient Spray Mixing Model of Diesel Combustion, SAE 760128 (1976).

5. **Wallace, F.J.**, "Presentation of Simulation Package ODES at University Internal Combustion Group (UNICEG) meeting", University College London, December 1993.

6. **Olikara, C., and Borman, G.L.**, "A Computer Program for Calculating Properties of Equilibrium Combustion Products with Some Application to ID Engines", SAE 750468 (1975).

APPENDIX B

Spray formation and spray-swirl interaction coding

B.1 Introduction

As has already been mentioned, the purpose of the spray submodel is to calculate the spray trajectory for a free jet based on relations discussed in sections 3.3.1.3 and 8.4, as well as spray penetration and deflection in swirling air based on relations discussed in section 8.5. Section B.2 lists the spray subroutine, which goes to make up the spray formation predictive submodel. This subroutine covers:

- Calculations of the burning undeflected spray
- Calculation of burning spray deflection in swirling air
- Calculation of the swirl generation and decay in the main cylinder and the combustion bowl based on a given swirl rate in the main cylinder at IVC.

In section B.3 the tabular summary of the spray propagation and deflection is shown.

B.2 Subroutine for spray formation including deflected spray and swirl generation

```
c  ------------------------------------------------------------------------------
c  Subroutine spray
c  S. Khalil-Arya    Aug. 2001
c  Calculation of spray trajectory and spray deflection with cross-flow
c  ------------------------------------------------------------------------------
      SUBROUTINE SPRAY2(iss,ijk,i)
      INCLUDE 'GLOBAL22.FOR'
      DIMENSION FDRAG(720)
      IF(NCYCLE.EQ.NCYCT)THEN
          ISS=ISS+1
          I=ISS-1
          PI=3.1415926
          THETA1=THETA*PI/180.0
          CON1=PI*TAN(THETA1)**2./3.0
          bore1=GV(IDV(3,3),1)
          Rbore=bore1/2.0
          RBOWL=BOWL/2.0
          VB=(PI/3.0)*RBOWL*RBOWL*(2.0*DEPTH1+DEPTH2)
          E1E2=(3.0/5.0)*((4.0*DEPTH1+DEPTH2)/(2.0*DEPTH1+DEPTH2))
          EE22=2.*DEPTH1+SQRT(RBOWL**2.+(DEPTH1-DEPTH2)**2.)
          EE12=EE22/((4.*DEPTH1+DEPTH2)/5.0)
      IF(ISS.NE.1)THEN
```

```
      IJK=720.0+1.0-GR(1,7)
      IF(ISS.LE.IJK)THEN
       OMEGA(I+1,1)=OMEGA(I,1)-FRIC*OMEGA(I,1)*OMEGA(I,1)*TSTEP*(2.0
     &          +(PI*RBORE**3.0/(SVOL(I,1)-VB)))
       OMEGB(I+1,1)=OMEGB(I,1)+((SVOL(I+1,1)-SVOL(I,1))/SVOL(I,1))
     &          *(OMEGB(I,1)-OMEGA(I,1)*(bore1/BOWL)**2.0/E1E2)
     &          -FRIC*OMEGB(I,1)**2.0*TSTEP*EE12
C ------------------------ SWIRL FIRING CONDITIONS -------------
       OMEGAF(I+1,1)=OMEGAF(I,1)-FRIC*OMEGAF(I,1)*OMEGAF(I,1)*TSTEP*(2.0
     &          +(PI*RBORE**3.0/(SVOL(I,1)-VB)))
       OMEGBF(I+1,1)=OMEGBF(I,1)+((SVOL(I+1,1)-SVOL(I,1))/SVOL(I,1))
     &          *(OMEGBF(I,1)-OMEGAF(I,1)*(bore1/BOWL)**2.0/E1E2)
     &          -FRIC*OMEGBF(I,1)**2.0*TSTEP*EE12
C ---------------------------------------------------------------
      ELSE
           OMEGB(I+1,1)=OMEGB(I,1)-FRIC*OMEGB(I,1)*OMEGB(I,1)*EE12*TSTEP
           OMEGA(I+1,1)=OMEGA(I,1)+(VB/(SVOL(I,1)*(SVOL(I,1)-VB)))*E1E2*
     &          (OMEGB(I,1)*(BOWL/bore1)**2.0-OMEGA(I,1))*
     &          (SVOL(I+1,1)-SVOL(I,1))-FRIC*OMEGA(I,1)**2.0*
     &          (2.0+(PI*RBORE**3.0/(SVOL(I,1)-VB)))*TSTEP
C ------------------------ SWIRL FIRING CONDITIONS -------------
     OMEGBF(I+1,1)=OMEGBF(I,1)-FRIC*OMEGBF(I,1)*OMEGBF(I,1)*EE12*TSTEP
     OMEGAF(I+1,1)=OMEGAF(I,1)+(VB/(SVOL(I,1)*(SVOL(I,1)-VB)))*E1E2*
     &          (OMEGBF(I,1)*(BOWL/bore1)**2.0-OMEGAF(I,1))*
     &          (SVOL(I+1,1)-SVOL(I,1))-FRIC*OMEGAF(I,1)**2.0*
     &          (2.0+(PI*RBORE**3.0/(SVOL(I,1)-VB)))*TSTEP
C ---------------------------------------------------------------
      ENDIF
      ENDIF
           ENDIF
          OMEGA(1,1)=RW*SS(1,3)*2.0*PI/60.0
          OMEGB(1,1)=OMEGA(1,1)
          OMEGAF(1,1)=OMEGA(1,1)
          OMEGBF(1,1)=OMEGB(1,1)
      IF(STEMP(ISS,1).NE.STZ(ISS,1).AND.(ISS-IJK).LT.30)THEN
          SVZ(ISS,1)=SZM(ISS,1)*RAIR1*STZ(ISS,1)/SPR(ISS,1)
          SMFUB(ISS)=SMFINJ(ISS)-SMFB(ISS)
          SPMASS(ISS,1)=(SMASS(ISS,1)-SZM(ISS,1))/5.0+0.5*SMFUB(ISS)
          DENZ1(ISS)=SZM(ISS,1)/SVZ(ISS,1)
      IF(ISP.EQ.1)THEN
          DELSS(ISS-1,1)=0.0
          XSP1(ISS-1)=0.0
      DELX(ISS-1,1)=0.0
          GAMA(ISS-1)=0.0
          PEN(ISS,1)=XL0
      DELS(ISS,1)=PEN(ISS,1)
          DELSS(ISS,1)=DELS(ISS,1)
          TETAIGDR=TETAIGD*PI/180.0
          DIASP(ISS)=2.0*XL0*TAN(TETAIGDR)
          DENSP(ISS)=DENSPIGD
          VEL(ISS,1)=PEN(ISS,1)/TIGND1
          DELSM(ISS,1)=0.5*PEN(ISS,1)
          VEL2(ISS,1)=(1.0+0.5*CF*DENAIR/DENSP(ISS))**0.5
     &          *2.0*DELSM(ISS,1)*TAN(TETAIGDR)
          VEL2(ISS,1)=SQRT(DENF/DENSP(ISS))*FVN*DNOZ/VEL2(ISS,1)
```

```
        YSP(ISS-1)=0.0
        YMS(ISS)=0.0
        Fdrag(iss-1)=0.0
        U2D2(ISS)=(VEL(ISS,1)*DIASP(ISS))**2.0
        SP1(ISS)=2.0*XL0**2.0/(PI*DENSP(ISS)*U2D2(ISS))
        SPVOL(ISS,1)=VSPIGND
        SP2(ISS)=SPVOL(ISS,1)*DENSP(ISS)/(TIGND1*DELS(ISS,1))
        SP3(ISS)=0.5*CF*DENAIR*DIASP(ISS)
        CALL ITERSP(ISS,IJK,I)
        Fdrag(iss)=Fdrag(iss-1)+0.5*Cf*denz1(iss)*diasp(iss)*pen(iss,1)*
     &      vs(iss)**2.0*cos(gama(iss))**2.0*5.0
        XSP1(ISS)=XSP1(ISS-1)+DELX(ISS,1)
        ISP=ISP+1
c ---------------------------------------------------------------
        BAVOL(ISS)=VB-(spvol(iss,1))*5.0
        BAMASS(ISS)=SPR(ISS,1)*BAVOL(ISS)/(RAIR1*STZ(ISS,1))
c ---------------------------------------------------------------
        IF(ISS.LE.IJK)THEN
C -------SWIRL FIRING CONDITIONS (During ignition delay (Before TDC ))-----
     OMEGAF(I+1,1)=OMEGAF(I,1)-FRIC*OMEGAF(I,1)*OMEGAF(I,1)*TSTEP*(2.0
     &          +(PI*RBORE**3.0/(SVOL(I,1)-VB)))
         OMEGBF(I+1,1)=OMEGBF(I,1)+((SVOL(I+1,1)-SVOL(I,1))/SVOL(I,1))
     &          *(OMEGBF(I,1)-OMEGAF(I,1)*(bore1/BOWL)**2.0/E1E2)-
     & (2.0/(BAMASS(ISS)*E1E2*rbowl*rbowl))*SPVOL(ISS,1)*5.0*DENSP(ISS)*
     & (VS(ISS)-VEL(ISS,1)*SIN(GAMA(ISS)))*0.5*pen(iss,1)
     & -FRIC*DENZ1(ISS)*OMEGBF(I,1)**2.0*PI*RBOWL**2.0*TSTEP*EE22/
     & (E1E2*BAMASS(ISS))
     & -Fdrag(iss)*DELSM(ISS,1)*TSTEP*2.0/(BAMASS(ISS)*E1E2*rbowl*rbowl)
     ELSE
C -------SWIRL FIRING CONDITIONS (During ignition delay (After TDC ))-----
         OMEGBF(I+1,1)=OMEGBF(I,1)-
     & (2.0/(BAMASS(ISS)*E1E2*rbowl*rbowl))*SPVOL(ISS,1)*5.0*DENSP(ISS)*
     & (VS(ISS)-VEL(ISS,1)*SIN(GAMA(ISS)))*0.5*pen(iss,1)
     & -FRIC*DENZ1(ISS)*OMEGBF(I,1)**2.0*PI*RBOWL**2.0*TSTEP*EE22/
     & (E1E2*BAMASS(ISS))
     & -Fdrag(iss)*DELSM(ISS,1)*TSTEP*2.0/(BAMASS(ISS)*E1E2*rbowl*rbowl)
         OMEGAF(I+1,1)=OMEGAF(I,1)+(VB/(SVOL(I,1)*(SVOL(I,1)-VB)))*E1E2*
     &          (OMEGBF(I,1)*(BOWL/bore1)**2.0-OMEGAF(I,1))*
     &          (SVOL(I+1,1)-SVOL(I,1))-FRIC*OMEGAF(I,1)**2.0*
     &          (2.0+(PI*RBORE**3.0/(SVOL(I,1)-VB)))*TSTEP
        ENDIF
C ---------------------------------------------------------------
     GOTO 38
        ENDIF
C ------------------------ SWIRL SPRAY INTRACTION -------------
     IF(ISP.EQ.2)THEN
        SPVOL(ISS-1,1)=(SVOL(ISS-1,1)-SVZ(ISS-1,1))/5.0
        ENDIF
C ---------------------------------------------------------------
        SPVOL(ISS,1)=(SVOL(ISS,1)-SVZ(ISS,1))/5.0
       DSMFINJ(ISS)=SMFINJ(ISS)-SMFINJ(ISS-1)
        DSMFB(ISS)=SMFB(ISS)-SMFB(ISS-1)
        DSMFUB(ISS)=SMFUB(ISS)-SMFUB(ISS-1)
        DSPMASS(ISS,1)=SPMASS(ISS,1)-SPMASS(ISS-1,1)
        DSPVOL(ISS,1)=SPVOL(ISS,1)-SPVOL(ISS-1,1)
```

```
      DENSP(ISS)=DSPMASS(ISS,1)/DSPVOL(ISS,1)
      DENZ1(ISS)=(DENZ1(ISS)+DENZ1(ISS-1))/2.0
      DELSS(ISS,1)=((DSPVOL(ISS,1)/CON1)+(DELSS(ISS-1,1))**3.)**(1./3.)
      DELS(ISS,1)=DELSS(ISS,1)-DELSS(ISS-1,1)
      PEN(ISS,1)=PEN(ISS-1,1)+DELS(ISS,1)
      VEL(ISS,1)=DELS(ISS,1)/tstep
      DELSM(ISS,1)=PEN(ISS,1)-0.5*DELS(ISS,1)
      VEL2(ISS,1)=(1.0+0.5*CF*DENZ1(ISS)/DENSP(ISS))**0.5
     &      *2.0*DELSM(ISS,1)*TAN(THETA1)
      VEL2(ISS,1)=SQRT(DENF/DENSP(ISS))*FVN*DNOZ/VEL2(ISS,1)
      DIASP(ISS)=2.0*DELSM(ISS,1)*TAN(THETA1)
      U2D2(ISS)=(VEL(ISS,1)*DIASP(ISS))**2.0
      SP1(ISS)=2.0*DELS(ISS,1)**2.0/(PI*DENSP(ISS)*U2D2(ISS))
      SP2(ISS)=DSPVOL(ISS,1)*DENSP(ISS)/(tstep*DELS(ISS,1))
      SP3(ISS)=0.5*CF*DENZ1(ISS)*DIASP(ISS)
      YMS(ISS)=YSP(ISS-1)+0.5*DELS(ISS,1)*SIN(GAMA(ISS-1))
    IF((ISS-IJK).LT.ISPDEF)THEN
C ------------------------ SWIRL SPRAY INTRACTION ------------
      BAVOL(ISS)=VB-SPVOL(ISS,1)*5.0
      BAMASS(ISS)=SPR(ISS,1)*BAVOL(ISS)/(RAIR1*STZ(ISS,1))
C ---------------------------------------------------------------
      CALL ITERSP(ISS,IJK,I)
      XSP1(ISS)=XSP1(ISS-1)+DELX(ISS,1)
      Fdrag(iss)=Fdrag(iss-1)+0.5*Cf*denz1(iss)*diasp(iss)*DELS(ISS,1)*
     &      vs(iss)**2.0*cos(gama(iss))**2.0*5.0
      IF((XSP1(ISS)-RBOWL).GE.0.001)THEN
      ISPDEF=ISS-IJK
      GOTO 66
    ENDIF
      IF(ISS.LE.IJK)THEN
C -------SWIRL FIRING CONDITIONS (During ignition delay (Before TDC ))-----
     OMEGAF(I+1,1)=OMEGAF(I,1)-FRIC*OMEGAF(I,1)*OMEGAF(I,1)*TSTEP*(2.0
     &      +(PI*RBORE**3.0/(SVOL(I,1)-VB)))
      OMEGBF(I+1,1)=OMEGBF(I,1)+((SVOL(I+1,1)-SVOL(I,1))/SVOL(I,1))
     &      *(OMEGBF(I,1)-OMEGAF(I,1)*(bore1/BOWL)**2.0/E1E2)-
     & 2.0*(DSPVOL(I+1,1)*5.0*DENSP(I+1))
     & *(VS(ISS)-VEL(ISS,1)*SIN(GAMA(ISS)))*XMSP(ISS)
     & /(BAMASS(ISS)*RBOWL*RBOWL*E1E2)
     & -FRIC*DENZ1(ISS)*OMEGBF(I,1)**2.0*PI*RBOWL**2.0*TSTEP*EE22/
     & (E1E2*BAMASS(ISS))
     & -Fdrag(iss)*DELSM(ISS,1)*TSTEP*2.0/(BAMASS(ISS)*E1E2*RBOWL*RBOWL)
C -------SWIRL FIRING CONDITIONS (During ignition delay (After TDC ))-----
    ELSE
    OMEGBF(I+1,1)=OMEGBF(I,1)-
     & 2.0*(SPVOL(ISS,1)*5.0*DENSP(ISS)-SPVOL(ISS-1,1)*5.0*DENSP(ISS-1))
     & *(VS(ISS)-VEL(ISS,1)*SIN(GAMA(ISS)))*XMSP(ISS)
     & /(BAMASS(ISS-1)*RBOWL*RBOWL*E1E2)
     & -FRIC*DENZ1(ISS)*OMEGBF(I,1)**2.0*PI*RBOWL**2.0*TSTEP*EE22/
     & (E1E2*BAMASS(ISS-1))
     &-Fdrag(iss)*DELSM(ISS,1)*TSTEP*2./(BAMASS(ISS-1)*E1E2*rbowl*rbowl)
      OMEGAF(I+1,1)=OMEGAF(I,1)+(VB/(SVOL(I,1)*(SVOL(I,1)-VB)))*E1E2*
     &      (OMEGBF(I,1)*(BOWL/bore1)**2.0-OMEGAF(I,1))*
     &      (SVOL(I+1,1)-SVOL(I,1))-FRIC*OMEGAF(I,1)**2.0*
     &      (2.0+(PI*RBORE**3.0/(SVOL(I,1)-VB)))*TSTEP
    endif
```

```
C -------------------------------------------------------------
      IF(SINOUS(ISS).GE.1.0)THEN
      WRITE(82,23)ISS-IJK,SINOUS(ISS)
 23  FORMAT(2X,45('-')/19X,'CA=',I3/19X,'SIN(GAMA)=',1F6.3/2X,45('-'))
   ISPDEF=ISS-IJK
      GOTO 66
   ENDIF
      ENDIF
 66  CONTINUE
      ISP=ISP+1
 38  CONTINUE
      ENDIF
      RETURN
      END
```

B.3 Tabular summary

Table B.1 summarises the undeflected spray results of the spray subroutine for an engine speed of 2000 rev/min, which tabulates the following parameters at each crank angle:

CA: crank angle

p_{cyl}: cylinder pressure

V_{cyl}: cylinder volume

T_{cyl}: cylinder temperature

T_{zl}: air zone temperature

m_{cyl}: cylinder mass

m_{zl}: air zone mass

V_{zl}: air zone volume

dm_{finj}: injected fuel mass increment

dm_{fb}: burnt fuel mass increment

dm_{fun}: unburnt fuel mass increment

dm_{sp}: spray mass increment

dV_{sp}: spray volume increment

ρ_{sp}: spray density

ρ_{zl}: air zone density

ds: spray tip penetration increment

s: total spray tip penetration

s_m: spray mid element penetration

v_1: spray mean velocity based on NO_x model

v_2: spray mean velocity based on phenomenological model

v_1: spray mean velocity based on NO_x model

v_2: spray mean velocity based on phenomenological model

Δs: spray tip penetration increment in the tangential direction

Δx: spray tip penetration increment in the axial direction

x_m: spray mid element penetration in the axial direction

The propagation velocity has been plotted versus propagation distance in figure B.1. It can be clearly seen that, as expected, spray velocity decreases along the spray propagation path.

Table B.1: Summary of undeflected spray results

CA deg	$p_{cyl.}$ kPa	$V_{cyl.}$ m^3	$T_{cyl.}$ K	T_{z1} K	m_{cyl} kg	m_{z1} kg	V_{z1} m^3	dmf_{inj} kg	dmf_b kg	dmf_{un} kg	dm_{sp} kg	dV_{sp} kg	ρ_{sp} kg/m^3	ρ_{z1} kg/m^3	ds m	s m	x_m m	v_1 m/s	v_2 m/s
-1	10261.6	2.55E-05	938.43	929.98	9.37E-04	9.34E-04	2.43E-05	0.00E+00	0.00E+00	0.00E+00	0.00E+00	0.00E+00	46.65	38.45	0.01605	0.01605	0.008025	104.56	104.44
TDC	10437.8	2.55E-05	952.19	925.98	9.37E-04	9.27E-04	2.36E-05	4.14E-07	6.56E-08	3.49E-07	1.59E-06	1.28E-07	12.36	38.86	0.004011	0.020061	0.018055	48.13	58.50
1	10673.6	2.55E-05	974.31	922.44	9.38E-04	9.17E-04	2.27E-05	4.14E-07	1.10E-07	3.04E-07	2.28E-06	1.81E-07	12.56	39.59	0.003829	0.02389	0.021975	45.95	47.66
2	10959.3	2.57E-05	1004.2	920	9.38E-04	9.04E-04	2.18E-05	4.14E-07	1.49E-07	2.66E-07	2.91E-06	2.20E-07	13.21	40.55	0.003436	0.027326	0.025608	41.23	40.10
3	11278.2	2.59E-05	1040.7	918.65	9.39E-04	8.88E-04	2.08E-05	4.14E-07	1.82E-07	2.33E-07	3.50E-06	2.49E-07	14.07	41.66	0.003053	0.030379	0.028852	36.63	34.73
4	11611.2	2.62E-05	1082.42	918.02	9.40E-04	8.69E-04	1.97E-05	4.14E-07	2.10E-07	2.04E-07	4.03E-06	2.68E-07	15.04	42.87	0.002722	0.0331	0.031739	32.66	30.77
5	11939.7	2.66E-05	1127.98	917.67	9.41E-04	8.48E-04	1.87E-05	4.14E-07	2.34E-07	1.80E-07	4.52E-06	2.82E-07	16.04	44.10	0.002447	0.035547	0.034324	29.36	27.75
6	12246.8	2.71E-05	1176.12	917.12	9.42E-04	8.24E-04	1.77E-05	4.14E-07	2.54E-07	1.61E-07	5.02E-06	2.93E-07	17.12	45.31	0.002234	0.037781	0.036664	26.80	25.33
7	12519.3	2.76E-05	1225.71	916.03	9.44E-04	7.99E-04	1.68E-05	4.14E-07	2.70E-07	1.44E-07	5.49E-06	3.03E-07	18.10	46.47	0.002061	0.039842	0.038811	24.74	23.40
8	12746.9	2.83E-05	1275.78	914.08	9.45E-04	7.71E-04	1.59E-05	4.14E-07	2.83E-07	1.31E-07	5.93E-06	3.13E-07	18.94	47.53	0.001924	0.041766	0.040804	23.09	21.85
9	12923	2.90E-05	1325.57	911.04	9.47E-04	7.40E-04	1.50E-05	4.14E-07	2.93E-07	1.21E-07	6.40E-06	3.25E-07	19.73	48.48	0.001824	0.04359	0.042678	21.89	20.54
10	13043.8	2.99E-05	1374.45	906.82	9.48E-04	7.08E-04	1.41E-05	4.14E-07	3.01E-07	1.13E-07	6.86E-06	3.37E-07	20.36	49.30	0.001745	0.045335	0.044463	20.94	19.46
11	13108.7	3.08E-05	1421.95	901.39	9.49E-04	6.73E-04	1.33E-05	4.14E-07	3.06E-07	1.08E-07	7.32E-06	3.51E-07	20.85	49.98	0.001685	0.04702	0.046178	20.22	18.55
12	13134.2	3.18E-05	1467.68	895.21	9.51E-04	6.36E-04	1.24E-05	4.14E-07	3.10E-07	1.04E-07	7.85E-06	3.70E-07	21.23	50.55	0.001652	0.048673	0.047846	19.83	17.76
13	13091.7	3.29E-05	1511.4	887.41	9.53E-04	5.96E-04	1.16E-05	4.14E-07	3.12E-07	1.02E-07	8.34E-06	3.86E-07	21.62	50.98	0.001612	0.050285	0.049479	19.34	17.05
14	13001.1	3.40E-05	1552.99	878.54	9.54E-04	5.60E-04	1.09E-05	4.14E-07	3.13E-07	1.02E-07	7.48E-06	3.79E-07	19.75	51.27	0.001489	0.051773	0.051029	17.87	17.00
15	12868	3.53E-05	1592.38	868.73	9.56E-04	5.22E-04	1.01E-05	4.14E-07	3.12E-07	1.02E-07	7.97E-06	4.00E-07	19.94	51.44	0.001483	0.053257	0.052515	17.80	16.46

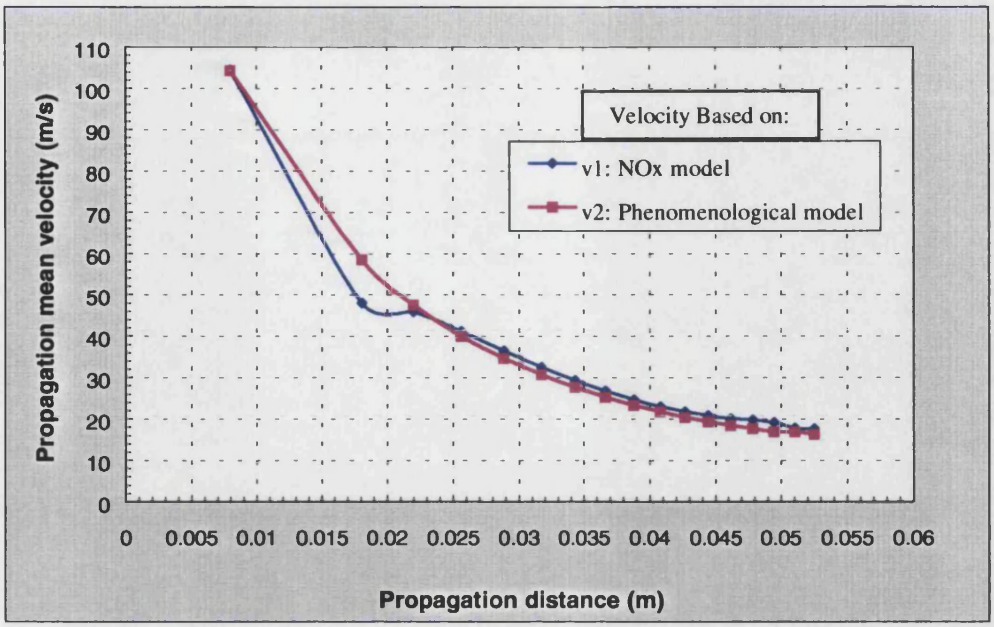

Figure B.1: Propagation mean velocity versus propagation distance

Table B.2 summarises the deflected spray results of the spray subroutine for an engine speed of 2000 rev/min, which tabulates the following parameters at each crank angle;

CA: crank angle

Δs: spray tip penetration increment in the tangential direction

Δx: spray tip penetration increment in the axial direction

x_m: spray mid element penetration in the axial direction

α: spray deflection angle

ω_b: swirl angular velocity in the combustion bowl

v_s: cross flow velocity

y: spray deflection distance

The spray deflection distance has been plotted versus mean propagation distance in figure B.1 before impingement.

TableB.2: Summary of spray deflection results

CA (deg)	Δs (m)	Δx (m)	x_m (m)	α (deg)	ω_b (rad/s)	v_s (m/s)	y (m)
-2	0	0	0	0	0	0	0
-1	1.60E-02	0.016048	8.02E-03	0.787	841.06	6.75	0.00022
TDC	4.01E-03	3.98E-03	1.80E-02	7.629	816.42	15.14	0.000753
1	3.83E-03	3.72E-03	2.19E-02	13.868	779.02	17.83	0.001671
2	3.44E-03	3.23E-03	2.54E-02	20.070	731.75	19.71	0.00285
3	3.05E-03	2.74E-03	2.83E-02	26.196	677.56	20.70	0.004197
4	2.72E-03	2.31E-03	3.09E-02	32.025	676.38	20.87	0.00564

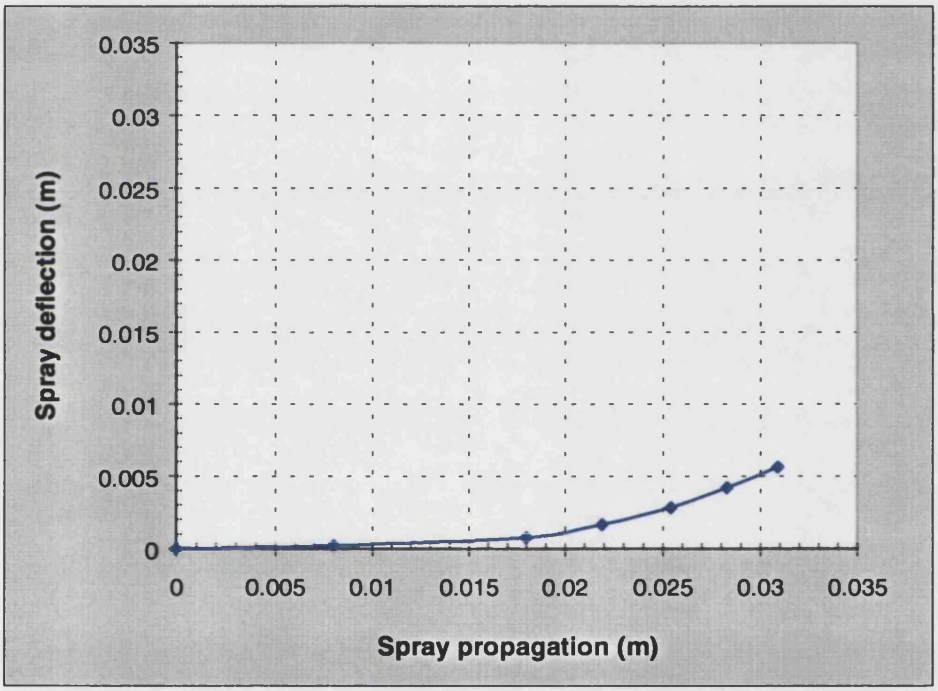

Figure B.2: Deflection spray in a cross-flow field

APPENDIX C

Overall programming structure of ODES 4-4

C.1 Introduction

As has already been mentioned ODES is an engine simulation package that has been developed by Prof. *F. J. Wallace et al.* at the University of Bath. The program can be used for the simulation of Diesel engines, Otto engines, Wankel engines, and other thermo-fluid plants such as air compressors and gas turbines. Over the years the program has been enhanced by the addition of a number of submodels. The thesis describes all new submodels developed by the writer and now incorporated in the expanded program ODES4-4.

This appendix introduces the main programming structure together with input file and block output file (ODES60.RES).

C.2 Main program structure

The ODES4-4 code is written in Fortran 77 in a modular and hierarchical form. This allows the flow of the program to be followed with ease and the extension of the program, by the addition of submodels, is relatively straightforward.

Each submodel is written as a separate subroutine and is as independent as possible. This provides the required flexibility for the simulation, and allows the selection of alternative models for a specific task, for example selection of different models for heat transfer or heat release.

The program utilises a global variables file, which may be accessed by all submodels within the program, to allow unconstrained transfer of data between submodels.

Figure C.1 illustrates the main file flowchart of the new integrated program ODES 4-4 code.

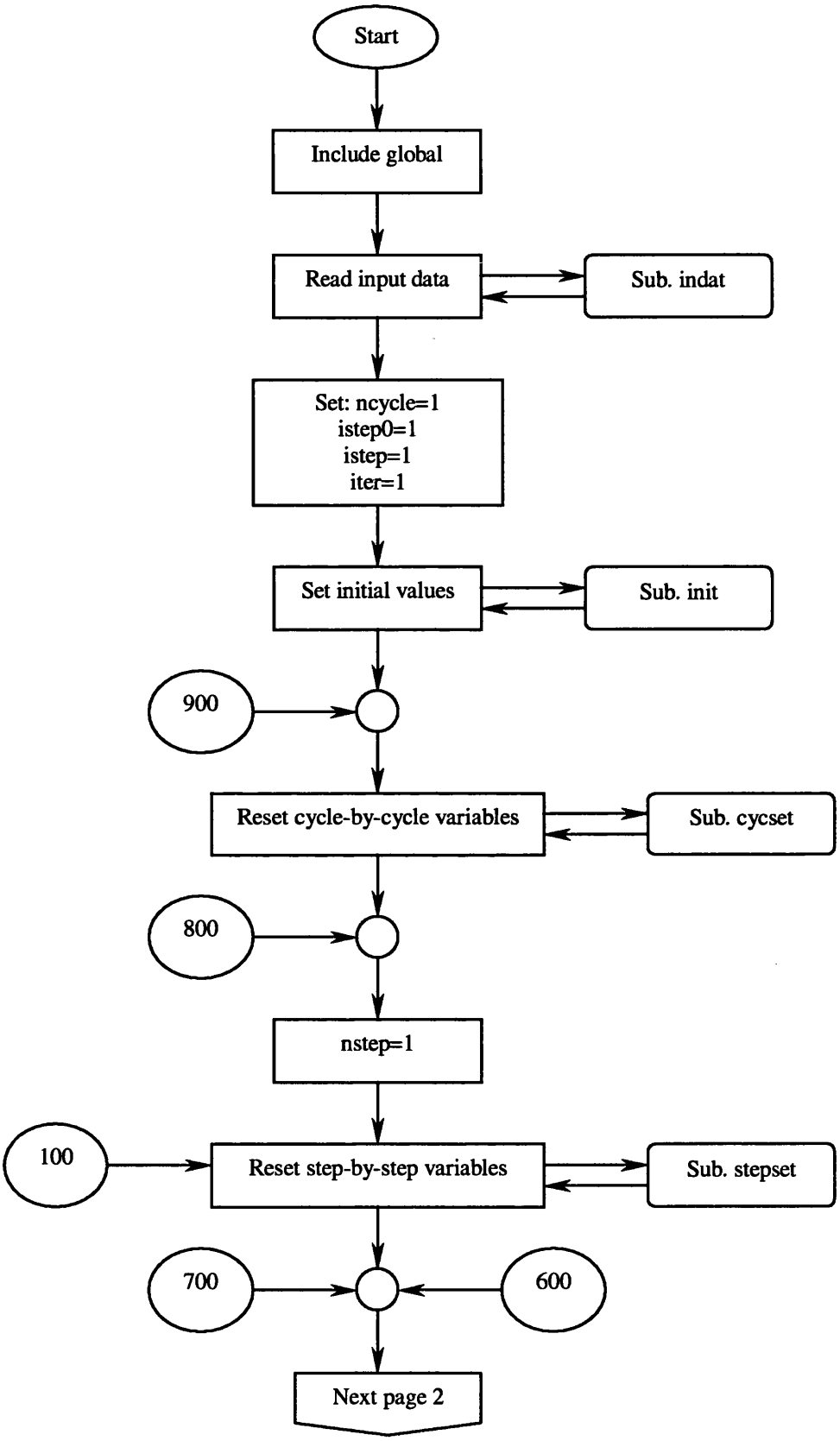

Figure C.1: The main file flow chart

Continue of figure C.1

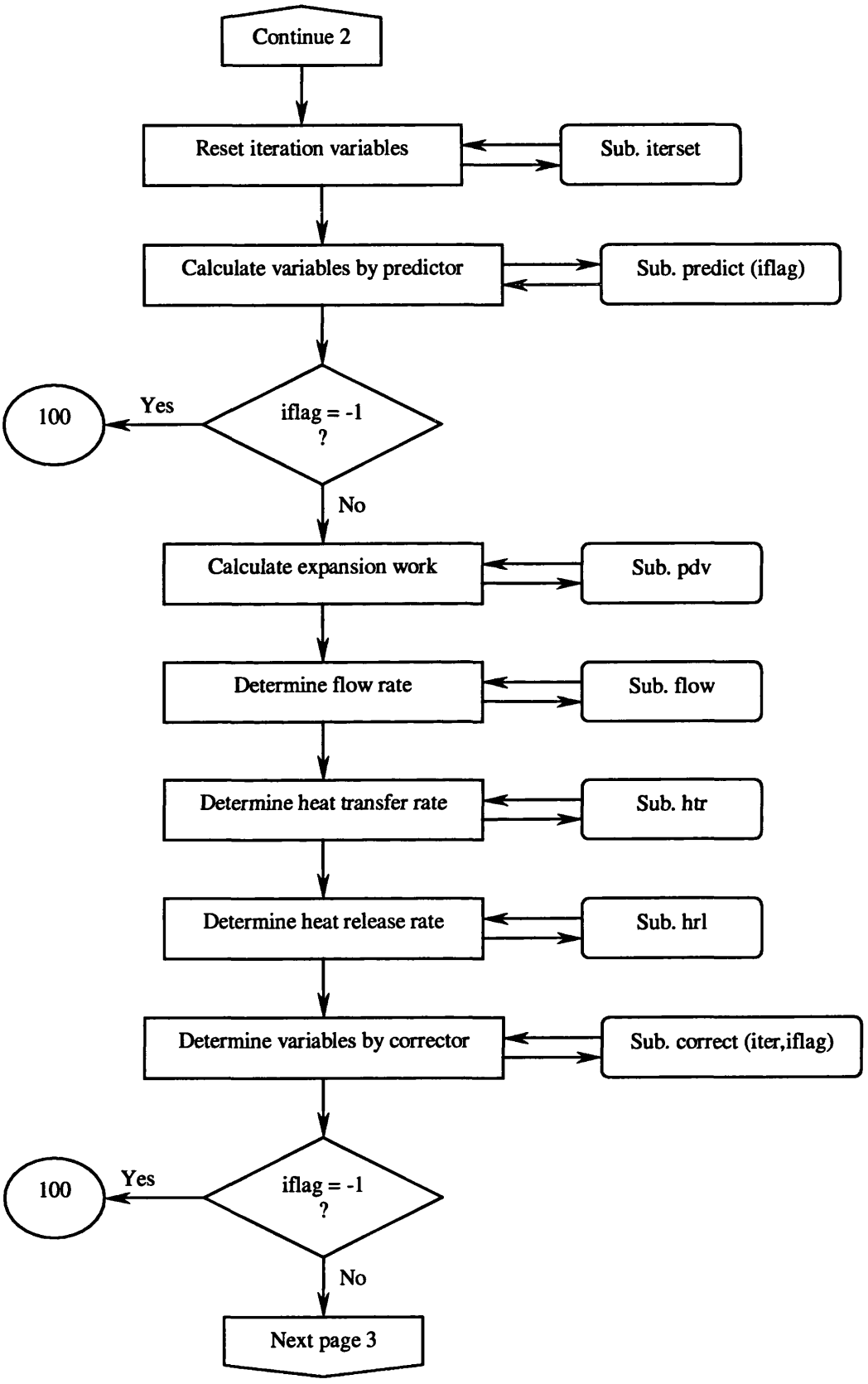

Continue of figure C.1

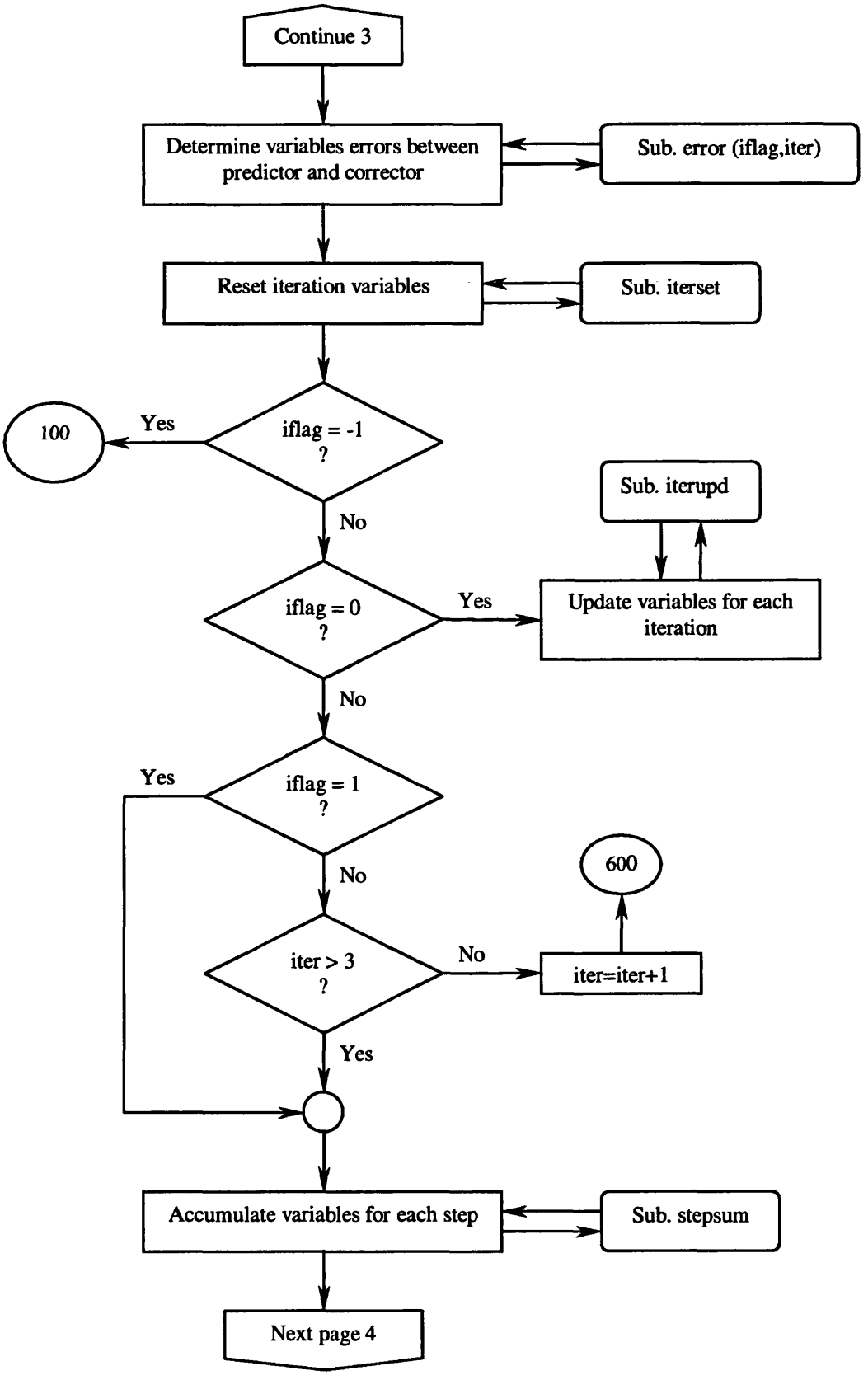

Continue of figure C.1

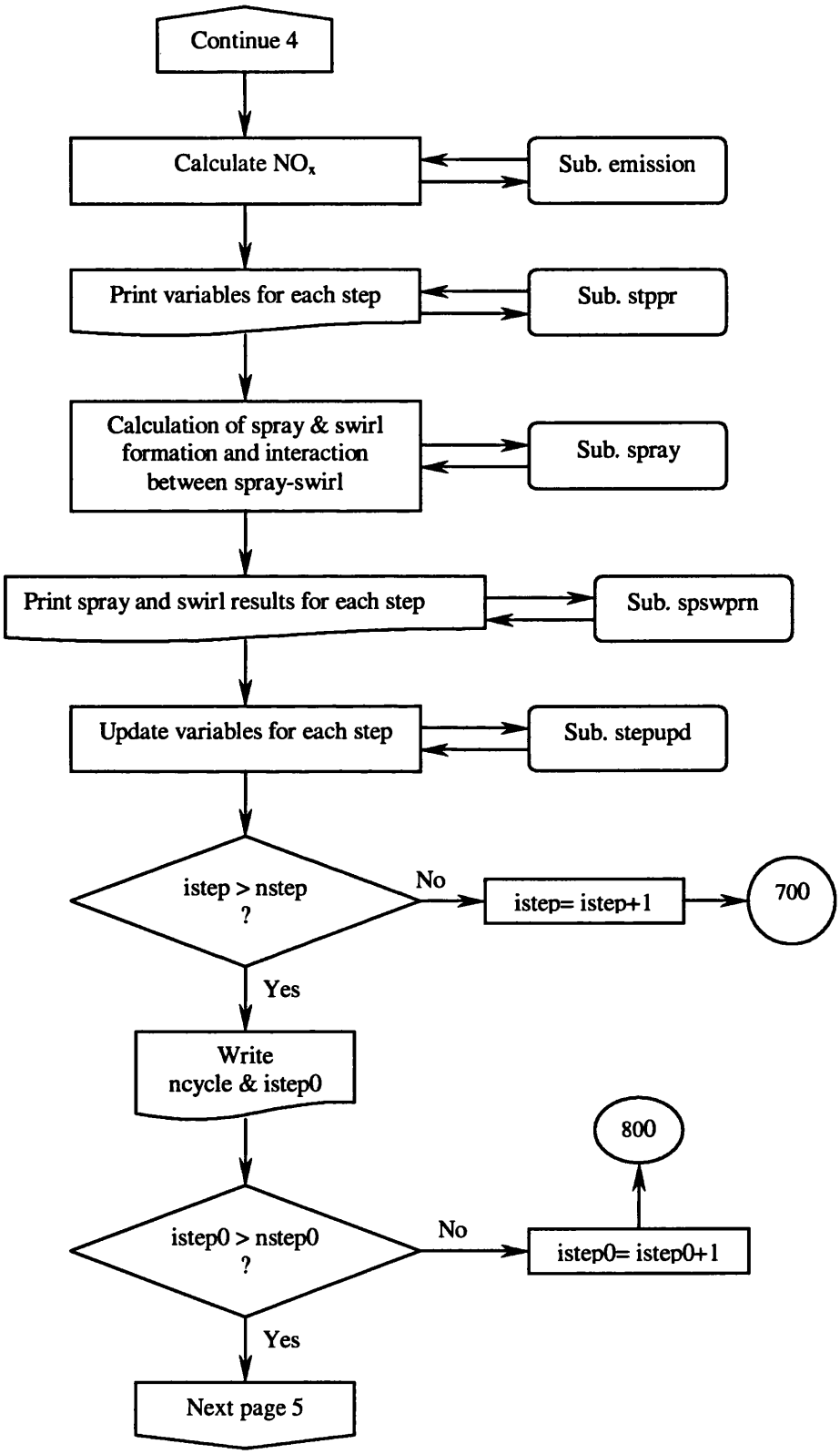

Continue of figure C.1

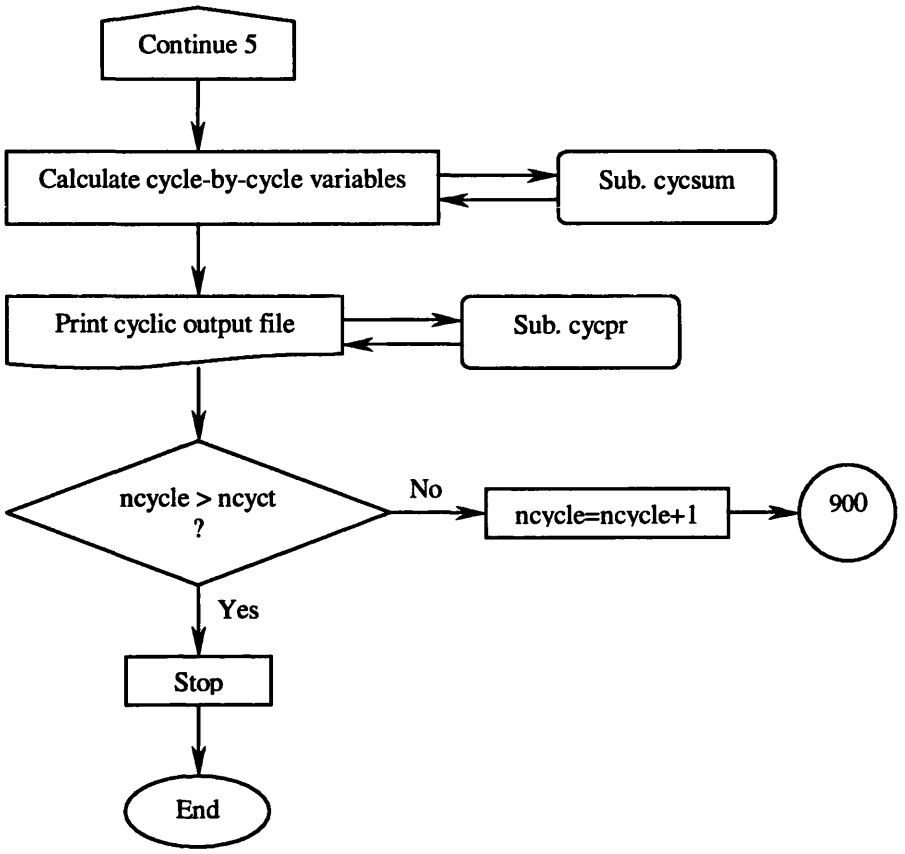

C.3 ODES4-4 Input file

There is one main input file for the ODES4-4 simulation package. This file provides the information, which defines the system being modelled. It contains information, which describes the configuration of the systems components and their geometry, the selection of submodels, and the relevant parameters required by these submodels. It also includes control data to determine, which mode of simulation is used and which output files are produced.

The specifications of the modelled Diesel engine and test conditions for the demonstration calculation (N_e = 2000 rev/min) are given in table C.1 (ODES.DAT).

Table C.1: ODES4-4 input data file (ODES.DAT)

```
################################################
#       ODES4-4 Engine Simulation Parameter File       #
#       Diesel Engine                                  #
#       4 Stroke / 4 Cylinder - Capacity 1753 cc       #
#       Direct Injection (DI) Combustion Chamber       #
################################################

# Group 1 - SYSTEM CONFIGURATION

# nv  nr  ns  nj  ngv  ngr  nht  nhr  nsc  nvalv  ncomp  nturb
6  11  1  0  3  5  2  1  1  2  0  0

# Group 2 - CONTROL VOLUME DEFINITION [idv(i,j)]

# type  cyc  cvgd  ht  htd  hr  hrd  fm  -  -  -
7  0  1  1  1  0  0  0  0  0  0  # cv 1 - Air Filter / Pre-Comp Manifold
7  0  3  1  1  0  0  0  0  0  0  # cv 2 - Pre Turbine / Exhaust Manifold
1  4  2  3  2  1  1  2  0  1  1  # cv 3 - Cylinder No.1
1  4  2  3  2  1  1  2  0  1  1  # cv 5 - Cylinder No.2
1  4  2  3  2  1  1  2  0  1  1  # cv 6 - Cylinder No.3
1  4  2  3  2  1  1  2  0  1  1  # cv 7 - Cylinder No.4

# Group 3 - FLOW RESTRICTION DEFINITION

# type  frgd  ncvu  ncvd  ncvfr
1  3  0  1  1     # fr 1 - Pre Filter / Inlet Orifice
3  1  1  3  3     # fr 4 - Cyl.4 Inlet Valve
3  1  1  4  4     # fr 5 - Cyl.3 Inlet Valve
3  1  1  5  5     # fr 6 - Cyl.2 Inlet Valve
3  1  1  6  6     # fr 7 - Cyl.1 Inlet Valve
3  2  6  2  6     # fr 8 - Cyl.1 Exhaust Valve
3  2  5  2  5     # fr 9 - Cyl.2 Exhaust Valve
3  2  4  2  4     # fr10 - Cyl.3 Exhaust Valve
3  2  3  2  3     # fr11 - Cyl.4 Exhaust Valve
1  4  2  7  0     # fr13 - Wastegate Orifice
1  5  2  1  0     # fr14 - Exhaust Orifice

# Group 4 - SHAFT DEFINITION

#Turbo shaft becomes a master shaft now it is NOT geared to crankshaft
```

```
# (goes from 0210 to 0211)
# ncvs   nfrs  load  mast
# cvnums
4    0    2    1        # s1 - Crankshaft
3    4    5    6

# Group 5 - SHAFT JUNCTION DEFINITION

# The turbocharger shaft is free running.
# There are NO shaft junctions in this model.
# sj  sh1  sh2  sh3

# Group 6 - CONTROL VOLUME GEOMETRIC DATA

#    Cylinder Bore = 82.5mm
# Crankshaft Stroke = 82.0mm
#    Con-Rod Length = 130.0mm
# Compression Ratio = 18:2
# gv1    gv2    gv3    gv4    gv5    gv6    gv7    gv8    Ident
0.005    0.0    0.0    0.0    0.0    0.0    0.0    0.0    # 1 - Post I/C / Inlet Manifold
0.0825   0.082  0.13   18.2   0.0    0.0    0.001  0.0    # 3 - Cylinder
0.05     0.0    0.0    0.0    0.0    0.0    0.0    0.0    # 6 - Post Turbine / Exh Pipe Manifold

# Group 7 - FLOW RESTRICTION GEOMETRIC DATA

# gr1  gr2     gr3     gr4      gr5    gr6     gr7    gr8   Ident
1.0  0.0364   0.011   0.003   45.0   354.0   572.0   1     # 4 - Inlet Valve
1.0  0.032    0.011   0.0025  45.0   123.0   367.0   2     # 5 - Exhaust Valve
1    0.005    0.0     0.0     0.0    0.0     0.0     0.0   # 6 - Pre-Filt/Inlet Orifice
1    0.005    0.0     0.0     0.0    0.0     0.0     0.0   # 7 - Exhaust Orifice
1    0.0000   0.0     0.0     0.0    0.0     0.0     0.0   # 8 - Wastegate Orifice

# Group 8 - HEAT TRANSFER GEOMETRIC DATA

# Simple H.T. Model used for Manifolds.
# 3 Wall H.T. Model used for Cylinders.
# mght
1                                                  # Manifolds
# ht1  ht2  ht3  ht4  ht5  ht6  ht7  ht8  ht9  ht10  ht11
1.0  0.22  0.0  0.0  0.0  0.0  0.0  0.0  0.0  0.0   0.0
# mght
3                                                  # Cylinders
```

```
# ht1  ht2  ht3   ht4    ht5   ht6  ht7 ht8   ht9   ht10   ht11
1.0  1.5  353.0 0.0073 0.007 0.174 0.0 0.001 500.0 0.0073 1.1   # Piston
1.0  3.0  353.0 0.0053 0.010 0.048 0.0 0.001 500.0 0.0053 0.1   # Cylinder Head
1.0  3.0  353.0 0.0213 0.010 0.048 0.0 0.001 450.0 0.0    0.0   # Liner
```

Group 9 - HEAT RELEASE GEOMETRIC DATA

```
# Adjust value for Static Injection (hr1) to get desired SOC in results.
# Leave HP injection pipe length fixed at 360mm (EURO3 spec. Bosch VP30 pump).
# When the Fuel Mass Injected (hr3) < 0 (i.e. a minus(-) sign in front of hr3)
# then the simulation is run with the specified Air-Fuel Ratio (hr4).
# Adjust Marzouk-Watson constants C1-C4 (hr9-hr12) to achieve desired shape
# of firing pressure curve.
# Fuel Injected
# Assume Diesel S.G. = 0.842 @ 15 DegC
#                    = 0.830 @ 35 DegC (Injection Temperature of Fuel)
# Conversions
# 0.0000083 kg/cyl/cyc = 10 mm3/shot
# 0.0000125 kg/cyl/cyc = 15 mm3/shot
# 0.0000166 kg/cyl/cyc = 20 mm3/shot
# 0.0000208 kg/cyl/cyc = 25 mm3/shot
# 0.0000249 kg/cyl/cyc = 30 mm3/shot
# 0.0000291 kg/cyl/cyc = 35 mm3/shot
# 0.0000332 kg/cyl/cyc = 40 mm3/shot
# 0.0000374 kg/cyl/cyc = 45 mm3/shot
# 0.0000415 kg/cyl/cyc = 50 mm3/shot
# hr1...hr2.....hr3....hr4..5..6....7.....8....9...10..11..12..13141516171819
717. 0.10  3.520E-05 20.0 0. 0. 42800. 0.068965 1.0 1.0 1.0 1.0 0 0 0 0 0 0 0 0
1.0 0. 0. 0. 0. 0. 0. 0.
```

Group 9a - SCAVENGE GEOMETRIC DATA

```
# sr1 = Perfect Displacement fraction 1-x
# sr2 = Short Circuiting fraction
# These values are ONLY assigned for 2-stroke engine models.
# This is a 4-stroke model - therefore all these values are zero.
# Alternatively, Set the number of scavenge models to 0 in Group 1
# and remove ALL values in this group
# sr1  sr2  sr3  sr4  sr5  sr6  sr7  sr8
```

Group 10 - SHAFT GEOMETRIC DATA

shd1 shd2 shd3 shd4 shd5 shd6 shd7 shd8 shd9 shd10 shd11 shd12

0.1 0.001 0.0 0.0 0.0 0.0 0.0 0.0 0.0 0.0 0.0 0.0

cvph

Engine Cylinder Firing Order 1-3-4-2

0.0 -540.0 -180.0 -360.0

Group 11 - SHAFT JUNCTION GEOMETRIC DATA

Turbo shaft is free-running.

There are NO shaft junctions in this model

Sjd1..2..3..4..5..6..7..8..9..10..11..12..13..14..15..sjd16

Group 12 - VALVE GEOMETRIC DATA

Inlet Poppet Valve

Head Dia. = 36.5mm

Cam Lift = 9.0mm - 0.35mm clearance (cold) = 8.65mm Valve Lift

Seat Width = 3.0mm

Seat Angle = 45 Deg

IVO = 6 Deg BTDC = 354 Deg

IVC = 32 Deg ABDC = 572 Deg

nva = Number of points in data set

ndt = Non-Dimensional Timing

ndfa = Non-Dimensional Flow Area

nddc = Non-Dimensional Discharge Coefficient

23

0.000 0.050 0.100 0.121 0.150 0.179

0.207 0.236 0.271 0.314 0.371 0.500

0.629 0.686 0.729 0.764 0.793 0.821

0.850 0.879 0.900 0.950 1.000

0.000 0.076 0.150 0.223 0.291 0.350

0.400 0.470 0.527 0.544 0.543 0.551

0.543 0.544 0.527 0.470 0.400 0.350

0.291 0.223 0.150 0.076 0.00

1.00 1.00 1.00 1.00 1.00 1.00

1.00 1.00 1.00 1.00 1.00 1.00

1.00 1.00 1.00 1.00 1.00 1.00

1.00 1.00 1.00 1.00 1.00

Exhaust Poppet Valve
Head Dia. = 32.0mm
Cam Lift = 10.0mm - 0.50mm clearance (cold) = 9.5mm Valve Lift
Seat Width = 2.5mm
Seat Angle = 45 Deg
EVO = 57 Deg BTDC = 123 Deg
EVC = 7 Deg ATDC = 367 Deg
nva = Number of points in data set
ndt = Non-Dimensional Timing
ndfa = Non-Dimensional Flow Area
nddc = Non-Dimensional Discharge Coefficient
23
0.000 0.050 0.100 0.121 0.150 0.179
0.207 0.236 0.271 0.314 0.371 0.500
0.629 0.686 0.729 0.764 0.793 0.821
0.850 0.879 0.900 0.950 1.000
0.000 0.062 0.134 0.215 0.290 0.351
0.415 0.468 0.508 0.537 0.556 0.567
0.556 0.537 0.508 0.468 0.415 0.351
0.290 0.215 0.134 0.062 0.00
1.00 1.00 1.00 1.00 1.00 1.00
1.00 1.00 1.00 1.00 1.00 1.00
1.00 1.00 1.00 1.00 1.00 1.00
1.00 1.00 1.00 1.00 1.00

Group 15 - INITIAL CONDITIONS

p / t / eq
ss
In.Man Exh.Man Cyl.1 Cyl.2 Cyl.3 Cyl.4
200.0 256.0 206.0 7690.0 155.0 338.0
314.0 750.0 334.0 1716.0 455.0 907.0
0.0 0.74 0.014 0.4379 0.201 0.573
Crank Speed
2000.0

Group 16 - AMBIENT CONDITIONS

Standard Conditions :- Pressure = 1 Bar = 100 kPa

```
#                Temperature = 25 DegC
# pa     ta     pin     tin      pb
100.0   290.0   200.0   314.0    256.0

# Group 17 - CYCLE SIMULATION & OUTPUT CONTROL

# Solution Control
# ncyct = No.of Cycles
# step0 = Step length in Deg C.A.
# ncyct  step0
6     1.0
# Output Control
# npr0  npr1  steppr  nvp  nfrp  nsp  nnvp  nnfrp  nnsp
6    6    1.0    3    5    1    1     0     0
# mvp / mfrp / msp / mmvp / mmfrp / mmsp
# Summary Printout (odes60.res)
1 3 2                    # Control Volumes
1 2 9 10 11                 # Flow Restrictions
1                        # Shafts
# Detailed Printout (odes61.res, odes62.res,...etc)
3                        # Control Volumes
0                        # Flow Restrictions
0                        # Shafts

# Group 18 - INITIAL CONDITIONS FOR SWIRL SIMULATION
#                IN 4 STROKE DIESEL ENGINES

# BOWL DIA.(M)  BOWL DEPTH1(M)  BOWL DEPTH2 (M)  SWIRL RATIO  FRIC.COEFF.
      0.060        0.0100             0.0016            3.0          0.005

# Group 19 - INITIAL DATA FOR NEW HEAT RELEASE
#              SIMULATION MODEL (AVL MODEL)

# ISH  ICMOD  CF1   CRATE   Alfah2  WH   Alphak2  WK    TOLE    CMOD
  0     0     1.0    0.08    0.5124  0.15   0.7     0.14   0.0001   0.0875
# DELTA   CUMHR   DINJ   pspeed
  0.62        0.95      18.0     2000.0
# WHF   DENF   PRAIL    PCYL    CMIU   DNOZ    TNN  BDUR  TETASOI
 0.557   830.  750.E05  100.4E05  0.763  0.15E-03  5.0   125.   717.0
```

Group 20 - INITIAL DATA FOR SPRAY DEFLECTION AND IGNITION DELAY
SIMULATION MODELS

# ISP	THETA	RAIR1	DIGND	CF	TOL1	ISPDEF	CIGD	CAIGD
1	10.0	0.287	2.0	0.45	0.00001	12	0.257	0.84

C.4: ODES4-4 output files

There are several possible output files from the ODES4-4 package. The step-by-step results, which summarise variation of some parameters such as cylinder pressure, temperature, volume, gross and net rate of heat release, gross and net cumulative heat release, spray tip penetration distance and velocity, spray deflection distance, swirl angular velocity in both main cylinder and combustion bowl, together with zonal distributions of mass, temperature, equivalence ratio, and NO_x in each crank angle step.

The overall results of the basic ODES4-4 package using above input data file are summarised in block-output results file called "ODES60.RES" as table C.2.

Table C.2: ODES4-4 output data file (ODES60.RES)

```
 oo   ddd   eeee   sss
o o   d d   e     s
o o   d d   eeee   ss
o o   d d   e       s
 oo   ddd   eeee   sss
==========================================================================
THERMAL POWER ENGINEERING,SCHOOL OF ENGINEERING UNIVERSITY OF BATH
==========================================================================
AMBIENT CONDITIONS:
Ambient Temp.(degK)290.0 Ambient Press(KN/M2)100.00 Back Press(KN/M2) 256.00
Inlet Temp.(degK)  314.0 Inlet Press(KN/M2)  200.00
--------------------------------------------------------------------------------
SYSTEM PERFORMANCE:
Total Output Power (KW)          0.00  Overall Thermal Eff.          0.0000
Overall B.S.F.C. (Kg/KW.H)     Infinity Total Fuel Flow Rate (Kg/S)  0.00235
--------------------------------------------------------------------------------
```

SHAFT PERFORMANCE:

Shaft Speed (REV/MIN)	2000.0	Shaft Power (KW)	38.64
Shaft Torque (N.M)	184.49		

MANIFOLD:

Temperature (degK) (t.a.)	317.1	Pressure (KN/M2) (t.a.)	199.9
Temperature (degK) (m.a.)	317.1	Pressure (KN/M2) (m.a.)	199.9
Heat Loss (KW)	0.00	Gas Temp (deg K) (htc a)	317.1
Mean H.T.C.(KW/M2/K)	0.2200		

ENGINE SPECIFICATION:

4 Stroke Open Chamber Diesel Engine

Bore (M)	0.0825	Stroke (M)	0.0820
Connecting Rod Length (M)	0.1300	Compression Ratio	18.200

Valve Timing (deg CA):

EVC 367.00 IVC 572.00 EVO 123.00 IVO 354.00

ENGINE PERFORMANCE:

Engine Speed (REV/MIN)	2000.	B.Power (KW)	9.7
I.M.E.P. (KN/M2)	1492.	B.M.E.P. (KN/M2)	1324.0
B.Torque (N.M)	46.18	Charging Eff. amb. 1.7132 inl.	0.9370
Brake Thermal Efficiency	0.3851	Mechanical Efficiency	0.8874
B.S.F.C. (KG/KW.HR)	0.2184	B.S.A.C. (KG/KW.HR)	5.56
Air Flow (KG/S)	0.0149	Air Volume Flow (m3/S)	0.0124
Trapped Air Fuel Ratio	26.08	Overall Air Fuel Ratio	26.79
Delivery Ratio amb. 1.701 inl.	0.930	Charge Purity	0.9797
Max. Cyl. Pressure (KN/M2)	13138.	Max. Cyl. Temperature (deg K)	1713.7
Fuel/cyl/cyc (G)	0.03520	Gas Heat Loss %	19.86

TRAPPED IN-CYLINDER CONDITIONS:

Temperature (deg.K)	345.91	Pressure (KN/M2)	211.26
Equivalent Ratio	0.01901	Mass (KG)	0.00094

Pumping Work (KJ)	-0.0300	P.M.E.P. (KN/m2)	-68.5

HEAT LOSS ANALYSIS:

Thermal Resistance:(deg C/KW):R1,R2,R4,R5,R7,R8,R9,R10

15.65 9.87 0.00 5.51 0.00 91.32 39.31 62.89

Energy Input (KW)	25.11	% Liner Heat Loss	5.20
% Piston Heat Loss	8.87	% Head Heat Loss	5.79
% Friction Loss	4.89	% Output Shaft Energy	38.51

Liner(mean) Temp. (deg K)	396.0	Piston Temp. (deg K)	441.8
Head Temp. (deg K)	500.7	Cooling Water Temp. (deg K)	353.0
Cooling Oil Temp. (deg K)	353.0	% Piston Heat Loss to Oil	3.34
Gas Mean H.T.C (KW/M2.K)	0.531	Gas Mean Temp. (deg K)	675.0
Gas Temp (deg K) (htc a)	1016.2	Piston Node Temp(K)	429.6
% Heat Piston-Liner	NaN	% Total Heat to Water	17.74
% Friction to Water	1.22	% Total Heat to Oil	7.00
% Air-Enthalpy In	18.55	% Gas-Enthalpy Out	49.15

COMBUSTION PARAMETERS: COMPRESSION IGNITION

Static Injection (degree)	717.0	Dynamic Injection (degree)	717.0
Ignition Delay (degree)	1.84	End of Burning (degree)	122.0
Ignition Point (degree)	718.8	Mode of Burning	0.000
Mean Temp During Delay (degK)	933.	Mean Press Dur Delay (KN/M2)	10063.

MANIFOLD:

Temperature (degK) (t.a.)	754.6	Pressure (KN/M2) (t.a.)	256.2
Temperature (degK) (m.a.)	754.6	Pressure (KN/M2) (m.a.)	256.2
Heat Loss (KW)	0.00	Gas Temp (deg K) (htc a)	754.6
Mean H.T.C.(KW/M2/K)	0.2200		

ORIFICE:

Orifice Area (Sq.M)	0.00500	Flow Rate (Kg/S)	0.0596
Exit Temp. (K) (t.a)	314.3	Exit Temp. (k) (m.a)	313.6

VALVE:

Flow Rate (Kg/S)	0.0149	Exit Temp. (K) (t.a)	331.5
Exit Temp. (k) (m.a)	311.0		

VALVE:

Flow Rate (Kg/S)	0.0155	Exit Temp. (K) (t.a)	706.6
Exit Temp. (k) (m.a)	711.3		

ORIFICE:

Orifice Area (Sq.M)	0.00500	Flow Rate (Kg/S)	0.0628
Exit Temp. (K) (t.a)	754.5	Exit Temp. (k) (m.a)	754.5

ORIFICE:

Orifice Area (Sq.M)	0.00000	Flow Rate (Kg/S)	0.0000
Exit Temp. (K) (t.a)	0.0	Exit Temp. (k) (m.a)	0.0
